



The
University
Of
Sheffield.

The role of surface wettability on bubble formation in air-water systems.

Daniel J. Wesley

A thesis submitted in fulfilment of the requirements for the degree of
Doctor of Philosophy

Department of Chemical and Biological Engineering

The University of Sheffield

August 2015

Acknowledgements.

Firstly I'd like to thank Prof. William Zimmerman and Dr Jonathan Howse for providing the opportunity and intellectual support to make this work possible. I'd also like to thank the workshop staff of CBE; particularly Andy Patrick, Steve Blackbourn, Adrian Lumby and Elliot Gunnard and CBE technicians Mark Jones and Keith Penny for continuous assistance. I'd also like to thank Dr Andrew Parnell for help with AFM studies. Special thanks go to Mr Paul Manear at Menear Engineering, Lichfield, Staffs for manufacture of the tank used during this work.

I'd like to thank the other members of the Howse group, namely Alireza Sadeghi, Daniel Toolan, Richard Hodgkinson, Jake Lane and Mahmoud Mohamed for assistance throughout.

I would like to thank my family for the support to reach this point in life. I apologise to Laura for the proof reading tasks endured, it is appreciated. Special thanks are reserved for Charlotte for keeping me motivated and cracking the whip sufficiently in equal measure. Finally, to the man whose Sunday morning outings to various scientific sites probably propelled me into this career, I say thank you Grandad Mike 'Flaxhill' Florendine.

Abstract.

The production of microbubbles is rapidly becoming of considerable global importance with many industries taking advantage of the increased mass transfer rates the bubbles can attain. Many factors have interrelated roles during bubble formation, with effects such as gas flow rate, liquid viscosity, pore size and pore orientation all imparting considerable influence during the formation process. Many of these features have been examined in detail and are relatively well understood. However, the role of surface wettability and the interactions at the gas-liquid-solid triple interface have for the most part been neglected, and it is the role of this wettability that is examined herein.

Utilising the well-studied wet chemistry surface modification techniques of silanes and thiols, many substrates have been modified and the wettability tested. Contact angle goniometry has been utilised to assess the wetting characteristics of each substrate, and the role of surface roughness has been discussed in relation to both the static Young's contact angle and the advancing and receding angles.

Modified porous plates have been used to generate bubbles, with controlled single pore, multiple controlled pore, and multiple randomised pore systems being investigated. A steady flow of air was bubbled into distilled water through the various diffuser plates. It has been observed a contact angle of 90° is of vital importance, with a significant increase of bubble size above the 90° angle, defined as the hydrophobic wetting region. On the contrary, bubble size is greatly reduced below this angle, in the region defined as the hydrophilic region. The effect is seen to increase as the density of pores increases when the plate from which they are emitted is relatively smooth. Upon roughening, the effect is seen to diminish, and mechanisms for this process have been postulated. It is thought that the surface topography disrupts the modifying layers and also physically restricts the growing bubble, preventing the growth of the bubbles emitted from a hydrophobic surface. Attempts have been made to support this hypothesis both qualitatively and quantitatively.

The fluidic oscillator of Zimmerman and Tesar has been examined, with numerous physical features being investigated. The oscillator was then added to the system to investigate the effect of wettability under substantial oscillation. It has been shown that the bubble size emitted from hydrophobic surfaces is significantly reduced when compared to the steady flow system. The effect is believed to be due to the 'suction' component of the oscillatory flow created by the oscillator. It has been seen via high speed photography that the growth rate of the growing bubble slows significantly as the flow begins to switch, before a reduction in size is seen as the gas is removed from the bubble. The opposing forces of buoyancy and suction act to elongate the bubble neck causing break off at a significantly reduced size. Although the diffuser plate is often observed to oscillate like the skin of a drum, this is not the predominant cause of the size reduction. Further experiments have been conducted using a synthetic actuator jet to create a pulsed air flow with only a positive component. Bubble size is not affected in this case, despite frequency sweeps being employed.

Contents

Aims and objectives.	xi
Chapter 1: Introduction.	1
1.1 Microbubbles – an introduction.	1
1.2 Commercial uses of microbubbles.	2
1.2.1 Biofuel from algae.	2
1.2.2 Separation by microflotation.	6
1.2.3 Dissolved Air Flotation.	7
1.2.4 Dispersed Air Flotation.	8
1.2.5 Electroflotation.	8
1.2.6 Microflotation.	9
1.3 Microbubbles in medicine.	11
1.3.1 Targeting.	11
1.3.2 Addition of a payload.	12
1.3.3 Therapeutic targeting and drug delivery.	12
1.3.4 Treatment of thrombosis.	15
1.3.5 Anticancer treatment.	15
1.4 Factors effecting microbubble formation.	16
1.4.1 Pore orientation.	16
1.4.2 Pore size.	17
1.4.3 Surface wettability.	20
1.4.4 Surface tension.	26
1.4.5 Stabilising effect of salts and surfactants.	26
1.4.6 Flow rate.	29
1.4.7 Liquid viscosity.	31
1.4.8 Liquid density.	31
1.4.9 Liquid height.	32
1.4.10 Chamber volume.	32
1.4.11 Thickness of the orifice plate.	33
1.4.12 Gas saturation of liquid phase.	33
1.5 Bubble growth process.	33
1.5.1 Bubble growth from multiple orifices.	35

1.5.2	Microbubbles by fluidic oscillation.	36
1.6	Contact angle and wettability.	42
1.6.1	Wenzel's state.	45
1.6.2	Cassie-Baxter state.	47
1.6.3	The rose petal effect.	49
1.6.4	The lotus leaf effect.	50
1.7	Surface modification by thiol chemistry.	52
1.7.1	Why investigate thiols on gold?	53
1.8	Formation of self-assembled monolayers of thiols on gold.	54
1.8.1	The sulphur gold bond.	54
1.8.2	The mechanism of SAM formation.	55
1.8.3	The structure of SAMs formed on gold.	61
1.9	Factors affecting SAM formation.	63
1.9.1	Alkyl chain length.	63
1.9.2	Solvent effects.	64
1.9.3	Temperature.	66
1.9.4	Adsorption of thiols and disulphides.	66
1.9.5	Fate of the hydrogen atom.	68
1.9.6	Adsorption of functionalised thiols.	69
1.9.7	Defects in the SAM.	71
1.10	Adsorption from the gas phase.	74
1.11	Surface modification by silanes – an introduction.	75
1.12	The silica surface.	76
1.13	The role of water on SAM formation.	78
1.14	The role of temperature on SAM formation.	80
1.15	Immersion time in solution and the adsorption mechanism.	83
1.16	The effect of solvent.	87
1.17	Packing of the self-assembled monolayer.	92
1.18	Stability of the silane SAM.	93
1.18.1	Stability of the silane SAM compared to other monolayers.	93
1.18.2	Stability of SAM under ambient conditions.	94
1.18.3	Stability of SAM under heating.	94
1.18.4	Stability of SAM in water and organic solvent.	94
1.18.5	Stability of SAM in acid or base.	95

1.18.6	The effect of baking.	95
1.19	SAM formation from trichlorosilanes and trialkoxysilanes.	96
1.20	Modification of alumina by silanes.	97
1.21	References	98
Chapter 2: Experimental techniques and materials.		110
2.1	Experimental techniques.	111
2.2	Physical vapour deposition.	111
2.2.1	Electron beam evaporation.	111
2.2.2	DC sputtering.	112
2.3	Plasma cleaning.....	114
2.4	Contact angle goniometry.....	115
2.5	Atomic Force Microscopy.	115
2.6	Scanning Electron Microscopy.	116
2.7	Materials and chemical abbreviations.....	118
2.7.1	Chemicals	119
2.7.2	Porous substrates	121
2.8	References	123
Chapter 3: Physical and chemical Modification of a surface.		124
3.1	Surface modification by silanes and thiols.....	125
3.2	Experimental.	126
3.2.1	Modification of silicon wafer by silanes – the effect of piranha immersion time. 126	
3.2.2	Silane treatment after Piranha cleaning.	127
3.2.3	Modification of silicon wafer by silanes – wafer with <5nm RMS.	127
3.2.4	Modification of silicon wafer by thiols – the effect of surface RMS and deposition type.	128
3.2.5	Polished wafer investigation.	129
3.2.6	Steel disk investigation.	129
3.2.7	Measuring contact angle hysteresis.	130
3.2.8	Spin coating and metal deposition for SEM analysis.	130
3.3	Results and discussion.	131
3.3.1	Effect of solvent type on Silane modification.	131
3.3.2	Effect of Piranha immersion time on Silane modification.	136
3.3.3	Effect of Silane solution immersion time on Silane modification.	137

3.3.4	Silane modification of a highly polished Si wafer.	140
3.3.5	Effect of surface roughness on the thiol modification of Silicon wafers.	141
3.3.6	Effect of physical vapour deposition type on the modification of Silicon wafers. 143	
3.3.7	Modification of rolled steel disks with thiols.	145
3.3.8	Contact angle hysteresis and its relation to the Young's contact angle.	146
3.3.9	SEM comparison of Ebeam and DC sputter coating.	152
3.3.10	AFM comparison of substrates.	154
3.4	Conclusions.	159
3.5	References.	160
Chapter 4: Bubbling under steady flow.		162
4.1	Experimental.	163
4.1.1	Preparation of controlled pore, rolled stainless steel disks.	163
4.1.2	Preparation of steel sinters.	164
4.1.3	Preparation of pointfour ceramic diffusers.	165
4.1.4	Bubbling under steady flow.	167
4.2	Results and discussion.	168
4.2.1	Effect of surface chemistry on bubbles emitted from a single 250 μm pore. ...	168
4.2.2	Effect of surface chemistry on bubbles emitted from an array of 250 μm pores. 173	
4.2.3	Effect of surface chemistry on bubbles emitted from a steel sinter with 5 μm pores. 178	
4.2.4	Effect of surface chemistry on bubbles emitted from a ceramic 'pointfour TM , sinter. 181	
4.3	Conclusions.	193
4.4	References.	196
Chapter 5: Bubbling under oscillating flow.		198
5.1	Synthetic actuator jets.	199
5.2	The fluidic oscillator.	200
5.3	Experimental.	205
5.3.1	Generation of an oscillating flow.	205
5.3.2	Preparation of controlled pore, rolled stainless steel disks.	207
5.3.3	Preparation of steel sinters.	208
5.3.4	Preparation of pointfour ceramic diffusers.	209
5.3.5	Bubbling under oscillatory flow.	210

5.4	Results and discussion.	211
5.4.1	The synthetic actuator and its effect on bubble size.	211
5.4.2	The effect of fluidic oscillation on bubble formation.	214
5.4.3	Effect of surface chemistry on bubbles emitted from a single 250 μm pore under an oscillating flow.	218
5.4.4	Effect of surface chemistry on bubbles emitted from an array of 250 μm pores under an oscillating flow.	229
5.4.5	Effect of surface chemistry on bubbles emitted from a steel sinter with 5 μm pores under an oscillating flow.	234
5.4.6	Effect on surface chemistry on bubbles emitted from a ceramic 'pointfour TM ' sinter under an oscillating flow.	235
5.5	Conclusions.	237
5.6	References.	239
Chapter 6: Conclusions and future work.		241
6.1	Conclusions.	242
6.2	Future work.	245
Chapter 7: Appendix.		247
7.1	The evolution of silicon cleaning technology.	248
7.2	Surface created by variations in cleaning.	254
7.3	References.	255
7.4	Derivations.	256
7.5	Publications.	257

Aims and objectives.

Over recent years microbubbles have begun to be utilised in a variety of industries, such as medical imaging, biofuel production and drug delivery. Many studies have been published on the production of small bubbles but there is little work on the effect surface chemistry has upon the formation process. This work aims to alleviate this issue and provide a thorough insight into the effect in the most commonly used system, air-water.

Beginning with a selection of modification techniques, several systems are investigated to discover the simplest, most reproducible method of surface modification, with the aim of producing a range of wettabilities ranging from hydrophilic (0° contact angle) to hydrophobic (110° contact angle). Different chemical techniques are discussed to provide a wide range of options that may be utilised to suit the broad range of diffuser materials used in both research and industrially.

Following the discussion of modification techniques, bubble formation under steady flow is discussed. Beginning with controlled pore systems, bubble formation is examined under a series of flow rates to discover the effect of wettability. Following this, industrially useful sintered diffusers are examined to investigate whether any effects observed in the controlled pore systems remain when switching to more commercially related ones.

Finally an oscillatory flow system is used to investigate the effect of wettability under oscillating flow conditions. The same controlled and sintered materials are examined and comparisons made between the steady flow and oscillatory flow systems.

Chapter 1: Introduction.

1.1 Microbubbles – an introduction.

Since the mid 1990's bubbles have become a 'hot topic' in engineering, with the number of applications growing and diversifying into a wide range of areas. Specifically the use of very small bubbles has become of great interest, with microbubbles, defined by the size range of 1 micrometre to 999 micrometres, being extensively studied. The current applications of microbubbles are wide and varied with industries such as pharmaceuticals, food technology, biotechnology and medicine taking advantage of bubble properties.

The reason microbubbles are so desirable is due to their ability to facilitate high levels of mass transfer. Mass transfer, the movement of mass from one location to another, is directly related to the interfacial area between two locations/ phases etc. This is characterised by Equation (1) below.

$$J = K_l S (c_g - c_l) \quad (1)$$

Where J is the interphase mass transfer rate (moles per second), K_l is the mass transfer coefficient (m/s), S is the interfacial area (m^2) and c_g and c_l are the molar concentrations of gas and liquid respectively. [1]

As can be seen from Equation (2), the ratio of the surface area of the bubble (S) to the volume of the bubble (V) resolves to an inverse relation to the bubble radius (r). Therefore, as the radius decreases, the ratio of S/V increases, and thus for a constant volume of gas, the surface area increases, which facilitates more efficient mass transfer.

$$\frac{S}{V} = \frac{4\pi r^2}{\frac{4}{3}\pi r^3} = \frac{3}{r} \quad (2)$$

Despite the increasing desire to use microbubbles, control of the formation process and size is still not fully understood due to the complex nature of microbubble generation. It is therefore still difficult to achieve low cost, energy efficient microbubble production on the large scales required by the various industrial applications. Commercial applications of microbubbles are prevalent in some specific instances however, and it is these applications and the fundamentals of microbubble formation on which this section of the review will be based.

1.2 Commercial uses of microbubbles.

1.2.1 Biofuel from algae.

Over recent years, the technological demands of the world have evolved greatly, with issues such as greenhouse gas emission becoming of high importance. The movement away from fossil fuels into cleaner forms of energy is currently at the forefront of science and engineering due to the unsustainability and environmental cost of their use. As of 2008, the global demand for liquid fuels such as oil made up around 66% of the total global demand for energy. [2] Despite this, the majority of renewable energy sources such as solar power, wind energy, hydroelectric and geothermal, all focus on production of electricity. As a result, more

Chapter 1: Introduction.

and more attention is being placed on biofuels, such as biodiesel, to satisfy the energy requirements of the world. Unfortunately the current processes are not very efficient at converting solar energy to biofuel. For example, Schenk [2] claims that if current biofuel crops were grown on all arable land on the planet - assuming 29.2% of Earth is land, 13% of which is arable - only 1% of the solar power would be converted to biomass, and 20% of this would be utilised as biofuel. This would still account for less than 50% of the current global energy demand.

Much of the current biofuel is produced from higher plant life that leads to the inefficiency outlined. It is for this reason that algae is of current interest to the scientific community, as it has the ability to efficiently convert solar energy into cellulose, oils and starch in high yields. [2-4] Furthermore, algae has been shown to be able to produce other forms of fuels such as glycogen and hydrogen. These have been discussed in the literature. [2, 5-8]

In order to maximise the biofuel yield from algae, the photosynthesis process must be optimised by ensuring the algae is exposed to high levels of carbon dioxide (CO₂) and sunlight. Several types of bioreactor have been designed to achieve this, with numerous examples of bubble columns and stirred tank bioreactors in the literature. Zimmerman et al [1] have commented on the design of an Airlift Loop Bioreactor (ALB) and this has been reviewed more thoroughly by Jones. [9] These ALBs are perceived to be more efficient than the other variants used for algal growth and they hold great promise for further study. [1] A schematic of such an ALB designed by Zimmerman for the use in algal growth is shown in Figure 1-1. [10]

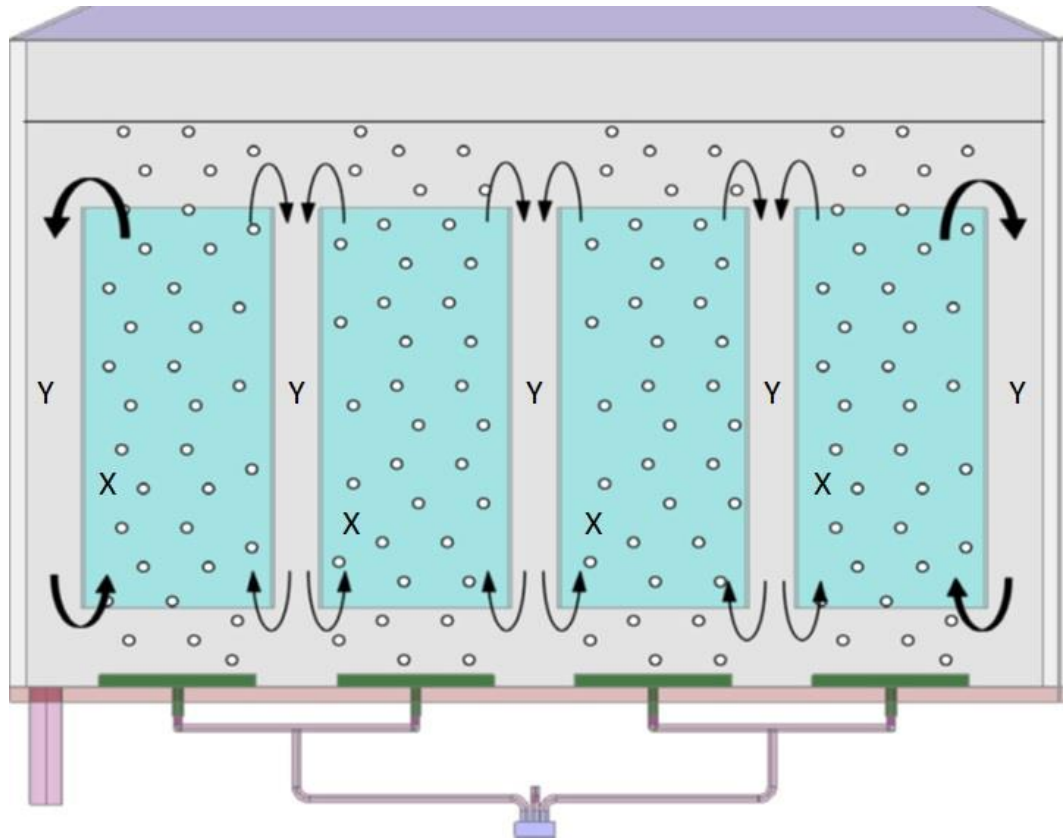


Figure 1-1 The design of an airlift loop bioreactor designed to promote mixing and proliferation of microalgae. The regions marked X are the 'riser regions' and those marked Y are the 'downcomer regions'. [10]

The reactor has been designed to promote mixing of the solution by microbubbles. The bubbles are created by an airflow through porous membranes fed by the fluidic oscillator of Zimmerman and Tesar, [11-14] discussed further in section 5.2. This system creates microbubbles with a mean diameter of 300 μm and allows efficient mass transfer of CO_2 to the growing algae. Work by Hanotu [15] and Ying [16] has indicated growth enhancement of algae by 30-40% with microbubbles. Hanotu showed that both microbubbles and fine bubbles (1-2 mm) saturated the solution with CO_2 , with steady growth of the algae being observed over a two week period when microbubbles were used. However, a plateau and then death region was observed when fine bubbles were used. This indicates that one of two mechanisms was occurring. The first is that the microbubbles can remove deleterious waste oxygen, generated

Chapter 1: Introduction.

by the algae during growth, more efficiently than the fine bubbles. Perhaps a less obvious consideration is the access to light. Areas away from the walls and top of the reactor would normally experience far less light than is necessary to sustain growth. However, the design of this ALB allows the algae to be carried to the surface of the reactor from the lower areas via the riser regions (X in Figure 1-1). The carrier bubbles then burst at the surface and drop the algae over the downcomer regions of the reactor (Y in Figure 1-1). The solution in these areas is denser than that in the riser regions and so the algae sink to the bottom of the reactor column. This rise and fall creates a continuous stirring motion within the reactor, drawing falling algae back into the riser region and as a result, periodically bringing it into contact with the light and promoting growth.

Zimmerman [10] carried out a pilot scale study on algae grown using the exhaust gases generated by the combustion of off-gases formed during steel production. Figure 1-2 shows how the levels of CO₂ and O₂ vary with time during an algal growth cycle. It can be seen that the levels of oxygen in the reactor fall quickly to the level inherent within the dosing gas upon commencement of bubbling. This shows that the microbubbles efficiently strip waste oxygen from the solution, promoting algal growth. It is also interesting to note the level of CO₂ in solution does not reach that of the dosing gas. Zimmerman postulates this is due to the absorption of a portion of the CO₂ by the algae. This would therefore show that the process is not limited by mass transfer of CO₂ and instead it is a combination of the oxygen stripping and the stirring motion of the bubbling that allows more efficient algal growth.

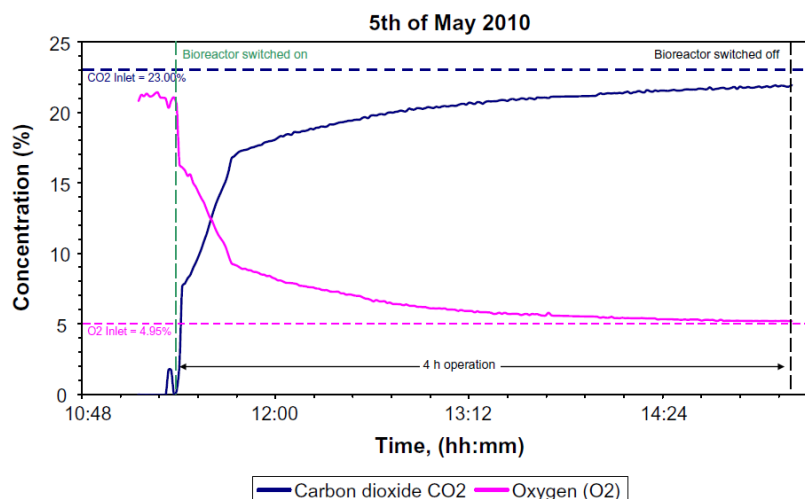


Figure 1-2 A study conducted on 5th May 2010 to investigate the uptake of CO₂ and the stripping of O₂ by microbubbles. The levels of CO₂ in the exhaust gas was a fairly constant 23% with O₂ levels around 5%. It was noted that the O₂ was efficiently stripped from solution at 80L/min flow rate of exhaust gas into the reactor. [10]

1.2.2 Separation by microflotation.

Flotation has become an important technique in several areas, ranging from oil emulsion separation [17] to yeast harvesting and dewatering [18] and colloidal particle separation from aqueous solutions. [19] The key to flotation is the generation of suitably sized bubbles that adhere to the hydrophobic particles and carry them to the surface.

Algal separation is one of the key challenges to commercial viability of biofuels. Gudín estimates that the harvesting step can account for around 20-30% of the overall production cost for algae, [20] although Molina [21] estimates that the recovery cost could be much higher: up to 60% of the overall cost. Historically the closest technique to flotation was separation by flocculation and bioflocculation followed by sedimentation. A development using the Jameson cell in an Induced Air Flotation (IAF) step, could reach high yields of up to

98% algal separation. Other techniques such as Dissolved Air Flotation (DAF) and Dispersed Air Flotation have also been tested as possible routes for algal separation. However, all of these techniques have drawbacks when compared to microflotation. They will be briefly discussed below.

1.2.3 Dissolved Air Flotation.

Dissolved Air Flotation (DAF) is probably the most widely used flotation technique and is based on Henry's Law (Equation (3)) where C is the solubility of the gas at a fixed temperature (mol/L), K_H is the Henry's law constant (mol/atm·L) and P is the pressure of the gas (atm).

$$C = K_H P \quad (3)$$

The process involves pumping gas into the liquid at high pressure, usually 4-6 bar [19, 22], to supersaturate the solution. As soon as the pressure drops, bubbles nucleate in the solution. This leads to microbubble generation, reported to be in the range of 10-120 μm in diameter, with a mean size of 40 μm [22], although bubble size has been shown to reduce with increasing pressure. Despite the small size range, DAF is very energy intensive due to the high pressures needed to saturate the solution with around 90% of the total energy used during the recycling and repressurisation of the solution. [17]

1.2.4 Dispersed Air Flotation.

Dispersed air flotation creates bubbles at the bottom of a column by forcing compressed air through a porous plate or nozzle. Surfactant is added to the solution to increase particle hydrophobicity and coagulate flocs of particles for removal, with the generated bubbles adhering to these flocs and drawing them to the column surface. The main drawback of this technique is difficulty in forming small, monodisperse bubbles. Bubble size is dependent on pore size and numerous sizes have been reported in the literature. However, reducing the pore sizes is not a guaranteed method of producing small bubbles (as will be discussed in section 1.4.2). In addition, reducing pore size leads to an increase in pressure to induce bubble formation, and also leads to an increase in friction and hence an increase in energy usage. [19, 22]

1.2.5 Electroflotation.

Electroflotation is a technique often used in the mineral industry to separate fine particles from solution. In this technique, a current is applied to the aqueous solution and the water is split, producing bubbles of hydrogen gas at the cathode and bubbles of oxygen at the anode. Bubbles have been reported in the range of 22-50 μm depending on conditions. However, this technique is limited to solutions of water, as well as by the high voltages needed to electrolyse water.

1.2.6 Microflotation.

Microbubble generation by a robust technique, such as the fluidic oscillator systems presented by Zimmerman and Tesar [11-14], have proven to be a breakthrough in energy efficient separation. Tailoring conditions such as flow rate, pressure and frequency, the bubble size can be tuned to meet the specific needs of each individual system. In addition, the lack of moving parts and robustness of the oscillator leads to energy usage that is 2 or 3 times lower than that used in DAF and dispersed air flotation for example. [19]

In the work by Hanotu [19], microflotation was presented as a viable alternative for algal separation. This work found that separation efficiencies of more than 96% could be achieved with the fluidic oscillator. Interestingly, the work also investigated the roles of pH and coagulant concentration on separation efficiency, as well as particle size effects. The coagulants $\text{Al}_2(\text{SO}_4)_3$ and $\text{Fe}_2(\text{SO}_4)_3$ were used in the study, with increasing concentrations of the two coagulants leading to increasing recovery efficiencies. This was attributed to the creation of larger flocs of algae by the increasing coagulant concentration. These large flocs have a higher probability of collision with the rising microbubbles and as a result, there is an increased probability of adhesion to the bubbles, entrapment of the bubbles by the particles and particle entrapment by the bubbles, thus promoting the rise of the flocs. pH also plays an important role in this process. At pH 6, the coagulants dissociate in solution, forming Al^{3+} and Fe^{3+} as the dominant species. These high positive charges readily stabilise the negative charges of the algae, bringing the overall charge close to zero. This means repulsion between flocs is reduced, promoting larger particle size formation, which as discussed promotes recovery. In addition, this also promotes adhesion to the negatively charged bubbles and facilitates rise. Hanotu noticed that under more basic conditions of pH 7-8, the increased hydroxyl (HO^-) concentration leads to neutralisation of the positively charged metal species in solution. This in

turn leads to less floc stabilisation and thus lower recovery efficiency, dropping to less than 80%. As pH increases further to pH 9, the hydroxyl concentration rises further, with increased adhesion to the algal flocs. This leads to large gelatinous clumps being formed in solution, which again are preferentially removed by flotation. It was noted that the acidic conditions (pH 6) gave higher recovery efficiency than the basic (pH 9) conditions.

Other uses of microbubble flotation have been investigated in literature. Oil emulsion separation exhibits many of the same characteristics as algal separation. When Hanotu [17] compared the use of fine bubbles (≈ 3 mm) to microbubbles, the fine bubbles lead to poorer separation of the emulsion. It is believed that the fine bubbles interact more vigorously with the oil flocs than the microbubbles, [17, 19] and in the process tend to break them apart. As is the case with algae, the larger flocs have a higher buoyancy and collision probability, and separation is inversely related to bubble size. Unlike the algal case however, addition of surfactant such as sodium dodecyl sulphate (SDS) to the emulsion leads to a greatly reduced separation efficiency. The surfactant acts to stabilise the small oil drops in the aqueous phase and as such the droplets remain small. These small droplets separate less efficiently than the large unstabilised drops. Microflotation is a slower separation technique than DAF, but the much lower energy cost makes it a viable industrial technique.

Yeast is also an important product commercially, with uses in bioethanol production, as feedstock in alcoholic beverage production, as animal feed and in the bioremediation of wastewater. [18] Similar to algae, yeast must be harvested and dewatered after culturing. Interestingly, bubbles in yeast solutions tend to be smaller than those in pure water under equivalent conditions. This is believed to be due to lower surface tension of the yeast solution. Separation is slightly increased when microflotation is used over sedimentation. However, this small increase in efficiency leads to large savings when scaled up. The bubbles also play a role in drying the yeast. During harvesting the yeast is carried to the top of the tank, where

continued bubbling builds up a layer of yeast at the liquid/ air interface. Continued growth of this layer by further bubbling leads to a crushing effect at the surface, meaning a portion of the layer is driven out of the liquid. This leads to a reduction of the moisture content of the harvested yeast by around 7%, meaning the drying process is more efficient.

1.3 Microbubbles in medicine.

Small bubbles used as ultrasound contrast enhancers were first discussed in relation to echocardiology of the aortic root by Gramiak in 1968 [23]. The bubbles were produced without a shell but were very short lived, so efforts have been made to stabilise the gas liquid interface. [24] To this effect, lipids are predominantly used as they can be chosen from an almost unlimited range to carry out many tasks; binding to specific drugs, genes and other compounds, expressing ligands and providing resistant layers. The lipid shell is also able to compress, rupture, buckle and repair during use in ultrasound techniques. More recently, other surface stabilising molecules have been added to the bubble shell. Both saccharin and proteins have been attached to bubbles, with the first commercially available microbubble contrast agents (Albunex and Optison) approved for use by the FDA in the 1980's.

1.3.1 Targeting.

Specific targeting of receptors can be achieved by incorporating specific functionality into the microbubble shell. For example, cationic groups within the shell can interact with tissues undergoing ischemia/reperfusion or inflammation by interactions with the immune system. These interactions, although simple in nature, are not specific enough for most medicinal uses. However, ligands may be incorporated to encourage more specific binding via

ligand receptor interactions. Attachment of the ligand to the bubble can be done in two ways. The first is to attach a biotinylated ligand to a biotinylated microbubble via an avidin bridge. This technique is straightforward but due to immunogenicity, it is not viable in humans. However, it does provide a proof of concept pathway. The second method is via covalent linkage to the ligand, which can be performed before or after bubble formation. Several ligands have been bound to microbubbles, including vitamins, antibodies and peptides. However, at the time of writing, all of these have limitations, ranging from short shelf life to temperature sensitivity. [24]

1.3.2 Addition of a payload.

Another use of microbubbles is targeted drug delivery to a specific site. Therapeutic incorporation into the lipid shell has been shown to be possible by the addition of oils into the lipid that can dissolve hydrophobic or lipophilic drug molecules. This technique has shown some promise in vitro and has been discussed further by Ferrara et al. [24] Additionally, drug molecules may be attached electrostatically or by ligand interactions as described above.

1.3.3 Therapeutic targeting and drug delivery.

The interaction of microbubbles with ultrasound puts them in a very unique position with regards to drug delivery. In the reverse of work by Czerski [25] who examined the sound waves emitted by the deformation of bubbles leaving nozzles, several groups have examined the effect ultrasound has on the shape of microbubbles, both in free space and in contact with walls/ boundaries. [26-28] It can be seen from Figure 1-3 that the application of an ultrasonic

frequency (1.7MHz) to the microbubble induces oscillations of various nodal forms. [27] This interaction is of vital importance for drug delivery.

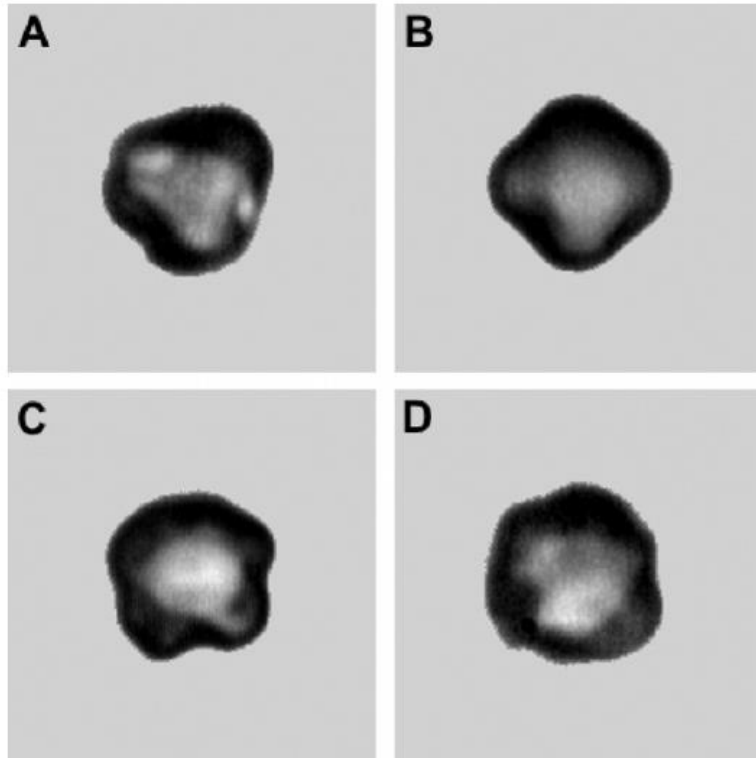


Figure 1-3 A and B show the identifiable nodes (3 and 4 respectively) of an ultrasound contrast microbubbles. C and D show unidentifiable nodes due to the mixing of various nodes within a single bubble. The excitation frequency was 1.7 MHz. [27]

There are several ways in which a drug payload can be delivered by, or in conjunction with, microbubble contrast agents. These mechanisms were represented well in the work by Ferrara [24] and are shown in Figure 1-4.

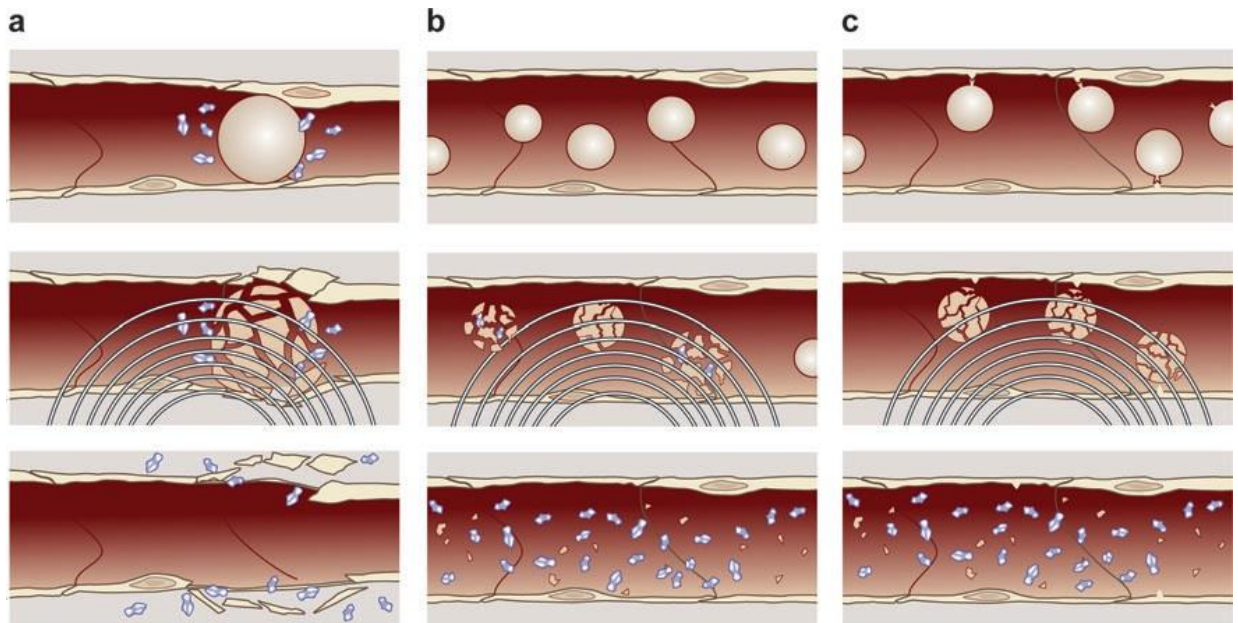


Figure 1-4 a) Microbubbles are circulating through blood vessels along with drug molecules (shown in blue) until an ultrasonic pulse excites the bubble, causing an expansion and rupturing the vessel. The drug can then exit the vessel to the target site. b) Drug laden microbubbles are circulating until the application of an ultrasonic pulse. This ruptures the bubbles and liberates the drug. Because the sound is applied specifically, the drug is delivered locally to a specific region. c) The microbubbles containing a specific ligand are freely circulating until coming into contact with the corresponding receptor binding site. Once bound, an ultrasound pulse is delivered, rupturing the bubble and delivering the payload.

The first method (Figure 1-4a) involves bubbles being injected into the blood stream along with the pharmaceutical agent. Targeted ultrasound is then applied, and the bubble oscillations within the smaller blood vessels perturb the vessels wall structure, allowing the extravasation of the drug molecules. This technique has been confirmed by feasibility studies using a variety of particles and dyes. The second method (Figure 1-4b) involves impregnation of the bubble with the pharmaceutical agent. The bubbles circulate until a targeted pulse of ultrasound is applied, causing bubble rupture in the specified area. This technique increases local drug concentration. Neither of these techniques prevents the spread of the pharmaceutical through the bloodstream however, meaning increased doses are required. The

third technique adds a receptor to the bubble surface, with its corresponding marker within the target. Target-receptor binding then proceeds before the application of ultrasound leading to increased specificity and lower doses. [24]

1.3.4 Treatment of thrombosis.

The first targeted microbubbles for thrombosis were reported in the late 1990's [24, 29, 30] and involved the avidin biotin modifier discussed above. These modifications and targeting increased the observed signal intensity fourfold. More recently, an arginine glycine aspartic acid (RGD) modifier has been used to increase bubble targeting. Upon attachment, the region is insonified by low frequency (1-2MHz) ultrasound. At these frequencies, the bubbles expand, contract and oscillate, disrupting the fibrin of the thrombosis and leading to increased break up. Thrombolytic drugs may also be incorporated to add to the mechanical destruction of the clot.

1.3.5 Anticancer treatment.

One of the biggest problems with current cancer therapy is the systemic toxicity of the drugs used. As discussed above, microbubbles allow for hydrophobic and lipophilic drugs to be incorporated into the bubble shells for delivery. It has been shown that these encapsulated drugs have a tenfold decrease in toxicity to the surrounding tissues when compared to free pharmaceuticals. [24] Although in the early stages of development, the ability to attach a wide range of receptor molecules to the bubble surface may lead to the creation of targeted anticancer therapies in the near future.

Of course, there are numerous challenges and issues to overcome before microbubble contrast agents and drug delivery systems become viable on a large scale. It was recommended in 1998 by the FDA that the dose of Paclitaxel (a commonly used anticancer drug) should be around 175 mg/ml. However, just 4 mg of the drug can currently be dosed into the lipid layer of the bubble. Of the 175 mg, only 5 mg is believed to be delivered to the therapeutic site and as a result, microbubble delivery to a targeted site may still hold promise. Despite the promise, the full effects of microbubbles in the body are not fully understood and more work is needed to rectify these problems before applications become clinically viable.

1.4 Factors effecting microbubble formation.

1.4.1 Pore orientation.

One of the most obvious aspects of bubble formation is the orientation of the porous plate, diffuser, nozzle etc. Scargiali [31] carried out work on a variously inclined nozzle, in which data was presented to show how altering orientation between vertical (upwards) and 150° from vertical affected bubble size. Perhaps unexpectedly, nozzle orientation was shown to have little effect, with the author claiming the effect of orientation was negligible at all flow rates and pore sizes. On the other hand, Yasuda [32] believes a smooth horizontal membrane provide the best orientation for small bubble production. On an inclined surface, bubbles can drift along the surface without fully detaching. Although subsequent detachment from the pore may occur, the bubble may remain sitting on the surface, until a following bubble forms and coalescence occurs. A horizontal pore removes this possibility and thus leads to smaller bubbles. Das [33] goes further and presents data showing that bubble volume from an orifice

within a plate increases with increasing tilt of the plate from horizontal. They indicate that the buoyancy force acting on the bubble is always vertical. However, the momentum of the bubble is always normal to the plate surface. As the tilt angle increases, the difference in direction of these two forces increases, leading to larger bubbles. Changjun [34] presented data indicating that bubbles formed at horizontal orifices are also smaller during early growth. Despite the large number of experiments investigating bubble formation, very few have investigated orifice orientation as a factor. However, of the data that does exist, it seems the tentative consensus is that smaller bubbles are produced from horizontally oriented plates. Nevertheless, the data is by no means comprehensive.

1.4.2 Pore size.

Several groups have commented on the relationship between bubble size and the pore size from which it is formed. [32, 35-38] There is a general agreement that bubble size increases with pore size. However, due to the dynamics of bubble formation, other factors can act to mask the true effect of pore size. Xie [36] showed that as pore diameter increased, the departure time of the bubble increased also. This would infer that bubble size increases with pore size. Interestingly, a smaller bubble departing from a small pore will result in a reduced gas pressure drop, and the subsequent bubble will form more readily. This was observed by the reduced wait time between bubbles and the pairing effect, discussed later. This short wait time leads to an increased probability of coalescence, meaning care must be taken to analyse and interpret data.

Yasuda [32] discusses the effect in more detail. Although they agree with the common consensus, they point out the important role of surface tension and its link to surface

wettability. In the domain where the contact angle (θ) is less than 45° , the bubble is restricted to the pore, and its volume is therefore dictated by the pore size. Conversely, in the domain where $\theta > 45^\circ$, the bubble can spread past the pore boundary and the contact area with the surface is increased. This increase in turn leads to a rise in the buoyancy force needed to detach the bubble from the surface and as a result, the volume increases. In fact, in this region, bubble size is independent of pore size, and decreasing the size of the orifice will not necessarily lead to a decrease in bubble volume. Yasuda points out that the bubble diameter is always greater than the diameter of the pore, and as such a high density of closely packed pores will lead to an increase in the likelihood of coalescence. Benzing [37] argues that the adhesive force of the bubble when attached to the pore is given by Equation (4).

$$F_A = \pi D \sigma \cos \theta \quad (4)$$

Where F_A is the adhesive force, D is the diameter of the pore, σ is the surface tension of the liquid-gas and θ is the contact angle of the forming bubble. Equation (4) indicates that as the diameter increases, the effect of contact angle increases (when $\theta \neq 90$). Therefore, it is actually the contact angle that is of greater importance to bubble size than the orifice diameter. This is in general agreement with Yasuda, although the key contact angle is open for debate.

In addition to the experimental data, numerical models to predict bubble size have been presented. Jamialahmadi correlates many in [39], and concludes that there is no coherent argument that accurately predicts bubble size under all conditions. This is typified by some groups [40, 41] arguing that orifice diameter plays no role in dictating bubble size, and

others [38] believing that the relationship is of great importance. Davidson [38] presents a hydrostatic equation to predict bubble size when a low gas flow rate passes through a pore above a reasonably small chamber (although no firm dimensions are ever presented). The relation is shown below in Equation (5).

$$V_b = \frac{2\pi r \sigma}{(\rho_l - \rho_g)g} \quad (5)$$

Where V_b is the bubble volume, r is the orifice radius, σ is the surface tension of the liquid phase, ρ_l and ρ_g are the densities of the liquid phase and gaseous phase respectively and g is the acceleration due to gravity.

Several groups believe the effect of pore size is different under varying conditions. The common belief amongst this group is that at very low flow rates, bubble volume is dictated primarily by orifice diameter and surface tension effects. [42, 43] As flow rate increases to intermediate levels, the consensus is less clear, with Leibson [42] of the belief that bubble size is still dependent on orifice diameter. Hayes [43] on the other hand, make no comment on the dependence on orifice size, but state bubble volume becomes more dependent on flow rate. At higher flow still, the effect of pore size decreases. These observations are difficult to compare however, as they are qualitative in nature and no direct comparison can be drawn with any confidence.

Few people [31] believe orifice size has no effect on bubble size. It is important once again to note the differences in experimental methods before drawing conclusions. There is a suggestion that bubble formation differs between microscale (<1 mm) and miniature scale (1-

10 mm) orifice diameters. There also appears to be discrepancies between data collected from capillaries, nozzles and porous plates. [44-48] It is most likely that orifice diameter plays an important role in bubble formation, but its effect can be masked by other contributory factors such as surface wettability.

1.4.3 Surface wettability.

Despite many groups alluding to the importance of wettability on bubble formation, very few fundamental studies exist on the effect of surface wettability on bubble size, especially in aqueous systems. Some studies exist describing the effects in molten metals, such as mercury and pig iron, but this review focuses predominantly upon water based bubble formation. [49]

It is important to recognise that the type of substrate from which the bubbles are emitted plays an important role in the formation. Bubbles created by a nozzle, capillary or needle have a small surface around the orifice. This means the effect of surface wettability is greatly reduced, and in some cases, negated altogether. This is exemplified by Zhu, [47] who used a glass capillary and a Polytetrafluoroethylene (PTFE) capillary. They found the departure time from the glass capillary was longer than that of the PTFE, which goes against the common belief outlined below.

Gerlach [50] modelled the process of bubble formation at a submerged orifice, finding that if the bubbles' instantaneous contact angle during growth (defined in [50] Figure 1) becomes equal to the Young's contact angle, found under equilibrium conditions, the bubble can grow outwards from the pore onto the surface of the diffuser plate. Kukizaki [35] corroborates this belief, and suggests that maintaining the surface contact angle at $\theta < 45^\circ$

prevents the bubble from growing past the orifice boundary. This view is supported by Yasuda. [32]

Many groups agree that the bubble volume at detachment from a surface with $\theta > 90^\circ$ is significantly larger than those from surfaces with $\theta < 90^\circ$ [48-51]. Corchero [52] carried out wettability experiments using a combination of acrylic and Teflon plates, drilled to contain a single pore of between 0.5-1 mm in diameter. They reported static contact angles of 68° and 123° respectively. To create an intermediate surface with $\theta = 90^\circ$, domestic Vaseline was smeared onto the surface. Although this methodology is somewhat primitive, several important factors were established. The first was that surface wettability played an important role in bubble formation. The volume of the bubbles produced from the acrylic sheet ($\theta = 68^\circ$) is lower than that of the Vaseline ($\theta = 90^\circ$) and the Teflon ($\theta = 123^\circ$). However it is important to point out that the flow rates for the three graphs are not equivalent, which is likely to influence the result. In addition, the scale of each graph is not the same, with the acrylic graph (Figure 1-5a) on a much smaller time scale than the other two. It is assumed that this is due to the bubble detaching, but this is not confirmed in the text. The data presented by Corchero is shown in Figure 1-5.

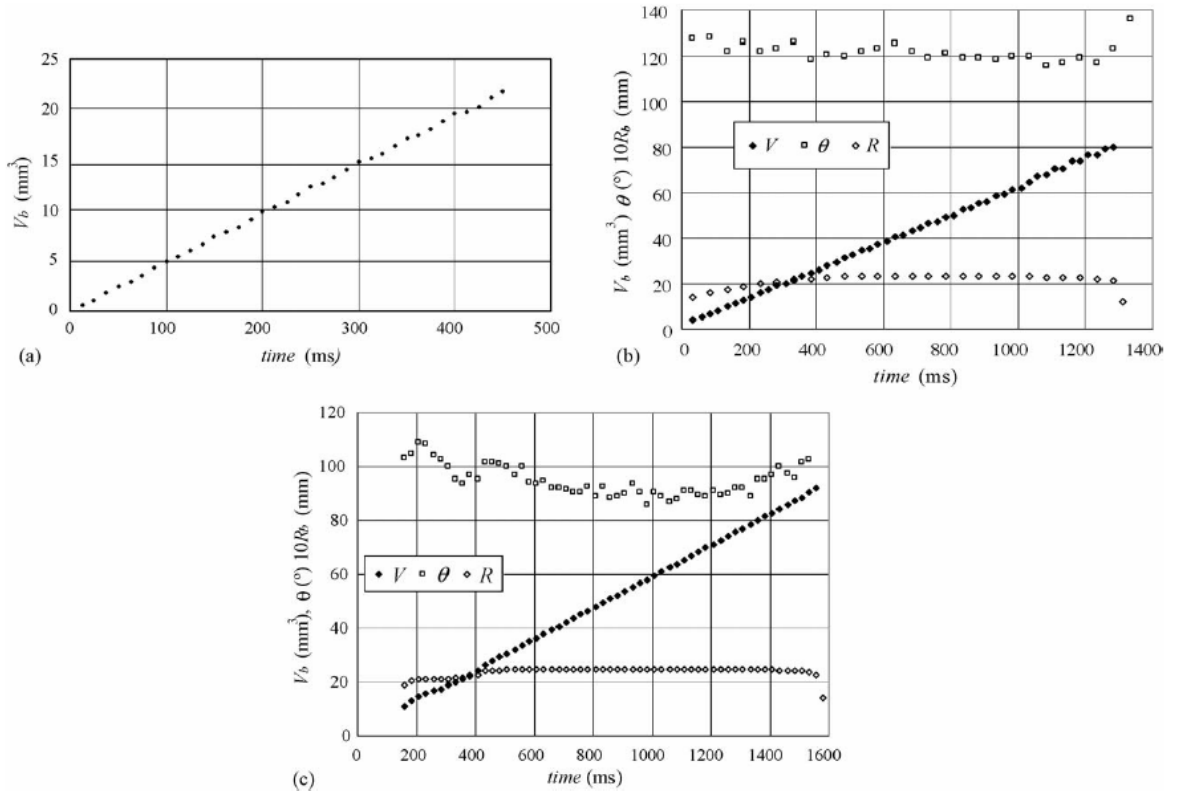


Figure 1-5 Comparison of bubble volumes created from 0.5mm pores drilled through a variety of chemically dissimilar plates. (a) acrylic sheet ($\theta=68^\circ$) with a flow rate of 48.4 mL/s , (b) Teflon ($\theta=123^\circ$) with a flow rate of 57.9 mL/s and (c) Vaseline ($\theta=90^\circ$) with a flow rate of 60.2 mL/s. [52]

The second observation by Corchero is that the shape of the bubble varies when the contact angle reaches 90° . Below 90° , the bubble base is tethered to the pore, with the bubble growing in a teardrop shape before necking and detachment. When the angle becomes greater than 90° , the bubble grows in a cylindrical fashion with a hemispherical cap, before reverting back to a stretched teardrop during necking and detachment. This cylindrical growth is in accordance with the bubble being able to grow across the plate surface. Corchero claims that as the height of the cylinder becomes approximately equal to its radius, buoyancy forces quickly distort the shape and lead to detachment. Many models of the growth and detachment process do not account for this spreading over the surface, and so care must be

taken when examining the data presented. [48] The third observation to note is that surface chemistry only plays a part at low flow rates; when the flow increases, the effect of wettability decreases. It also plays no role in bubble formation from a needle, as is shown by several other groups. [48, 53, 54]

Yasuda [32] agrees with Corchero, that if $\theta > 90^\circ$, the bubble is cylindrical in shape with a hemispherical cap. In this regime, the base of the bubble can grow to more than ten times the diameter of the pore, but recedes back to the pore upon detachment. However, there must be enough surface for this expansion to occur, and is the likely reason why no significant effect is observed when bubbling through a modified needle. Yasuda postulates that $\theta > 45^\circ$ allows the bubble to spread, and below this the bubble size is dictated by the orifice diameter.

Kukizaki [55] used a more robust method to test the effect of surface wettability on microbubble formation. Kukizaki modified Shirasu porous glass (SPG) membranes with silanes. Unlike other studies that used single controlled pores, SPG is a sintered glass powder with a random distribution of numerous small pores. Using organosilanes, Kukizaki modified the surface of the SPG to yield a variety of surface wettabilities before bubbling. The results obtained are shown in Figure 1-6. Once again, an apparent switch at $\theta = 45^\circ$ is seen.

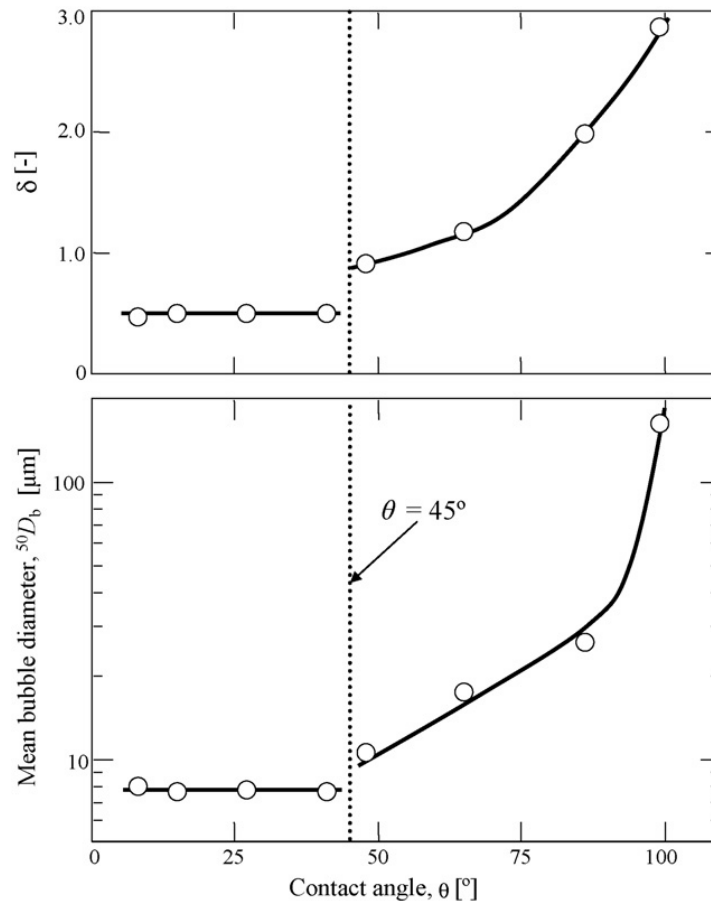


Figure 1-6 The effect of contact angle (θ) on the mean bubble diameter $^{50}D_b$ and the particle size dispersion coefficient (δ). [55]

Gnyloskurenko [48] presented data indicating bubble volume increased with increasing contact angle of a sessile water droplet on the substrate surface. In addition, all bubbles emerge from the pore as a spherical segment which then evolves into a hemisphere before progressing on to form the final bubble. This is a belief also held by Zhu. [47] During the necking stage of detachment, the initial neck is always larger than the pore size, but smaller than the hemispherical cap of the bubble. At the end of the necking process, just before detachment, the neck shrinks to a smaller size than the pore. Interestingly, after detachment Gnyloskurenko believes that around 1% of the bubble volume is left at the orifice, trapped on the surface.

Many of the above studies focused on bubble formation from single pores. However, industrial processes often use diffuser plates and spargers with a high density of pores in close proximity to one another. Kukizaki [55] and Yasuda [32] both agree that as the surface becomes more and more hydrophobic, the potential for bubbles to spread to multiple pores increases greatly, with the result that a single bubble is fed by multiple pores. This would influence subsequent bubble formation and will be discussed further in section 4.2. A representation of this phenomenon is shown in Figure 1-7.

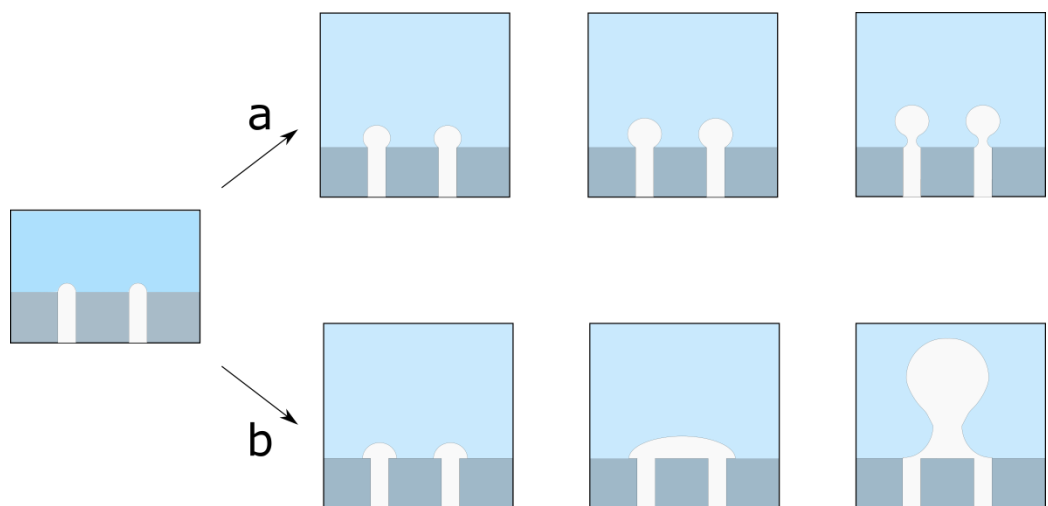


Figure 1-7 Schematic of bubble formation from multiple pores on a) a hydrophilic surface where the bubble is tethered to the pore and b) a hydrophobic surface where the bubble can spread and be fed by multiple pores.

Finally, it is worth noting that reports exist of bubble nucleation at hydrophobic surfaces from saturated liquids. These bubbles are stable and sit for extended periods on the surface. There is potential for bubbles to sit on such surfaces after formation, coalescing with others in subsequent bubbling. [56, 57]

1.4.4 Surface tension.

The effect of surface tension is thought to only have noticeable effects at very low flow rates. [42, 43, 45, 58] It is believed that in this regime the bubble size is dictated purely by a balance between the buoyancy force and surface tension. In low viscosity liquids, as flow rate increases, the effect of surface tension becomes diminished to a point where it becomes negligible. Ramakrishnan [58] postulates that at high flow rates, the bubble size will be the same for a fixed flow rate irrespective of the surface tension. Experiments were conducted using the same orifice in both water and a 10% isopropyl alcohol solution to test this hypothesis. At low flow rates the difference in bubble size was significant. As the flow rate increased, the difference between the volumes decreased until the two sets of data overlaid onto one another. These tests show how surface tension has a significant effect under low flow conditions in a low viscosity liquid. For highly viscous liquids, the flow rate at which the surface tension becomes negligible is much smaller. Similarly, when very small orifices are used, the effect of surface tension is greatly reduced. [58] It was also noted by several groups that a lower surface tension acted to stabilise the smaller bubbles, thus the addition of just 1.6% butanol by Leibson led to a marked increase in small bubbles observable in solution.

1.4.5 Stabilising effect of salts and surfactants.

There is a general belief that the surface of a bubble carries a negative charge: the zeta potential of a microbubble in distilled water at pH 5.8 with no electrolyte added was around -35 mV. There is said to be no correlation between the zeta potential and the bubble size. [59, 60] Many groups have explained the observation by the occurrence of ionisation at the bubble

surface or the adsorption of surfactant. However, Takahashi's [60] study in distilled water eliminated the possibility of ionic surfactants in solution, and the experimental technique did not ionise the gas. This means that the negative charge on the bubble surface must be due to the hydroxyl ions (HO^-) in solution. Most groups now explain this by the increased hydroxyl concentration at the bubble surface when compared to the H^+ concentration. This is either due to the change in hydration energy between HO^- (-489 kJ/mol) and the H^+ (-1127 kJ/mol) or due to the dipole of water molecules at the interface. HO^- moieties point inwards towards the gaseous component of the bubble, whereas the H^+ point outwards, causing an electrostatic attraction and build-up of HO^- at the bubble surface. [61-63] The zeta potential becomes more negative as an increase in pH is carried out, as expected due to the increasing concentration of HO^- in solution. In fact pH must decrease below 3.5 before the zeta potential approaches 0 and finally becomes positive at lower pH values. This shows that HO^- is more readily adsorbed at the interface than H^+ ions.

Takahashi then investigated the effect of inorganic salts on the zeta potential of microbubbles. Addition of both sodium chloride (NaCl) and magnesium chloride (MgCl_2) reduced the zeta potential of the microbubbles. The hydration energy of the Cl^- anion is -317 kJ/mol, indicating it should spend more time at the liquid gas interface (a more negative enthalpy of hydration would preferentially be in the bulk water) than both the Na^+ ion (-406 kJ/mol) and the Mg^{2+} ion (-1904 kJ/mol). The result is that the addition of both salts should lead to a more negative zeta potential, which is not the case. Takahashi believes this is an indicator that the energy of hydration is not a key factor in determining the bubbles surface charge. Ionic charge is believed to be the main factor in accumulating charge at the bubble surface via an electrical double layer. An increase of counter ions at the interface leads to a reduction in zeta potential, with the attraction of the ions depending on valency. A charge of 2+ on the magnesium ion will lead to a greater attraction, and thus a larger decrease in zeta

potential when compared to the 1+ charge of sodium and H^+ . The reduction of zeta potential with salt addition was also observed by Cho, [64] upon the addition of NaCl and $CaCl_2$.

Tsang [65] presented data investigating the effect of salt on coalescence at two adjacent capillaries. They found that as the salt concentration increased, the percentage of bubbles coalescing decreased substantially, thus decreasing the average size of bubbles. These reductions in bubble size are somewhat counterintuitive. Electrolytes often lead to a slight increase in surface tension [65] and also a reduction in zeta potential; both would ordinarily lead to an increase in bubble size. This is the observation of Jamialahmadi [39] who found that bubble size increased upon addition of electrolyte. Further work is clearly needed to validate the observations and provide a clearer picture of the effect of electrolytes on bubble formation.

Yoon [63] conducted studies into the effect of surfactant on zeta potentials of microbubbles using a modified electrophoresis cell to measure the electrophoretic mobility's (from which the zeta potential can be calculated). Using sodium dodecyl sulphate (SDS) with its negatively charged end group, and dodecylamine hydrochloride (DAH) with its positively charged end group, Yoon was able to show the variation in the bubbles' zeta potential with surfactant concentration. When SDS was added the bubbles remained negatively charged, with an increasing negativity as the concentration of surfactant increased. Conversely, the DAH added positive charge to the bubble surface, again increasing in magnitude as the concentration increased. As the critical micelle concentration (CMC) of both was approached, the zeta potential plateaued at a maximum value. Xu [59] confirmed the results of Yoon, with increasing SDS concentrations leading to a larger zeta potential. Xu then tested the effect of SDS concentration on the size and stability of the microbubbles formed. They found that as SDS concentrations increased, bubble size reduced and the stability increased. Cho [64] also carried out similar tests with SDS and nanobubbles. They found that as the ratio of the SDS

concentration : CMC approached unity, bubble size decreased. As the ratio further increased, bubble size continued to decrease until a plateau when the concentration of SDS was around 3 times that of the CMC. The stability of the smaller nanobubbles increases for two reasons. The first is that as SDS concentration increases, causing a rise in zeta potential, the negative charges at the bubbles' surface act to repel one another and eliminate coalescence in solution. The second is that addition of SDS reduces the surface tension on the bubble from its initial 72 dyn/cm to 38 dyn/cm at the CMC (25 °C). Both Leibson [42] and Jamialahmadi [39] found that a variety of alcohols reduced surface tension and increased stability of smaller bubbles.

1.4.6 Flow rate.

The effect of flow rate on bubble formation is a generally well accepted observation. Under low flow conditions, the volume of the detaching bubble is not affected by slight increases in gas flow rate. Instead, an increase in flow leads to a higher frequency of bubble formation. [43, 49] At these low flow rates, bubble size is determined predominantly by orifice size, liquid density and surface tension effects. [37, 39, 42, 43, 45, 66] As flow rate increases the bubble size begins to be affected, with surface tension effects being reduced. [37, 39] As progression is made from low flow, where single bubbles are formed at regular intervals, to a higher flow bubbles begin to form in pairs. These pairs often contain a large bubble and a smaller one, with gaps between their formations. At higher flow still, bubbles form clusters of 3, 4 or 5 with gaps in between groups, [38, 43, 67] with newly forming bubbles being affected by the previously formed bubbles. In the region of low flow, the bubble volume may be predicted by the hydrostatic equation (5), presented by Davidson [38] and agreed with by McCann [68] for flows under 1 mL/s.

Chapter 1: Introduction.

When the bubbles are emitted as pairs, there is a possibility of the second bubble penetrating the first. The process can proceed in several ways. The first is that the second bubble shoots rapidly from the pore, passing through the first bubble completely and emerging above it. In this regime, the first bubble absorbs part of the second, leaving it as a smaller satellite. Alternatively, the second may be fully absorbed. As flow rate increases further, this coalescence occurs closer and closer to the orifice. A further increase in flow can lead to a phenomenon known as 'double coalescence', whereby the large bubbles formed by previous coalescence coalesce themselves, forming large unstable bubbles. However this region of flow is generally very turbulent and so good data is difficult to obtain. [38, 39, 42, 44] Zhang adds to the work of Davidson, pointing out that the wake of the first bubble of a pair causes the second to elongate, accelerate upon detachment, and rise in a counter clockwise swirling motion. [42, 68]

When coalescence occurs, the top segment of the bubble retains its hemispherical shape, but the bottom accelerates quickly towards the bubble centre, creating a 'helmet with a flat bottom' shape as described by Leibson. [42] This causes the unstable oscillations in the bubble and turbulence that can affect subsequent bubble formation. Many models do not account for this. The oscillations dampen over time and the bubble eventually becomes spherical. [66]

Vafaei [45, 69] observed that the bubble volume had a 'U' shaped dependence on the flow rate, with an initial decrease in volume as flow rate increased, followed by an increase. Lin [70] observed no real deviation in volume at low flow rates. These studies were carried out using nozzles.

1.4.7 Liquid viscosity.

The effect of liquid viscosity has been less well studied than other aspects of bubble formation. However, Ramakrishnan [58] investigated the formation of bubbles under constant flow conditions at varying liquid viscosities. It was found that for a low viscosity liquid, as the flow rate increased, the effect of surface tension decreased and eventually becomes negligible. In more viscous liquids, the point at which the surface tension effect becomes negligible is at a lower flow rate than the less viscous liquid. In general, an increase in liquid viscosity leads to an increase in bubble size. This finding is similar to that of Jamialahmadi [39] who found that the effect of viscosity was negligible at low flow rates, but becomes more significant at higher flows, with an increase in viscosity leading to an increase in bubble size. Benzing [37] suggested that liquid viscosity played no role in bubble formation. However, their study was carried out under low flow rates, so would fit into the observation of Jamialahmadi [39] that the effect was negligible at low flow rates.

1.4.8 Liquid density.

There are essentially two views on density. The first is that density has no effect on bubble formation. The second is that bubble volume decreases with an increase in liquid density. Ramakrishnan believes that in low viscosity liquids with small orifices at high flow rates, the effect of liquid density is negligible. A similar effect for highly viscous liquids and small orifices is observed: an increase in density leads to a reduction in bubble size. [58] Despite this work, there is very little data investigating the effect of density. Examining

equation (5), it can be seen that an increase in liquid density should lead to a decrease in bubble volume, which corroborates the theory outlined above.

1.4.9 Liquid height.

Very little data exists on the effect of liquid height. Hayes [43] has shown liquid height seems to have no effect on bubble size, as long as the height is larger than two bubble diameters. Jamialahmadi [39] agrees that the effect is minimal.

1.4.10 Chamber volume.

The volume of the chamber that delivers air to the orifice must also be carefully designed to ensure system stability. The chamber includes all tubing and pipework back to the first restriction of the flow, [38] with most groups agreeing that if the chamber volume is much larger than the average bubble volume, no pressure and flow fluctuations occur. [42, 50] Leibson [42] discussed how a small chamber volume leads to a slight pressure decrease when the bubble is forming. This leads to a deceleration of bubble growth, which must wait until the pressure in the chamber has increased to drive growth once more. They further state that if the chamber was 10,000 times bigger than that of the individual bubble, no pressure variation would occur. Hayes [43] agrees that a large volume is necessary, and adds that the chamber diameter should be at least 4.5 times larger than the pore to have no effect.

1.4.11 Thickness of the orifice plate.

Hayes briefly investigated the effect of plate thickness on bubble formation. It is believed the ratio of thickness to pore size must be over 100:1 to have an effect, which agrees with the data of Hughes. [71] Leibson [42] and Vafaei [69] reported no difference between the effects of thin and a thick plate on bubble formation. Benzing [37] reported that if the plate thickness was less than the pore diameter, bubble volume was decreased. This area needs more fundamental study to investigate this aspect further.

1.4.12 Gas saturation of liquid phase.

Microbubbles can readily undergo gas exchange with the surrounding liquid, with total gas exchange achievable in a matter of seconds, although the mechanism and time frames of gas exchange are dependent on the surface coating of the bubble. [72] Microbubbles created in liquids with 100% gas saturation exist for at least 6 times longer than those in just 70% saturation. A reduction of just 10% saturation leads to a decrease in persistence by more than 50%. [73] As a result, gas bubbles for use as contrast agents in vivo must be generated in saturated solutions, contrary to popular belief, in order to increase efficiency.

1.5 Bubble growth process.

Many groups have examined the growth process of bubbles being emitted from a pore, with most agreeing that the process can be summarised into three or four steps. [36, 45,

47, 48, 68] The initial step is the nucleation step, where the bubble initially begins to form. Many groups have indicated that at this point the radius of curvature of the forming bubble is essentially infinite. [45, 74] According to the Young-Laplace law, equation (6), the pressure difference (ΔP) between the liquid and gaseous phases is inversely proportional to the radius of curvature (R), with σ equal to the surface tension of the interface.

$$\Delta P = \frac{2\sigma}{R} \quad (6)$$

From (6) it can be seen that if the radius of curvature is infinite, the pressure difference tends to 0. The result is that air can readily flow into the bubble and begin expansion. [74] As the bubble grows, the radius of curvature decreases as the bubble volume increases and as a result, the pressure inside the bubble increases meaning the bubble grows in a stable regime termed the steady growth period. This phase continues until the bubble cap reaches a hemispherical shape. At this point, the radius increases with increasing volume and once again leads to a decrease in ΔP . The decrease in pressure leads to an influx of gas into the bubble, which increases the volume. This in turn increases the radius, and ΔP falls further, leading to an influx of gas and the cycle repeats. This stage of the bubble growth is the 'sped up growth' period. There is no restriction to growth in this period, and the result is rapid growth until the final stage. The final stage is the detachment of the bubble. When the buoyancy force begins to exceed the anchoring force, the bubble elongates with its neck becoming thinner as the bubble begins to rise. Finally the neck is broken and the bubble detaches.

1.5.1 Bubble growth from multiple orifices.

The method of bubble growth from an array of theoretically identical orifices is far from simple, with considerable difficulty involved in ensuring all orifices generate bubbles. The reason links to the Young-Laplace equation (6) once again. Initially, all pores may be considered equal, with the potential for all pores to begin bubble generation. However, in reality, pores are highly unlikely to be equivalent. This can be due to manufacturing limitations, design of the reactor, the position of the air flow, or even turbulence within the incumbent airflow. The result of this non-equivalence is that one bubble will reach a hemispherical shape before all others. As discussed previously, this point leads to a decrease in the bubble pressure. This pressure drop leads to an instantaneous advantage for this bubble and is followed by a rapid influx of air into this bubble. This leads to an increase in the radius of curvature and further inflow to the rapidly growing bubble due to the path of least resistance being established. The process may lead to a halt in bubble production from the other pores, or even a reversal and shrinking as air preferentially flows into the large bubble. For this reason, bubbling through a multi pore diffuser plate leads to polydispersity of bubble sizes and all pores are not engaged in bubble production. [74, 75] A schematic of this process is shown in Figure 1-8.

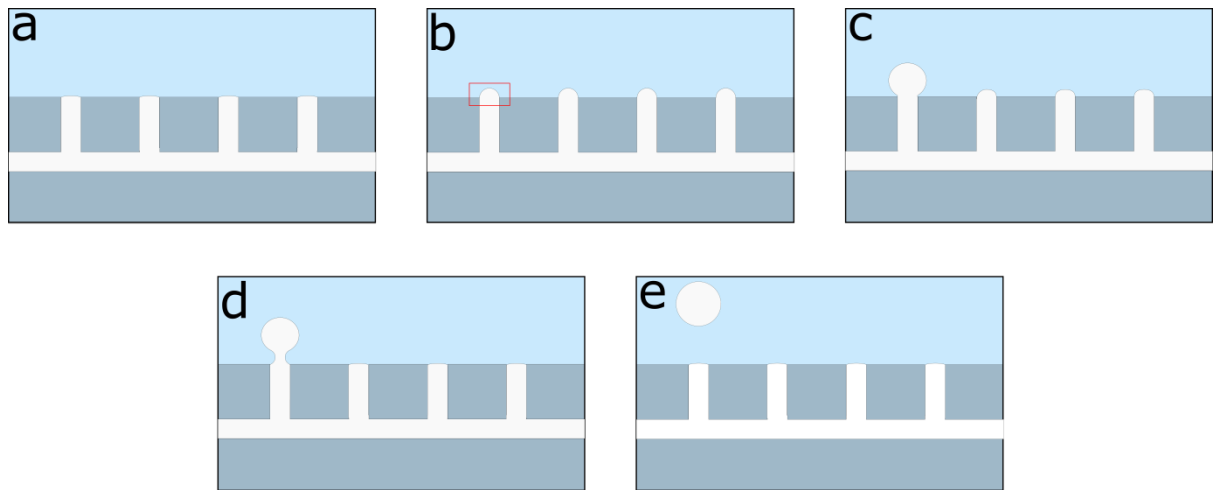


Figure 1-8 a) Bubble formation begins at all pores b) Growth continues until one bubble (shown with a red rectangle) reaches a hemispherical shape before the rest c) This bubble grows preferentially over the rest, which remain static or shrink in size d) The growth and shrinking process continues until necking e) The bubble detaches and the system reverts back to the beginning.

1.5.2 Microbubbles by fluidic oscillation.

Fluidic oscillators of the type described by Zimmerman [1, 10, 12, 75] and Tesar [11, 13, 74, 76] are devices that take in a steady flow and convert it into a pulsating or even an alternating flow. Originally designed in the 1950's for use in fluidic logic circuits, they have no moving parts, so are robust and act to reduce the energy consumption of an oscillatory system by removing frictional forces and bottlenecks. Zimmerman [1] calculated a 6.7% energy reduction when the oscillator was used over steady flow systems, with an increase in energy saving with increasing input flow. The fluidic oscillator has been used to generate microbubbles in a series of experiments by Zimmerman and Tesar over the last decade, with an observable benefit to their use.

Chapter 1: Introduction.

In early work by Zimmerman [75] a nozzle bank with 600 μm pores was supplied with a steady flow of air and a pulsed air jet generated by fluidic oscillation. It was found that the bubbles generated by the oscillator were monodisperse, and sub millimetre in size with uniform spacing. Oxygen transfer efficiency was increased by more than 8x with the use of these bubbles. A subsequent study with a bank of 60 μm pores again led to bubble sizes of the same order of the orifice, with an 8 fold increase in size in the absence of the oscillator.

In similar work by Hanotu [19] pore sizes of 38 μm were used. Under steady flow, the average bubble size was 1059 μm : more than 28 times greater than the size of the pore. Under fluidic oscillation, the bubble size decreased to 86 μm , which was only 2-3 times the size of the pore. This trend was confirmed in a later work [18] with the generation of bubbles 2-3 times larger than the pore using oscillation into water. However, in a yeast solution bubble size was closer to the size of the pore. Hanotu assigns this decrease in size to a reduction in the surface tension of the liquid by the addition of yeast. Data from this study is shown in Figure 1-9. Note the different scales for each data set.

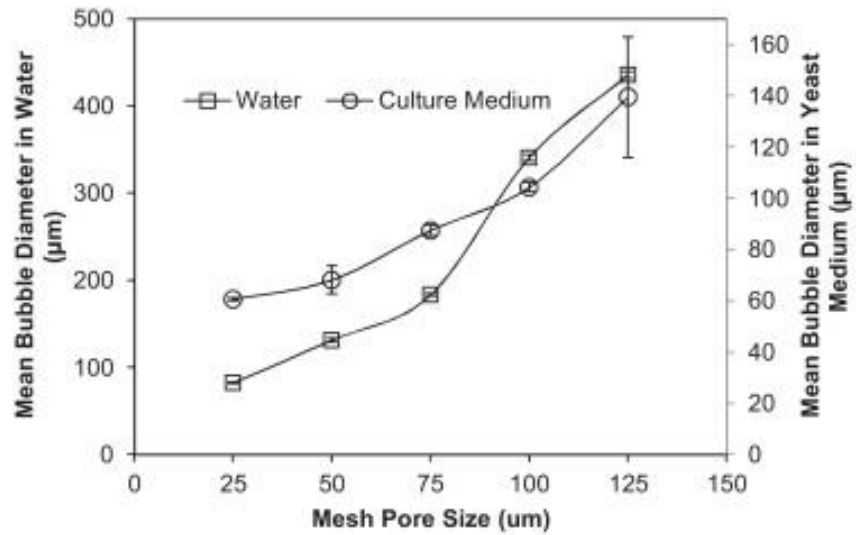


Figure 1-9 The relationship between bubble size and pore size under fluidic oscillation in water and a yeast solution. The error bars are standard error. [18]

The effect of flow rate on bubble size was also investigated and is shown in Figure 1-10. [17]

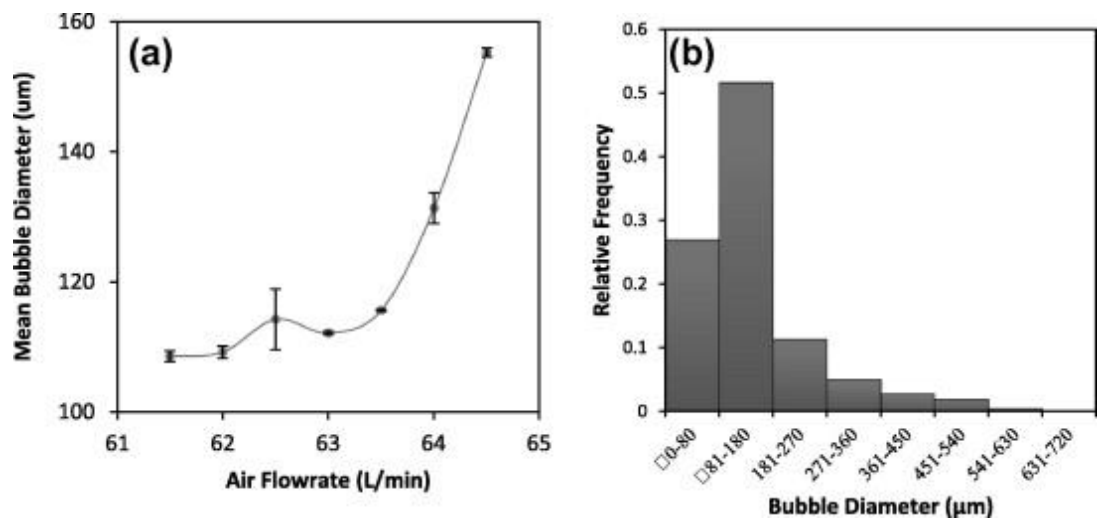


Figure 1-10 The effect of flow rate on bubble diameter. a) As flow increases bubble size increases, in a similar way to steady flow. b) Bubble size distribution created from a 50 µm pore under 64 L/min flow rate.

Chapter 1: Introduction.

Data presented in [10, 12] suggest that the frequency of oscillation should be set at between 200-300 Hz for optimisation of the process. Devices with moving parts would rapidly deteriorate under these conditions. [14]

Tesar [74] presented a theory as to why production of small bubbles is energetically disfavoured. The surface energy of the bubble is given by equation (7).

$$E = 4\pi r^2 \sigma \quad (7)$$

Surface energy (E) is given by the bubble surface area, where r is the radius of the bubble multiplied by the surface tension (σ) of the liquid gas interface. Splitting a single bubble of volume V, into two equal bubbles with a volume of V/2, the relationship between the two radii is given by equation (8).

$$r_2 = 2^{-\frac{1}{3}} r_1 \quad (8)$$

Where r_2 is the radius of the smaller daughter bubble, and r_1 is the radius of the larger parent bubble. This leads to a surface area of the two daughter bubbles to increase to equation (9) and the energy to increase to equation (10).

$$S_2 = 2 \times 4\pi(2^{-\frac{1}{3}})^2 r_1^2 = 2 \times (2^{-\frac{7}{3}})\pi r_1^2 \quad (9)$$

$$E_2 = 2\sigma \times (2^{-\frac{7}{3}})\pi r_1^2 \quad (10)$$

Splitting of this original bubble into 'm' equally sized bubbles leads to an increase in energy with each additional bubble. The relationship is shown in Figure 1-11. [74]

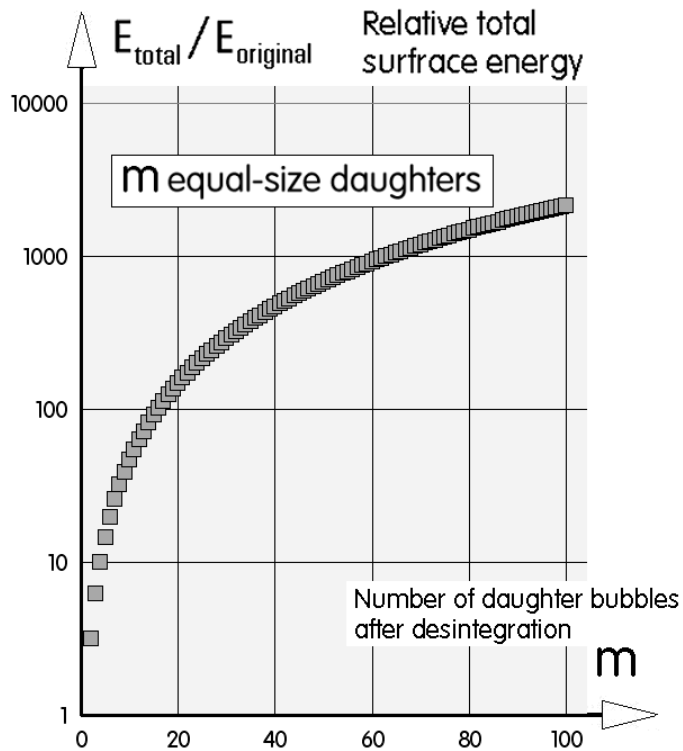


Figure 1-11 The energy to split a single bubble into m equally sized daughters. E_{original} is the surface energy of the initial large bubble. E_{total} is the sum of the surface energy of all daughters.

[74]

In addition to this large energy increase as m increases, splitting a bubble into two equal daughters carries the highest energetic penalty, as seen in Figure 1-12. 'n' represents the fraction of the original bubble contained within the smaller of the two daughters. For example an $n=3$ represents a daughter with $1/3$ of the volume of the original, and thus its partner must have $2/3$. It can be seen that as the size difference between the two daughters increases, the energy penalty to form them falls.

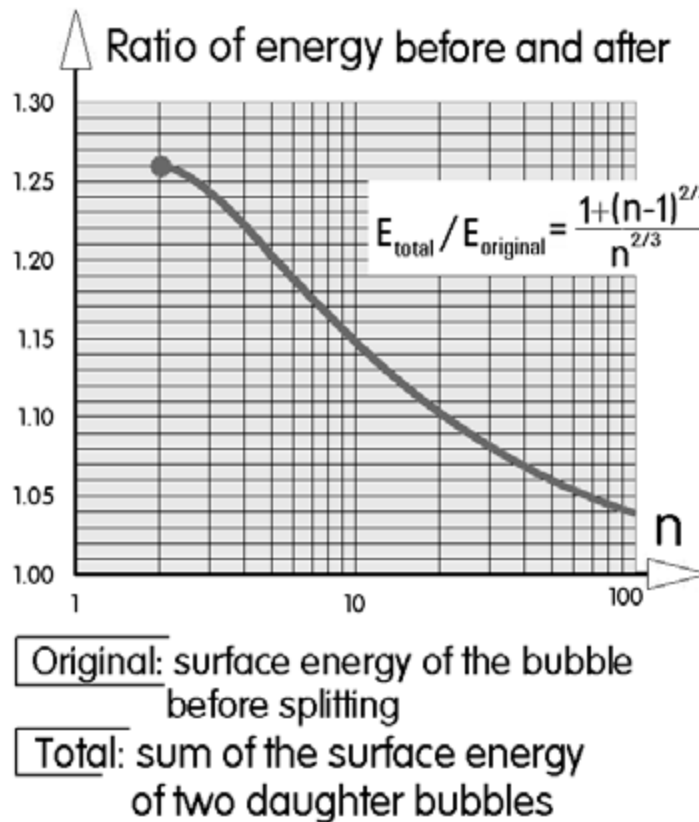


Figure 1-12 The increase in energy between the original bubble and the daughter bubbles of different sizes. n is the fraction of the original bubble that the smaller of the daughters contains. For example an $n = 3$ indicates the smaller of the bubbles contains $1/3$ of the original bubble volume.

The energy increase for splitting bubbles into smaller sized bubbles must be supplied from an external source. In the case of fluidic fragmentation, the extra energy must come from

the fluidic oscillator. This would go some way to explaining why the oscillator has been observed to produce smaller bubbles.

1.6 Contact angle and wettability.

Many people consider Thomas Young to be the father of surface wettability and contact angle study, with work in the early 1800's outlining the physical cohesion of liquids. [77] However, it may be noted that the concepts have been discussed as far back as Aristotle (384-322 BC), Archimedes (287-212 BC) and Galileo (1564-1642). [78]

Since the early days, wettability has attracted a great deal of interest, with both fundamentals and applications being investigated. Currently, countless utilisations of wettability exist, with areas such as lubrication, printing and oil recovery all taking advantage of controlled surface wettability. More recently, the increased understanding of superhydrophobicity has led to the development of new applications such as self-cleaning materials and electrowetting. [79]

The work by Young [77] outlined the description of contact angle (θ) as it is known today. A liquid droplet sitting on a horizontal surface (sessile) has an inherent surface tension between the liquid and solid phase (σ_{SL}), the solid and gaseous phase (σ_{SG}) and the liquid and gaseous phase (σ_{LG}). The balance between these forces dictates the extent to which the liquid wets the solid surface. The commonly accepted representation of the contact angle (CA) is given in Figure 1-13 a) $\theta < 90^\circ$ b) $\theta = 90^\circ$ c) $\theta > 90^\circ$.

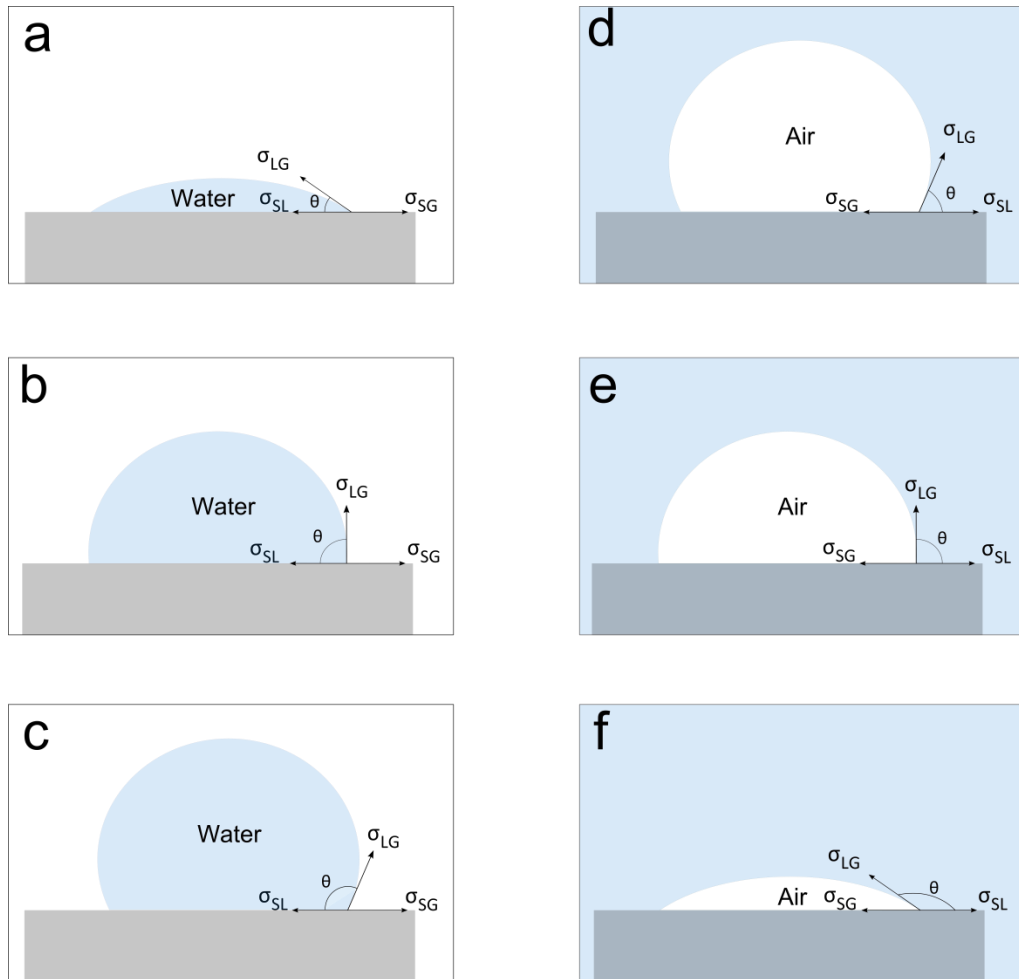


Figure 1-13 The contact angles (θ) of a sessile liquid drop (water) on a solid horizontal surface in air; a) $\theta < 90^\circ$ b) $\theta = 90^\circ$ c) $\theta > 90^\circ$ and an air bubble sitting on a solid surface in water; d) $\theta < 90^\circ$ e) $\theta = 90^\circ$ f) $\theta > 90^\circ$.

The CA is defined as the intersection of the liquid solid interface and the liquid vapour interface. The point where the three phases meet is known as the three phase contact line. A surface with a CA of $\theta < 90^\circ$ is classified as hydrophilic due to the favourable spreading of the liquid over the solid. Perfect wetting is achieved when $\theta = 0^\circ$ and the liquid forms an almost indistinguishable puddle on the surface. A surface with a CA of $\theta > 90^\circ$ is classified as hydrophobic, as the wetting of the surface is disfavoured and the liquid acts to minimise its interaction with the solid. Superhydrophobicity is usually defined as $\theta > 150^\circ$, with the lotus leaf effect being a well studied example. [79]

As described by Young [77] the contact angle of a liquid on a solid horizontal surface is given by the equilibrium between the three interfacial tensions shown in Figure 1-13 to yield Young's equation (11).

$$\sigma_{SG} = \sigma_{SL} + \sigma_{LG} \cos\theta \quad (11)$$

Where (σ_{SL}) is the liquid-solid interfacial tension, (σ_{SG}) is the solid-gas interfacial tension, (σ_{LG}) is the liquid-gas interfacial tension and θ is the contact angle.

Despite the general acceptance of Young's equation, [80-83] the CA often gives a broad range of results on a given surface, where it should give a single constant value. The reason for this variation in the CA is due to surface roughness. Young's equation assumes a flat, rigid and chemically homogeneous surface, with no perturbation by chemical or absorptive routes. As the liquid droplet moves across the surface, it encounters surface topography that can act to pin the contact line of the drop. This pinning leads to a number of metastable states which causes the variation in observed contact angle. This moving (dynamic) contact angle is composed of constituent parts, with the angle created as the drop spreads over the surface known as the advancing contact angle (θ_a) and the angle created as the droplet shrinks away from the surface known as the receding contact angle (θ_r). The advancing contact angle approaches the maximum value for the system, and the receding angle approaches a minimum. The difference between the two angles is known as hysteresis and is shown in equation (12). [79]

$$H = \sigma_a - \sigma_r \quad (12)$$

The general consensus on hysteresis is that it arises due to deviations from the ideality, required by Young's equation, into a surface with heterogeneity and roughness. A non-homogenous surface contains domains that act to pin the contact angle as it advances across the surface. The same domains will act to hold back the receding liquid and cause a decrease in the CA. There are currently no guidelines to explain how smooth a surface must be in order for Young's equation to become valid. [83] Nevertheless, it is believed that the advancing contact angle gives a good approximation to the Young's contact angle. Since the realisation that roughness is an important factor in surface wettability, other wetting modes have been discussed. Wetting on a rough surface is now believed to fit into one of two regimes, the Wenzel mode or the Cassie-Baxter mode. Both will be discussed below.

1.6.1 Wenzel's state.

In his work in the 1930's [84] Wenzel first discussed the importance of surface roughness on contact angle measurement. The geometric area of the surface, defined by the theoretical interface between the liquid/vapour or liquid/liquid phase, will always be smaller than the actual surface area of any real solid due to roughness. Wenzel compared these values directly in his 'roughness factor', defined below in equation (13) as the ratio between the actual surface and the geometric surface areas. It is important to note that root mean square analysis and peak height analysis cannot be used to calculate the roughness factor. [85, 86] Instead gas adsorption may be used to calculate a value for the roughness.

$$\text{Roughness factor } (r) = \frac{\text{actual surface area}}{\text{geometric surface area}} \quad (13)$$

Addition of this roughness factor led to the Wenzel equation for wetting a rough surface equation (14), where θ_w is the apparent Wenzel contact angle and θ_Y is the fundamental Young's contact angle.

$$\cos\theta_w = r\cos\theta_Y \quad (14)$$

It can be seen from equation (14) that as the roughness factor tends to unity, the Wenzel angle approaches the Young's angle. At $r=1$ the two values become equivalent. It was observed that rough surfaces showed more resistance to wetting than a smooth surface. It was proposed that water penetrates the small roughness features on the solid surface and provides a barrier to wetting. The extent of wetting is then governed by the energy used to form a gas-solid interaction by removal of water from the surface features, compared with the energy gained from forming the gas-solid interface at the expense of the gas-liquid interfacial energy.

1.6.2 Cassie-Baxter state.

The ideas of Wenzel were built upon in the 1940's by Cassie and Baxter. [87] By defining the total solid-liquid interfacial area as f_1 and the total liquid-air interface as f_2 it can be seen that as the liquid spreads over an area of f_1 , an energy equivalent to $f_1\gamma_{SG}$ is gained by the destruction of the solid-gas interface. By definition, an energy equal to $f_1\gamma_{SL}$ is used in the formation of the solid-liquid interface, where γ_{SG} and γ_{SL} are the solid-gas and solid-liquid interfacial energies respectively. The liquid-gas interface is also expanded by $f_2\gamma_{LG}$ where γ_{LG} is the liquid-gas interfacial energy. Therefore, the energy (E) of expanding the interface is given by equation (15).

$$E = f_1(\gamma_{LS} - \gamma_{SG}) + f_2\gamma_{LG} \quad (15)$$

If the Young equation (11) is taken to define $\cos\theta$, then rearranging to give equation (16) means equation (15) can be written as (17).

$$\gamma_{LS} = -\gamma_{LG}\cos\theta + \gamma_{SG} \quad (16)$$

$$E = \gamma_{LG}(f_2 - f_1\cos\theta) \quad (17)$$

Since $(\gamma_{LS} - \gamma_{SG})$ is the energy required to form an area of solid-liquid interface, equation (16) may be rearranged to give equation (18) and thus the apparent Cassie-Baxter contact angle is given by equation (19), where θ_{CB} is the apparent Cassie-Baxter contact angle.

$$\cos\theta = \left(\frac{\gamma_{SG} - \gamma_{LS}}{\gamma_{LG}} \right) = \frac{-E}{\gamma_{LG}} \quad (18)$$

$$\cos\theta_{CB} = - \left(\frac{E}{\gamma_{LG}} \right) = f_1 \cos\theta - f_2 \quad (19)$$

The Cassie-Baxter equation (19) May also be shown as (20) because of the relation $f_1 + f_2 = 1$, and therefore $f_2 = 1 - f_1$.

$$\cos\theta_{CB} = f_1 \cos\theta - 1 + f_1 \quad (20)$$

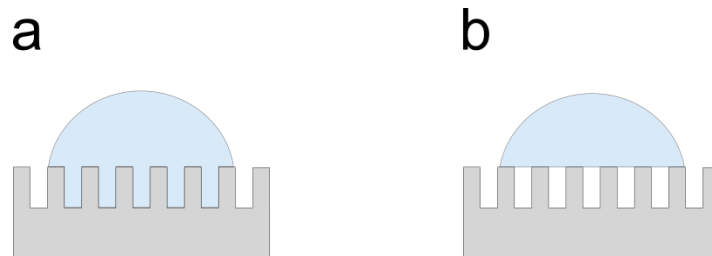


Figure 1-14 a) Shows a schematic representation of The Wenzel state and b) The Cassie-Baxter state. [88]

Figure 1-14 shows the difference between the Wenzel and Cassie-Baxter state. It can be seen that the Wenzel state assumes the liquid wets between the microstructure of the surface whereas the Cassie-Baxter state does not. The Cassie-Baxter state traps air between the liquid drop and the surface, accounting for its removal with an energetic penalty. Both states can be seen in nature, with the lotus leaf effect and the petal effect as discussed below. It is also pointed out by Cassie [89] that for contact angles where $\theta > 90^\circ$, roughening the surface will act to increase the observed contact angle. Similarly, roughening the surface where $\theta < 90^\circ$ will reduce the observed angle.

1.6.3 The rose petal effect.

The petal effect is an example of a surface with a high contact angle, but also high adhesion of water droplets. In fact, different varieties of rose wet to different extents based on the micro and nano structure of the petal. [90] Bhushan showed by AFM and SEM that a low adhesion petal had a higher density of larger peaks within the petal structure. The petal's waxy hydrophobic coating and surface roughness acts to yield a high contact angle and the common perception would be that the droplet would roll off the surface. This is the case when the microstructure is dense and has large peaks. This would imply that water can penetrate less readily into the surface features and remain in the Cassie-Baxter state. When the petal tilts away from horizontal the droplet can roll off the surface. However, when the microstructure of the petal is less dense or the features are smaller, the water can penetrate into the pores and sit in the Wenzel state. As the petal tilts, it is more likely that the droplet will remain on the surface and not roll off. In fact it has been shown that the droplet can remain when the petal is turned upside down. The drop will only detach when the effect of gravity breaks the structure. The petal effect is shown in Figure 1-15. [90, 91]

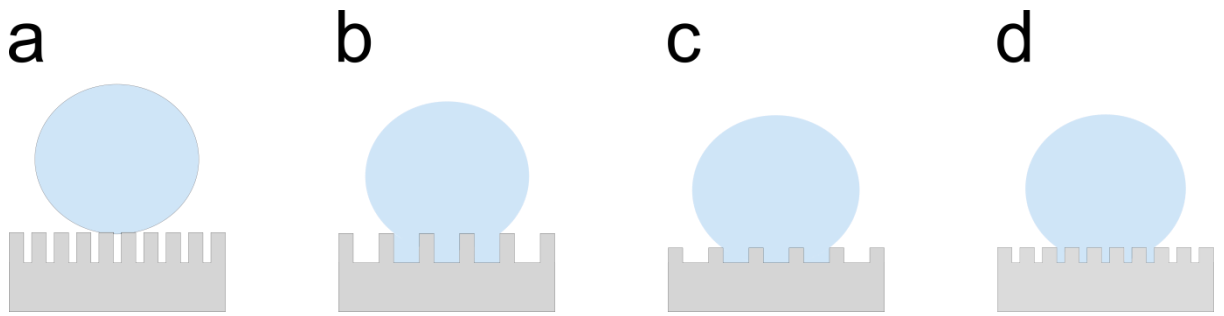


Figure 1-15 a) High density and high peak height leads to a Cassie-Baxter state. b) Low density and high peak height, c) Low density and low peak height, d) high density and low peak height all lead to a Wenzel state.

1.6.4 The lotus leaf effect.

The lotus leaf effect is an extension of the petal effect whereby nanostructures are present on the larger micron sized surface features. This nanoscale roughness causes the water droplet to sit in the Cassie-Baxter state on the leaf surface and prevents its penetration into the structure. The presence of the nanostructure adds a level of heterogeneity, a mix of solid and air pockets trapped below the water. This, along with the highly hydrophobic waxy coating leads to superhydrophobicity and contact angles in excess of 150° along with low adhesion. As a result, any tilt leads to the droplet rolling from the lotus leaf surface. The lotus benefits from this process, as the droplet gathers dust and debris as it rolls, acting to clean the flower. This phenomenon has led to the development of synthetic self-cleaning systems as well as non-wetting materials. A schematic of the lotus leaf effect is shown in Figure 1-16. [88, 92]

Chapter 1: Introduction.

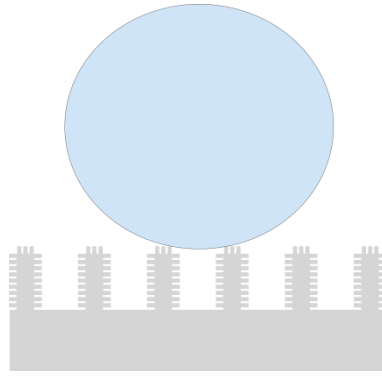


Figure 1-16 The lotus leaf effect with its microscale and nanoscale structure preventing wetting.

1.7 Surface modification by thiol chemistry.

Reproducing and creating controlled surfaces has become an increasingly popular area of research over recent years. The desire to investigate complex systems using a known surface/ substrate as a starting point, as well as the wide range of physical properties that can be accessed, has driven the development of surface modification techniques and the inherent understanding therein. There are many examples of this, from silane modification of silicon, to carboxylic acid modification of metals.[93] However, one of the largest areas of research is the modification of coinage metals (Au, Ag, Cu) by thiols. This section of the review will focus mainly on the self-assembly of thiols onto gold. It will discuss modifications from both solution and vacuum, the mechanisms involved, the influence of conditions and reagents, bonding and structure and other key areas of interest.

1.7.1 Why investigate thiols on gold?

The answer to this question has numerous components. One of the main reasons is historical. [94] Although modern technology has allowed a far greater selection of materials to be used in nanoscience, gold has historically been readily available. It can be found in many forms, such as thin films, colloids, wire and powder to name a few. In fact, thin films of gold are easy to produce by physical vapour deposition (PVD), sputtering or electrochemically in a laboratory environment but can also be purchased as both deposited films and single crystals. The high affinity of thiols for gold is also a key consideration. The adsorption of thiols onto gold readily displaces adventitious contaminants from the surface, meaning special measures such as inert atmospheres or clean rooms do not need to be employed during sample preparation. Another reason for its use is that gold is easy to pattern by numerous techniques such as lithography, chemical etching and micromachining, allowing the user to access a wide range of structures. Furthermore, gold is often used in many analytical processes such as Reflection Absorption Infra-Red Spectroscopy (RAIRS), Ellipsometry and Surface Plasmon Resonance (SPR) spectroscopy. Interestingly cell adhesion to gold is possible, as gold has low toxicity, allowing contact between the substrate and biological sample for extended periods of time. This widens the scope and potential application of thiol coated gold to a much broader field.[94]

In addition, Whitesides [95] found that the monolayers formed are indefinitely stable in air, water and ethanol at room temperature. This adds to the attractiveness of such systems.

1.8 Formation of self-assembled monolayers of thiols on gold.

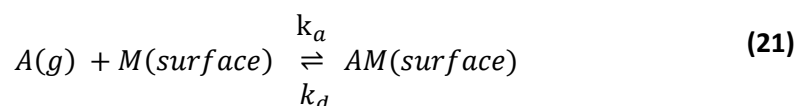
Self-assembled monolayers (SAMs) are assemblies of organic molecules formed from solution or the gas phase formed on a surface in either crystalline or semi crystalline arrays [94], and it is often credited to Zisman [96] for originating the concept. Many factors influence SAM formation with early work performed by numerous groups [95, 97-104] focusing on the fundamentals of SAM formation. Since then, a far more complex understanding of the self-assembly process has developed, covering a wide range of subjects.

1.8.1 The sulphur gold bond.

As would be expected, one of the key aspects of thiol SAM formation is the gold-sulphur bond (Au-S). It is this strong interaction that drives the monolayer formation and gives the primary structure discussed below in 1.8.2 and 1.8.3. The Au-S bond allows the production of SAMs in the presence of other functional groups, and its strength of 167-188 kJ/mol [104, 105] means it is preferential to the Van der Waals (VDW) interaction of contaminating hydrocarbons that may physisorb to the Au surface. Similarly, Whitesides et al [95] indicate that the sulphur moiety binds preferentially over all other functional groups. The result is that any tail group may be added to the thiol molecule and SAM formation will still proceed preferentially. Whitesides also indicated that the binding of thiols is favoured over disulphide adsorption by a factor of at least 10:1 [95] and in some cases up to 75:1. [99]

1.8.2 The mechanism of SAM formation.

Upon initial examination, the adsorption mechanism of thiols onto gold from the gaseous phase can be described by the Langmuir adsorption isotherm. The isotherm relates the fractional coverage of the surface (θ) to the pressure of the adsorbate gas at a given temperature. The dynamic equilibrium between associative and dissociative processes is given by equation (21), with k_a as the adsorption rate constant, k_d as the dissociation rate constant, A as the adsorbent and M as the metal surface.



From this equation, the rate of adsorption can be written along with the rate of desorption as in equation (22) and equation (23) respectively.

$$\frac{d\theta}{dt} = k_a p N (1 - \theta) \quad (22)$$

Where p is the partial pressure of adsorbent gas, N is the total number of sites and θ is the surface coverage. It can be seen that the rate of change of surface coverage is proportional to the partial pressure and the number of vacant sites $N(1-\theta)$.

$$\frac{d\theta}{dt} = -k_d N \theta \quad (23)$$

The rate of desorption is proportional to the number of adsorbed species $N\theta$. At equilibrium there is no net change in surface coverage, and so the sum of (22) and (23) is equal to zero.

Solving for θ yields the Langmuir isotherm, equation (26). A full derivation is shown in appendix 7.4.

$$k_a p N (1 - \theta) = k_d N \theta \quad (24)$$

$$K = \frac{k_a}{k_d} \quad \theta = \frac{\frac{k_a p}{k_d}}{\left(\frac{k_d}{k_d} + \frac{k_a p}{k_d}\right)} \quad (25)$$

$$\theta = \frac{Kp}{1 + Kp} \quad (26)$$

However this model is based on several assumptions. The first is that the adsorbate cannot proceed past monolayer coverage. The second is that the surface is uniformly flat and featureless thus making all sites equivalent. Finally the adsorption of molecules is independent of all other sites. In reality thiol adsorption onto gold violates these assumptions. Although it may be argued that assembly proceeds to monolayer coverage before ceasing, surface roughness is far more difficult to control. Similarly, thiol molecules interact with one another, with packing into SAMs being greatly affected by neighbouring molecules. Discussion of these interactions, namely Van der Waals forces between methylene groups within aliphatic chains, will be discussed later in section 1.9.1. Several groups [95, 100, 106, 107] have shown that a simple Langmuir model would not adequately describe the true kinetics, where either roughness or chain interactions diverge from the model. Peterlinz [108] goes further, indicating that experimental data deviates from the simple isotherm, but not in the early stage of adsorption. They put this down to physisorption onto the initial chemisorbed alkanethiolate layer. The latter 'second phase' of adsorption has a zeroth order rate and is dependent on both

chain length and concentration. Peterlinz also suggests that the first step kinetics fit a second order Langmuir isotherm, equation (29) which is derived fully in appendix 7.4.

$$\frac{d\theta}{dt} = k_a p (N(1 - \theta))^2 \quad (27)$$

$$K = \frac{k_a}{k_d} \quad \theta = \frac{k_a^{1/2} P^{1/2}}{k_d^{1/2} + k_a^{1/2} P^{1/2}} \quad (28)$$

$$\theta = \frac{(Kp)^{1/2}}{1 + (Kp)^{1/2}} \quad (29)$$

Poirier [109] has presented experimental Scanning Tunnelling Microscopy images (STM) that show SAM growth in fine detail. The STM data shows progression from uncoated Au (111) with a herringbone structure, to a highly mobile 'gas phase' in which flat-laying thiol molecules physisorb to the surface. When the concentration of these molecules reaches a saturation point, stable structured islands begin to form. These islands continue to grow and form striped phase islands which are aligned with the substrate's (121) direction. These islands have 22 Å inter row separation distances and 5 Å between each sulphur atom within the rows. This structure is not consistent with the $(\sqrt{3} \times \sqrt{3})R30^\circ$ lattice commonly accepted for the equilibrium saturation state of thiol coverage (section 1.8.3). Instead Poirier suggests that the sulphur atoms bond to the nearest neighbour in the striped phase. Helium diffraction methods conducted by Camillone [110] show a correlation between alkanethiol chain length and interchain distance, which lends support to this theory. Balzer et al [111] added weight to the theory with a combinative study using LEED and X-ray Photoelectron Spectroscopy (XPS) of

decanethiol deposited films. Both studies agree that the laying molecules can be described via a rectangular unit cell in the form $(m \times \sqrt{3})$ where m is dependent on chain length (in this case 11), as described by Schreiber [112] and shown below in Figure 1-17.

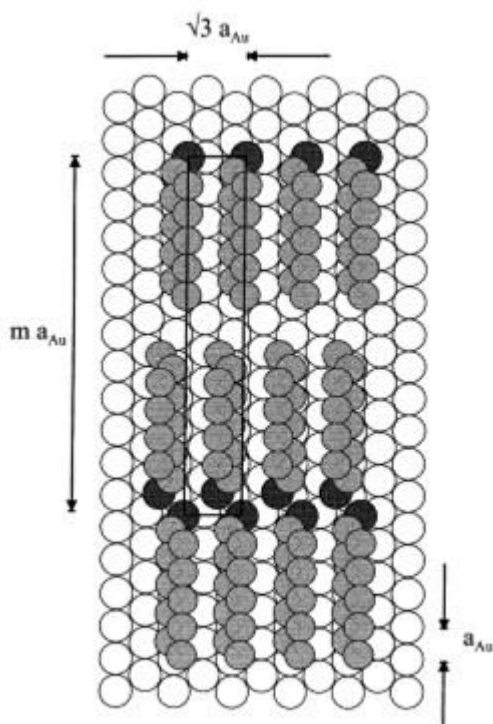


Figure 1-17 A real space schematic of the laying phase of alkane thiols on Au(111). For decanethiol, the unit cell can be described as $p(m \times \sqrt{3})$, where $m=11$. [112]

After this initial phase, continued exposure to thiol molecules results in the continued growth of the striped phase regimes until a saturation limit is reached. At this point lateral pressures drive the molecules to undergo a phase transition towards a more 'solid' phase in which the molecular axis is oriented towards the surface normal. These densely packed regions coexist with the surface aligned island phase and begin to dominate as time progresses.

Schreiber et al [113] found using Grazing Incidence X-ray Diffraction and LEED studies that the

Chapter 1: Introduction.

development of the standing solid phase proceeds around 500 times slower than the initial adsorption phase.

From the information provided above, a generalised mechanism of formation may be proposed. The mechanism is a multi-step process, each with different kinetics and time scales. A schematic of this process is represented below in Figure 1-18.

Chapter 1: Introduction.

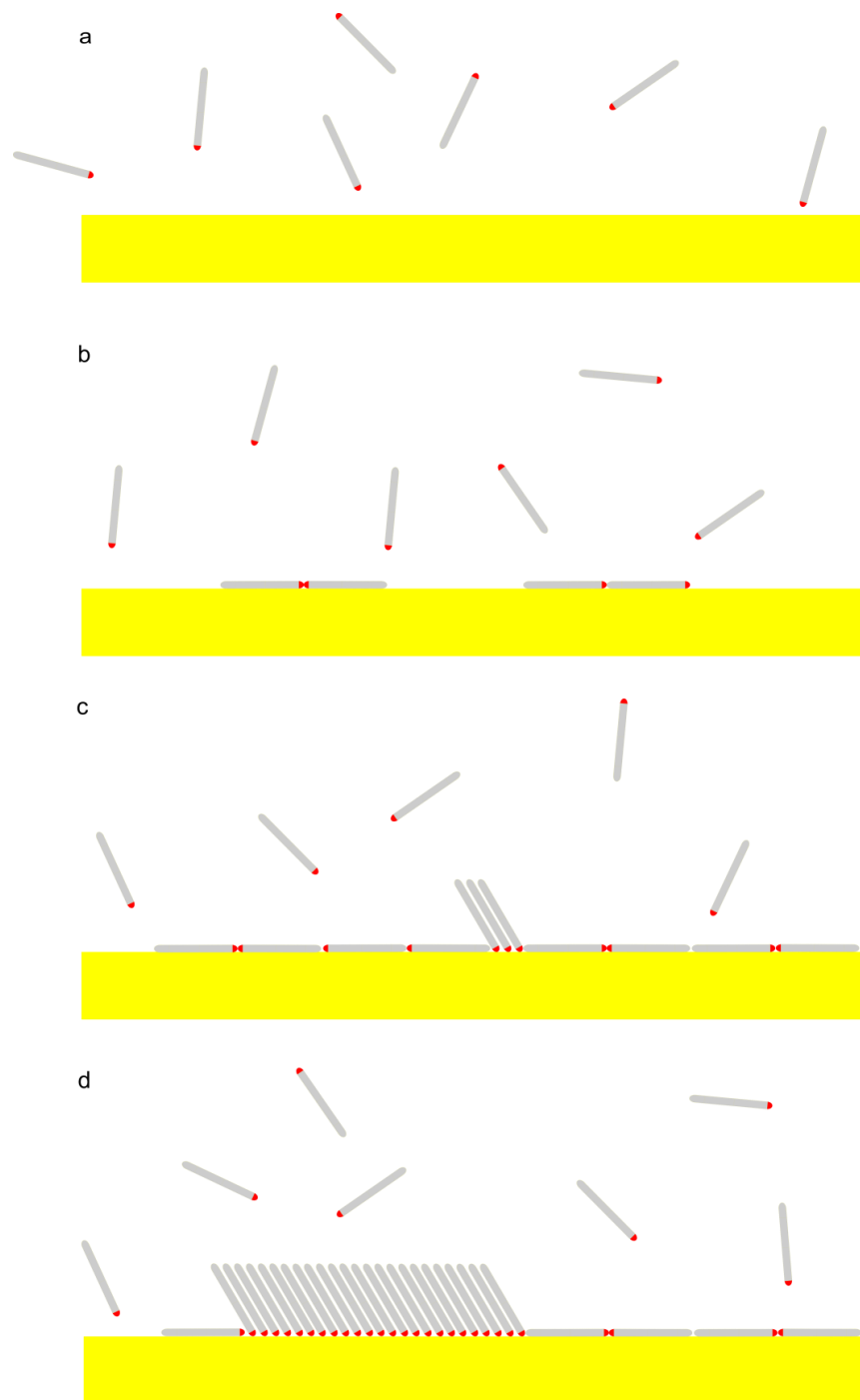


Figure 1-18 Schematic of thiol adsorption onto a gold surface. Initial state of immersion (a) proceeds to striped phase island growth (b). Islands continue to grow and early stage solid phase begins to form (c). Continued growth and formation of a full SAM (d).

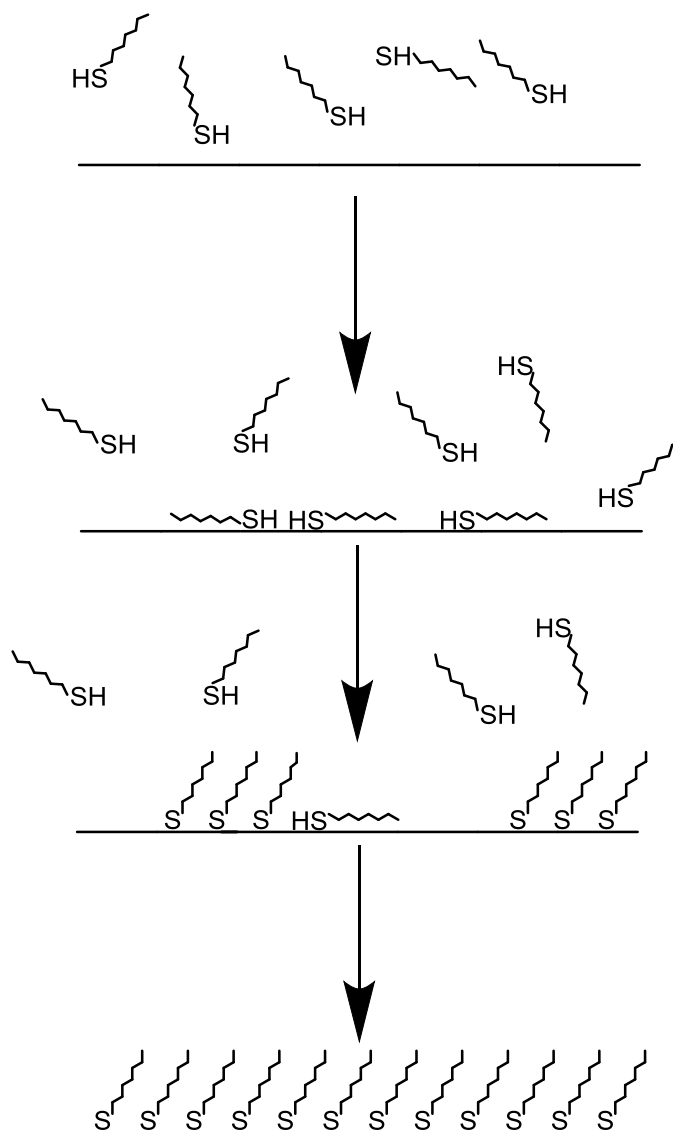


Figure 1-19 Thiol adsorption process outlined in Figure 1-18.

1.8.3 The structure of SAMs formed on gold.

Early work on thiol self-assembly carried out in the early 1980's focused predominantly on fundamental studies with specific conditions and reagents. As the field developed, groups such as Porter et al [103] and Nuzzo et al [104] began to notice oddities with the SAM thickness when compared to expected values, for example when compared to the adsorption of carboxylic acids onto aluminium as carried out by Nuzzo [114] in 1985. Porter noted

however that the structure of the thiol molecules were not perturbed by SAM formation, as the Infra-Red Spectroscopy (IR Spec) images did not deviate greatly from the spectra of bulk condensed alkanethiols. Porter proposed that for alkanethiols of the form $\text{H}_3\text{C}(\text{CH}_2)_n\text{SH}$ with $15 < n < 21$, the adsorbed molecules tilt from the surface normal by 20-30°. As the sulphur head is approximately the same size as the alkyl chain diameter ($\approx 0.5\text{Å}$), head groups need to be sufficiently spaced to allow the tilt to occur. This leads to irregularities in structure, as can be seen by the electrochemical tests carried out by Porter [103]. This 30° cant of the chains has become a commonly accepted observation with several groups agreeing that many SAMs are tilted [98, 100, 115-117]. In addition, it has been shown by IR spectrometry that the aliphatic chains are in an all trans conformation within the monolayer [117] and the sulphur atoms bond to the Au(111) in a simple $(\sqrt{3} \times \sqrt{3})R30^\circ$ structure (Helium diffraction [118] and Atomic Force Microscopy [119]) as shown in Figure 1-20. The sulphur-sulphur distance in this structure is around 4.99Å , which is around three times the VDW diameter of a sulphur atom, thus the interaction between adjacent sulphur atoms is believed to be minimal [116, 120, 121].

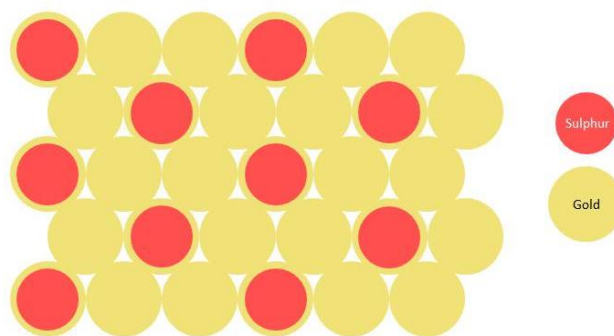


Figure 1-20 A $(\sqrt{3} \times \sqrt{3})R30^\circ$ overlayer of sulphur on gold. The gold is face centred cubic (fcc)

1.9 Factors affecting SAM formation.

The self-assembly process of alkyl thiols is driven by the chemisorption of the thiol head group to the gold surface, Van der Waals interactions between alkyl chain tails, and the overall increase in entropy of the system due to desolvation of the gold surface.

1.9.1 Alkyl chain length.

Alkyl chain length is one of the most studied parameters in SAM production. Early work by Whitesides *et al* showed how SAM formation has a preference for longer chain alkyl thiols over shorter chain variants. This implies that the adsorption process is under thermodynamic control as shorter chain thiols would have higher diffusion rates and lower desolvation barriers to overcome. Increasing the difference between chain lengths leads to an increase in preference for the longer chain. [100] Xu [122] also suggests that the larger alkanethiols are less mobile than the shorter chain molecules. The result of this is that the lying down phase described earlier exists for less time for long chain thiols than the corresponding shorter chains, and that formation of an organised chemisorbed structure proceeds more quickly for longer chains because of this.

In addition, long chain alkyl groups pack more closely than the short chains due to the increase in VDW interactions between backbones. The result of this is that long chain thiols form a more ordered crystalline-like structure, whereas shorter chains generate a liquid-like structure which is more mobile and as a result less ordered [95]. This packing density may be seen in work by Porter [103] in which ellipsometry data varies from calculated models. Long chain thiols give ellipsometric thicknesses that are greater than the calculated values, but

shorter chains give a smaller ellipsometric thickness than expected. This discrepancy may be due to changes in the refractive index of the adsorbed material. More densely packed layers have a higher refractive index (around 1.5) than less densely packed layers (1.45). These observations are in agreement with the work carried out by Nuzzo in 1987 [123], but disagrees with Nuzzo and Allara's work on the adsorption of acids on aluminium [114]. Despite the discrepancies highlighted, Porter shows through electrochemical tests that long chains pack tightly, disallowing passage of either chloride or perchlorate ions through the structure. Shorter chains on the other hand do allow passage, thus indicating a less densely packed layer. Many groups have observed that chains are all trans and fully extended in structure [97, 100, 105, 116, 120]. This tilted structure occurs to maximise the VDW interactions of the backbone.

1.9.2 Solvent effects.

Although ethanol is the most commonly used solvent during modification through solution, several other solvents have been studied and are believed to influence SAM structure. Whitesides [102] believes that the structure of the solvent influences the SAM by changing the activity of the thiol in solution. Changes in the solvent may alter the equilibrium structure of the SAM, which would be most apparent for mixed monolayers. This is likely to be because of changes in mixing between certain thiols and corresponding solvents. For example geometrical matches will increase mixing; long linear chain thiols such as 1-Octadecanethiol ($\text{CH}_3(\text{CH}_2)_{16}\text{CH}_2\text{SH}$) will mix well with hexadecane ($\text{CH}_3(\text{CH}_2)_{14}\text{CH}_3$).

Another influence on SAM structure is strong specific interactions such as hydrogen bonds. If the thiol molecule contains a tail group with which the solvent can interact, tail-tail and tail-solvent interactions influence the solid/ liquid interface, thus affecting the kinetic and

thermodynamic properties of the SAM formation. Despite the influence of solvent on SAM formation, Whitesides found little evidence of solvent within the SAM structure.

Schneider [124] conducted studies using electrochemical quartz crystal microbalance (EQCM) techniques to probe SAM formation in different solvents. They found initial alkane thiol adsorption to form submonolayer structures from dimethylformamide (DMF) at millimolar concentrations was rapid (seconds) but did not proceed to form a well ordered SAM. However, adsorption from acetonitrile (ACN) proceeded more slowly (minutes) but formed a well ordered SAM. They propose that the quality of the final SAM is inversely proportional to the solubility of each mercaptan in solvent.

Several groups have investigated solvent effect on the kinetics of adsorption with most groups using alkanethiols. Dannenberger [125] presented data indicating adsorption from hexane was faster than from ethanol, which in turn was faster than dodecane and finally hexadecane. As pointed out by Schwartz, [93] this order coincides with solvent viscosity and would thus affect thiol diffusibility in solution, but there is ample evidence to suggest that SAM formation is not limited by diffusion at micromolar concentrations or above. Peterlinz [108] agrees with Dannenberger and suggests that the initial stage of SAM growth is around 35% faster in hexane than in ethanolic solutions. In addition, Karpovich [116] found no significant difference when hexane and cyclohexane were compared. From this information, Schwartz suggests that the limiting step may involve the displacement of the solvent from the gold surface. Therefore, solvents which have stronger interactions with the surface would be displaced more slowly by the adsorbate molecules and SAM formation would proceed more slowly.

1.9.3 Temperature.

The role of temperature is often overlooked in thiol based experiments with the common belief that temperature has a role in the kinetics of SAM formation but not on the final thermodynamic structure. However, several authors claim better order may be achieved by lowering the substrate temperature. [117, 120, 126]

1.9.4 Adsorption of thiols and disulphides.

It has been reported [95] that thiol solutions may oxidise over time to produce disulphide species. Debono [105] reports that the UV adsorption spectra of disulphides exhibit two clear peaks, one at 210 nm and one at 255 nm, whereas thiols exhibit a single adsorption band at 205 nm. 500 μ M thiol solutions did not exhibit disulphide at concentrations above 0.4% when using the parent thiol in hexane, hexadecane and dodecane. Subsequent bubbling of air through these parent solutions for 24 hours did not show an increase in disulphide concentration [105].

Despite the presence of both thiol and disulphide in solution, the final SAMs produced are indistinguishable from the pure thiol or disulphide SAMs. This is because of two reasons. The first is that many of the macroscopic properties of the SAM are dictated by a few atoms at the surface of the layer. The second is because the disulphide bond dissociates to form Au-SR bonds. These bonds are analogous to those formed by thiol adsorption onto gold via the loss of hydrogen gas. Nuzzo et al [104] showed by Electron-Energy-Loss-Spectroscopy (EELS) that there is little evidence to suggest a S-S bond forms when adsorbing from a disulphide. This is shown in Figure 1-21 below.

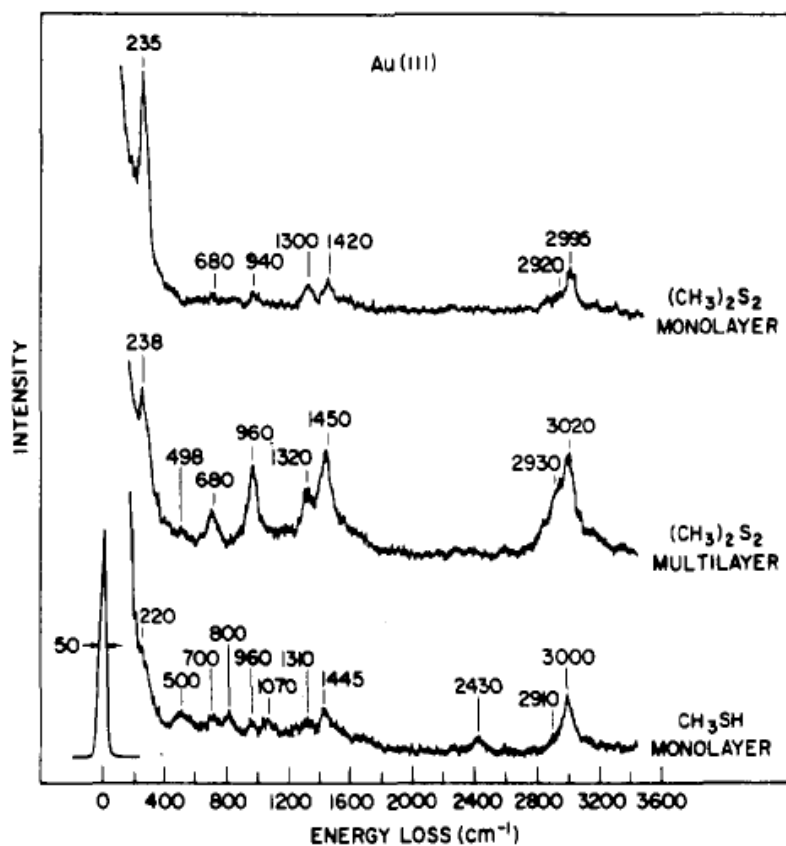


Figure 1-21. High resolution EELS spectra indicating a dimethyl disulphide formed monolayer (Top), a dimethyl disulphide multilayer (Middle) and a methanethiol monolayer (Bottom). The figure was taken from [104].

Despite the similarity of the final structures, thiols are used preferentially over disulphides because they are more soluble in organic solvents, such as the commonly used ethanol [94]. Several groups [95, 99] believe that the preferential adsorption of thiol molecules over disulphides is kinetic due to the steric hindrance of the disulphide compared to the thiol. Dialkylsulphides may also be used to produce SAMs, but are less robust than other methods. This is because the sulphur of a dialkylsulphide interacts datively with the metal surface, whereas bonding occurs via a thiolate in the case of thiols and disulphides. The dative bond is much weaker and thus the SAM is less stable to degradation. Another negative aspect to dialkylsulphide use is that they do not readily replace surface impurities. As a result, more care

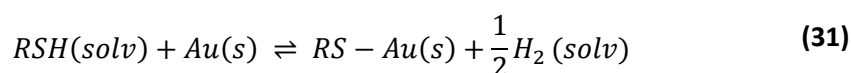
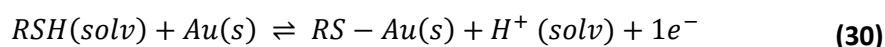
must be taken during sample preparation. On the other hand nearest neighbour control can be achieved using dialkylsulphides, unlike other methods.

Early work on the bonding energy of disulphides was carried out by Nuzzo and Dubois in 1987 [104]. They found that recombinative desorption of disulphides is an activated process with a barrier lying close to 126 kJ/mol. This energy indicates that significant charge transfer to the sulphur must occur. This belief is supported by theoretical calculations [127] and subsequent work into both physisorption and chemisorption carried out using alternative methods. [128] Despite these values being accepted, Whitesides et al [95] reported a lower value for the desorption process, 117 kJ/mol, as did Yang et al [129] who quote 117-126 kJ/mol as the dissociation energy in ultrahigh vacuum (UHV) and 109 kJ/mol in solution. It must be noted however that the latter studies were performed in Decalin, where Whitesides used hexadecane. In addition, Schlenoff measured the desorption energies for a variety of sulphur containing molecules from gold [130]. From the varied data accrued, Love et al [94] formulated an estimate for the Au-S bond strength to be around 209 kJ/mol. In contrast Schlenoff calculated a value of 167 kJ/mol. Of most importance however, is the indication that the Au-S bond is moderately strong, with thermal stability up to around 80 °C [130] before any deviation in coverage begins to be observed.

1.9.5 Fate of the hydrogen atom.

For some time the fate of the hydrogen atom during SAM formation was an unanswered question. However more recently, several groups have presented data to answer the question. Nuzzo [104, 131] claims that the hydrogen atom weakly binds to the gold surface, and then readily desorbs as hydrogen gas at temperatures below 120 °C. Work carried

out by Porter [132, 133] shows that the hydrogen atom is removed as a neutral atom, with the formal oxidation state of the sulphur atom being reduced by 1, before desorption as hydrogen gas (H_2). In addition, in the presence of oxygen, the H_2 gas may desorb as hydrogen peroxide (H_2O_2). From the data obtained by Porter, Karpovich [116] estimated ΔG_{ads} for the production of a proton to be $\Delta G_{ads} = -41.43$ kJ/mol (equation (30)) and for production of neutral hydrogen to be $\Delta G_{ads} = -15.48$ kJ/mol (equation (31)).



1.9.6 Adsorption of functionalised thiols.

From the standpoint of macroscopic properties of the SAM, such as wettability, it is the chain terminating group which plays the most crucial role. By far the most studied chain terminus is the methyl group and several studies have been carried out using Infrared spectroscopy (IR) [115, 134] and Raman spectroscopy [135] to investigate the orientation of the terminal methyl group by comparing vibrational stretching modes. The data obtained indicates that sequential addition of methylene groups between the sulphur and methyl groups leads to a systematic variation of the orientation of the terminal group. In addition these tests indicate that there is no change in methylene stretching frequencies, showing that the reorientation is restricted to the methyl group, and does not alter the bulk methylene positions.

LEED [131] and helium scattering studies [118] have shown that the methyl groups follow the $(\sqrt{3} \times \sqrt{3})R30^\circ$ structure of the bound sulphur atoms. Further examination shows additional splitting of the diffraction spectra, which indicates that there must be more than one methyl group per unit cell [120].

Adsorption of thiols with polar end groups is not as straight forward as the methyl terminated chains. Groups which can form hydrogen bonds do so, leading to more complex structures. IR spectroscopy has once again been used to probe this structure and some orientations are shown in Figure 1-22.

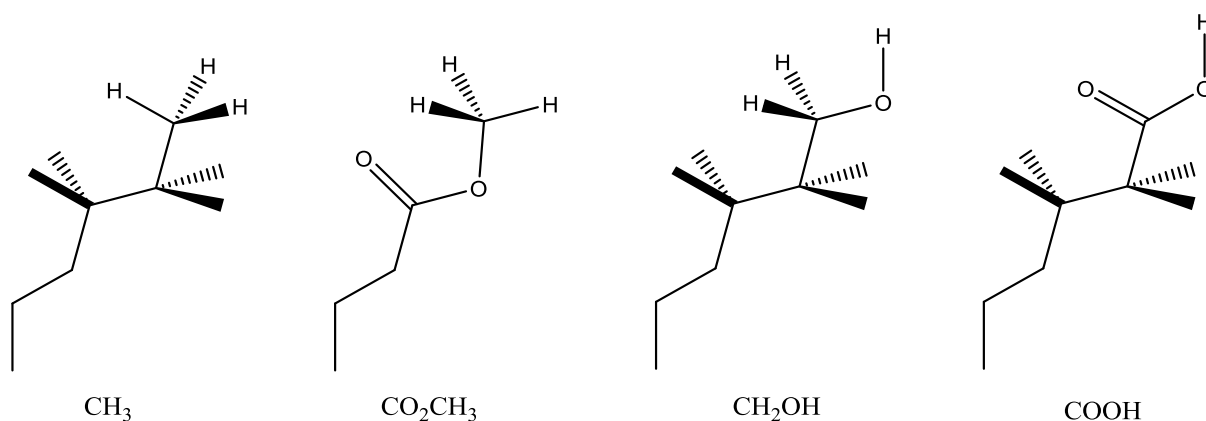


Figure 1-22 Projections of various terminal groups, adapted from work by Dubois. [120]

The only requirement for good packing of these tails is that the terminal group is small enough to fit within the interchain distance of around 5\AA , although larger groups may be accommodated by forming mixed monolayers with a smaller tail group.

Whitesides et al [95] carried out work on the acid terminated thiols such as $\text{HS}(\text{CH}_2)_{15}\text{COOH}$, with the packing of these acid terminated species being monitored via contact angle goniometry as seen in Figure 1-23.

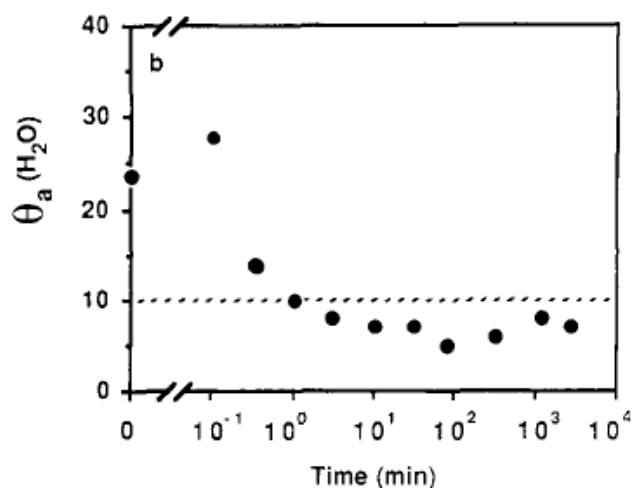


Figure 1-23 The advancing contact angle of water on a self-assembled monolayer of HS(CH₂)₁₅COOH. The dotted line represents the point at which Whitesides considers the surface to be wet by water. [95]

The apparent rise in Figure 1-23 is due to the formation of the laying down phase as described above. This phase shields the hydrophilic gold from the water, and exposes hydrophobic methylene groups. As time progresses these laying molecules begin to reorient into the standing phase. This process slowly exposes more of the COOH group and thus the contact angle is reduced. This process continues until the SAM is highly ordered and the contact angle becomes more constant.

1.9.7 Defects in the SAM.

Several factors can lead to defects in the SAM which in turn can result in oddities in the macroscopic properties of the surface. One such factor is the size of the head and tail groups of the thiol used. As discussed previously, the sulphur and methylene chain have a diameter of around 5Å. The greater the mismatch between the tail group and this Van der Waals diameter, the more disordered the packing.

Other defects include adatoms, where atoms or even clusters of atoms sit on the crystalline gold plane. In addition, vacancies and step edges alter the height of the terminal groups, thus adding disorder. These phenomena are outlined in Figure 1-24.

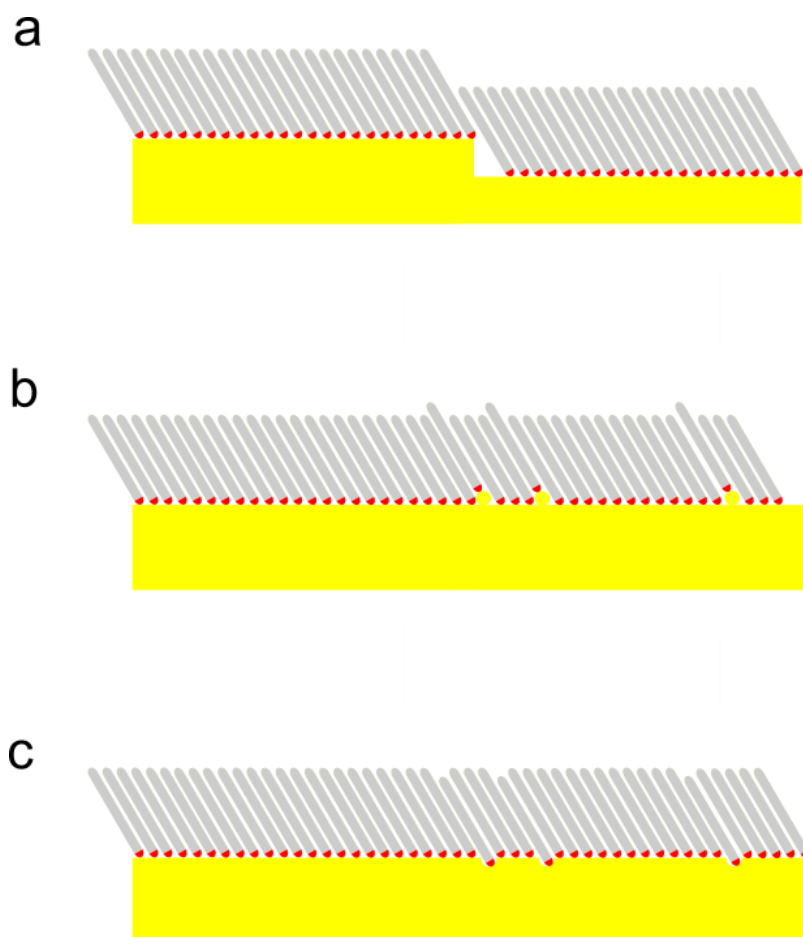


Figure 1-24 A schematic representation of a step edge (a), adatoms (b) and vacancies (c) within the underlying gold layer and their effect on SAM organisation.

Another source of defects is created during mixed monolayer formation. Whitesides [97, 102] conducted several neat experiments to investigate the disorder created by mixed monolayers. By changing the ratio of two hydroxyl terminated thiols, $\text{HS}(\text{CH}_2)_{11}\text{OH}$ and $\text{HS}(\text{CH}_2)_{19}\text{OH}$, a clear increase can be seen for an intermediate ratio, corresponding to between 1-50% $\text{HS}(\text{CH}_2)_{19}\text{OH}$ (Figure 1-25).

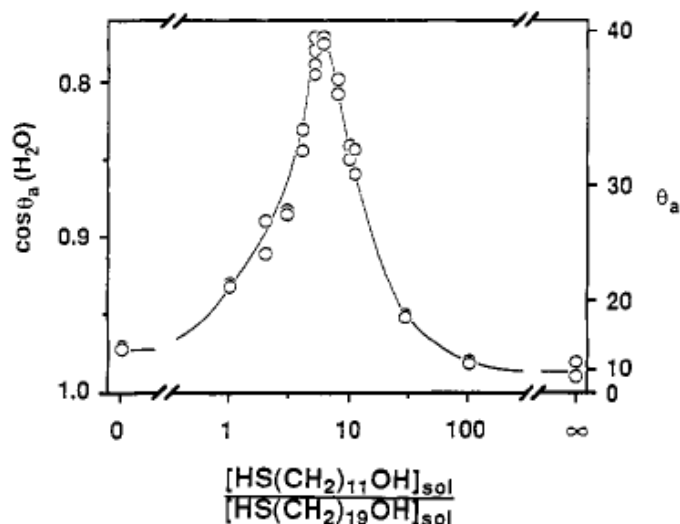


Figure 1-25 Mixed monolayers of $\text{HS}(\text{CH}_2)_{11}\text{OH}$ and $\text{HS}(\text{CH}_2)_{19}\text{OH}$ adsorbed from solutions of ethanol. The advancing contact angle of water is shown. [100]

This increase in contact angle for mixed monolayers is due to the exposure of backbone methylene groups within the hydroxylated surface. For monolayers containing single components, or close to single components, better ordering of the SAM can be achieved. As more of the second thiol is added to the solution, regions of the SAM become disordered, with longer chains folding and laying on top of the hydroxylated surface and folding within it. This leads to an exposure of the hydrophobic methylene backbone, increasing the contact angle. A representation of this disordering process may be seen in Figure 1-26

Love et al [94] review the area of defects more thoroughly, however any process which causes changes in the properties and structure of the underlying gold layer, whether intrinsic or extrinsic, leads to defective SAMs that deviate from the ideal structure. The fact that thiols coat gold surfaces closely following topographical features is both a positive and negative for many research areas. These changes in underlying structure must be controlled in order to achieve high levels of order within the fabricated SAM.

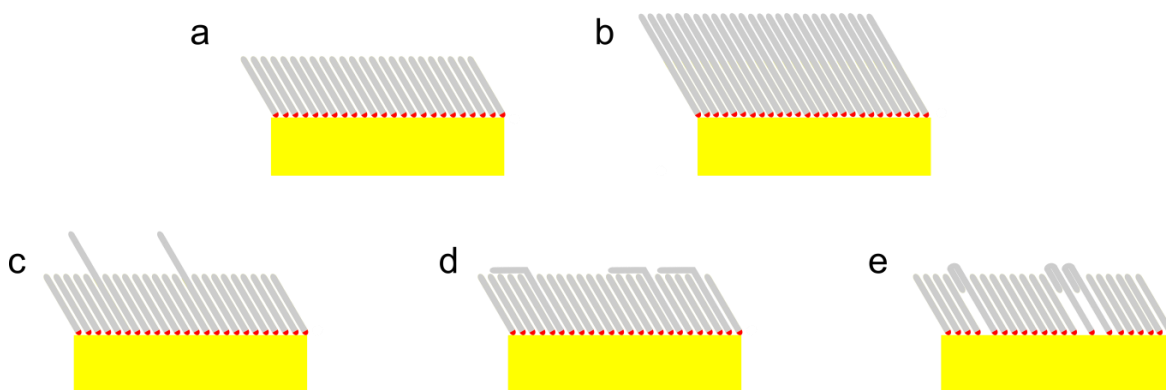


Figure 1-26 Schematic of potential defects within mixed monolayers. (a) and (b) are two, single component monolayers. (c), (d) and (e) are mixed monolayers in which the longer backbone chains can fold and curl to disrupt the packing of the layer. Similarly, short chains can disrupt a predominantly long chain SAM.

1.10 Adsorption from the gas phase.

Growth of SAMs under ultra high vacuum (UHV) is another, less common method of surface preparation. Its use is more limited and requires considerably more effort than solution deposition. [94, 107] Alkanethiols with the structure $\text{HS}(\text{CH}_2)_n\text{CH}_3$ where $n \geq 11$ lack adequate vapour pressure to undergo deposition from the gas phase.

Whitesides [99] and Love [94] have suggested that there is a significant barrier between the physisorbed lying phase and the chemisorbed standing phase, with the dissociation of the thiol S-H bond to the thiolate moiety acting as a kinetic bottleneck. Under UHV conditions this barrier may not be met, especially for short chain alkanethiols, due to the low sticking probability and heat of adsorption of such molecules.

Despite the difficulties associated with UHV deposition, this technique does have benefits. Substrate cleanliness can be better controlled, and the lack of solvent means early stage growth of the SAM may be investigated by numerous techniques [107]. It allows preparation of sub monolayer systems to be probed, and in fact much of the current knowledge of the adsorption mechanism has been found from in situ experiments on samples prepared under UHV. The process has been reviewed in depth by Schreiber [112].

1.11 Surface modification by silanes – an introduction.

The development of controlled surface functionalisation is not limited to the adsorption of thiols onto gold. Numerous silicon containing molecules have been used as modifiers, including chlorosilanes, alkoxysilanes and polysiloxanes. Such silane chemistry presents a pathway to the modification of surfaces containing terminal hydroxyl groups such as silica, alumina, zirconia and thorin [136].

Silane modification holds great promise as the modifiers covalently bond to the substrate, providing a stable structure that can be used in a variety of applications. A current global need to reduce carbon dioxide (CO₂) emissions has led to many technological advances in carbon capture and storage. Leger et al [136] have shown that by careful modification of ceramic membranes gas permeability can be reduced. They also postulate that modification of porous membrane with an appropriately sized silane can lead to the blockage of pores. Tailoring this approach could lead to a method of gas separation and provide a new pathway to carbon capture and utilisation.

Another global application of silane modification is within the electronics industry with new devices such as biosensors and photovoltaics making use of surface modification of the

native silica surface. Despite the growth in the field, one of the biggest problems with current electronics technologies is their protection from environmentally induced failure. Plastic packaging is of course an economic option; however permeability can cause a water layer to be present at the surface of the electronic component. This water can lead to the reduction in adhesion of the surface to its protective coatings, corrosion and finally failure of the part. Angst [137] presented work on this area in the early 1990's.

In addition, silanes have found uses in chromatography, [138-141] optics, water resistant coatings, anti-fouling coatings and nanoparticle fabrication [140-143] to name but a few. Despite the number and variety of applications, silane modification is understood far less than the corresponding self-assembly of thiols onto gold. It is this understanding and the effects of several factors including the role of water, temperature and solvent in SAM formation, as well as the bonding mechanism and the conflicting reports in these areas that will be reviewed in this section.

1.12 The silica surface.

Silica (or quartz) is the main constituent of sand and takes the form SiO_2 (Figure 1-27). This SiO_2 is taken and purified to >99% by crushing and heating in an electric arc furnace. Using the Czochralski method, single crystal silicon wafers are grown and have the structure shown below in Figure 1-28.

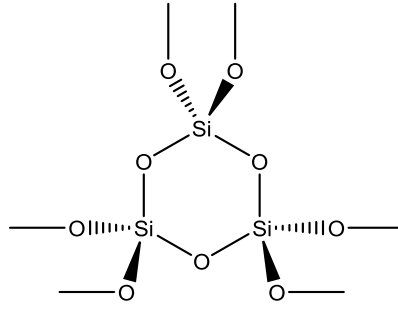


Figure 1-27 Structure of silica.

The single crystal is then sawn and polished. Due to the high energy of the finished product, the silicon surface readily oxidises to form surface silanol groups. It is these that are important for silanisation as discussed later, although silanisation can occur from other surfaces as discussed by Thissen et al [144].

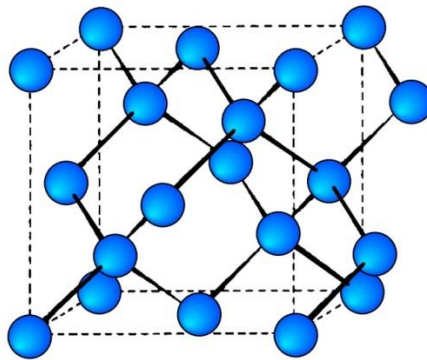


Figure 1-28 The crystal structure of pure single crystal silicon.

The state of the silicon surface is dependent on the cleaning mechanism undertaken before use. Several cleaning methods have been developed and are discussed in detail in appendix 7.1.

1.13 The role of water on SAM formation.

One of the factors that became apparent in the early work on silanisation in the 1980's was the importance of the role of water. There are many studies and conclusions presented in the literature, but the true role of water is still not fully understood. Work by Sagiv [145] initially suggested that the chloro or alkoxy moieties of the modifying silane were hydrolysed in solution to trihydroxy species. These species then approached the surface and a condensation reaction forming a Si-O-Si bridge occurred, creating a covalent link to the silicon surface. Adjacent hydroxyl groups of the newly attached silanes could then undergo further condensation reactions, creating a polymerised network and adding to the robustness of the SAM as a result. This process is schematically shown in Figure 1-29.

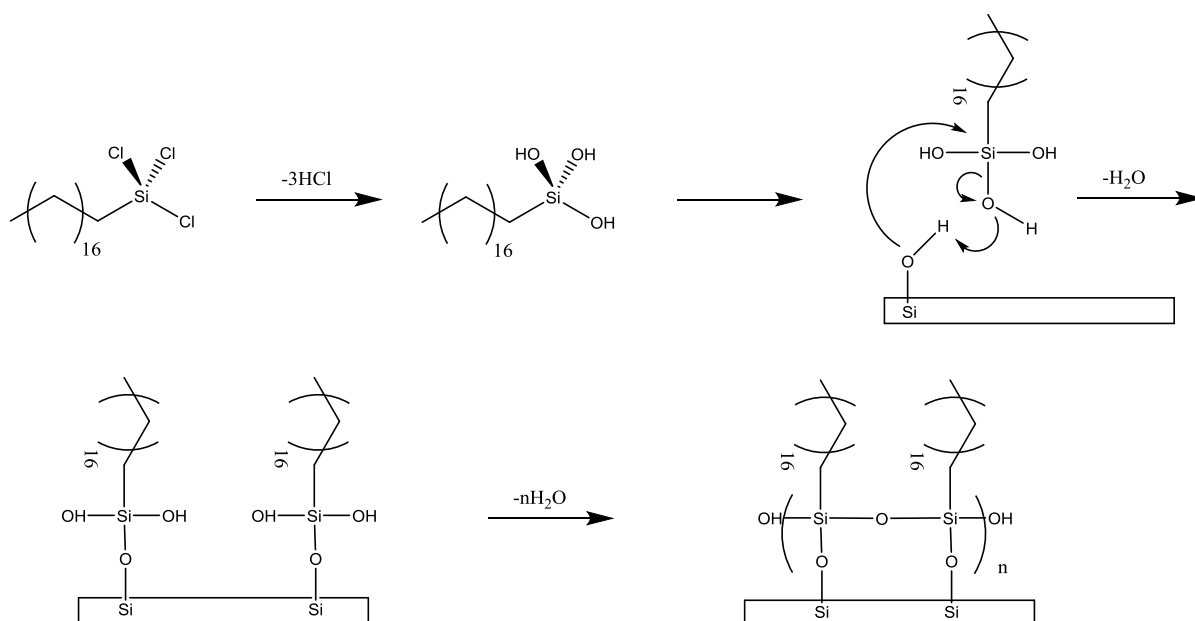


Figure 1-29 Schematic of the hydrolysis and attachment of trichloro alkylsilane to a hydroxylated silicon surface.

Chapter 1: Introduction.

Since this hypothesis was presented, many other groups [139, 146-149] have modified the theory due to the work by Finklea [150] who found SAMs of octadecyltrichlorosilane could be formed on hydroxyl free gold substrates. The current most accepted theory is that very few linkages occur to the silicon surface. Instead, silane molecules physisorb to the surface and are then hydrolysed by surface water, which is eliminated. Adjacent silane molecules can then polymerise together to form 2D networks, with intermittent links to the silicon surface as shown Figure 1-30.

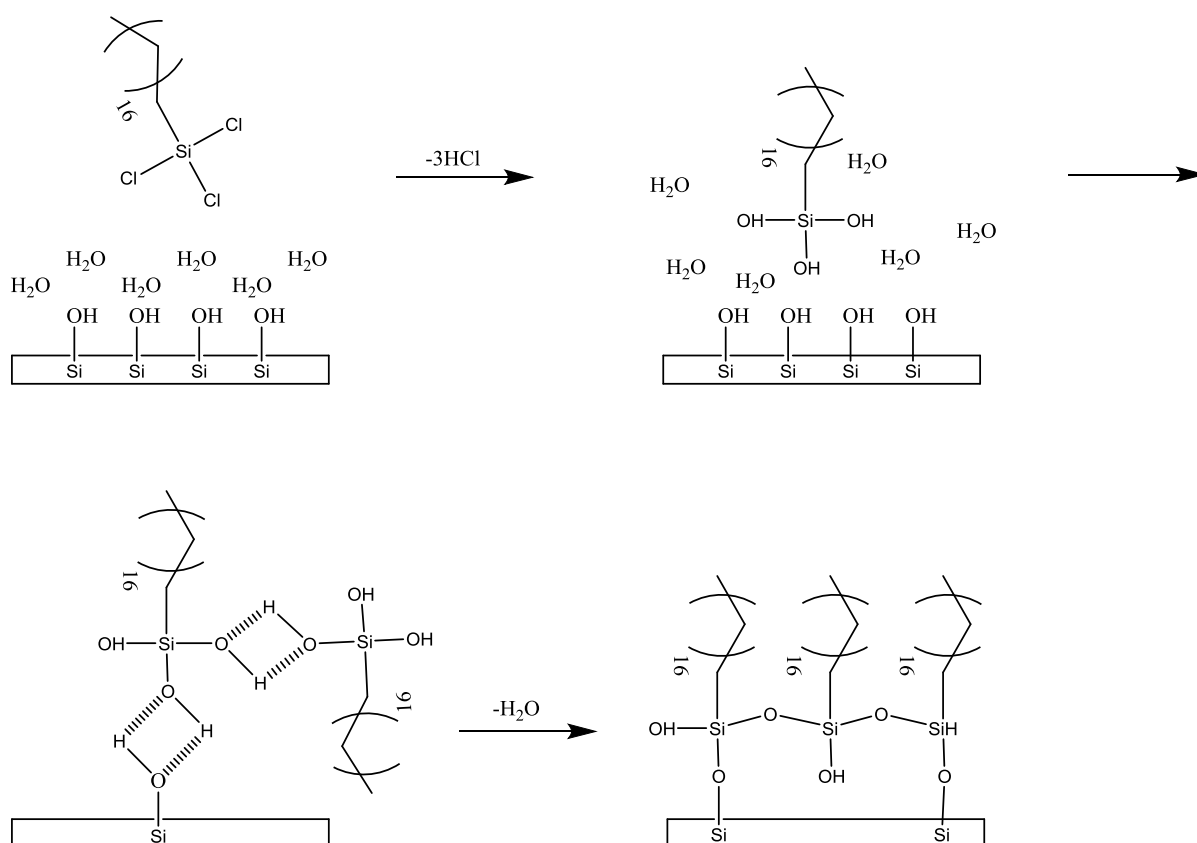


Figure 1-30 The hydrolysis and attachment of trichloro alkylsilanes by a surface water layer.
The final polymerised network has fewer silane/substrate linkages than Figure 1-29.

Angst [137] built on this theory, indicating that soaking the silicon in water before silanisation increases the number of surface hydroxyl groups. This means that extra layers of water can be adsorbed onto the surface, leading to faster reactions and higher coverage by more organised layers. This is important as silanols are relatively stable and as a result their condensation is slow, so increasing water content at the surface will increase the rate of surface coverage. [151, 152]

Water content in solution is also key to the mechanism of adsorption. Coverage by island growth will be discussed in sections 1.14 and 1.15, however, higher water content in solution leads to islands of larger size which grow more quickly. An increase from 12.7 mmol/L to 17 mmol/L leads to a large increase in island size despite the relatively small increase in water concentration. [153] Glaser also found that this increase in water concentration led to no real increase of aggregate size in solution (by Dynamic light scattering). However Bunker [154] found a critical water concentration at which large spherical agglomerates formed in solution. They believe these structures to be inverse micelles. It must be noted that both groups performed their experiments on different silane systems, and different temperatures. Glaser highlighted the subtle interplay of temperature and water concentration and the effect both parameters have as a pair. It is therefore difficult to compare these results critically and draw accurate conclusions. McGovern suggests that 0.15 mg of water per 100 mL of solvent is a tipping value for good coverage. Below this value, incomplete layers are formed. However, solvents with high water dissolution capability are equally disfavoured. [155]

1.14 The role of temperature on SAM formation.

An equally important factor in SAM formation is the role of temperature, although it is often studied much less than the effect of water. Aswal [156] indicates that SAM formation is

generally carried out between -30 °C and room temperature. Adding that the temperature should be tailored to the reacting silane in order to achieve an ordered SAM, with shorter chain silanes needing colder temperatures to form well ordered layers. For example a chain containing 10 carbon atoms should use a formation temperature of 0 °C, whilst a longer 22 carbon chain should be carried out at 38 °C. This relationship is shown in Figure 1-31. [138]

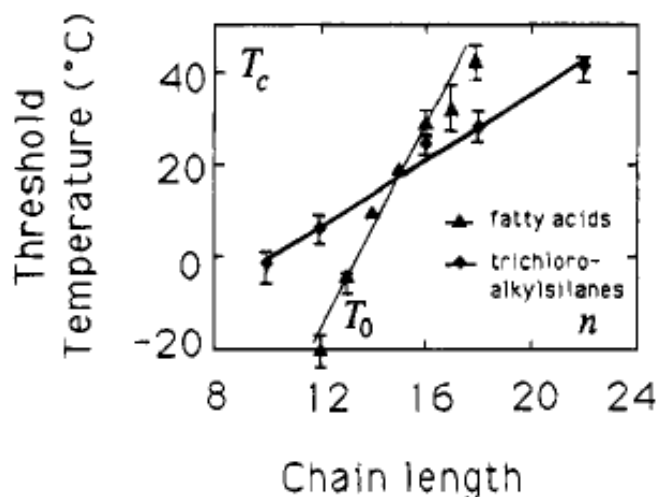


Figure 1-31 The interplay of chain length and solution temperature as investigated by Brzoska. [138]

Brzoska has defined a 'critical threshold temperature' (T_c) which is a property of each silane to be grafted. Below T_c , the system can reach its highest packing density, as evidenced by low contact angle hysteresis. The effect is also present for fluorinated silanes.

Glaser [153] went further and investigated the interplay between temperature and water content of the deposition solutions. Dynamic light scattering (DLS) studies showed that aggregates formed in solution had a small distribution in hydrodynamic radius around 200 nm, independent of temperature and moisture content. They also showed that these aggregates formed more slowly at higher temperatures and lower water content and fastest at low temperature and high water content. It was also observed that below a characteristic

Chapter 1: Introduction.

temperature, which varied for each silane, the concentration of aggregates in solution increased with decreasing temperature until a plateau was reached, below which the concentration of aggregates was constant. It was also claimed that increasing temperature led to smaller island growth, with eventual increase leading to homogeneous growth of the SAM by single molecule adsorption. The final result is a much more disordered monolayer, which is consistent with the decreasing temperature/ increasing order argument outlined above. It is therefore postulated that growth mechanisms and rates can be tailored to suit the user's needs. Glaser showed by AFM that islands of equal size could be produced under different combinations of temperature and water content. However it is worth noting that the data was taken at differing immersion times, and may not be truly comparable to one another. Despite this, there is some potential usefulness to this observation for controlling SAM formation in future work. The AFM images are shown in Figure 1-32.

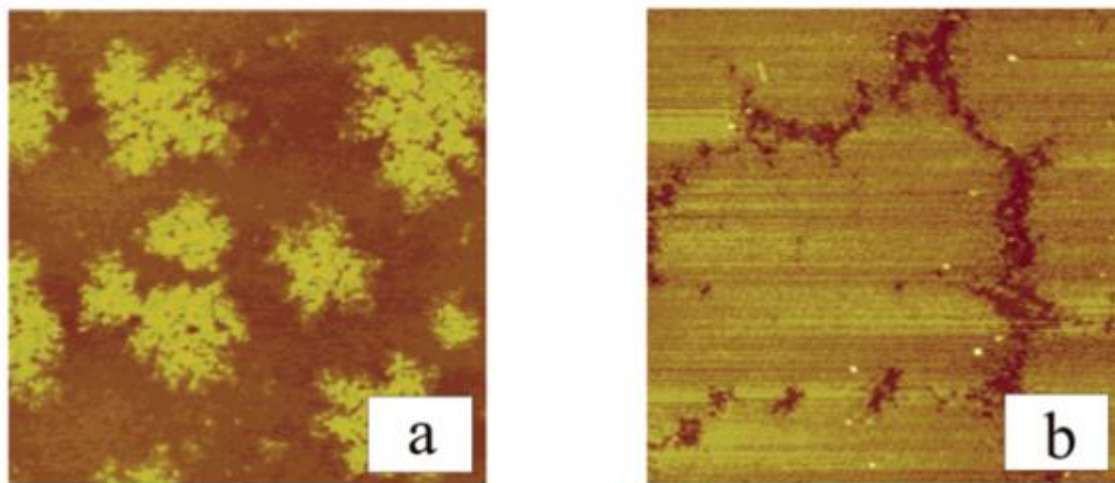


Figure 1-32 AFM images ($5\mu\text{m} \times 5\mu\text{m}$) of islands formed during the growth of octadecyl trichlorosilane on silicon. a) Temperature = $13.5\text{ }^{\circ}\text{C}$, $c(\text{H}_2\text{O}) = 12\text{ mmol/L}$, adsorption time = 15s. (b) Temperature = $28\text{ }^{\circ}\text{C}$, $c(\text{H}_2\text{O}) = 18\text{ mmol/L}$, adsorption time = 5s. [153]

Other groups [157-159] have investigated the effect of temperature after monolayer formation during an annealing step (discussed further in section 1.18.6). Pastermack observed that the stability of the SAM of 3-(Aminopropyl)triethoxysilane (APS) increased with increasing temperature. This is due to an increase in crosslinking between adjacent APS molecules and more extensive horizontal polymerisation.

1.15 Immersion time in solution and the adsorption mechanism.

Early work on the self-assembly process of silanes generated conflicting reports about the mechanism of SAM formation. Wasserman [160] used X-ray reflectivity to probe the growth mechanism, concluding that growth proceeds by a 'uniform' pathway in which molecules of silane are evenly spread over the substrate surface, initially in submonolayer concentrations, before a full SAM is formed after a period in solution. Cohen [161] used

Fourier Transform Infrared Spectroscopy (FTIR) to present a conflicting argument that growth proceeds via the 'island' pathway in which ordered regions of silane form on the surface with unmodified regions, or regions of disorder, in between. However, as pointed out by Bierbaum [140], both FTIR and X-ray reflectivity are techniques which examine a large area and report average findings. Other characterisation techniques such as AFM would give a clearer picture of the adsorption process. Indeed subsequent AFM studies have been performed and provide evidence to corroborate Cohen's work. [140] However, there is also some suggestion that island growth can be avoided under specific conditions with tight control of moisture and temperature as discussed previously above. [153]

Bierbaum was amongst the first to study growth by AFM. [140] This work shows clear evidence of island growth as shown in Figure 1-33. After initial immersion in solution, small agglomerate structures attach to the surface and initiate the growth of large islands with diameters of 0.6-0.9 μm . Smaller secondary islands then form between the primary islands, with the size of these primary islands decreasing slightly. This indicates that the SAM is mobile at this stage and suggests that these secondary islands grow by nucleation of diffusing silanes on the surface. The final SAM, with scarring due to the primary islands, is formed after more than 35 minutes. Bierbaum also carried out similar studies with a propyl variant of the silane. However, the kinetics of the reaction are so fast it was difficult to detect island formation by AFM. This is probably due to steric hindrance with longer chains.

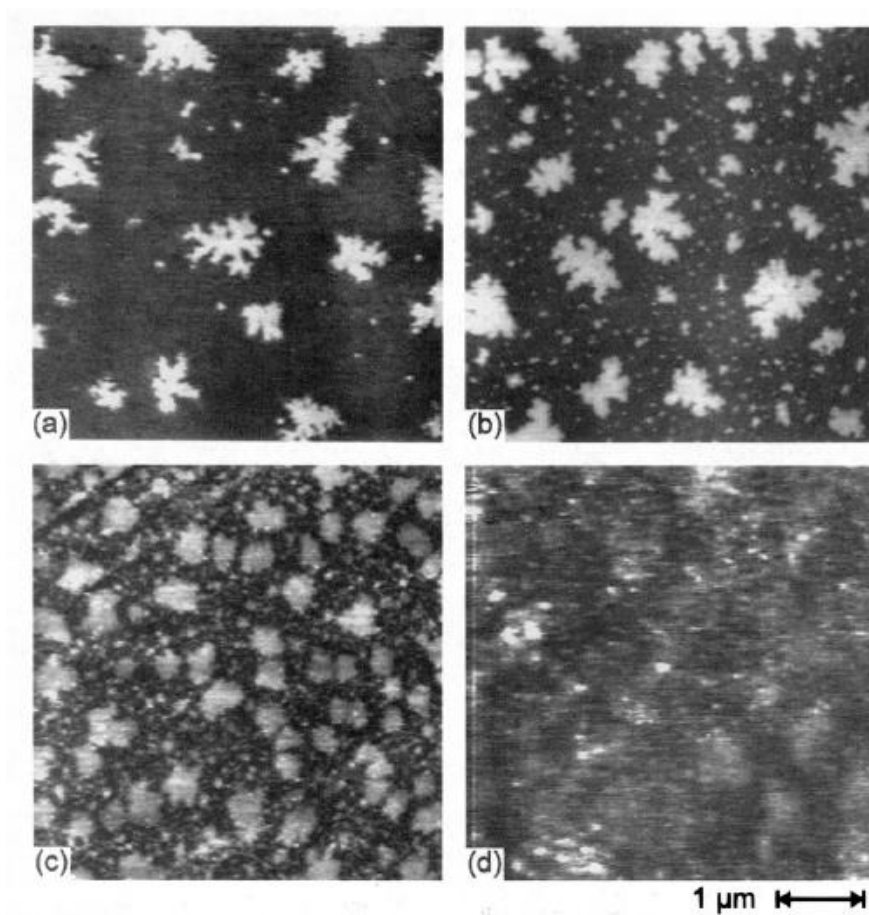


Figure 1-33 AFM images ($5\mu\text{m} \times 5\mu\text{m}$) showing the growth process of octadecyl trichlorosilane on silicon. a) after 15s of immersion, irregularly shaped islands of $0.6\text{-}0.9\mu\text{m}$ diameters form on the silicon substrate; b) smaller islands of silane form between the original islands after 1 minute immersion; c) after 5 minutes immersion, the gaps between islands begin to fill; d) after 35 minutes, full coverage is achieved with scarred regions where the original islands were formed. [140]

Onclin [162] agrees with Bierbaum that shorter chain alkylsilanes do not appear to produce islands on the surface. Maoz [163] has presented data to show that island growth proceeds via molecules that are in a perpendicular orientation to the surface, irrespective of coverage. Brunner [164] has shown how high water content in solution favours island growth, although Wang [165] has more recently shown that even with trace amounts of water, island growth is still possible.

Chapter 1: Introduction.

Jung [142] agrees with the island mechanism and presents further AFM data to support this. They also agree that at submonolayer coverage, the layer has liquid like structure that is considerably disordered and mobile, later orienting into an ordered SAM. Other groups agree. [156]

Leitner [151] and Glaser [153] found that increasing water content led to increasing island size and growth rate. Glaser stated that a small increase in water concentration, from 12.7 mmol/L to 17 mmol/L, causes a large increase in island size (Figure 1-34); whereas increasing the temperature and decreasing the water content decreases island size, and eventually a homogeneous growth regime proceeds. This is because as temperature increases the agglomerates in solution begin to disappear and no nucleation sites for island growth can adhere to the substrate as a result.

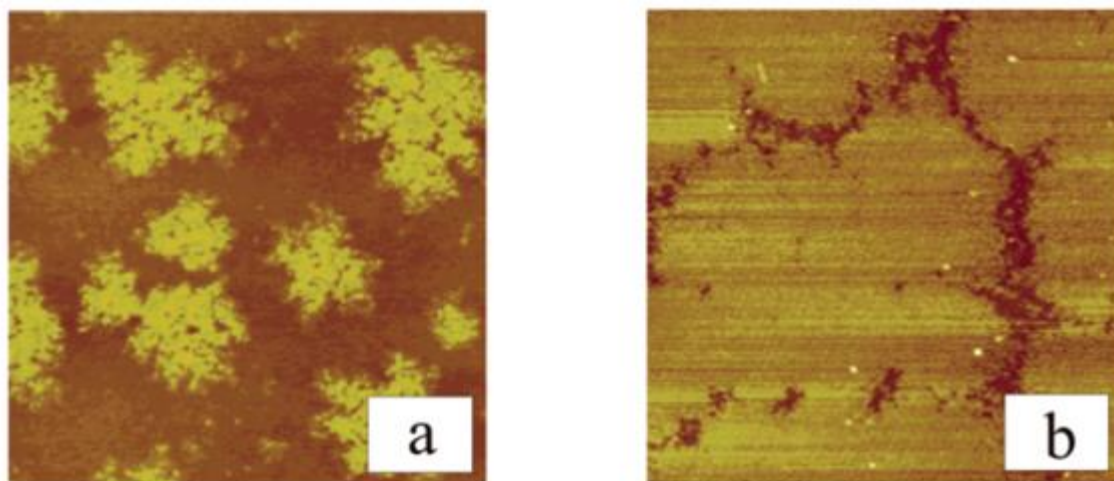


Figure 1-34 AFM images ($5\mu\text{m} \times 5\mu\text{m}$) taken after 15s in solution at 20°C under varying water concentration; a) 12.7 mmol/L and b) 17 mmol/L. [153]

Rozlosnik et al [166] conducted an AFM study to examine surface coverage as a function of time. Their results are shown in Figure 1-35. It can be seen that the SAM is formed

by island growth and eventual filling of the gaps between islands as outlined above. The images taken in Figure 1-35 were produced by the adsorption of by octadecyl trichlorosilane from dodecane, but the authors present similar results for other solvents, concluding all solvents generate full coverage SAMs after 180 minutes. In addition, SAM formation under all solvent conditions studied proceeded via island formation through similar processes. The difference in deposition time is likely due to the ability of the silane to mix with each solvent.

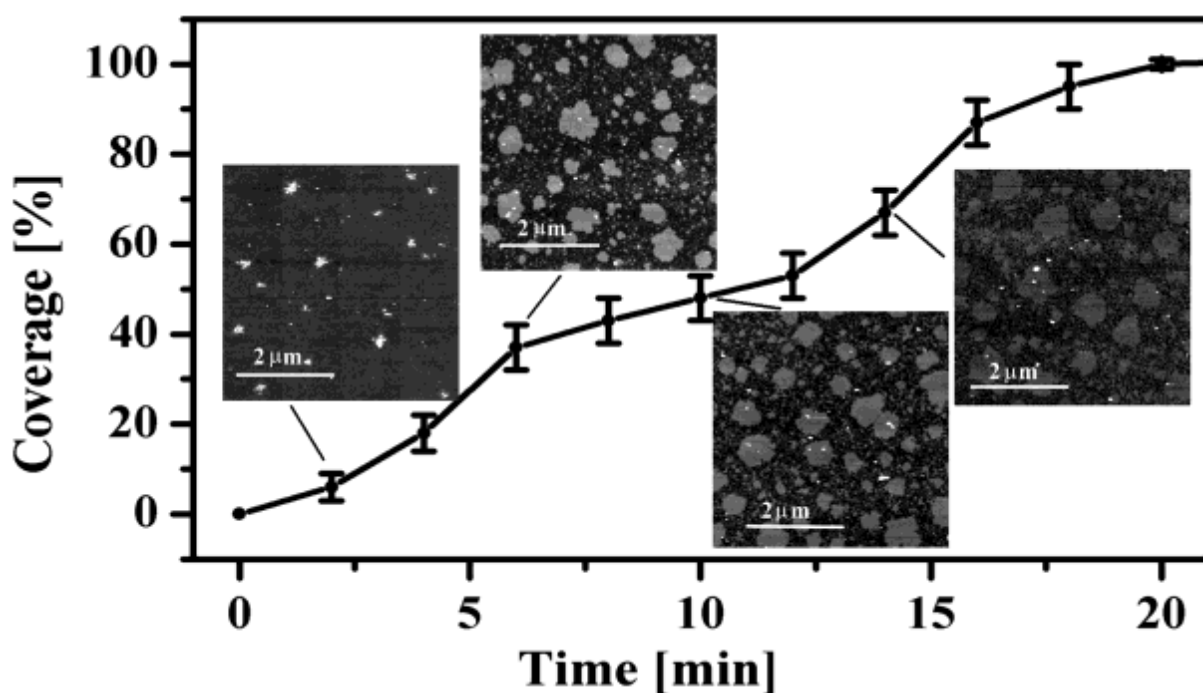


Figure 1-35 AFM images of surface coverage by octadecyl trichlorosilane on silicon as a function of time. Coverage was calculated by bearing analysis. [166]

1.16 The effect of solvent.

The effect of solvent is poorly understood in comparison to many other aspects of silane treatment. Cheng et al [167] carried out a direct comparison of octadecyl trichlorosilane adsorption onto silicon from solutions with varying solvents. AFM images of the surfaces formed are shown in Figure 1-36. It can be seen that the monolayers formed from hexadecane

and toluene have very little detrimental effect on the root mean square (rms) roughness of the samples. However, as progression is made to chloroform and subsequently to dichloromethane (DCM), the rms value increases and visible grains begin to appear on the silicon surface. Cheng attributes the features on the dichloromethane surface to aggregates of silane with sizes in the range of 2-6 nm. The rms data along with solvent viscosity and polarity are shown in Table 1-1

Table 1-1 Solvent viscosity, polarity and SAM rms roughness for systems investigated by Cheng et al . [167]

Solvent	Viscosity η_c (mPas)	Polarity c (D)	SAM rms (pm)
Hexadecane	3.34	0	69.8
Toluene	0.59	0.36	73.1
Chloroform	0.56	1.08	246.7
Dichloromethane	0.39	1.14	1296

Cheng points out the trend between the viscosity: polarity pairs and the rms. At high viscosity and low polarity, the rms roughness is relatively low, but as polarity increases and viscosity decreases the rms increases. This observation may not be representative of the true phenomena occurring, as increasing polarity is likely to increase the prevalence of water in the solvent. Indeed DCM has been shown to contain high levels of water. [168]

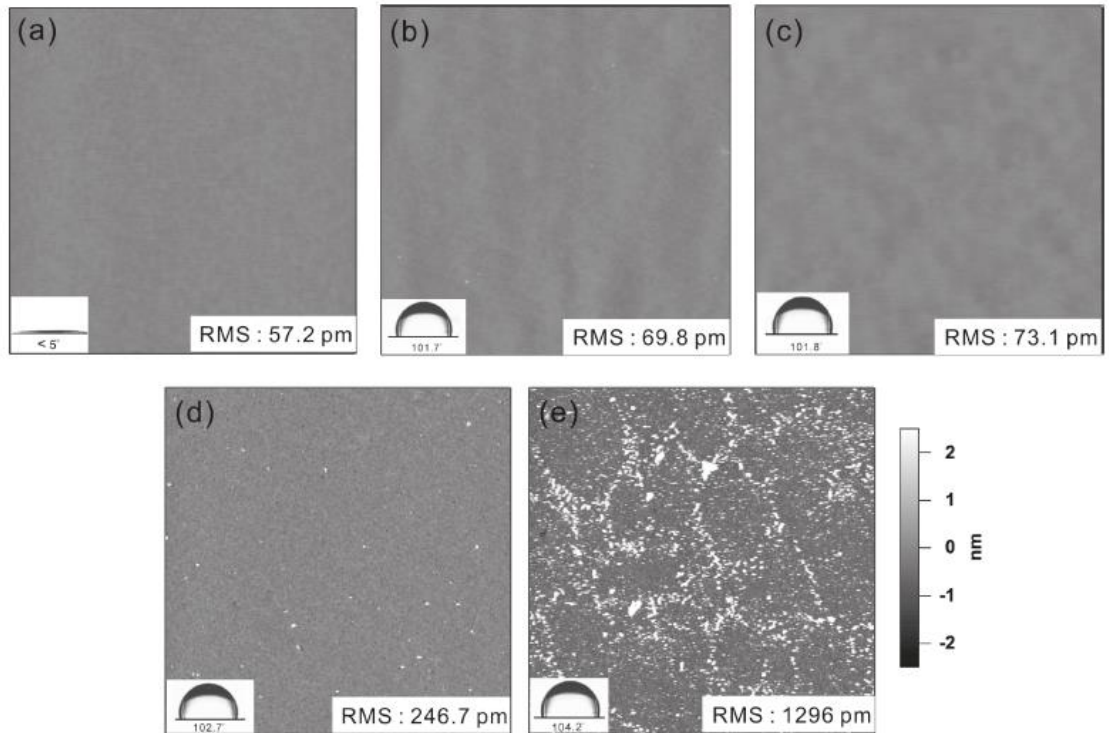


Figure 1-36 AFM images ($5\mu\text{m} \times 5\mu\text{m}$) of octadecyl trichlorosilane adsorbed onto silicon. a) bare silicon; b) Hexadecane; c) Toluene; d) Chloroform; e) Dichloromethane.

Manifar [168] conducted similar experiments to investigate solvent effects using a variation of the solvents used by Cheng, but also using octadecyl trichlorosilane. The SEM images are shown in Figure 1-37 along with AFM images in Figure 1-38.

Chapter 1: Introduction.

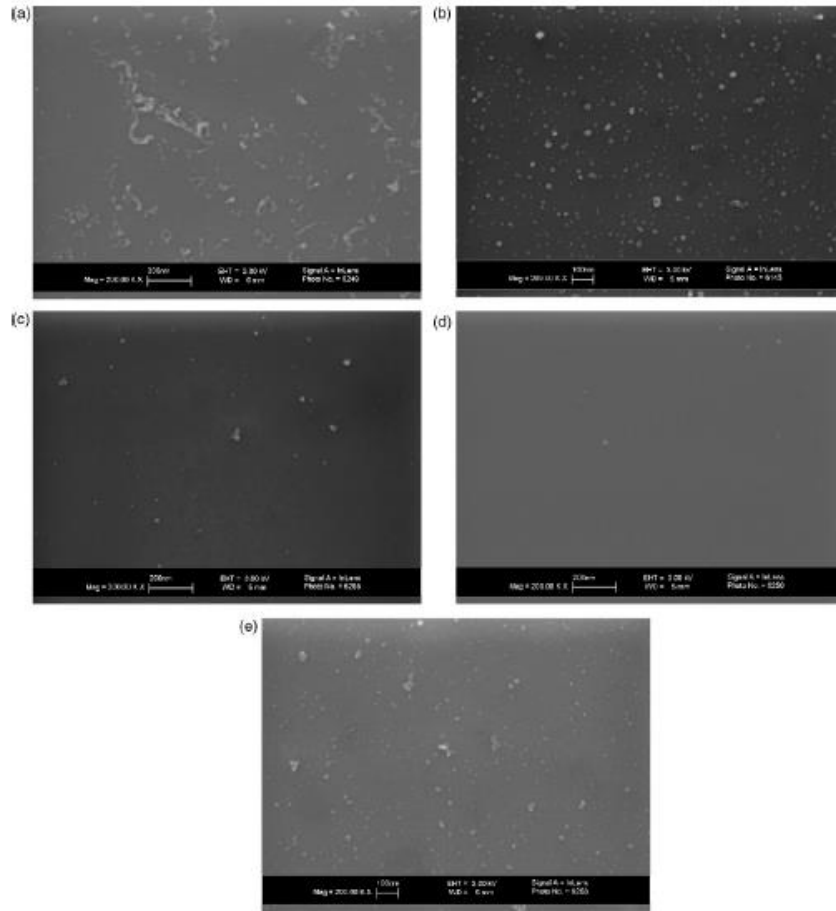


Figure 1-37 SEM images of octadecyl trichlorosilane adsorbed onto silicon from a) Hexane; b) Toluene; c) Tetrahydrofuran; d) Dichloromethane; e) Diethyl ether. [168]

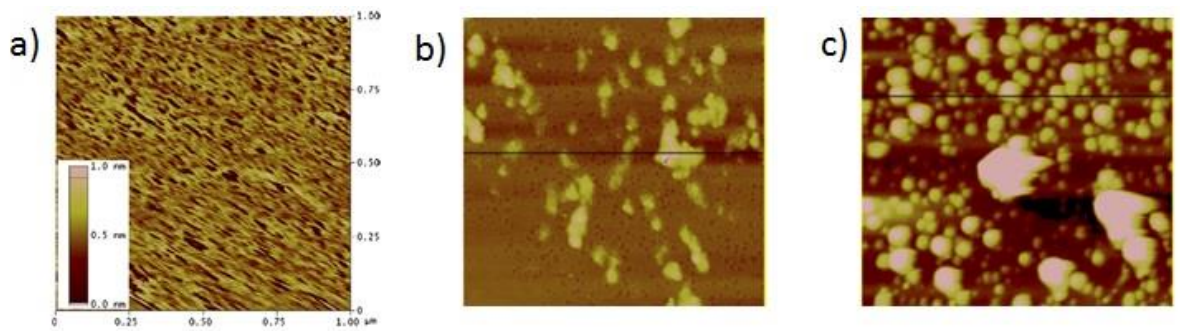


Figure 1-38 AFM images ($1\mu\text{m} \times 1\mu\text{m}$) of octadecyl trichlorosilane adsorbed onto silicon from a) Dichloromethane; b) Hexane; c) Toluene. [168]

Chapter 1: Introduction.

It can be seen from Figure 1-37 and Figure 1-38 that Manifar came to the opposite conclusion to Cheng. Manifar indicates that the SAM formed from DCM is of the highest quality according to their results, as opposed to Cheng who claimed it was the worst. The AFM images, although not directly comparable due to the scan area being different in each case, show that in Cheng's case the DCM layer has a high rms roughness in excess of 1.2 nm and agglomerates on the surface of 2-6 nm in size. However, it can be seen from Manifar's work that the DCM layer has no sign of agglomerates and the peak heights are <1 nm. Upon inspection of the two groups' experimental procedures, Manifar dried all solvents over an alumina column before use, reducing the water content to <2 ppm. Cheng makes no mention of drying. These two experiments show the complexity of the self-assembly process, and how consistent methodology is required to draw accurate conclusions.

Other groups have discussed solvent effects, with Aswal [156] claiming hexane and heptane yield closely packed monolayers, which is agreed with by Rozlosnik [166]. Sagiv [169] indicates that toluene or bicyclohexyl are the best solvents for tightly packed SAMs whereas MCGovern [155] prefers aromatic solvents such as benzene or toluene. All of these groups have investigated the adsorption of octadecyl trichlorosilane.

Several groups have indicated that the choice of solvent is important for SAM formation because of the solvents' ability to incorporate within the SAM itself, causing defects and thus a less ordered monolayer. Sagiv was the first to mention such a possibility [169] with solvent shape and similarity to the adsorbing silane key to its incorporation into the SAM, for example in the case of octadecyl trichlorosilane and hexadecane. However, hydrophobic interactions between the silane and solvent lead to the displacement of hexadecane and a tightly packed monolayer forms. In contrast, the smaller hexane or pentane may aggregate between adsorbed silane molecules, and pose steric problems for their removal. [155]

Gangoda et al [170] have presented ^2H NMR data to show that incorporation of hexane into the SAM was occurring, and was also thermodynamically favourable.

The influence of solvent on SAM formation is therefore ambiguous with conflicting reports in the literature. To add further complexity, surfaces prepared in dry, glove box conditions [166] show little deviation from one another when the solvent is changed. Therefore, it is likely that the solvent is a secondary effect that influences SAM production by its ability to imbibe water and to hydrate the silicon surface to allow monolayer formation as outlined previously. Careful solvent choice must be carried out in order to prevent incorporation into the SAM. However, little work has been carried out into this area, so further investigation is needed to ascertain conditions that promote solvent incorporation into the forming SAM.

1.17 Packing of the self-assembled monolayer.

The packing of silanes on silicon is poorly studied in comparison to the packing of thiols on gold, partly due to the difficulty in sample reproducibility. However it has been shown that similarities to thiol monolayers do exist.

The first similarity is between inter-chain packing. As with thiols, the aliphatic carbon chains of alkyl silanes pack to maximise Van der Waals (VDW) forces between them. This means that the chains are all trans in a highly ordered SAM, with an increasing packing density leading to more order between chains due to a reduction in the silane tilt angle. [156, 166] These VDW interactions are less than 41.84 kJ/mol. In order to achieve this high packing density, the substrate must be heavily populated with surface hydroxyl groups. A low density of hydroxyls is more likely to lead to disordered, liquid-like SAMs. [137] Angst claims that

soaking the silicon substrate in water before use leads to an increase in surface hydroxyl numbers, and thus a more densely packed SAM.

Both Pomerantz [171] and Tillman [172] used FTIR data to show that the silane molecules have a tilt angle of less than 10° from the surface normal. Although several groups have indicated how the silanes are almost perpendicular to the surface, even during island formation, while the regions between the islands have random tilts. [141] This tilt is less than that of thiol SAMs on gold, indicating that silane SAMs are more closely packed, with one chain per 20 \AA^2 as opposed to the thiol SAM, which have one chain per 21.6 \AA^2 . [160] Pomerantz used FTIR to show that the packing is the same for alkyl chains of varied length.

1.18 Stability of the silane SAM.

1.18.1 Stability of the silane SAM compared to other monolayers.

It is commonly accepted that the silane SAM is more stable than the corresponding thiol SAM due to the strong covalent nature of the Si-O-Si linkage between the silane molecule and the substrate. The associated binding energy is between 167.4-188.4 kJ/mol [156] compared with the thiol binding energy of $\cong 120$ kJ/mol. Silane SAMs are also more stable than the corresponding Langmuir-Blodgett monolayers, which has industrial importance, particularly in micro electromechanical systems (MEMS) which require stability at temperatures approaching 400°C .

1.18.2 Stability of SAM under ambient conditions.

Aswal reported stability of the SAM in an airtight container at room temperature for over 18 months. Similarly Brzoska reports that silane modified silicon can be stored under ambient conditions indefinitely without damage. [138] Wei reported stability of SAMs formed on glass in air. [173]

1.18.3 Stability of SAM under heating.

Thermal stability of the SAM has been investigated by numerous groups. The well studied octadecyl trichlorosilane SAM being shown to be stable to 350 °C [156] as has perfluorodecyl triethoxysilane [174]. It is claimed that this stability is independent of chain length. [156, 175] Using High Energy Electron Loss spectroscopy (HEELS), it was shown that this degradation of the SAM above 350 °C was due to the cleavage of the C-C bond rather than the Si-O bond, which only begins to decompose at 725 °C. Numerous groups have reported stability of octadecyl trichlorosilane SAMs in air when heated to 150 °C, in addition to the work by Aswal. [161, 162, 176, 177]

1.18.4 Stability of SAM in water and organic solvent.

Self-assembled monolayers have been shown to be stable in hot tap water and organic solvent by Aswal. [156] Both Brzoska [138] and Tillman [172, 178] agree, with Brzoska claiming silane SAMs are stable for extended periods (between 2-24 hours) in boiling water. The SAM is

also stable to washes with detergent and organic solvents. Conversely, Pomerantz [171] claims that monolayer degradation by deionised water occurs after only a few hours, although pre-annealing the silicon at 70 °C before SAM formation leads to a much slower degradation. Wei et al [173] reported deterioration of SAMs formed on glass, silica and quartz when stored in water, but witnessed stability of SAMs formed on the glass substrates when stored in air or organic oil. Brzoska believes that the deterioration observed by these groups is due to incomplete SAM formation or poor packing of the silane molecules on the substrate surface.

1.18.5 Stability of SAM in acid or base.

Self-assembled monolayers have been shown to be stable for several days in acidic conditions, although exposure to 2.5 M sulphuric acid in boiling dioxane or 48% HF solution degrades the SAM. [179] However, SAMs deteriorate rapidly in basic conditions with complete removal being achieved after just 60 minutes due to hydrolysis of the Si-O bond by 0.1 M sodium hydroxide solution. [160]

1.18.6 The effect of baking.

Several groups have exposed the SAM to a post deposition bake to increase stability by driving crosslinking between adjacent silane moieties. Pomerantz exposed a monolayer of 3-(aminopropyl)triethoxysilane on silicon to both a pre annealing and post annealing step at 70 °C. The FTIR data obtained for the post annealed sample showed no significant change compared to the non-annealed spectra. However, the pre annealed sample showed less CH₃

stretch, indicating more horizontal polymerisation of bonding to the surface by the silane.

[171] On the other hand Kessel [180] claims that it is necessary to bake the formed SAM at 120 °C for 2 hours to achieve a stable monolayer. The temperature can be decreased and the time increased to achieve the same results, as can increasing the temperature and decreasing the time. However, too much of an increase in temperature degrades the SAM.

1.19 SAM formation from trichlorosilanes and trialkoxysilanes.

Both trichlorosilanes (TCS) and trialkoxysilanes (TAS) have been readily used to modify hydroxylated surfaces, however subtle differences exist in both kinetics and thermodynamics of SAM formation by the two systems. It is commonly accepted that TCS are more reactive than their TAS counterparts. [156, 162, 180] The reason for this, according to Kessel [180], is that when a TCS is hydrolysed, a by-product of the reaction is a chloride ion, or a hydrochloric acid molecule. This acid proceeds to catalyse further hydrolysis reactions and is the reason why moisture must be rigorously excluded from TCS solutions to minimize/ exclude gelation. In addition, the hydrolysis of TCS is more exothermic than the hydrolysis of TAS, as implied by the Hammond postulate, meaning the progression from reagents to products will have a lower activation energy and the reaction will proceed more readily. This has been shown experimentally by Aswal [156] who shows that SAMs of TCS form in about an hour, and by contrast a SAM formed from either a trimethoxysilane or triethoxysilane takes around two days to form.

Despite the slow reactivity, TAS are useful as no special procedures need to be taken in regards to storage. In addition, more functionality can be added to the ω end of TAS. Extensive functionality has been discussed in the review by Onclin. [162]

1.20 Modification of alumina by silanes.

Several groups have shown that alumina can be modified in the same way as silicon and silica using organosilanes. [181-184] Sah [185] has shown by Diffuse Reflectance Infra Red Spectroscopy the presence of a peak at $1000\text{-}1130\text{ cm}^{-1}$, which indicates the presence of Si-O-Si bonds, implying the presence of polymerised silane on the alumina surface. The ability to silanise the alumina surface is again related to surface water of the alumina substrate. Prado et al [186] have presented IR data which showed that alumina retained a surface layer of water even after 2 days baking in an oven at $150\text{ }^{\circ}\text{C}$.

The stability of silanes on alumina is also similar to that of silanes on silicon as discussed previously. Szczepanski [187] showed how silanes that do not contain amine groups are stable indefinitely in organic solvents, but if left in water or phosphate buffer saline (PBS) solution the surface concentration of silanes decreases within a week. Adding amine groups to the silane leads to a much faster degradation of the modifying layer. Szczepanski also noted that the Al-O bond is more polar than the Si-O bond. Consequently this means the Al-O bond is polarised and, as a result, more susceptible to acid and base attack. Mitchon showed that silane modified alumina is stable in air for periods of months. In addition, the Van der Waals forces between chains increased by 7 kJ/mol per methylene group within the chain below chains with < 8 methylenes. For chains with > 8 methylenes, an additional 7 kJ/mol is added per CH_2 , for example for $(\text{CH}_2)_{17}\text{CH}_3$ has a VDW stability of around 125 kJ/mol . [188]

Jani et al [189] carried out investigations on anodic aluminium oxide (AAO) membranes. They found that modification of the membranes with 3-(aminopropyl)triethoxysilane led to water contact angles of 55° . They also noted that pentafluorophenyl dimethylchlorosilane can modify both the top surface of the AAO and within the pores for porous membranes with 30 nm pore diameters and 80 nm interpore

distances. Other groups have investigated blocking the pores with silanes. However, these pores have diameters in the region of 5 nm. [136, 185] Velleman carried out similar work modifying AAO with perfluorodecyl dimethylchlorosilane. They found contact angles of 109° and 12° for the fluorinated and unmodified surfaces respectively, and that the silane had penetrated inside the porous structure.

Hyun et al [190] carried out Differential Scanning Calorimetry (DSC) work to test the stability of silane layers on alumina. They observed DSC peaks at 380 °C for the desorption of the silane molecules. As discussed earlier, other groups have reported temperatures of 350 °C. Using Energy Dispersive X-ray Spectroscopy (EDS) Hyun reported the post silanised alumina to have the following elemental properties: Al = 88.764 %; Si = 10.060 % and Ca 1.084 %.

1.21 References

- [1] W. B. Zimmerman, B. N. Hewakandamby, V. Tesař, H. C. H. Bandulasena, and O. A. Omotowa, "On the design and simulation of an airlift loop bioreactor with microbubble generation by fluidic oscillation," *Food and Bioprocess Processing*, vol. 87, pp. 215-227, 2009.
- [2] P. M. Schenk, S. R. Thomas-Hall, E. Stephens, U. C. Marx, J. H. Mussgnug, C. Posten, O. Kruse, and B. Hankamer, "Second generation biofuels: high-efficiency microalgae for biodiesel production," *Bioenergy research*, vol. 1, pp. 20-43, 2008.
- [3] J. R. Benemann and W. J. Oswald, "Systems and economic analysis of microalgae ponds for conversion of CO₂ to biomass. Final report," California Univ., Berkeley, CA (United States). Dept. of Civil Engineering 1996.
- [4] A. A. Shastri and J. A. Morgan, "A transient isotopic labeling methodology for ¹³C metabolic flux analysis of photoautotrophic microorganisms," *Phytochemistry*, vol. 68, pp. 2302-2312, 2007.
- [5] D. Das and T. N. Veziroğlu, "Hydrogen production by biological processes: a survey of literature," *International Journal of Hydrogen Energy*, vol. 26, pp. 13-28, 2001.
- [6] H. Gaffron and J. Rubin, "Fermentative and photochemical production of hydrogen in algae," *The Journal of general physiology*, vol. 26, pp. 219-240, 1942.
- [7] B. Hankamer, F. Lehr, J. Rupprecht, J. H. Mussgnug, C. Posten, and O. Kruse, "Photosynthetic biomass and H₂ production by green algae: from bioengineering to bioreactor scale-up," *Physiologia Plantarum*, vol. 131, pp. 10-21, 2007.
- [8] A. Melis, L. Zhang, M. Forestier, M. L. Ghirardi, and M. Seibert, "Sustained Photobiological Hydrogen Gas Production upon Reversible Inactivation of Oxygen Evolution in the Green Alga *Chlamydomonas reinhardtii*," *Plant physiology*, vol. 122, pp. 127-136, 2000.
- [9] S. T. Jones, *Gas-liquid mass transfer in an external airlift loop reactor for syngas fermentation*: ProQuest, 2007.

- [10] W. B. Zimmerman, M. Zandi, H. C. Hemaka Bandulasena, V. Tesař, D. James Gilmour, and K. Ying, "Design of an airlift loop bioreactor and pilot scales studies with fluidic oscillator induced microbubbles for growth of a microalgae *Dunaliella salina*," *Applied Energy*, vol. 88, pp. 3357-3369, 2011.
- [11] V. Tesař, C.-H. Hung, and W. B. Zimmerman, "No-moving-part hybrid-synthetic jet actuator," *Sensors and Actuators A: Physical*, vol. 125, pp. 159-169, 2006.
- [12] W. B. Zimmerman, V. Tesař, and H. C. H. Bandulasena, "Towards energy efficient nanobubble generation with fluidic oscillation," *Current Opinion in Colloid & Interface Science*, vol. 16, pp. 350-356, 2011.
- [13] V. Tesař, "Configurations of fluidic actuators for generating hybrid-synthetic jets," *Sensors and Actuators A: Physical*, vol. 138, pp. 394-403, 2007.
- [14] V. Tesař, "Microbubble generation by fluidics. Part i: Development of the oscillator," in *Proc. of Colloquium Fluid Dynamics*, 2012.
- [15] J. Hanotu, "Algal growth enhancement mediated by CO₂ enriched microbubbles," *MSc in environmental and energy engineering dissertation, University of Sheffield*, 2009.
- [16] K. Ying, D. J. Gilmour, Y. Shi, and W. B. Zimmerman, "Growth Enhancement of *Dunaliella salina* by Microbubble Induced Airlift Loop Bioreactor (ALB)—The Relation between Mass Transfer and Growth Rate," 2013.
- [17] J. Hanotu, H. C. H. Bandulasena, T. Y. Chiu, and W. B. Zimmerman, "Oil emulsion separation with fluidic oscillator generated microbubbles," *International Journal of Multiphase Flow*, vol. 56, pp. 119-125, 2013.
- [18] J. Hanotu, E. Karunakaran, H. Bandulasena, C. Biggs, and W. B. Zimmerman, "Harvesting and dewatering yeast by microflotation," *Biochemical Engineering Journal*, vol. 82, pp. 174-182, 2014.
- [19] J. Hanotu, H. Bandulasena, and W. B. Zimmerman, "Microflotation performance for algal separation," *Biotechnology and bioengineering*, vol. 109, pp. 1663-1673, 2012.
- [20] C. Gudin and C. Thepenier, "Bioconversion of solar energy into organic chemicals by microalgae," *Advances in biotechnological processes (USA)*, 1986.
- [21] E. M. Grima, E.-H. Belarbi, F. A. Fernández, A. R. Medina, and Y. Chisti, "Recovery of microalgal biomass and metabolites: process options and economics," *Biotechnology advances*, vol. 20, pp. 491-515, 2003.
- [22] S. Burns, S. Yiacomou, and C. Tsouris, "Microbubble generation for environmental and industrial separations," *Separation and purification technology*, vol. 11, pp. 221-232, 1997.
- [23] R. Gramiak and P. M. Shah, "Echocardiography of the aortic root," *Investigative radiology*, vol. 3, pp. 356-366, 1968.
- [24] K. Ferrara, R. Pollard, and M. Borden, "Ultrasound microbubble contrast agents: fundamentals and application to gene and drug delivery," *Annu. Rev. Biomed. Eng.*, vol. 9, pp. 415-447, 2007.
- [25] G. B. Deane and H. Czerski, "A mechanism stimulating sound production from air bubbles released from a nozzle," *J Acoust Soc Am*, vol. 123, pp. EL126-32, Jun 2008.
- [26] H. J. Vos, B. Dollet, M. Versluis, and N. De Jong, "Nonspherical shape oscillations of coated microbubbles in contact with a wall," *Ultrasound Med Biol*, vol. 37, pp. 935-948, 2011.
- [27] B. Dollet, S. M. Van Der Meer, V. Garbin, N. De Jong, D. Lohse, and M. Versluis, "Nonspherical oscillations of ultrasound contrast agent microbubbles," *Ultrasound Med Biol*, vol. 34, pp. 1465-1473, 2008.
- [28] M. Versluis, D. E. Goertz, P. Palancon, I. L. Heitman, S. M. van der Meer, B. Dollet, N. De Jong, and D. Lohse, "Microbubble shape oscillations excited through ultrasonic parametric driving," *Physical Review E*, vol. 82, p. 026321, 2010.

- [29] A. L. Klibanov, "Targeted delivery of gas-filled microspheres, contrast agents for ultrasound imaging," *Advanced drug delivery reviews*, vol. 37, pp. 139-157, 1999.
- [30] G. M. Lanza, K. D. Wallace, S. E. Fischer, D. H. Christy, M. J. Scott, R. L. Trousil, W. P. Cacheris, J. G. Miller, P. J. Gaffney, and S. A. Wickline, "High-frequency ultrasonic detection of thrombi with a targeted contrast system," *Ultrasound Med Biol*, vol. 23, pp. 863-870, 1997.
- [31] F. Scargiali, A. Busciglio, F. Grisafi, and A. Brucato, "Bubble Formation at Various Inclined Nozzles," *Chemical Engineering & Technology*, vol. 37, pp. 1507-1514, 2014.
- [32] H. Yasuda and J. Lin, "Small bubbles oxygenation membrane," *Journal of Applied Polymer Science*, vol. 90, pp. 387-398, 2003.
- [33] A. K. Das and P. K. Das, "Bubble evolution and necking at a submerged orifice for the complete range of orifice tilt," *AIChE Journal*, vol. 59, pp. 630-642, 2013.
- [34] L. Changjun, B. LIANG, T. Shengwei, and M. Enze, "Effects of Orifice Orientation and Gas-Liquid Flow Pattern on Initial Bubble Size," *Chinese Journal of Chemical Engineering*, vol. 21, pp. 1206-1215, 2013.
- [35] M. Kukizaki and Y. Baba, "Effect of surfactant type on microbubble formation behavior using Shirasu porous glass (SPG) membranes," *Colloids and Surfaces A: Physicochemical and Engineering Aspects*, vol. 326, pp. 129-137, 2008.
- [36] J. Xie, X. Zhu, Q. Liao, H. Wang, and Y.-D. Ding, "Dynamics of bubble formation and detachment from an immersed micro-orifice on a plate," *International Journal of Heat and Mass Transfer*, vol. 55, pp. 3205-3213, 2012.
- [37] R. J. Benzing and J. E. Myers, "Low frequency bubble formation at horizontal circular orifices," *Industrial & Engineering Chemistry*, vol. 47, pp. 2087-2090, 1955.
- [38] L. Davidson and E. H. Amick, "Formation of gas bubbles at horizontal orifices," *AIChE Journal*, vol. 2, pp. 337-342, 1956.
- [39] M. Jamialahmadi, M. Zehtaban, H. Müller-Steinhagen, A. Sarrafi, and J. Smith, "Study of bubble formation under constant flow conditions," *Chemical Engineering Research and Design*, vol. 79, pp. 523-532, 2001.
- [40] R. Winterson, "A simple method of predicting bubble size in bubble columns," *Chemical Engineering and Processing: Process Intensification*, vol. 33, pp. 1-5, 1994.
- [41] K. Akita and F. Yoshida, "Bubble size, interfacial area, and liquid-phase mass transfer coefficient in bubble columns," *Industrial & Engineering Chemistry Process Design and Development*, vol. 13, pp. 84-91, 1974.
- [42] I. Leibson, E. G. Holcomb, A. G. Cacosso, and J. J. Jacmic, "Rate of flow and mechanics of bubble formation from single submerged orifices. II. Mechanics of bubble formation," *AIChE Journal*, vol. 2, pp. 300-306, 1956.
- [43] W. B. Hayes, B. W. Hardy, and C. D. Holland, "Formation of gas bubbles at submerged orifices," *AIChE Journal*, vol. 5, pp. 319-324, 1959.
- [44] L. Zhang and M. Shoji, "Aperiodic bubble formation from a submerged orifice," *Chemical Engineering Science*, vol. 56, pp. 5371-5381, 2001.
- [45] S. Vafaei and D. Wen, "Bubble formation on a submerged micronozzle," *Journal of Colloid and Interface Science*, vol. 343, pp. 291-297, 2010.
- [46] N. Kyriakides, E. Kastrinakis, S. Nychas, and A. Goulas, "Bubbling from nozzles submerged in water: transitions between bubbling regimes," *The Canadian Journal of Chemical Engineering*, vol. 75, pp. 684-691, 1997.
- [47] X. Zhu, Q. Liao, H. Wang, L. Bao, J. Xie, and C. Lin, "Experimental Study of bubble growth and departure at the tip of capillary tubes with various wettabilities in a stagnant liquid," *Journal of superconductivity and novel magnetism*, vol. 23, pp. 1141-1145, 2010.
- [48] S. Gnyloskurenko, A. Byakova, O. Raychenko, and T. Nakamura, "Influence of wetting conditions on bubble formation at orifice in an inviscid liquid. Transformation of

- bubble shape and size," *Colloids and Surfaces A: Physicochemical and Engineering Aspects*, vol. 218, pp. 73-87, 2003.
- [49] J.-L. Liow and N. Gray, "A model of bubble growth in wetting and non-wetting liquids," *Chemical Engineering Science*, vol. 43, pp. 3129-3139, 1988.
- [50] D. Gerlach, G. Biswas, F. Durst, and V. Kolobaric, "Quasi-static bubble formation on submerged orifices," *International Journal of Heat and Mass Transfer*, vol. 48, pp. 425-438, 2005.
- [51] A. Byakova, S. Gnyloskurenko, T. Nakamura, and O. Raychenko, "Influence of wetting conditions on bubble formation at orifice in an inviscid liquid: Mechanism of bubble evolution," *Colloids and Surfaces A: Physicochemical and Engineering Aspects*, vol. 229, pp. 19-32, 2003.
- [52] G. Corchero, A. Medina, and F. Higuera, "Effect of wetting conditions and flow rate on bubble formation at orifices submerged in water," *Colloids and Surfaces A: Physicochemical and Engineering Aspects*, vol. 290, pp. 41-49, 2006.
- [53] J. Davidson and B. Schöler, "Bubble formation at an orifice in a viscous liquid," *Chemical Engineering Research and Design*, vol. 75, pp. S105-S115, 1997.
- [54] H. N. Oguz and A. Prosperetti, "Dynamics of bubble growth and detachment from a needle," *Journal of Fluid Mechanics*, vol. 257, pp. 111-145, 1993.
- [55] M. Kukizaki and T. Wada, "Effect of the membrane wettability on the size and size distribution of microbubbles formed from Shirasu-porous-glass (SPG) membranes," *Colloids and Surfaces A: Physicochemical and Engineering Aspects*, vol. 317, pp. 146-154, 2008.
- [56] W. A. Ducker, "Contact angle and stability of interfacial nanobubbles," *Langmuir*, vol. 25, pp. 8907-8910, 2009.
- [57] J. Yang, J. Duan, D. Fornasiero, and J. Ralston, "Very small bubble formation at the solid-water interface," *The Journal of Physical Chemistry B*, vol. 107, pp. 6139-6147, 2003.
- [58] S. Ramakrishnan, R. Kumar, and N. Kuloor, "Studies in bubble formation—I bubble formation under constant flow conditions," *Chemical Engineering Science*, vol. 24, pp. 731-747, 1969.
- [59] Q. Xu, M. Nakajima, S. Ichikawa, N. Nakamura, P. Roy, H. Okadome, and T. Shiina, "Effects of surfactant and electrolyte concentrations on bubble formation and stabilization," *Journal of Colloid and Interface Science*, vol. 332, pp. 208-214, 2009.
- [60] M. Takahashi, "ζ potential of microbubbles in aqueous solutions: electrical properties of the gas-water interface," *The Journal of Physical Chemistry B*, vol. 109, pp. 21858-21864, 2005.
- [61] C. Yang, T. Dabros, D. Li, J. Czarnecki, and J. H. Masliyah, "Measurement of the zeta potential of gas bubbles in aqueous solutions by microelectrophoresis method," *Journal of Colloid and Interface Science*, vol. 243, pp. 128-135, 2001.
- [62] J.-Y. Kim, M.-G. Song, and J.-D. Kim, "Zeta potential of nanobubbles generated by ultrasonication in aqueous alkyl polyglycoside solutions," *Journal of Colloid and Interface Science*, vol. 223, pp. 285-291, 2000.
- [63] R.-H. Yoon and J. L. Jordan, "Zeta-potential measurements on microbubbles generated using various surfactants," *Journal of Colloid and Interface Science*, vol. 113, pp. 430-438, 1986.
- [64] S.-H. Cho, J.-Y. Kim, J.-H. Chun, and J.-D. Kim, "Ultrasonic formation of nanobubbles and their zeta-potentials in aqueous electrolyte and surfactant solutions," *Colloids and Surfaces A: Physicochemical and Engineering Aspects*, vol. 269, pp. 28-34, 2005.
- [65] Y. H. Tsang, Y.-H. Koh, and D. L. Koch, "Bubble-size dependence of the critical electrolyte concentration for inhibition of coalescence," *Journal of Colloid and Interface Science*, vol. 275, pp. 290-297, 2004.

- [66] O. Pamperin and H.-J. Rath, "Influence of buoyancy on bubble formation at submerged orifices," *Chemical Engineering Science*, vol. 50, pp. 3009-3024, 1995.
- [67] A. A. Kulkarni and J. B. Joshi, "Bubble formation and bubble rise velocity in gas-liquid systems: A review," *Industrial & Engineering Chemistry Research*, vol. 44, pp. 5873-5931, 2005.
- [68] D. McCann and R. Prince, "Regimes of bubbling at a submerged orifice," *Chemical Engineering Science*, vol. 26, pp. 1505-1512, 1971.
- [69] S. Vafaei, P. Angeli, and D. Wen, "Bubble growth rate from stainless steel substrate and needle nozzles," *Colloids and Surfaces A: Physicochemical and Engineering Aspects*, vol. 384, pp. 240-247, 2011.
- [70] J. Lin, S. Banerji, and H. Yasuda, "Role of interfacial tension in the formation and the detachment of air bubbles. 1. A single hole on a horizontal plane immersed in water," *Langmuir*, vol. 10, pp. 936-942, 1994.
- [71] R. R. Hughes, A. E. Handlos, H. I. Evans, and R. L. Maycork,, *Chemical Engineering Progress*, vol. 51, p. 557, 1955.
- [72] J. J. Kwan and M. A. Borden, "Microbubble dissolution in a multigas environment," *Langmuir*, vol. 26, pp. 6542-6548, 2010.
- [73] H. Mulvana, E. Stride, M. X. Tang, J. V. Hajnal, and R. J. Eckersley, "The influence of gas saturation on microbubble stability," *Ultrasound Med Biol*, vol. 38, pp. 1097-1100, Jun 2012.
- [74] V. Tesař, "Microbubble generation by Fluidics. Part II: Bubble formation mechanicsm," in *Proc. of Colloquium Fluid Dynamics, Prague*, 2012.
- [75] W. B. Zimmerman, V. Tesar, S. Butler, and H. C. Bandulasena, "Microbubble generation," *Recent patents on engineering*, vol. 2, pp. 1-8, 2008.
- [76] V. Tesař, *Pressure-driven microfluidics*: Artech House Boston/London, 2007.
- [77] T. Young, "An Essay on the Cohesion of Fluids," *Philosophical Transactions of the Royal Society of London*, vol. 95, pp. 65-87, 1805.
- [78] R. J. Good, "Contact angle, wetting, and adhesion: a critical review," *Journal of adhesion science and technology*, vol. 6, pp. 1269-1302, 1992.
- [79] Y. Yuan and T. R. Lee, "Contact angle and wetting properties," in *Surface science techniques*, ed: Springer, 2013, pp. 3-34.
- [80] T. Baum, J. Satherley, and D. J. Schiffrin, "Contact angle, gas bubble detachment, and surface roughness in the anisotropic dissolution of Si (100) in aqueous KOH," *Langmuir*, vol. 14, pp. 2925-2928, 1998.
- [81] R. Tadmor, "Line energy and the relation between advancing, receding, and young contact angles," *Langmuir*, vol. 20, pp. 7659-7664, 2004.
- [82] A. Marmur, "Contact angle equilibrium: the intrinsic contact angle," *Journal of adhesion science and technology*, vol. 6, pp. 689-701, 1992.
- [83] W. Possart and H. Kamusewitz, "Wetting and scanning force microscopy on rough polymer surfaces: Wenzel's roughness factor and the thermodynamic contact angle," *Applied Physics A: Materials Science & Processing*, vol. 76, pp. 899-902, 2003.
- [84] R. N. Wenzel, "Resistance of solid surfaces to wetting by water," *Industrial & Engineering Chemistry*, vol. 28, pp. 988-994, 1936.
- [85] A. Terriza, R. Alvarez, F. Yubero, A. Borrás, and A. R. González-Elipe, "Comments on "An Essay on Contact Angle Measurements": Determination of Surface Roughness and Modeling of the Wetting Behavior," *Plasma Processes and Polymers*, vol. 8, pp. 998-1002, 2011.
- [86] R. N. Wenzel, "Surface Roughness and Contact Angle," *The Journal of Physical Chemistry*, vol. 53, pp. 1466-1467, 1949.
- [87] A. Cassie and S. Baxter, "Wettability of porous surfaces," *Transactions of the Faraday Society*, vol. 40, pp. 546-551, 1944.

- [88] A. Marmur, "The lotus effect: superhydrophobicity and metastability," *Langmuir*, vol. 20, pp. 3517-3519, 2004.
- [89] A. Cassie, "Contact angles," *Discussions of the Faraday Society*, vol. 3, pp. 11-16, 1948.
- [90] B. Bhushan and M. Nosonovsky, "The rose petal effect and the modes of superhydrophobicity," *Philosophical Transactions of the Royal Society of London A: Mathematical, Physical and Engineering Sciences*, vol. 368, pp. 4713-4728, 2010.
- [91] L. Feng, Y. Zhang, J. Xi, Y. Zhu, N. Wang, F. Xia, and L. Jiang, "Petal effect: a superhydrophobic state with high adhesive force," *Langmuir*, vol. 24, pp. 4114-4119, 2008.
- [92] Y. T. Cheng, D. Rodak, C. Wong, and C. Hayden, "Effects of micro-and nano-structures on the self-cleaning behaviour of lotus leaves," *Nanotechnology*, vol. 17, p. 1359, 2006.
- [93] D. K. Schwartz, "Mechanisms and kinetics of self-assembled monolayer formation," *Annu Rev Phys Chem*, vol. 52, pp. 107-37, 2001/10/01 2001.
- [94] J. C. Love, L. A. Estroff, J. K. Kriebel, R. G. Nuzzo, and G. M. Whitesides, "Self-Assembled Monolayers of Thiolates on Metals as a Form of Nanotechnology," *Chemical Reviews*, vol. 105, pp. 1103-1170, 2005/04/01 2005.
- [95] C. D. Bain, E. B. Troughton, Y. T. Tao, J. Evall, G. M. Whitesides, and R. G. Nuzzo, "Formation of monolayer films by the spontaneous assembly of organic thiols from solution onto gold," *Journal of the American Chemical Society*, vol. 111, pp. 321-335, 1989.
- [96] W. C. Bigelow, D. L. Pickett, and W. A. Zisman, "Oleophobic monolayers: I. Films adsorbed from solution in non-polar liquids," *Journal of Colloid Science*, vol. 1, pp. 513-538, 1946.
- [97] C. D. Bain and G. M. Whitesides, "Correlations between wettability and structure in monolayers of alkanethiols adsorbed on gold," *Journal of the American Chemical Society*, vol. 110, pp. 3665-3666, 1988/05/01 1988.
- [98] C. D. Bain and G. M. Whitesides, "Depth sensitivity of wetting: monolayers of .omega.-mercapto ethers on gold," *Journal of the American Chemical Society*, vol. 110, pp. 5897-5898, 1988/08/01 1988.
- [99] C. D. Bain, H. A. Biebuyck, and G. M. Whitesides, "Comparison of self-assembled monolayers on gold: coadsorption of thiols and disulfides," *Langmuir*, vol. 5, pp. 723-727, 1989/05/01 1989.
- [100] C. D. Bain and G. M. Whitesides, "Formation of monolayers by the coadsorption of thiols on gold: variation in the length of the alkyl chain," *Journal of the American Chemical Society*, vol. 111, pp. 7164-7175, 1989.
- [101] C. D. Bain and G. M. Whitesides, "A study by contact angle of the acid-base behavior of monolayers containing .omega.-mercaptocarboxylic acids adsorbed on gold: an example of reactive spreading," *Langmuir*, vol. 5, pp. 1370-1378, 1989.
- [102] C. D. Bain, J. Evall, and G. M. Whitesides, "Formation of monolayers by the coadsorption of thiols on gold: variation in the head group, tail group, and solvent," *Journal of the American Chemical Society*, vol. 111, pp. 7155-7164, 1989.
- [103] M. D. Porter, T. B. Bright, D. L. Allara, and C. E. Chidsey, "Spontaneously organized molecular assemblies. 4. Structural characterization of n-alkyl thiol monolayers on gold by optical ellipsometry, infrared spectroscopy, and electrochemistry," *Journal of the American Chemical Society*, vol. 109, pp. 3559-3568, 1987.
- [104] R. G. Nuzzo, B. R. Zegarski, and L. H. Dubois, "Fundamental studies of the chemisorption of organosulfur compounds on gold (111). Implications for molecular self-assembly on gold surfaces," *Journal of the American Chemical Society*, vol. 109, pp. 733-740, 1987.

- [105] R. F. Debono, G. D. Loucks, D. D. Manna, and U. J. Krull, "Self-assembly of short and long-chain n-alkyl thiols onto gold surfaces: A real-time study using surface plasmon resonance techniques," *Canadian Journal of Chemistry*, vol. 74, pp. 677-688, 1996.
- [106] O. Dannenberger, J. J. Wolff, and M. Buck, "Solvent dependence of the self-assembly process of an endgroup-modified alkanethiol," *Langmuir*, vol. 14, pp. 4679-4682, Aug 18 1998.
- [107] J. Stettner, "Self assembled monolayer formation of alkanethiols on gold: Growth from solution versus physical vapor deposition," Doctoral thesis, Graz University of Technology, 2010.
- [108] K. A. Peterlinz and R. Georgiadis, "In situ kinetics of self-assembly by surface plasmon resonance spectroscopy," *Langmuir*, vol. 12, pp. 4731-4740, 1996.
- [109] G. Poirier and E. Pylant, "The self-assembly mechanism of alkanethiols on Au (111)," *Science*, vol. 272, pp. 1145-1148, 1996.
- [110] N. Camillone, T. Y. B. Leung, P. Schwartz, P. Eisenberger, and G. Scoles, "Chain Length Dependence of the Striped Phases of Alkanethiol Monolayers Self-Assembled on Au(111): An Atomic Beam Diffraction Study," *Langmuir*, vol. 12, pp. 2737-2746, 1996/01/01 1996.
- [111] F. Balzer, R. Gerlach, G. Polanski, and H. G. Rubahn, "Chain length dependence of the structure of alkane thiol films on Au(111)," *Chemical Physics Letters*, vol. 274, pp. 145-151, 1997.
- [112] F. Schreiber, "Structure and growth of self-assembling monolayers," *Progress in Surface Science*, vol. 65, pp. 151-257, 2000.
- [113] F. Schreiber, A. Eberhardt, T. Leung, P. Schwartz, S. Wetterer, D. Lavrich, L. Berman, P. Fenter, P. Eisenberger, and G. Scoles, "Adsorption mechanisms, structures, and growth regimes of an archetypal self-assembling system: Decanethiol on Au (111)," *Physical Review B*, vol. 57, p. 12476, 1998.
- [114] D. L. Allara and R. G. Nuzzo, "Spontaneously organized molecular assemblies. 1. Formation, dynamics, and physical properties of n-alkanoic acids adsorbed from solution on an oxidized aluminum surface," *Langmuir*, vol. 1, pp. 45-52, 1985.
- [115] P. E. Laibinis, G. M. Whitesides, D. L. Allara, Y. T. Tao, A. N. Parikh, and R. G. Nuzzo, "Comparison of the structures and wetting properties of self-assembled monolayers of n-alkanethiols on the coinage metal surfaces, copper, silver, and gold," *Journal of the American Chemical Society*, vol. 113, pp. 7152-7167, 1991/09/01 1991.
- [116] D. Karpovich and G. Blanchard, "Direct measurement of the adsorption kinetics of alkanethiolate self-assembled monolayers on a microcrystalline gold surface," *Langmuir*, vol. 10, pp. 3315-3322, 1994.
- [117] R. G. Nuzzo, E. M. Korenic, and L. H. Dubois, "Studies of the temperature-dependent phase behavior of long chain n-alkyl thiol monolayers on gold," *The Journal of Chemical Physics*, vol. 93, pp. 767-773, 1990.
- [118] C. E. Chidsey, G. Y. Liu, P. Rowntree, and G. Scoles, "Molecular order at the surface of an organic monolayer studied by low energy helium diffraction," *The Journal of Chemical Physics*, vol. 91, pp. 4421-4423, 1989.
- [119] C. A. Alves, E. L. Smith, and M. D. Porter, "Atomic scale imaging of alkanethiolate monolayers at gold surfaces with atomic force microscopy," *Journal of the American Chemical Society*, vol. 114, pp. 1222-1227, 1992.
- [120] L. H. Dubois and R. G. Nuzzo, "Synthesis, structure, and properties of model organic surfaces," *Annual Review of Physical Chemistry*, vol. 43, pp. 437-463, 1992.
- [121] D. M. Collard and M. A. Fox, "Use of electroactive thiols to study the formation and exchange of alkanethiol monolayers on gold," *Langmuir*, vol. 7, pp. 1192-1197, 1991.

- [122] S. Xu, S. J. Cruchon-Dupeyrat, J. C. Garno, G.-Y. Liu, G. Kane Jennings, T.-H. Yong, and P. E. Laibinis, "In situ studies of thiol self-assembly on gold from solution using atomic force microscopy," *Journal of Chemical Physics*, vol. 108, pp. 5002-5012, 1998.
- [123] R. G. Nuzzo, F. A. Fusco, and D. L. Allara, "Spontaneously organized molecular assemblies. 3. Preparation and properties of solution adsorbed monolayers of organic disulfides on gold surfaces," *Journal of the American Chemical Society*, vol. 109, pp. 2358-2368, 1987.
- [124] T. W. Schneider and D. A. Buttry, "Electrochemical quartz crystal microbalance studies of adsorption and desorption of self-assembled monolayers of alkyl thiols on gold," *Journal of the American Chemical Society*, vol. 115, pp. 12391-12397, 1993.
- [125] O. Dannenberger, M. Buck, and M. Grunze, "Self-assembly of n-alkanethiols: A kinetic study by second harmonic generation," *The Journal of Physical Chemistry B*, vol. 103, pp. 2202-2213, 1999.
- [126] L. H. Dubois, B. R. Zegarski, and R. G. Nuzzo, "Temperature induced reconstruction of model organic surfaces," *Journal of Electron Spectroscopy and Related Phenomena*, vol. 54, pp. 1143-1152, 1990.
- [127] D. Fischer, A. Curioni, and W. Andreoni, "Decanethiols on Gold: The Structure of Self-Assembled Monolayers Unraveled with Computer Simulations," *Langmuir*, vol. 19, pp. 3567-3571, 2003/04/01 2003.
- [128] D. J. Lavrich, S. M. Wetterer, S. L. Bernasek, and G. Scoles, "Physisorption and Chemisorption of Alkanethiols and Alkyl Sulfides on Au(111)," *The Journal of Physical Chemistry B*, vol. 102, pp. 3456-3465, 1998/04/01 1998.
- [129] G. Yang, N. A. Amro, Z. B. Starkewolfe, and G.-y. Liu, "Molecular-Level Approach To Inhibit Degradations of Alkanethiol Self-Assembled Monolayers in Aqueous Media," *Langmuir*, vol. 20, pp. 3995-4003, 2004/05/01 2004.
- [130] J. B. Schlenoff, M. Li, and H. Ly, "Stability and Self-Exchange in Alkanethiol Monolayers," *Journal of the American Chemical Society*, vol. 117, pp. 12528-12536, 1995/12/01 1995.
- [131] L. H. Dubois, B. R. Zegarski, and R. G. Nuzzo, "Molecular ordering of organosulfur compounds on Au (111) and Au (100): Adsorption from solution and in ultrahigh vacuum," *The Journal of Chemical Physics*, vol. 98, pp. 678-688, 1993.
- [132] D. E. Weisshaar, B. D. Lamp, and M. D. Porter, "Thermodynamically controlled electrochemical formation of thiolate monolayers at gold: characterization and comparison to self-assembled analogs," *Journal of the American Chemical Society*, vol. 114, pp. 5860-5862, 1992.
- [133] C. A. Widrig, C. Chung, and M. D. Porter, "The electrochemical desorption of n-alkanethiol monolayers from polycrystalline Au and Ag electrodes," *Journal of electroanalytical chemistry and interfacial electrochemistry*, vol. 310, pp. 335-359, 1991.
- [134] R. G. Nuzzo, L. H. Dubois, and D. L. Allara, "Fundamental studies of microscopic wetting on organic surfaces. 1. Formation and structural characterization of a self-consistent series of polyfunctional organic monolayers," *Journal of the American Chemical Society*, vol. 112, pp. 558-569, 1990.
- [135] M. A. Bryant and J. E. Pemberton, "Surface Raman scattering of self-assembled monolayers formed from 1-alkanethiols: behavior of films at gold and comparison to films at silver," *Journal of the American Chemical Society*, vol. 113, pp. 8284-8293, 1991.
- [136] C. Leger, H. D. L. Lira, and R. Paterson, "Preparation and properties of surface modified ceramic membranes. Part III. Gas permeation of 5 nm alumina membranes modified by trichloro-octadecylsilane," *Journal of Membrane Science*, vol. 120, pp. 187-195, 1996.

- [137] D. L. Angst and G. W. Simmons, "Moisture absorption characteristics of organosiloxane self-assembled monolayers," *Langmuir*, vol. 7, pp. 2236-2242, 1991.
- [138] J. Brzoska, I. B. Azouz, and F. Rondelez, "Silanization of solid substrates: a step toward reproducibility," *Langmuir*, vol. 10, pp. 4367-4373, 1994.
- [139] C. Tripp and M. Hair, "An infrared study of the reaction of octadecyltrichlorosilane with silica," *Langmuir*, vol. 8, pp. 1120-1126, 1992.
- [140] K. Bierbaum, M. Grunze, A. Baski, L. Chi, W. Schrepp, and H. Fuchs, "Growth of self-assembled n-alkyltrichlorosilane films on Si (100) investigated by atomic force microscopy," *Langmuir*, vol. 11, pp. 2143-2150, 1995.
- [141] K. Bierbaum, M. Kinzler, C. Wöll, M. Grunze, G. Hähner, S. Heid, and F. Effenberger, "A near edge X-ray absorption fine structure spectroscopy and X-ray photoelectron spectroscopy study of the film properties of self-assembled monolayers of organosilanes on oxidized Si (100)," *Langmuir*, vol. 11, pp. 512-518, 1995.
- [142] M.-H. Jung and H.-S. Choi, "Characterization of octadecyltrichlorosilane self-assembled monolayers on silicon (100) surface," *Korean Journal of Chemical Engineering*, vol. 26, pp. 1778-1784, 2009.
- [143] J. Dong, A. Wang, K. Y. S. Ng, and G. Mao, "Self-assembly of octadecyltrichlorosilane monolayers on silicon-based substrates by chemical vapor deposition," *Thin Solid Films*, vol. 515, pp. 2116-2122, Dec 5 2006.
- [144] P. Thissen, O. Seitz, and Y. J. Chabal, "Wet chemical surface functionalization of oxide-free silicon," *Progress in Surface Science*, vol. 87, pp. 272-290, 2012.
- [145] J. Sagiv, "Organized monolayers by adsorption. 1. Formation and structure of oleophobic mixed monolayers on solid surfaces," *Journal of the American Chemical Society*, vol. 102, pp. 92-98, 1980.
- [146] D. L. Allara, A. N. Parikh, and F. Rondelez, "Evidence for a unique chain organization in long chain silane monolayers deposited on two widely different solid substrates," *Langmuir*, vol. 11, pp. 2357-2360, 1995.
- [147] C. Tripp and M. Hair, "Direct observation of the surface bonds between self-assembled monolayers of octadecyltrichlorosilane and silica surfaces: a low-frequency IR study at the solid/liquid interface," *Langmuir*, vol. 11, pp. 1215-1219, 1995.
- [148] P. Silberzan, L. Leger, D. Ausserre, and J. Benattar, "Silanation of silica surfaces. A new method of constructing pure or mixed monolayers," *Langmuir*, vol. 7, pp. 1647-1651, 1991.
- [149] J. Le Grange, J. Markham, and C. Kurkjian, "Effects of surface hydration on the deposition of silane monolayers on silica," *Langmuir*, vol. 9, pp. 1749-1753, 1993.
- [150] H. Finklea, L. Robinson, A. Blackburn, B. Richter, D. Allara, and T. Bright, "Formation of an organized monolayer by solution adsorption of octadecyltrichlorosilane on gold: electrochemical properties and structural characterization," *Langmuir*, vol. 2, pp. 239-244, 1986.
- [151] T. Leitner, G. Friedbacher, T. Vallant, H. Brunner, U. Mayer, and H. Hoffmann, "Investigations of the growth of self-assembled octadecylsiloxane monolayers with atomic force microscopy," *Microchimica Acta*, vol. 133, pp. 331-336, 2000.
- [152] M. Hancer, "The effect of humidity on the stability of octadecyltrichlorosilane for the self-assembled monolayer coating applications," *Progress in Organic Coatings*, vol. 63, pp. 395-398, 2008.
- [153] A. Glaser, J. Foisner, H. Hoffmann, and G. Friedbacher, "Investigation of the Role of the Interplay between Water and Temperature on the Growth of Alkylsiloxane Submonolayers on Silicon," *Langmuir*, vol. 20, pp. 5599-5604, 2004.
- [154] B. C. Bunker, R. W. CarPick, R. A. Assink, M. L. Thomas, M. G. Hankins, J. A. Voigt, D. Sipola, M. P. de Boer, and G. L. Gulley, "The impact of solution agglomeration on the deposition of self-assembled monolayers," *Langmuir*, vol. 16, pp. 7742-7751, 2000.

- [155] M. E. McGovern, K. M. Kallury, and M. Thompson, "Role of solvent on the silanization of glass with octadecyltrichlorosilane," *Langmuir*, vol. 10, pp. 3607-3614, 1994.
- [156] D. Aswal, S. Lenfant, D. Guerin, J. Yakhmi, and D. Vuillaume, "Self assembled monolayers on silicon for molecular electronics," *Analytica chimica acta*, vol. 568, pp. 84-108, 2006.
- [157] R. M. Pasternack, S. Rivillon Amy, and Y. J. Chabal, "Attachment of 3-(aminopropyl) triethoxysilane on silicon oxide surfaces: dependence on solution temperature," *Langmuir*, vol. 24, pp. 12963-12971, 2008.
- [158] C. O'Connor, "Kinetics of interaction of 3-aminopropyltriethoxysilane on a silica gel surface using elemental analysis and diffuse reflectance infrared Fourier transform spectra," *Journal of the Chemical Society, Faraday Transactions*, vol. 93, pp. 1971-1979, 1997.
- [159] J. H. Moon, J. W. Shin, S. Y. Kim, and J. W. Park, "Formation of uniform aminosilane thin layers: an imine formation to measure relative surface density of the amine group," *Langmuir*, vol. 12, pp. 4621-4624, 1996.
- [160] S. R. Wasserman, Y. T. Tao, and G. M. Whitesides, "Structure and reactivity of alkylsiloxane monolayers formed by reaction of alkyltrichlorosilanes on silicon substrates," *Langmuir*, vol. 5, pp. 1074-1087, 1989.
- [161] S. R. Cohen, R. Naaman, and J. Sagiv, "Thermally induced disorder in organized organic monolayers on solid substrates," *The Journal of Physical Chemistry*, vol. 90, pp. 3054-3056, 1986.
- [162] S. Onclin, B. J. Ravoo, and D. N. Reinhoudt, "Engineering Silicon Oxide Surfaces Using Self-Assembled Monolayers," *Angewandte Chemie International Edition*, vol. 44, pp. 6282-6304, 2005.
- [163] R. Maoz, J. Sagiv, D. Degenhardt, H. Möhwald, and P. Quint, "Hydrogen-bonded multilayers of self-assembling silanes: structure elucidation by combined Fourier transform infra-red spectroscopy and X-ray scattering techniques," *Supramolecular Science*, vol. 2, pp. 9-24, 1995.
- [164] H. Brunner, T. Vallant, U. Mayer, and H. Hoffmann, "Formation of Ultrathin Films at the Solid-Liquid Interface Studied by In Situ Ellipsometry," *Journal of Colloid and Interface Science*, vol. 212, pp. 545-552, 1999.
- [165] Y. Wang and M. Lieberman, "Growth of ultrasmooth octadecyltrichlorosilane self-assembled monolayers on SiO₂," *Langmuir*, vol. 19, pp. 1159-1167, 2003.
- [166] N. Rozlosnik, M. C. Gerstenberg, and N. B. Larsen, "Effect of solvents and concentration on the formation of a self-assembled monolayer of octadecylsiloxane on silicon (001)," *Langmuir*, vol. 19, pp. 1182-1188, Feb 18 2003.
- [167] Y.-a. Cheng, B. Zheng, P.-h. Chuang, and S. Hsieh, "Solvent effects on molecular packing and tribological properties of octadecyltrichlorosilane films on silicon," *Langmuir*, vol. 26, pp. 8256-8261, 2010.
- [168] T. Manifar, A. Rezaee, M. Sheikhzadeh, and S. Mittler, "Formation of uniform self-assembly monolayers by choosing the right solvent: OTS on silicon wafer, a case study," *Applied Surface Science*, vol. 254, pp. 4611-4619, 2008.
- [169] J. Gun and J. Sagiv, "On the formation and structure of self-assembling monolayers: III. Time of formation, solvent retention, and release," *Journal of Colloid and Interface Science*, vol. 112, pp. 457-472, 1986.
- [170] M. Gangoda and R. Gilpin, "Deuterium nuclear magnetic resonance investigations of the dynamics of alkyl-modified silica in the presence of solvent, surfactant, and mesogenic molecules," *Langmuir*, vol. 6, pp. 941-944, 1990.
- [171] M. Pomerantz, A. Segmüller, L. Netzer, and J. Sagiv, "Coverage of Si substrates by self-assembling monolayers and multilayers as measured by IR, wettability and X-ray diffraction," *Thin Solid Films*, vol. 132, pp. 153-162, 1985.

- [172] N. Tillman, A. Ulman, J. S. Schildkraut, and T. L. Penner, "Incorporation of phenoxy groups in self-assembled monolayers of trichlorosilane derivatives. Effects on film thickness, wettability, and molecular orientation," *Journal of the American Chemical Society*, vol. 110, pp. 6136-6144, 1988.
- [173] M. Wei, R. S. Bowman, J. L. Wilson, and N. R. Morrow, "Wetting properties and stability of silane-treated glass exposed to water, air, and oil," *Journal of Colloid and Interface Science*, vol. 157, pp. 154-159, 1993.
- [174] A. Chandekar, S. K. Sengupta, and J. E. Whitten, "Thermal stability of thiol and silane monolayers: A comparative study," *Applied Surface Science*, vol. 256, pp. 2742-2749, 2010.
- [175] A. Ulman, *An Introduction to Ultrathin Organic Films: From Langmuir--Blodgett to Self-Assembly*: Academic press, 2013.
- [176] R. Wang, G. Baran, and S. L. Wunder, "Packing and thermal stability of polyoctadecylsiloxane compared with octadecylsilane monolayers," *Langmuir*, vol. 16, pp. 6298-6305, 2000.
- [177] R. Wang and S. L. Wunder, "Thermal stability of octadecylsilane monolayers on silica: curvature and free volume effects," *The Journal of Physical Chemistry B*, vol. 105, pp. 173-181, 2001.
- [178] N. Tillman, A. Ulman, and T. L. Penner, "Formation of multilayers by self-assembly," *Langmuir*, vol. 5, pp. 101-111, 1989.
- [179] M. R. Linford, P. Fenter, P. M. Eisenberger, and C. E. Chidsey, "Alkyl monolayers on silicon prepared from 1-alkenes and hydrogen-terminated silicon," *Journal of the American Chemical Society*, vol. 117, pp. 3145-3155, 1995.
- [180] C. R. Kessel and S. Granick, "Formation and characterization of a highly ordered and well-anchored alkylsilane monolayer on mica by self-assembly," *Langmuir*, vol. 7, pp. 532-538, 1991.
- [181] C. Picard, A. Larbot, F. Guida-Pietrasanta, B. Boutevin, and A. Ratsimihety, "Grafting of ceramic membranes by fluorinated silanes: hydrophobic features," *Separation and purification technology*, vol. 25, pp. 65-69, 2001.
- [182] K. J. Shea and D. A. Loy, "Bridged polysilsesquioxanes. Molecular-engineered hybrid organic-inorganic materials," *Chemistry of materials*, vol. 13, pp. 3306-3319, 2001.
- [183] R. M. De Vos and H. Verweij, "Improved performance of silica membranes for gas separation," *Journal of Membrane Science*, vol. 143, pp. 37-51, 1998.
- [184] S. A. Younssi, A. Iraqi, M. Rafiq, M. Persin, A. Larbot, and J. Sarrazin, " γ Alumina membranes grafting by organosilanes and its application to the separation of solvent mixtures by pervaporation," *Separation and purification technology*, vol. 32, pp. 175-179, 2003.
- [185] A. Sah, H. Castricum, A. Bliiek, D. Blank, and J. Ten Elshof, "Hydrophobic modification of γ -alumina membranes with organochlorosilanes," *Journal of Membrane Science*, vol. 243, pp. 125-132, 2004.
- [186] L. A. Prado, M. Sriyai, M. Ghislandi, A. Barros-Timmons, and K. Schulte, "Surface modification of alumina nanoparticles with silane coupling agents," *Journal of the Brazilian Chemical Society*, vol. 21, pp. 2238-2245, 2010.
- [187] V. Szczepanski, I. Vlassioux, and S. Smirnov, "Stability of silane modifiers on alumina nanoporous membranes," *Journal of Membrane Science*, vol. 281, pp. 587-591, 2006.
- [188] L. N. Mitchon and J. White, "Growth and analysis of octadecylsiloxane monolayers on Al₂O₃ (0001)," *Langmuir*, vol. 22, pp. 6549-6554, 2006.
- [189] A. M. M. Jani, E. J. Anglin, S. J. McInnes, D. Losic, J. G. Shapter, and N. H. Voelcker, "Nanoporous anodic aluminium oxide membranes with layered surface chemistry," *Chemical Communications*, pp. 3062-3064, 2009.

Chapter 1: Introduction.

- [190] S. H. Hyun, S. Y. Jo, and B. S. Kang, "Surface modification of γ -alumina membranes by silane coupling for CO₂ separation," *Journal of Membrane Science*, vol. 120, pp. 197-206, 1996.

Chapter 2: Experimental techniques and materials.

2.1 Experimental techniques.

All pressures within this work are absolute (bar) unless otherwise stated. In this case the pressures will be detailed as the gauge pressure (barg).

2.2 Physical vapour deposition.

Surface coating of metals was carried out in a Moorfield minilab 080 metal evaporator utilising two methods: DC sputtering and electron beam evaporation (Ebeam).

2.2.1 Electron beam evaporation.

Ebeam evaporation is carried out under ultra high vacuum (UHV), ca 8×10^{-10} bar. Samples are placed above the water cooled copper bed, which contains a crucible produced of appropriate material (in this case vitrified carbon) filled to a suitable level with the material to be evaporated. A tungsten coil is supplied with a high voltage (10kV) and electrons are emitted as a beam perpendicular to the coil. The emitted beam intensity is dictated by the supplied current, providing a method of control. The beam passes through two sets of deflector magnets which act to direct the beam into the top of the crucible and onto the sample. A further electromagnet below the crucible allows fine control over beam position and diffuseness. Upon collision with the sample material, the electron beam energy is converted to heat, and thus a process for highly controlled local heating is achieved. When enough energy is supplied to the sample material, it melts and evaporates in an upwards direction, coating the substrates above. The thickness of coating is monitored by a

quartz crystal microbalance located above the crucible, at a height as close to the substrate as possible. This is because coating rate and thickness are directional, with items closer to the source coated more quickly than those positioned further away, and those directly above the crucible coated more readily than those at angles away from the vertical. A schematic of the Ebeam is shown in Figure 2-1.

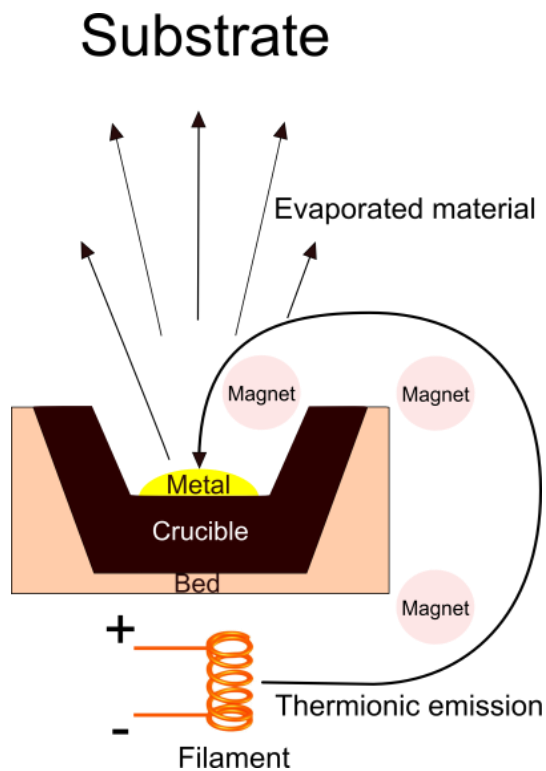


Figure 2-1 Schematic of Ebeam evaporation.

2.2.2 DC sputtering.

DC sputtering initially requires a low pressure similar to Ebeam deposition to remove ambient air from the chamber. Once achieved, argon is introduced to bring the pressure back up to ca 5×10^{-6} bar. A target material, usually in the shape of a circular disk, is placed onto a

cathode contained within the 'magnetron' sputter head. Power is applied to the cooled magnetron and argon gas is ionised between the anode and cathode when a high enough voltage is reached. This is termed glow discharge. At this point the positively charged argon ions are attracted to the cathode, and thus collide with the target material at high velocity. This liberates atoms, or clumps of atoms, which vary in size based on the collision energy of the ion. This liberated material collides with other material or gas within the chamber until it collides with a surface, to which it adheres. These collisions impart a random walk element on the material direction and thus sputtering is less directional than Ebeam evaporation. The thickness and rate of deposition depend on the supplied power, the distance between the magnetron and the sample, and the gas pressure. As with e-Beam, both are measured with a quartz crystal microbalance. Sputtering holds an advantage over Ebeam because of the ease with which samples may be sputtered, whereas high melting point materials may be difficult to evaporate by Ebeam. In addition, the sputtering process is low temperature, so may hold benefits with regards to preventing substrate destruction if it is particularly sensitive to temperature. A schematic of DC sputtering is shown in Figure 2-2.

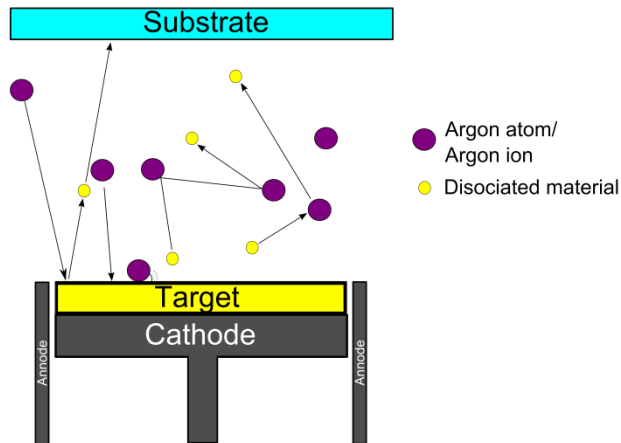


Figure 2-2 Schematic of DC sputtering

2.3 Plasma cleaning.

Plasma cleaning was carried out using a Diener Zepto plasma cleaner. Initially, low chamber pressure is created by means of a rotary vacuum pump. Once a pressure of less than 0.1 mbar is reached, the working gas is introduced and the pressure is raised to between 0.1-1.0 mbar. Once pressure has been reached, the generator is switched on to induce microwave (2.45 GHz) production. An aerial is permanently fixed into an electron tube oscillator, based on Tesla coils, which oscillates to produce a sinusoidal wave at a single fixed frequency. The aerial must not be in the vacuum chamber, and for this reason it sits outside and is directed through a glass window and into the chamber. The microwaves excite the gas and create plasma. The sample to be cleaned is exposed to this plasma, and in the case of oxygen the cleaning process is twofold. The created oxygen plasma acts to oxidise contaminants chemically, with the IR/UV components of the plasma destroying carbon chains.

2.4 Contact angle goniometry.

Contact angle goniometry was performed with a First Ten Angstroms FTA200 series goniometer. A 500 μL glass syringe (SGE analytical science) with 27 gauge flat tipped needle (ID 0.254 mm, OD 0.406 mm) was used to apply a 3 μL drop of 15 M Ω -cm deionised water (Elga Purelab Option filtration system) onto the sample surface. An image was captured on the Lumenera infinity 2 camera with 2.0 megapixel CCD sensor at a resolution of 696x520 pixels.

Videos of the advancing and receding drop were also taken on the the Lumenera infinity 2. A syringe pump with 500 μL glass syringe and 27 gauge needle as above was used to add deionised water to the substrate surface. The droplet was expanded until it filled the frame, before the pump was reversed and the water was sucked back into the syringe.

The contact angle was calculated using a custom written Laboratory Virtual Instrument Engineering Workbench (LabVIEW) code, calibrated using standards provided by FTA instruments.

2.5 Atomic Force Microscopy.

Surface topography information was investigated using a Veeco Dimension 3100 Atomic Force Microscope (AFM) operating in tapping mode. The AFM tips were standard Olympus tapping tips with a resonance around 275 kHz. The AFM images were analysed using the analysis program ImageSXM to calculate the root mean square roughness. In tapping mode a cantilever arm, with an AFM tip attached to one end, is oscillated at or just below the resonance frequency with an amplitude of around 20-100 nm. This oscillation is controlled by a piezoelectric crystal, where a change in voltage changes the amplitude of oscillation. A laser

beam is directed onto the cantilever to be detected at a reflected angle by the split photovoltaic sensor. When the tip engages with the surface at the bottom of its swing, the wave is perturbed. By monitoring the root mean square (RMS) of the wave, a feedback loop can adjust the piezo input voltage to maintain a constant interaction with the sample surface during the scan. Topographical information is calculated based on the RMS and cantilever perturbation detected by the photovoltaic.

In addition, a phase image is taken during the scan. As the tip impacts the surface, the wave detected is slightly out of phase with the input wave and the more the tip 'sticks' the higher the perturbation. The phase image provides data on the crystal/ grain structure of the surface.

2.6 Scanning Electron Microscopy.

Scanning electron microscopy (SEM) was carried out on a JOEL JSM 6010LA nanoscope SEM. Images were taken under various conditions, specified with each image. A tungsten wire filament (0.1 mm diameter) is heated to around 2800K to induce thermionic emission of electrons. The emitted electrons are gathered by a positively charged anode (1-30 kV) containing a hole at its centre, through which the electrons flow to form a focussed beam. The current of the electron beam can be altered by placing a Wehnelt electrode between the anode and cathode and supplying it with a negative voltage. At this point the electron beam is highly focused, with the finest focal point being known as the crossover. This point is commonly seen as the electron beam source, and is often around 20 μm in diameter.

Wire coils are used to generate a magnetic field, which are enclosed by yokes containing a small gap known as the polepiece. This system acts to increase the density of the

magnetic flux, thus allowing for a lens with a shorter focal length. The power of the lens may be adjusted by altering the current passing through the coils, a feature not possible with regular optical lenses. Two coils are placed below the electron emitter to focus the beam to a fine spot, necessary for SEM. They are known as the condenser lens and the objective lens. Placing an aperture between the two lenses restricts the amount of the electron beam that reaches the objective lens. Increasing excitation of the condenser lens acts to broaden the electron beam, and thus less of the beam passes through the aperture and onto the objective. As a result the probe diameter and probe current may be controlled. The objective enables the user to focus.

Secondary electron detection occurs at a fluorescent coated substrate (scintillator) which is held under high voltage (10 kV) during detection. The emitted electrons are attracted to this high voltage, causing the fluorescent substrate to emit upon impact of electrons. This light passes into a photomultiplier tube and is converted back to electrons before further amplification.

There are numerous ways in which electrons may interact with a specimen. They may be transmitted, backscattered or undergo secondary electron emission. Secondary electron emission occurs when the incident electron beam collides and removes valence electrons from the constituent atoms within the surface. As secondary electrons have a small energy, those emitted deep within the sample are absorbed by it and thus only surface electrons are emitted. The final result is that secondary electron scans are sensitive to the surface, but are less effective for examining thick specimens. In addition, more electrons are emitted when the incoming beam enters the sample at a non-perpendicular angle. Therefore, the user observes high contrast images, with regions of brightness dictated by the angle of incidence.

Backscattered electrons are those scattered by the sample and emitted backwards towards the source. Backscattered electrons are higher energy than the secondary electrons

and so possess information about relatively deep components of the sample. An area consisting of heavier atoms appears bright in the image, as the backscattered electron yield is higher from heavier atoms. Specimens with surface roughness lead to an increase in backscattered electrons in the direction of specular reflection. As a result, topographical information can be extracted. Penetration depth of the electron beam is influenced by accelerating voltage, with a higher voltage leading to deeper penetration. [1]

2.7 Materials and chemical abbreviations.

All chemicals were of reagent grade and were used as received unless otherwise stated. The following silanes were obtained from Sigma Aldrich (Gillingham, UK) and are shown with the abbreviations used throughout the text.

2.7.1 Chemicals

1*H*,1*H*,2*H*,2*H*-Perfluorooctyltriethoxysilane 98% - **PFO**, (3-Aminopropyl) trimethoxysilane 97% - **3APTMS**, 3-(Trimethoxysilyl)propyl acrylate 92% - **Acrylate**, Hexadecyltrimethoxysilane 85% - **Hexadecyl**, *N*-[3-(Trimethoxysilyl)propyl]ethylenediamine 97% - **N3TMSPED**. *tert*-Butyltrichlorosilane 96% - **t-BU**, Trichloro(octadecyl)silane >90% **TCODS**, Trichloro(octyl)silane 97% - **TCOS** and Trimethoxy(octadecyl)silane >90% **TMODS**.

The following silane was obtained from Alfa Aesar (Lancashire, UK) and is shown with the abbreviation used throughout the text.

(3-Glycidoxypropyl)trimethoxysilane 97% - **3GTMS**.

The following thiols were obtained from Sigma Aldrich (Gillingham, UK) and are shown with the abbreviations used throughout the text.

1-octadecanethiol 98% - **1ODT**, 1-octanethiol 98.5% - **1OT**, 2-Methyl-2-propanethiol 99% - **2M2PT**, 2-propanethiol >98% - **2PT**, 3-mercaptopropionic acid 99% - **3MPA**, 8-Mercapto-1-octanol 98% - **8M1O**, 8-Mercaptooctanoic acid 95% - **8MOA**, 11-Mercapto-1-undecanol 97% - **11MUD** and 11-mercaptoundecanoic acid 98% - **11MUDA**.

The following reagents were purchased from the respective companies and were used as received.

n-Heptane (anhydrous) 99% from Fisher Scientific (Loughborough, UK)

Methanol, 99% purchased from Alfa Aesar (Lancashire, UK)

Chapter 2: Experimental techniques and materials.

Ethanol (absolute) >99.8% from Sigma Aldrich (Gillingham, UK)

Hydrogen peroxide >30% w/v from Fisher Scientific (Loughborough, UK)

Sulphuric acid > 95% from Fisher Scientific (Loughborough, UK)

All thiol and silane structures are shown in Figure 2-3.

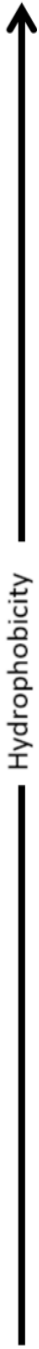
	Silane	Thiol
 Hydrophobicity	 1H,1H,2H,2H-Perfluorooctyltriethoxysilane (PFO)	 1-octadecanethiol (1ODT)
	 Trimethoxy(octadecyl)silane (TMODS)	 1-octanethiol (1OT)
	 Trichloro(octyl)silane (TCOS)	 2-Methyl-2-propanethiol (2M2PT)
	 Hexadecyltrimethoxysilane (Hexadecyl)	 2-propanethiol (2PT)
	 <i>tert</i> -Butyltrichlorosilane (t-Bu)	 8-Mercapto-1-octanol (8M1O)
	 3-(Trimethoxysilyl)propyl acrylate (Acrylate)	 11-mercaptoundecanoic acid (11MUDA)
	 <i>N</i> -[3-(Trimethoxysilyl)propyl]ethylenediamine (N3TMSPED)	 3-mercaptopropionic acid (3MPA)
	 (3-Aminopropyl) trimethoxysilane (3APTMS)	 11-Mercapto-1-undecanol (11M1O)
	 (3-Glycidoxypropyl)trimethoxysilane (3GTMS)	 8-Mercaptooctanoic acid (8MOA)

Figure 2-3 Chemical structures and abbreviations of thiols and silanes used in this investigation.

2.7.2 Porous substrates

70 μm thick rolled stainless steel disks (25 mm diameter) with photoetched holes of 250 μm diameters were obtained from photofabrication services, St Neots, UK. A single pore was

Chapter 2: Experimental techniques and materials.

etched through the centre to create the 'single pore' disks. A pattern of 7 holes was etched through the disks to give a central hole with a hexagonal group of holes surrounding it, with centre to centre distance of 2.25 mm between all adjacent holes as in Figure 2-4. This diffuser acted as a pseudo multi pore system and allowed a level of control to assist understanding.

Sintered steel disks (25 mm diameter, 3 mm thick) were obtained from Hengko technology co. Ltd (Shenzhen City, China) with a random array of 5 μm pores, Figure 2-4.

Pointfour™ Micro Bubble Diffuser plate was obtained from Pentair Aquatic eco-systems (Apopka, FL, USA) and cut into 25 mm diameter disks with a thickness of 3 mm.

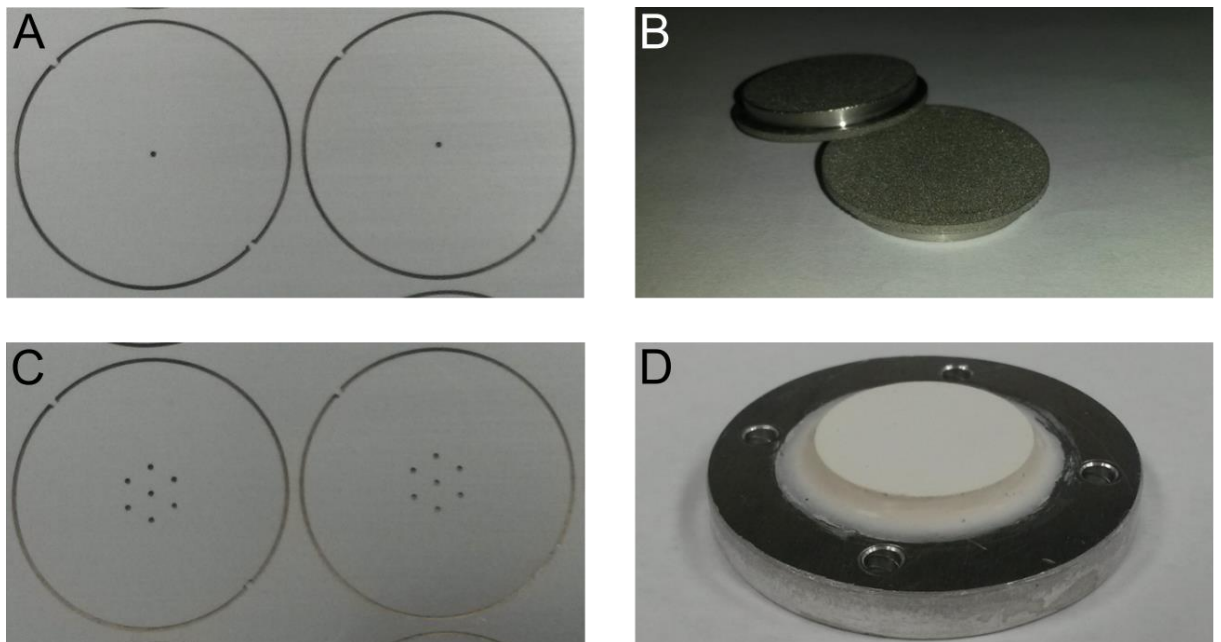


Figure 2-4 Diffuser materials used in this investigation. A) single pore, B) sintered steel diffuser, C) 7 controlled pores, D) pointfour sintered ceramic diffuser.

2.8 References

- [1] JOEL.Ltd, "Scanning Electron Microscope A to Z " *JOEL Ltd UK*, 2015.

Chapter 3: Physical and chemical Modification of a surface.

3.1 Surface modification by silanes and thiols.

The phenomenon of surface wettability is a well studied one in general, with both organosilanes and organothiols being used as surface modifiers. The organothiol (RSH), where R is an arbitrary organic group such as an alkane, bonds to gold surfaces as explained in section 1.7. Many factors influences monolayer formation, with the structure of the 'R' group, the cleanliness of the gold substrate, temperature and solvent all playing roles in the complex mechanism of self-assembled monolayer (SAM) formation. Similarly, the formation of silane SAMs on silicon wafer has been studied. Once again numerous factors can affect SAM formation, with several discussed in section 1.11.

Due to the potential deviations outlined above, this chapter focuses on the modification of clean silicon wafers by silanes and also on the physical vapour deposition of gold by both electron beam (Ebeam) evaporation and DC sputtering, followed by subsequent thiol modification. Tests were carried out on various surfaces to check for deviations in wetting behaviour due to roughness, in accordance with the work of both Wenzel [1, 2] and Cassie. [3, 4] In addition Atomic Force microscopy (AFM) data is presented to give an indication of roughness and structure of each surface. It is important to note that this data is by no means quantitative and the root mean square (RMS) data cannot be used to give an accurate numerical value to the Wenzel roughness factor, r , as discussed in section 1.6.1. However, this data may be used to provide a handle on the wetting properties of the individual surfaces, and will be used later (Chapter 3 and Chapter 4) to explain the bubble formation process at various porous surfaces.

3.2 Experimental.

3.2.1 Modification of silicon wafer by silanes – the effect of piranha immersion time.

3.2.1.1 Short Piranha immersion.

Silicon wafer (Si) (100) was cut into strips of around 1 cm x 5 cm by the 'score and snap' method. The cut wafer strips were blown with compressed air to remove Si fragments/dust from the surface before being rinsed with ethanol. The strips were subsequently blown dry with compressed air before being placed into a 20 cm Pyrex oven dish. Piranha solution (400 mL, H₂O₂ : H₂SO₄ 1:1) was added to the dish to cover the samples. The wafer was left immersed in the Piranha solution for 30 minutes before removal. Each strip was thoroughly rinsed with 15 mΩ deionised water (3x25 mL) to ensure removal of the cleaning solution. The strips were blown dry under a stream of dry nitrogen for 30 seconds before being immersed into the silane solutions (described below) immediately.

3.2.1.2 Long Piranha immersion.

Si wafer was cut and pre-cleaned as above. The wafers were then placed in Piranha solution for 6 hours before removal and rinsing. Silane solutions were made as described below and the clean dry wafers were placed into solution for various time periods, before the rinsing process outlined below.

3.2.2 Silane treatment after Piranha cleaning.

Ethanol, methanol and heptane were respectively added to each silane in 50 mL polypropylene corning tubes to form 3mM (50mL) solutions under ambient conditions. Clean, dry wafer strips were added to the solutions before sealing with paraffin film. The solutions were left for 24 hours under ambient conditions. Upon removal, each strip was rinsed with the parent solvent before being immersed in 50 mL of fresh solvent and placed in an ultrasonic bath for 30 seconds at 25 °C to remove physically adsorbed layers. A final rinse with further fresh solvent and drying by a stream of nitrogen followed before contact angle measurements were taken.

In addition a set of samples were stored for 24 days in the silane solution where the corning tube had been sealed with paraffin film. After the 24 days, the samples were removed and exposed to the same rinsing step as above before contact angle data was taken.

3.2.3 Modification of silicon wafer by silanes – wafer with <5nm

RMS.

A silicon wafer with an RMS of <5 nm was cut into 1 cm x 5 cm strips by the 'score and snap' method. The strips were pre-cleaned as above and then immersed in Piranha solution for 30 minutes, before removal and rinsing as detailed. The strips were placed into silane solutions (50 mL, 3 mM in Heptane) for 24 hours and rinsed as detailed. Contact angle data was then taken.

3.2.4 Modification of silicon wafer by thiols – the effect of surface RMS and deposition type.

Si (100) was cut into strips of around 1 cm x 5 cm by the 'score and snap' method. The cut wafer strips were blown with compressed air to remove Si fragments/ dust from the surface before being rinsed with ethanol. The strips were subsequently blown dry with compressed air before being placed into a 20 cm Pyrex oven dish. Piranha solution (400 mL, H₂O₂ : H₂SO₄ (1:1)) was added to the dish to cover the samples. The wafer was left immersed in the Piranha solution for 30 minutes before removal. Each strip was thoroughly rinsed with 15 mΩ deionised water (3x25 mL) to ensure removal of the cleaning solution. The strips were blown dry under a stream of dry nitrogen for 30 seconds before being loaded into a Moorfield minilab 080 metal evaporator for coating.

One set of strips was coated by electron beam evaporation (Ebeam) as detailed in section 2.2. The base pressure of the chamber was taken to $<1 \times 10^{-9}$ bar and evaporation was carried out. First, a chromium (Cr) adhesion layer was added to the Si at a 10 nm thickness (4 mA, 10 kV, rate: 0.2 Å/s) followed by a 100 nm gold layer (40 mA, 10 kV, rate: 0.48 Å/s).

A second set of strips was coated by DC sputtering as detailed in section 2.2. The base pressure of the chamber was taken to $<1 \times 10^{-9}$ bar before argon (Ar) was introduced to re-pressurise to 6.3×10^{-6} bar. Once the pressure stabilised, it was maintained for 5 minutes before a base layer of Cr (10 nm) was added (0.158 A, 287 V, rate: 0.1 4Å/s). After chromium deposition, the chamber was maintained at constant pressure for 5 minutes before the deposition of gold (100 nm) was carried out (0.118 A, 359 V, rate: 0.45 Å/s).

Thiol solutions (50 mL, 3 mM) were made using ethanol that was degassed under a steady stream of nitrogen for 30 minutes before use. Freshly coated Si strips were placed into

the solutions and immediately sealed. The gold coated wafer was left in solution for 18 hours before removal. Upon removal the strips were washed with copious ethanol (100 mL) before drying under a constant stream of nitrogen.

3.2.5 Polished wafer investigation.

As above, a set of strips was coated by Ebeam and a set was coated by DC sputtering. The coated strips were placed into 3 mM thiol solutions for 18 hours and subsequently rinsed and dried as outlined.

3.2.6 Steel disk investigation.

70 μm thick stainless steel disks (25 mm diameter) were rinsed with acetone and ethanol to remove contaminants before being placed into a Diener Zepto plasma cleaner. A vacuum was applied for 10 minutes before the introduction of oxygen gas at 1 barg pressure for a further 5 minutes. After this time the generator was turned on and a plasma was struck. The disks were left in the plasma for 5 minutes to remove all organic contaminants. The clean dry disks were then placed into a Moorfield minilab 080 for coating.

The disks were coated by DC sputtering as follows. The base pressure of the chamber was taken to $<1 \times 10^{-9}$ bar before argon (Ar) was introduced to re-pressurise to 6.5×10^{-6} bar. Once the pressure stabilised, it was maintained for 5 minutes before a base layer of Cr (10 nm) was added (0.163 A, 301.4 V, rate: 0.18 \AA/s). After chromium deposition, the chamber was

maintained at constant pressure for 5 minutes before the deposition of gold (100 nm) was carried out (0.118 A, 362 V, rate: 0.47 Å/s).

Thiol solutions (50 mL, 3 mM) were made using ethanol that was degassed under a steady stream of nitrogen for 30 minutes before use. Freshly coated disks were placed into the solutions and immediately sealed. The gold coated disks were left in solution for 18 hours before removal. Upon removal they were washed with a copious volume of ethanol (100 mL) before drying under a constant stream of nitrogen.

3.2.7 Measuring contact angle hysteresis.

A 500 µL glass syringe (SGE analytical science) was fitted with a 27 gauge flat-tipped needle and 15 mΩ deionised water was added to the surface at a constant rate (3 µL/s) for 15 s, or until the droplet filled the field of view. At this point the pump was reversed and the droplet was removed from the surface. The captured AVI was analysed using calibrated LabVIEW software written by the author.

3.2.8 Spin coating and metal deposition for SEM analysis.

Solutions of Polystyrene (PS) particles (1wt%, TS20 20.4 µm , TS80, 80.85 µm) were made up in water before being spin coated at 3000 rpm for 2 minutes onto ethanol rinsed glass slides.

One set of slides was coated by electron beam evaporation (Ebeam) as detailed. The base pressure of the chamber was taken to $<1 \times 10^{-9}$ bar and evaporation was carried out. First,

a chromium (Cr) adhesion layer (10 nm) was added to the Si (4 mA, 10 kV, rate: 0.18 Å/s) followed by a 100 nm gold layer (40 mA, 10 kV, rate: 0.52 Å/s).

A second set of slides was coated by DC sputtering as detailed. The base pressure of the chamber was taken to $<1 \times 10^{-9}$ bar before argon (Ar) was introduced to re-pressurise to 6.5×10^{-6} bar. Once the pressure stabilised, it was maintained for 5 minutes before a base layer of Cr (10 nm) was added (0.158 A, 287 V, rate: 0.18 Å/s). After chromium deposition, the chamber was maintained at constant pressure for 5 minutes before the deposition of gold (100 nm) was carried out (0.118 A, 359 V, rate: 0.48 Å/s). SEM images were then collected under BEC mode at 18 kV.

3.3 Results and discussion.

3.3.1 Effect of solvent type on Silane modification.

The effect of solvent type on silane modification was investigated using Piranha cleaned silicon wafers as outlined above. The results are summarised in Table 3-1 and Table 3-2 and shown in Figure 3-1 and Figure 3-2. Contact angle measurements are a mean average with $n=10$. Errors are reported as 95% error in the mean.

Table 3-1 Contact angle and standard deviation of a 3 μ L, 15 m Ω deionised water, droplet on silane modified silicon wafer following 24 hours immersion and a short Piranha clean.

	Ethanol		Heptane		Methanol	
	Contact angle (°)	Standard deviation	Contact angle (°)	Standard deviation	Contact angle (°)	Standard deviation
3APTMS	50.8	2.58	55.8	3.15	51.1	4.93
3GPTMS	60.6	6.35	39.3	3.35	54.0	3.60
Acrylate	38.2	1.70	57.87	2.58	46.9	2.63
Hexadecyl	38.3	1.92	97.73	4.06	46.6	5.80
N3TMSPED	57.3	5.75	35.1	1.83	52.0	3.05
PFO	31.3	2.27	103.0	2.43	56.6	4.41
t-BU	36.6	2.61	66.5	1.76	20.7	3.48
TCOS	42.3	3.03	97.6	4.77	38.3	4.11
TMODS	45.3	2.89	96.7	0.81	54.8	4.19

Table 3-2 Contact angle and standard deviation of a 3 μ L, 15 m Ω deionised water, droplet on silane modified silicon wafer following 24 days immersion and a short Piranha clean.

	Ethanol		Heptane		Methanol	
	Contact angle (°)	Standard deviation	Contact angle (°)	Standard deviation	Contact angle (°)	Standard deviation
3APTMS	49.8	2.83	51.5	1.85	41.9	2.04
3GPTMS	62.8	2.93	46.7	5.57	49.1	2.43
Acrylate	39.7	1.75	67.7	4.94	47.4	1.17
Hexadecyl	47.7	5.02	95.9	2.20	56.4	2.62
N3TMSPED	62.1	1.36	54.8	3.70	45.5	1.95
PFO	45.6	3.27	103.9	4.39	49.9	2.27
t-BU	34.3	3.01	65.2	4.35	27.4	3.03
TCOS	45.5	1.05	99.5	1.55	51.2	4.92
TMODS	54.3	2.52	100.4	1.05	53.5	1.71

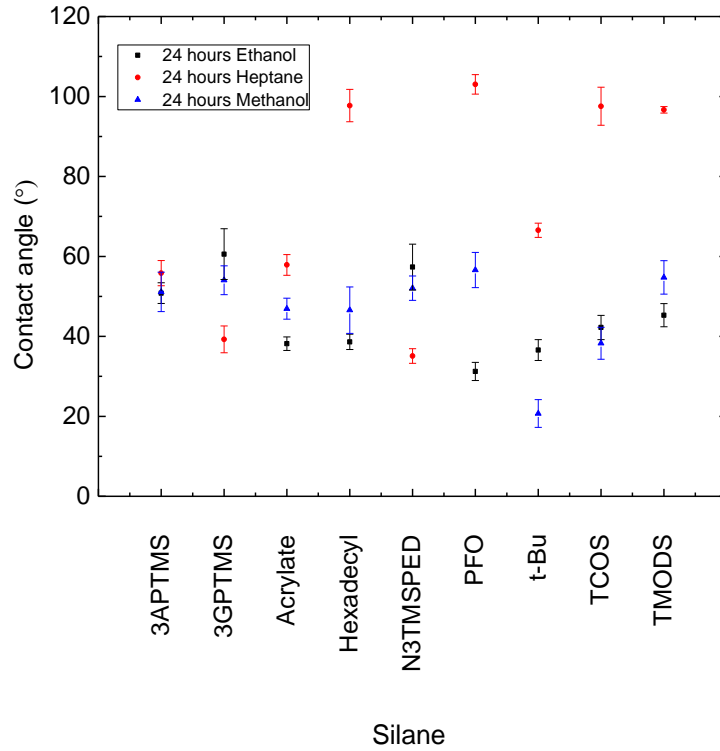


Figure 3-1 Contact angles of silanes after 24 hours immersion in solution following a short Piranha clean.

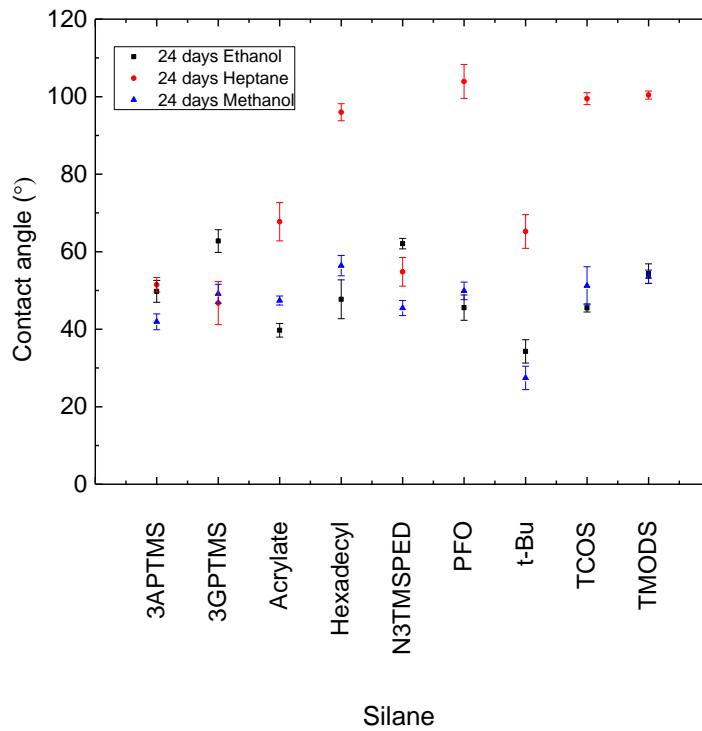


Figure 3-2 Contact angles of silanes after 24 days immersion in solution following a short Piranha clean.

It can be seen from Figure 3-1 and Figure 3-2 that there is a striking difference in contact angles when heptane and the more polar ethanol and methanol are used. This difference is seen most prominently when examining the more aliphatic silanes; PFO, t-Bu, TCOS, hexadecyl and TMODS all show a much larger contact angle in heptane than in methanol and ethanol. It is believed that this is the case because the aliphatic chains mix more readily with the heptane, but remain in micelle like configurations in the ethanol and methanol.

In addition, it can be noticed that the ethanol and methanol solutions yield a similar angle to one another. The apparent angles in the region 40-60° are typical for surface contaminants and exposed methylene groups. It is likely that the SAMs formed from 3APTMS, 3GPTMS, N3TMSPED and acrylate are significantly disordered and the results deviate significantly from those in the literature. 3APTMS has previously been reported to have a CA of <15° [5] and it is expected that the N3TMSPED would be similar. The 3GPTMS and acrylate are more similar to the expected values, with 3GPTMS settling at a CA of around 70°. [6]

AFM data presented in section 3.3.10 may explain the observed effects. The discrepancies observed may be related to the roughness of the Si surface. As already outlined, the surface roughness plays an important role in wettability. It is postulated that this roughness causes the deviations in the contact angles, a theory supported by Chauhan. [5] However, the important fact is that heptane seems to give the most reliable coverage over all silanes, although it may not necessarily be the best solvent for each. This agrees with the work of Aswal and Rozlosnik. [7, 8]

3.3.2 Effect of Piranha immersion time on Silane modification.

The effect of Piranha immersion time was studied to ensure no deleterious etching effects were modifying the nature of the surface. As can be seen from Figure 3-3, there is no consistent pattern regarding the effect of immersion time in Piranha. The hydrophobic silanes, affected to a lesser extent by surface roughness, show little deviation when Piranha immersion time is altered. As a result, it is believed that a 1 hour immersion in Piranha solution is adequate to facilitate cleaning.

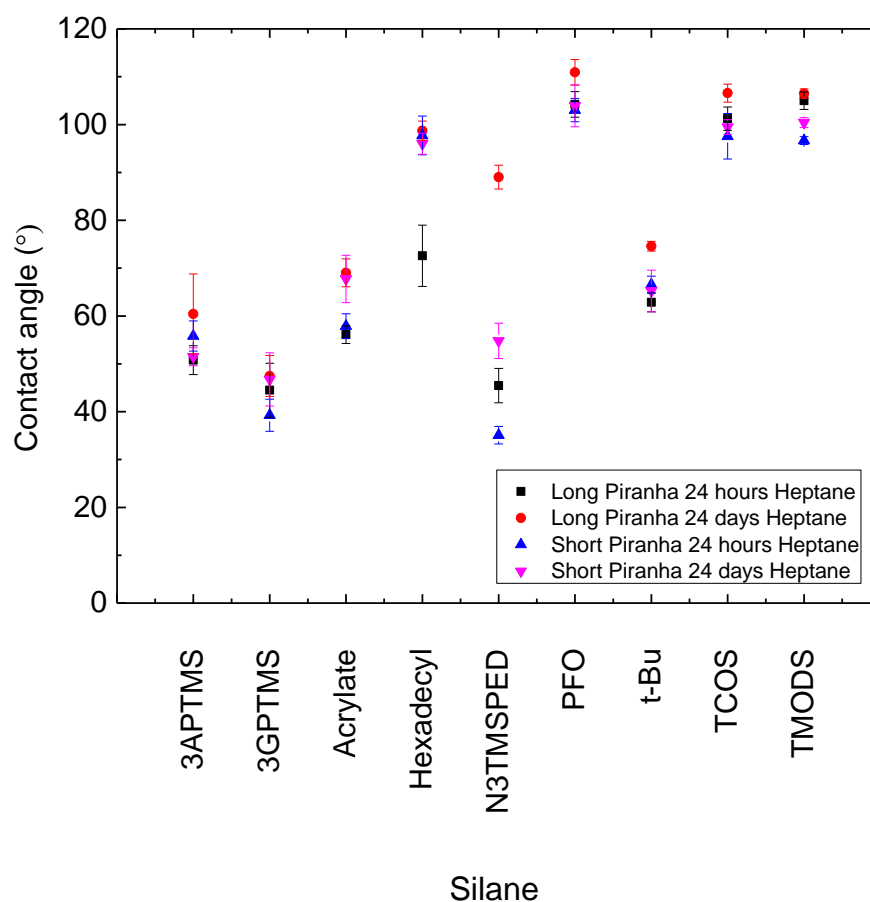


Figure 3-3 The effect of Piranha immersion time on modified Si wafers. A short Piranha clean is classified as 1 hour immersion, and a long Piranha clean is 6 hours immersion. Cleaned wafer was left immersed in silane solution for 24 hours or 24 days in each case.

3.3.3 Effect of Silane solution immersion time on Silane modification.

It can be seen from Figure 3-4 that an increase in immersion time acts to increase the contact angle in most cases. It is believed that extended immersion in aliphatic silane solutions acts to increase SAM packing and thus exposes more terminal CH_3 groups at the surface, leading to an increase in the observed contact angle. Prolonged exposure of polar silanes to

the parent solution may lead to multilayer formation. The polar groups, such as the amine of 3APTMS, may form intermolecular interactions with free molecules in solution. This results in the exposure of CH₂ groups at the surface, increasing the observed contact angle. Therefore it is important to remove the modified substrate from solution after 24 hours and rinse thoroughly to remove the physisorbed moieties.

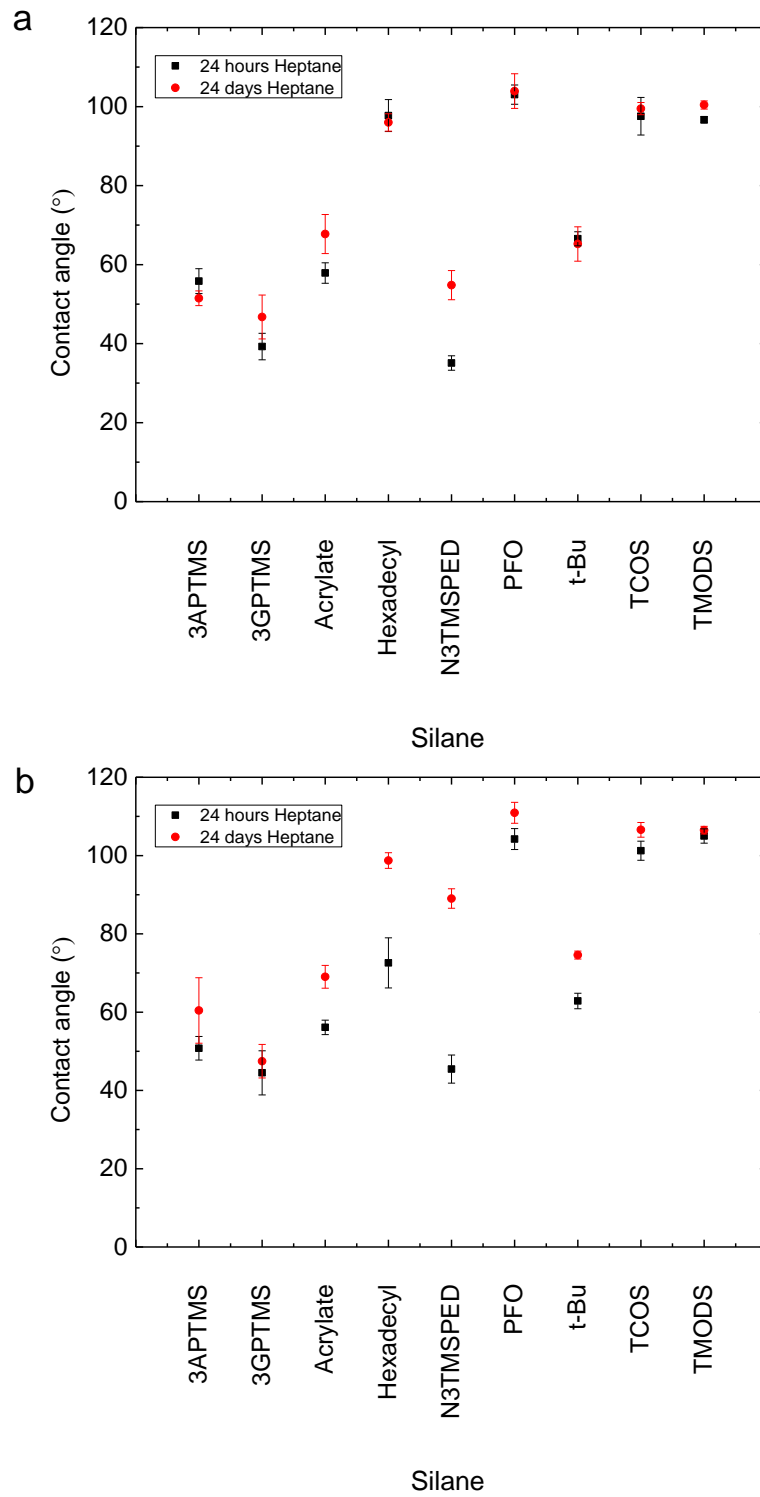


Figure 3-4 Effect of immersion time in silane solution on Si wafer modification. a) after a 1 hour Piranha clean and b) after a 6 hour Piranha clean

3.3.4 Silane modification of a highly polished Si wafer.

Table 3-3 shows the contact angles of silane modified silicon wafer with an RMS <5 nm, measured by AFM. It can be seen that the angles are generally lower than those measured previously, Table 3-1 and Table 3-2. The standard deviation is also generally much lower on the smooth wafer, which is symptomatic of the contact angle departing from the Wenzel state and approaching that of the Young's contact angle, and thus an ideal flat surface. [1, 2]

Table 3-3 Contact angle and standard deviation of a 3 μ L, 15 m Ω deionised water, droplet on silane modified silicon wafer with RMS < 5 nm.

	Contact angle (°)	Standard deviation
3APTMS	46.8	1.56
3GPTMS	34.3	1.92
ACRYLATE	53.2	1.00
HEXADECYL	94.5	1.10
N3TMSPED	44.9	2.95
PFO	100.8	2.39
t-BU	59.6	1.25
OCTYL	93.4	1.26
OCTADECYL	91.9	1.10

3.3.5 Effect of surface roughness on the thiol modification of Silicon wafers.

The effect of surface roughness can be seen in the modification of a surface by thiols, Figure 3-5. Similar to silanes discussed previously, increasing surface roughness in conjunction with aliphatic thiol molecules acts to increase the contact angle, in accordance with Wenzel's equation. Similarly, an increase in roughness leads to a decrease in contact angle for polar thiols. This is also in agreement with Wenzel's equation.

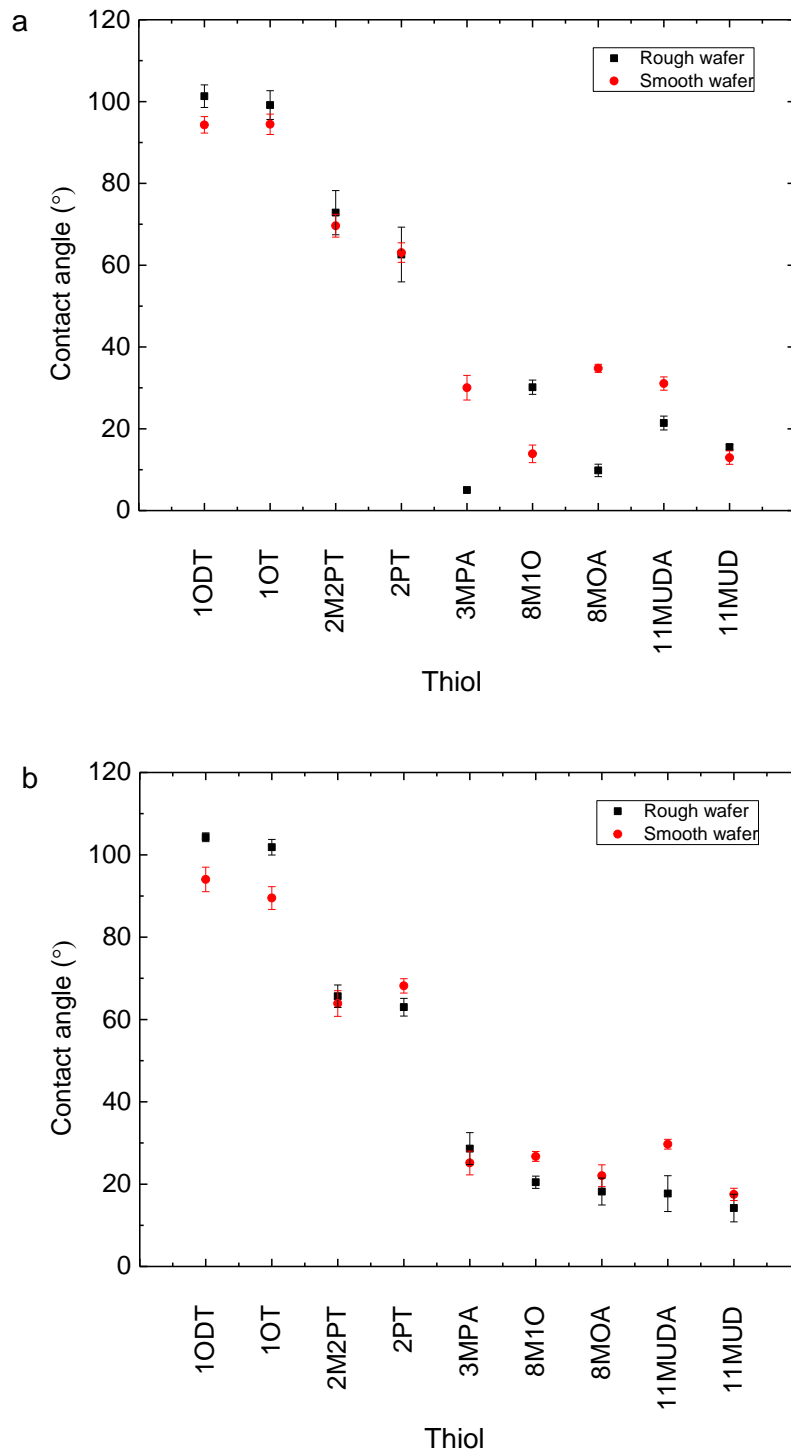


Figure 3-5 Effect of surface roughness on contact angles of Si wafer modified by gold and thiol coating. a) Ebeam coated wafers, b) DC sputtering coated wafers.

3.3.6 Effect of physical vapour deposition type on the modification of Silicon wafers.

Figure 3-6 shows the variation in contact angle when a Si wafer is coated by Ebeam and DC sputtering. In general there is no difference between the two PVD techniques, with many deviations falling within error of one another. This may be unexpected due to the directionality of Ebeam evaporation and the potential for a heterogeneous coating. In addition, DC sputtering can cause variations in particle size based on operating conditions. It therefore follows that a heterogeneous surface may be formed by the increased polydispersity in the sputtered grain size. However, it seems the thiol molecules pack well on both types of surface, generating similar contact angles in the process.

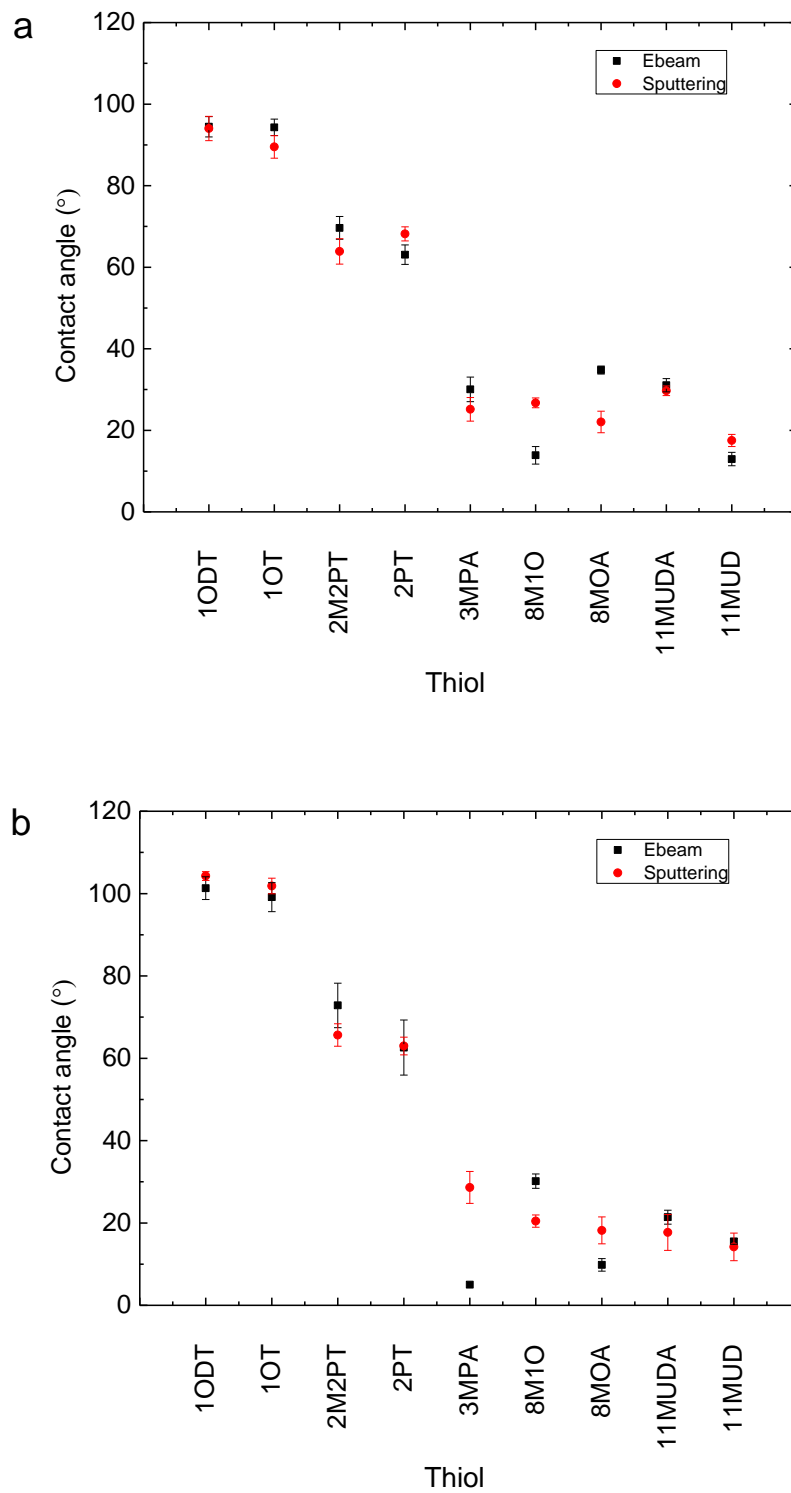


Figure 3-6 Effect of the physical vapour deposition technique on contact angle on both a) a smooth wafer and b) a rough wafer.

3.3.7 Modification of rolled steel disks with thiols.

Rolled steel disks were modified by DC sputtering and subsequent thiol coating as outlined, with the results shown in Table 3-4. It can be seen that there is a good correlation between the contact angles shown, and those presented in Figure 3-5 and Figure 3-6. Once again it is believed that the surface roughness acts to play a considerable role in the surface wettability, with the relatively large standard deviation testament to the moderate levels of surface roughness present.

Table 3-4 Contact angle and standard deviation of a 3 μL , 15 m Ω deionised water droplet on thiol modified, gold coated, rolled stainless steel disks.

	Contact angle (°)	Standard deviation
1ODT	107.9	4.52
1OT	98.1	1.22
2M2PT	79.2	3.56
2PT	60.7	6.94
3MPA	16.9	4.57
8M1O	24.5	6.41
8MOA	5.5	3.55
11MUDA	18.8	7.11
11MUD	13.1	4.64

3.3.8 Contact angle hysteresis and its relation to the Young's contact angle.

Despite the phenomenon of contact angle hysteresis being observed since the 1940's [9, 10] there is still no consensus as to what the hysteresis means physically, and how it can be related to the system under investigation. Many believe the hysteresis arises from surface heterogeneity, with an increase in roughness leading to a larger hysteresis, although this has not yet been quantified. [11, 12] The advancing and receding contact angles of thiol modified silicon were measured dynamically and plotted as a function of droplet base width. For a 1ODT modified silicon wafer with surface features <5 nm the advancing contact angle (θ_A) = 103°, and the receding contact angle (θ_R) = 88, Figure 3-7.

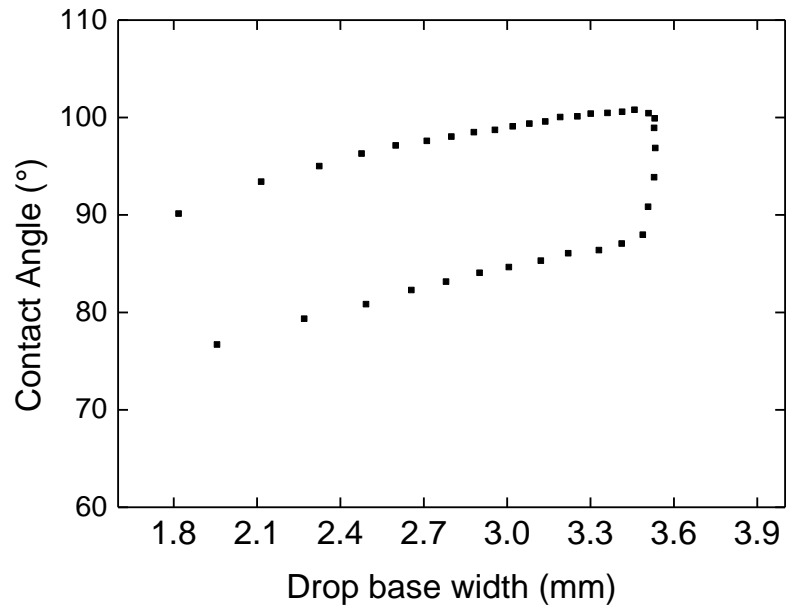


Figure 3-7 The advancing (θ_A) and receding (θ_R) contact angles of 15 mΩ deionised water on a 1ODT modified silicon wafer.

Following the work of Tadmor [13] and Chibowski [14] a relationship between the advancing and receding contact angle with the static contact angle (θ_0) was proposed, as shown in (32).

$$\theta_0 = \cos^{-1} \left(\frac{\Gamma_a \cos \theta_A + \Gamma_r \cos \theta_R}{\Gamma_a + \Gamma_r} \right) \quad (32)$$

Where:

$$\Gamma_a = \left(\frac{\sin^3 \theta_A}{2 - 3 \cos \theta_A + \cos^3 \theta_A} \right)^{1/3} \quad (33)$$

$$\Gamma_r = \left(\frac{\sin^3 \theta_R}{2 - 3\cos\theta_R + \cos^3 \theta_R} \right)^{1/3} \quad (34)$$

In the case of 1ODT, the advancing and receding contact angles yield an expected θ_0 of 93.9°, which correlates extremely well to the measured static angle of $94.31 \pm 2.02^\circ$.

Similarly, the trend is observed in other thiol systems, as indicated in Figure 3-8 for an 11MUD modified surface, showing an advancing angle (θ_A) = 24°, and the receding contact angle (θ_R) = 6°. This yields a calculated angle θ_0 of 11.85° and a measured angle of $12.95 \pm 1.653^\circ$. Once again there is a strong correlation between the measured and calculated values. Table 3-5 summarises the trend between the calculated and measured contact angles of further thiol modified surfaces.

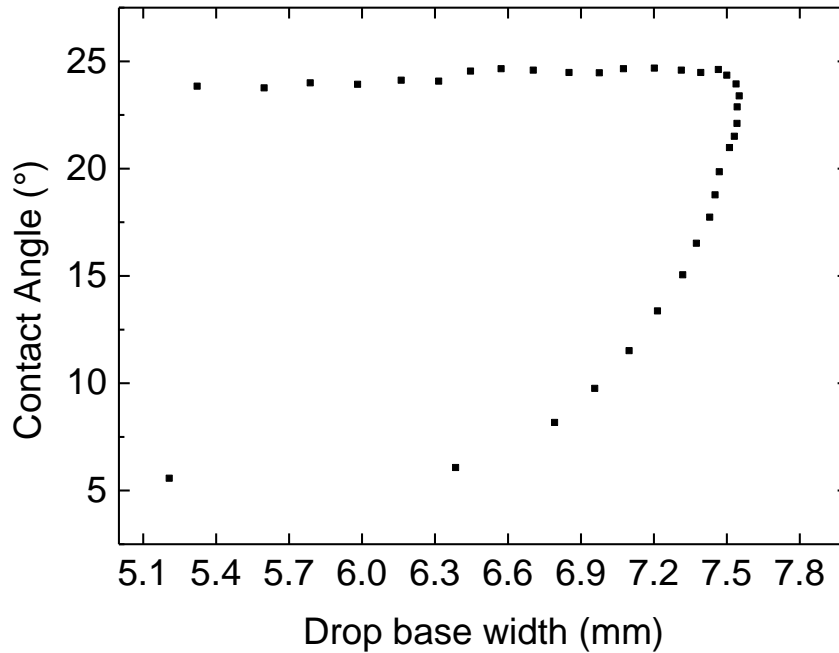


Figure 3-8 The advancing (θ_A) and receding (θ_R) contact angles of 15 mΩ deionised water on an 11MUD modified silicon wafer.

There is a similar trend for the silanisation of silicon wafers, however the deviation between the calculated and measured angles is larger in this case. It is believed that this is due to the poorer packing of the silanes onto the silicon when compared with the thiol packing on gold. A looser packing would result in a surface with exposed methylene groups interwoven amongst regions of closely packed silanes, with no control over the packing and thus its influences on the contact angle. This is likely to vary from sample to sample, and even between regions on the same surface. The data relating to TMODS is shown in Figure 3-9 and is summarised for all silanes in Table 3-6.

Table 3-5 The measured static contact angle of thiol modified surfaces and the comparative calculated values as determined by (32). [13]

	Measured contact angle (°)	Standard deviation	Advancing angle (θ_A)	Receding angle (θ_R)	Calculated contact angle θ_R (°)
1ODT	94.3	2.02	103	88	93.90
1OT	94.5	2.49	96	86	90.33
2M2PT	69.7	2.79	81	59	67.54
2PT	63.1	2.38	78	55	63.89
3MPA	30.0	3.02	50	20	30.49
8M10	13.9	2.15	18	6	10.33
8MOA	34.8	0.98	43	30	35.67
11MUDA	31.1	1.62	45	20	29.26
11MUD	12.9	1.65	24	6	11.85

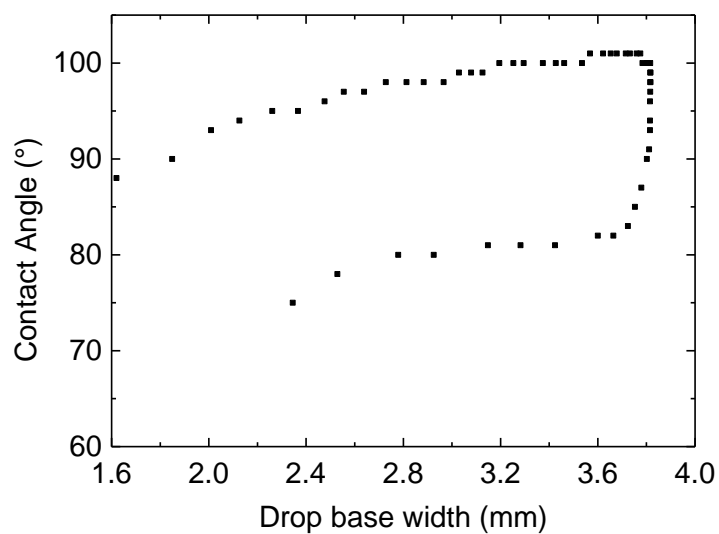


Figure 3-9 The advancing (θ_A) and receding (θ_R) contact angles of 15m Ω deionised water on an TMODS modified silicon wafer.

Table 3-6 The measured static contact angle of silane modified silicon wafers and the comparative calculated values as determined by (32). [13]

	Measured contact angle (°)	Standard deviation	Advancing angle (θ_A)	Receding angle (θ_R)	Calculated contact angle θ_R (°)
3APTMS	46.8	1.56	70	30	42.77
3GPTMS	34.3	1.92	53	21	31.99
ACRYLATE	53.2	1.00	62	50	55.32
HEXADECYL	94.5	1.10	95	78	94.53
M-3	44.9	2.95	68	18	30.55
PFO	100.8	2.39	113	91	98.29
t-BU	59.6	1.25	70	53	60.11
OCTYL	93.4	1.26	103	81	88.81
OCTADECYL	91.9	1.09	101	78	86.15

3.3.9 SEM comparison of Ebeam and DC sputter coating.

In order to investigate the directionality of the Ebeam and DC sputtering techniques, polystyrene (PS) particles were spin coated onto clean glass slides and exposed to 10 nm of chromium and 100 nm of gold coating by each technique. SEM images were collected to investigate whether the hemisphere of the particles would block areas on the slide surface. The results of the study are shown in Figure 3-10. It can be seen that a dark crescent encases one side of the particles, where a region of the substrate surface has not been coated by the evaporation process. As the 'T' shape rotates, the crescent surrounding the particles rotates at the same time, indicating that the feature is inherent within the sample and not an SEM artefact. The implication of this directionality suggests that substrates with highly textured surfaces may not be uniformly coated by the Ebeam evaporation method. The effect is also observable for 80 μm PS particles, as seen in Figure 3-11.

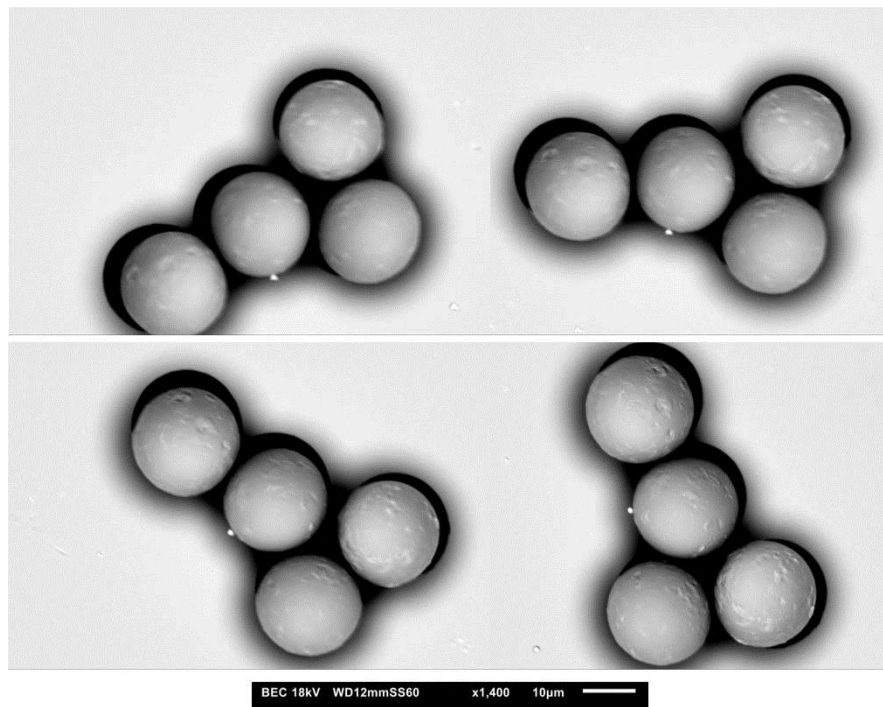


Figure 3-10 20 μm PS spheres coated via Ebeam evaporation (10 nm Cr, 100 nm Au)

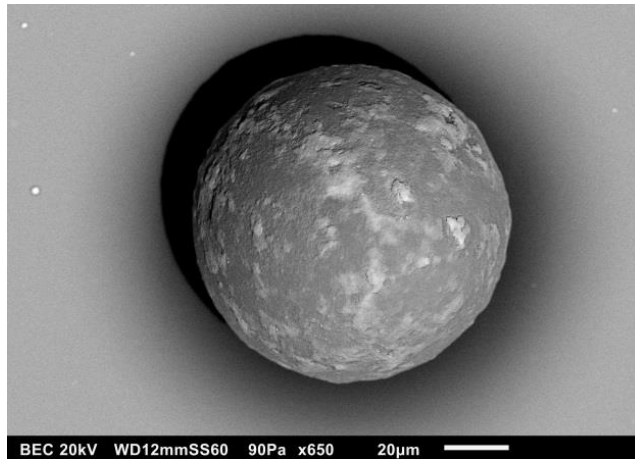


Figure 3-11 An 80 μm PS particle coated via Ebeam evaporation (10 nm Cr, 100 nm Au)

On the other hand, Figure 3-12 shows the effect of DC sputtering. No crescent shape is observed around the particle, indicating that the sputter process is less directional and more randomised than the Ebeam. The result is that sputter deposition should yield a more thorough coating than Ebeam. Both sets of images show a halo around the particle. It is suggested these halo effects are due to charging effects on or around the particles, as they disappear upon removal of the sphere, as seen in Figure 3-13.

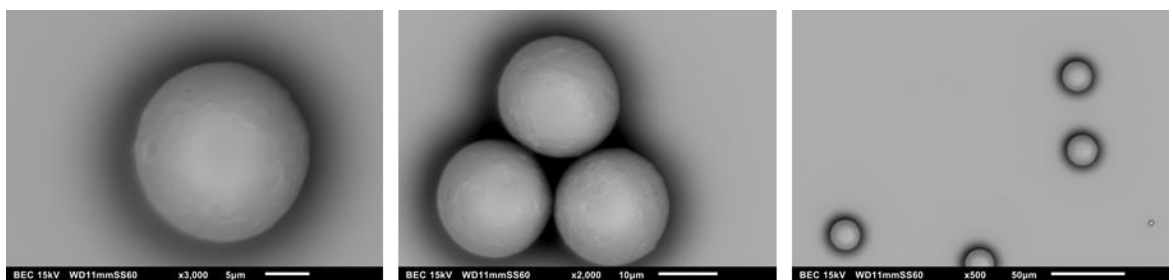


Figure 3-12 20 μm PS spheres coated via DC sputtering (10 nm Cr, 100 nm Au)

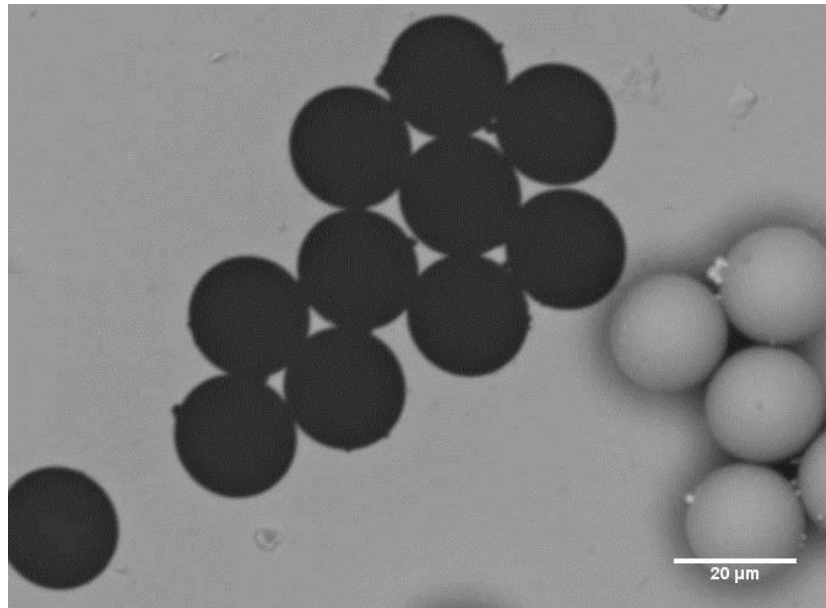


Figure 3-13 20 μm PS spheres coated via Ebeam evaporation (10 nm Cr, 100 nm Au). The dark areas are holes where particles were before removal post coating.

3.3.10 AFM comparison of substrates.

AFM data was taken of each substrate in an attempt to quantify the deviations in contact angle data. Si (100) test grade wafer with a polished coated side (PCS) and unpolished uncoated side (UUS), a Si (100) test grade wafer with a polished uncoated side (PUS) and rolled steel disks (RSD) were all investigated. Experiments were conducted with the help of Dr Andrew Parnell (Department of Physics and astronomy, Sheffield).

For reference the following studies were undertaken using the following wafers; piranha immersion time (3.3.2), solvent type (3.3.1), silane immersion time (3.3.3), effect of roughness (3.3.5) and the effect of PVD type (3.3.6) utilised (UUS) wafer in their study. Silane modification of a highly polished wafer (3.3.4) and contact angle hysteresis studies (3.3.8) utilised (PUS) wafer. The effect of roughness (3.3.5) and the effect of PVD type (3.3.6) also utilised (PCS) wafers. Finally studies on rolled steel (3.3.7) used (RSD) disks.

3.3.10.1 Polished coated wafer – effect of PVD type on roughness.

PCS wafer was examined as an uncoated, Ebeam coated and sputter coated sample set and the AFM data is shown in Figure 3-14. It can be seen that, in its uncoated form, the PCS wafer was very smooth with an average peak height of just 1.61 nm and RMS of 0.68 nm. Coating by Ebeam evaporation (10 nm Cr, 100 nm Au) leads to a slight, but negligible increase in the average peak height to 6.84 nm with an RMS of 1.80 nm. PCS wafer was also coated by DC sputtering as shown in Figure 3-15.

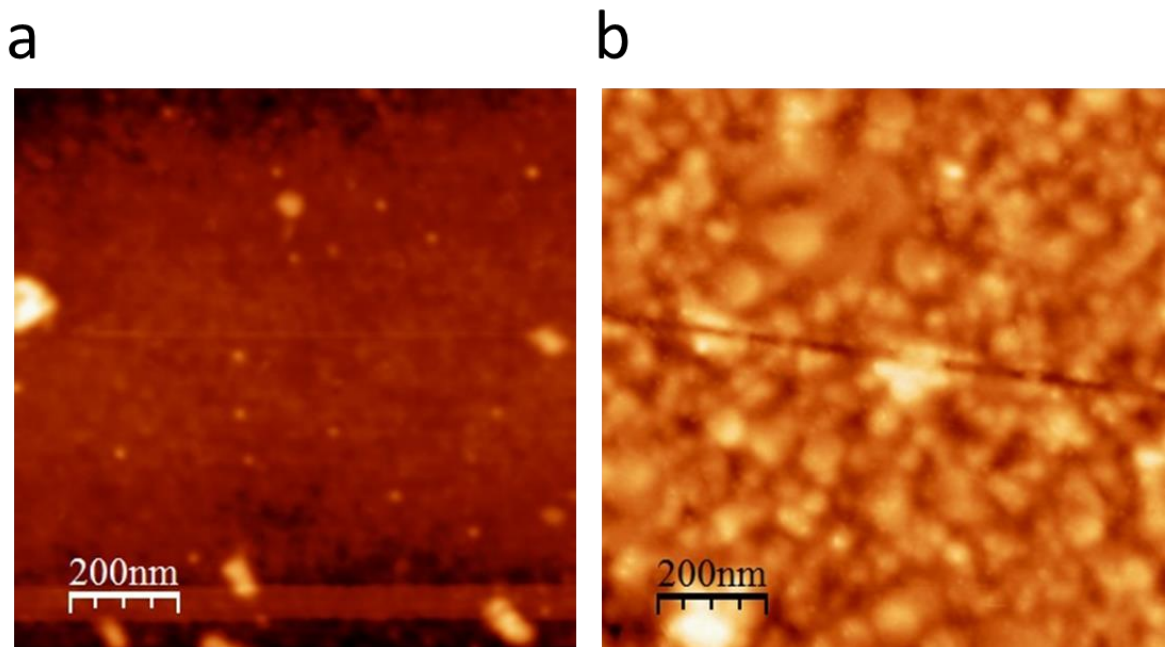


Figure 3-14 AFM images (1 μm x 1 μm) tapping mode of a) uncoated PCS wafer, max peak height 7.4 nm, an average peak height of 1.61 nm and an RMS of 0.68 nm. b) Ebeam coated (10 nm CR, 100 nm Au) PCS wafer, max peak height 10.29 nm, an average peak height of 6.84 nm and an RMS of 1.80 nm

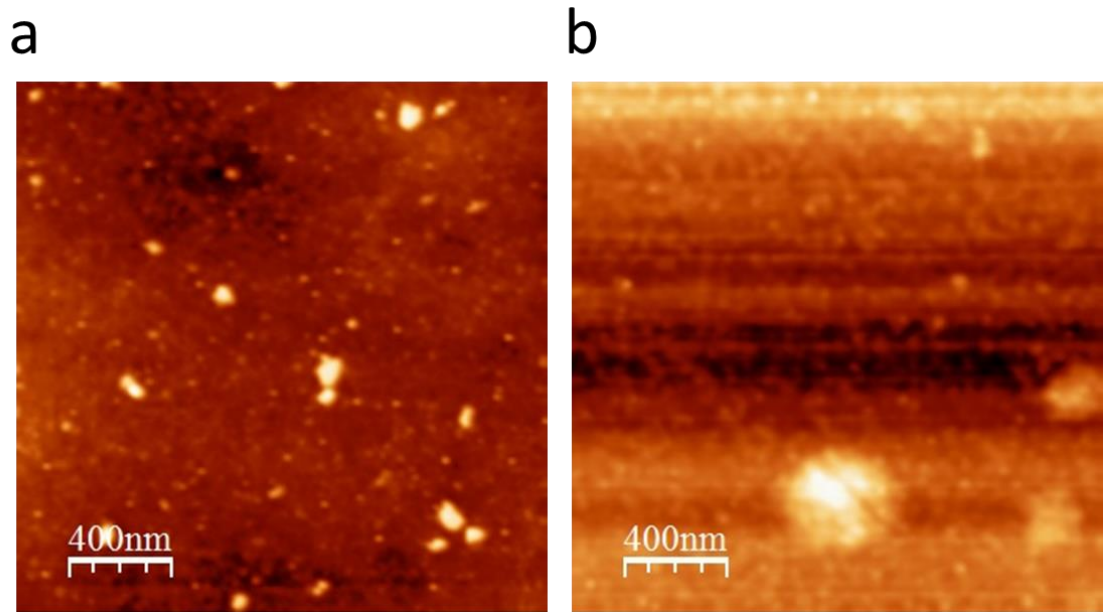


Figure 3-15 AFM images (2 μm x 2 μm) tapping mode of a) uncoated PCS wafer, max peak height 6.67 nm, an average peak height of 1.47 nm and an RMS of 0.60 nm. b) sputter coated (10 nm CR, 100 nm Au) PCS wafer, max peak height 17.49 nm, an average peak height of 2.70 nm and an RMS of 1.90 nm.

As previously observed the PCS wafer is inherently smooth with an average peak height of 1.47 nm and an RMS of 0.60 nm in this case. Modification by sputter coating leads to a very slight increase to 2.70 nm and 1.90 nm respectively. This is even less than the Ebeam sample, although there is a considerable possibility this is due to substrate variations.

UUS wafer was also examined as in Figure 3-16. The unpolished wafer can be seen to have elevated roughness of around 180 nm. Interestingly, the deposition of metals reduces this roughness significantly, by around 20 nm for Ebeam and 60 nm for sputtering. One possible reason for this is the surface mobility of the deposited metal, which acts to reduce roughness by filling concavities in the surface. [15] In addition, at relatively large values of thickness, the surface becomes more continuous and thus the defects become less prevalent. Surface mobility is influenced by many parameters such as the kinetic energy of the incident species, the sticking coefficient of the substrate and the deposited species, the deposition rate

and the temperature, to name but a few. It has been extensively reported that the average energy of sputtered neutral atoms is much greater than the energy of evaporated material. [16-19] As a result, the sputtered material has extra energy upon deposition to allow migration over the surface and facilitate the formation of larger grains, lowering the overall roughness of the surface. [15]

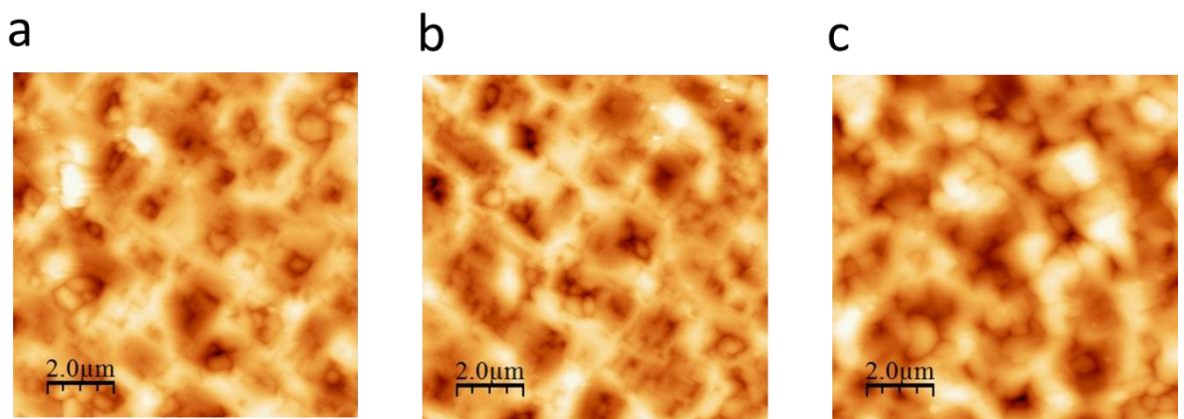


Figure 3-16 AFM images ($10\ \mu\text{m} \times 10\ \mu\text{m}$) tapping mode of a) uncoated UUS wafer, max peak height 177.35 nm, an average peak height of 149.29 nm and an RMS of 40.56 nm. b) Ebeam coated (10 nm CR, 100 nm Au) UUSS wafer, max peak height 151.40 nm, an average peak height of 130.48 nm and an RMS of 37.40 nm. c) sputter coated (10 nm CR, 100 nm Au) UUS wafer, max peak height 120.84 nm, an average peak height of 118.8 nm and an RMS of 33.82 nm.

UUS wafer was subjected to a Piranha clean before coating and collection of AFM data as shown in Figure 3-17. There is no significant difference between the piranha cleaned and non-piranha cleaned samples. However, once again the coating of the substrate by both Ebeam and sputtering leads to decreased roughness.

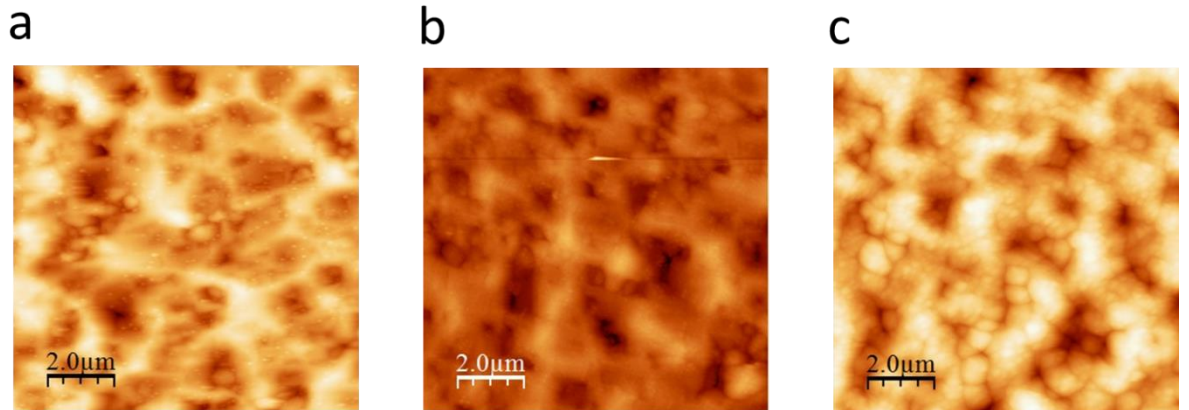


Figure 3-17 AFM images (10 μm x 10 μm) tapping mode of a) uncoated UUS wafer, max peak height 184.51 nm, an average peak height of 179.03 nm and an RMS of 41.18 nm. b) Ebeam coated (10 nm CR, 100 nm Au) UUS wafer, max peak height 151.39 nm, an average peak height of 128.98 nm and an RMS of 35.04 nm. c) sputter coated (10 nm CR, 100 nm Au) UUS wafer, max peak height 138.25 nm, an average peak height of 104.85 nm and an RMS of 33.18 nm.

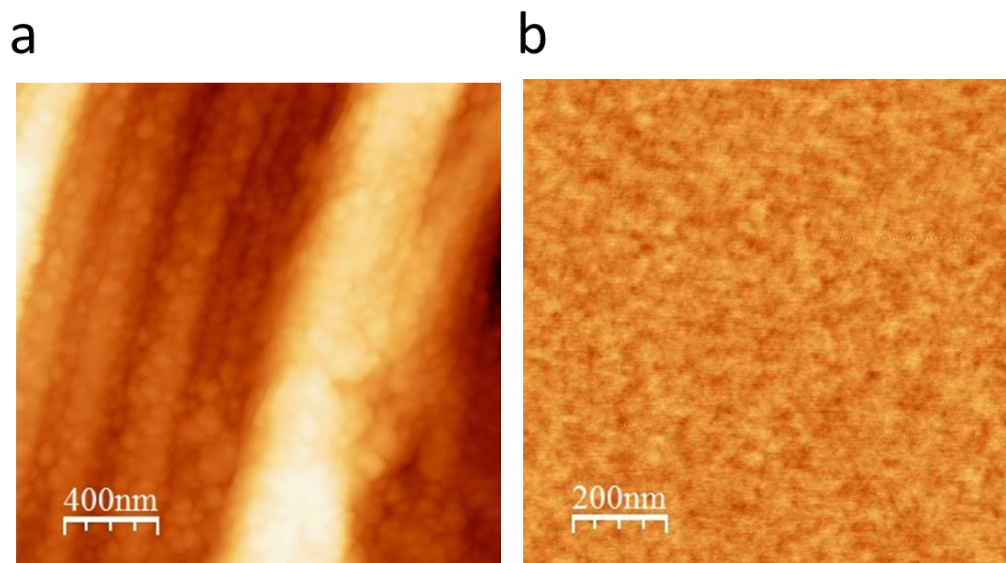


Figure 3-18 a) AFM image (1 μm x 1 μm) tapping mode of a RSD, max peak height 181.90 nm, an average peak height of 114.06 nm and an RMS of 52.37 nm. b) AFM image (2 μm x 2 μm) tapping mode of PUS wafer, max peak height 2.88 nm, an average peak height of 0.99 nm and an RMS of 0.24 nm.

The projected surface area of the PUS wafer was estimated to be just 0.759% larger than the ideal geometric surface area, thus leading to a roughness factor of 1.008 according to

the definition provided by Wenzel. [1, 2] Referring to Table 3-5, the observed angle for a 1ODT modified wafer is 94.31° . Applying the roughness factor of 1.00759 and calculating for the expected Young's angle, a value of 94.27° is found. This varies from the 93.90° calculated via the hysteresis argument of Tadmor and thus it seems likely that the droplet exists in a Cassie-Baxter state, where the fraction of the surface that is wet by the water is unknown. As a result, a theoretical Young's angle cannot be calculated due to the heterogeneity of the surface.

3.4 Conclusions.

Surface modification was carried out via a number of routes under various conditions. The first observation is that solvent choice is key to producing well ordered silane self-assembled monolayers. From the study carried out, it was found that heptane generated the most ordered SAMs (based on contact angle measurements), with both ethanol and methanol yielding SAMs that deviated significantly from the expected values, particularly where aliphatic silanes were concerned.

The effect of piranha immersion time on SAM formation was also investigated. No consistent pattern was observed by varying the immersion time between an hour and 6 hours.

Extended immersion time in silane solutions after cleaning leads to an increase in contact angle for all of the silanes studied. It is believed that increased immersion time can lead to multilayer build up, which is particularly prevalent for the more polar silanes. It is therefore deemed that samples should be removed from solution after no more than 24 hours to minimise the detrimental effects observed. However, it is possible to remove these multilayers by thorough rinsing and sonication.

It was shown by AFM studies that the PVD of chrome/ gold by both Ebeam and sputtering reduces the apparent surface roughness of silicon wafers. Sputtering appears to reduce the roughness more than Ebeam, although both techniques yield SAMs with similar wettabilities. In addition, it has been shown by SEM studies that the Ebeam evaporation can be shadowed by large surface features, creating regions of exposed, uncoated surface.

The relationship between the measured advancing and receding contact angle has been shown to yield a calculated static angle in good agreement with the measured static angle based on the work of Tadmor [13] and Chibowski. [14] The closeness of fit between the measured and calculated values is greater for the thiol modified surfaces than the silane modified ones, probably due to the tighter packing of the thiol SAM.

A broad range of contact angles have been shown to be accessible by the various surface modification techniques outlined. These coating mechanisms have been optimised and various aspects of the process such as solvent type, immersion time and cleaning method have been shown to influence SAM formation to varying degrees. Utilising this knowledge, the following chapters will show how these modification techniques can be used to effect bubble size, first under steady flow and then under oscillating flow.

3.5 References.

- [1] R. N. Wenzel, "Resistance of solid surfaces to wetting by water," *Industrial & Engineering Chemistry*, vol. 28, pp. 988-994, 1936.
- [2] R. N. Wenzel, "Surface Roughness and Contact Angle," *The Journal of Physical Chemistry*, vol. 53, pp. 1466-1467, 1949.
- [3] A. Cassie and S. Baxter, "Wettability of porous surfaces," *Transactions of the Faraday Society*, vol. 40, pp. 546-551, 1944.
- [4] A. Cassie, "Contact angles," *Discussions of the Faraday Society*, vol. 3, pp. 11-16, 1948.
- [5] A. K. Chauhan, D. K. Aswal, S. P. Koiry, S. K. Gupta, J. V. Yakhmi, C. Sürgers, D. Guerin, S. Lenfant, and D. Vuillaume, "Self-assembly of the 3-aminopropyltrimethoxysilane multilayers on Si and hysteretic current-voltage characteristics," *Applied Physics A*, vol. 90, pp. 581-589, 2008/03/01 2008.

- [6] C. D. Corso, A. Dickherber, and W. D. Hunt, "An investigation of antibody immobilization methods employing organosilanes on planar ZnO surfaces for biosensor applications," *Biosensors and Bioelectronics*, vol. 24, pp. 805-811, 2008.
- [7] D. Aswal, S. Lenfant, D. Guerin, J. Yakhmi, and D. Vuillaume, "Self assembled monolayers on silicon for molecular electronics," *Analytica chimica acta*, vol. 568, pp. 84-108, 2006.
- [8] N. Rozlosnik, M. C. Gerstenberg, and N. B. Larsen, "Effect of solvents and concentration on the formation of a self-assembled monolayer of octadecylsiloxane on silicon (001)," *Langmuir*, vol. 19, pp. 1182-1188, Feb 18 2003.
- [9] G. D. Yarnold, "The Hysteresis of the Angle of Contact of Mercury," *Proceedings of the Physical Society of London*, vol. 58, pp. 120-127, 1946.
- [10] S. J. Gregg, "Hysteresis of the Contact Angle," *Journal of Chemical Physics*, vol. 16, pp. 549-550, 1948.
- [11] Y. Yuan and T. R. Lee, "Contact angle and wetting properties," in *Surface science techniques*, ed: Springer, 2013, pp. 3-34.
- [12] W. Possart and H. Kamusewitz, "Wetting and scanning force microscopy on rough polymer surfaces: Wenzel's roughness factor and the thermodynamic contact angle," *Applied Physics A: Materials Science & Processing*, vol. 76, pp. 899-902, 2003.
- [13] R. Tadmor, "Line energy and the relation between advancing, receding, and young contact angles," *Langmuir*, vol. 20, pp. 7659-7664, 2004.
- [14] E. Chibowski and K. Terpilowski, "Surface free energy of sulfur—Revisited: I. Yellow and orange samples solidified against glass surface," *Journal of Colloid and Interface Science*, vol. 319, pp. 505-513, 2008.
- [15] K. Wasa and S. Hayakawa, "Handbook of Sputter Deposition Technology: Principles, Technology, and Applications (Park Ridge: Noyes), 1992.
- [16] K. Wasa, T. Tohda, Y. Kasahara, and S. Hayakawa, "Highly-reliable temperature sensor using rf-sputtered SiC thin film," *Review of Scientific Instruments*, vol. 50, pp. 1084-1088, 1979.
- [17] K. Wasa and S. Hayakawa, "Reactively sputtered titanium resistors, capacitors and rectifiers for microcircuits," *Microelectronics Reliability*, vol. 6, pp. 213-221, 1967.
- [18] P. Srivastava, V. Vankar, and K. Chopra, "High rate reactive magnetron sputtered tungsten carbide films," *Journal of Vacuum Science & Technology A*, vol. 3, pp. 2129-2134, 1985.
- [19] P. Srivastava, T. Rao, V. Vankar, and K. Chopra, "Synthesis of tungsten carbide films by rf magnetron sputtering," *Journal of Vacuum Science & Technology A*, vol. 2, pp. 1261-1265, 1984.

Chapter 4: Bubbling under steady flow.

The production of microbubbles is of great interest industrially with numerous applications and potential applications in a wide range of areas. Bubble formation from a submerged orifice is highly complex, with many factors influencing the formation process. Many of these factors are interlinked and have been studied to various extents in the literature. Surprisingly however, there is relatively little data surrounding the role of surface chemistry on bubble formation. Several groups [1-4] have begun to investigate the area, but this chapter hopes to expand this work and provide a more thorough, rigorous examination of the role of surface chemistry effects on bubble formation under steady flow.

4.1 Experimental.

4.1.1 Preparation of controlled pore, rolled stainless steel disks.

70 μm thick rolled stainless steel disks (25 mm diameter) with photoetched holes of 250 μm diameters were obtained from Photofabrication services, St Neots, UK. A single pore was etched through the centre to create the 'single pore' disks. A pattern of 7 holes was etched through the disks to give a central hole with a hexagonal group of holes surrounding it, with centre to centre distance of 2.25 mm between all adjacent holes as in Figure 2-4. This diffuser acted as a pseudo multi pore system and allowed a level of control to assist understanding.

The disks were rinsed with acetone and ethanol to remove contaminants before being placed into a Diener Zepto plasma cleaner. A vacuum was applied for 10 minutes

before the introduction of oxygen gas at 1 barg pressure for a further 5 minutes. After this time the generator was turned on and a plasma was struck. The disks were left in the plasma for 5 minutes to remove all organic contaminants. The clean dry disks were then placed into a Moorfield minilab 080 for coating.

The disks were coated by DC sputtering as follows. The base pressure of the chamber was taken to $<1 \times 10^{-9}$ bar before argon (Ar) was introduced to re-pressurise to 6.5×10^{-6} bar. Once the pressure stabilised, it was maintained for 5 minutes before a base layer of Cr (10 nm) was added (0.163 A, 301.4 V, rate: 0.18 \AA/s). After chromium deposition, the chamber was maintained at constant pressure for 5 minutes before the deposition of gold (100 nm) was carried out (0.118 A, 362 V, rate: 0.47 \AA/s).

Thiol solutions (50 mL, 3 mM) were made using ethanol that was degassed under a steady stream of nitrogen for 30 minutes before use. Freshly coated disks were placed into the solutions and immediately sealed. The gold coated disks were left in solution for 18 hours before removal. Upon removal they were washed with a copious volume of ethanol (100 mL) before drying under a constant stream of nitrogen.

4.1.2 Preparation of steel sinters.

Sintered steel disks (25 mm Diameter, 3 mm thick) were obtained from Hengko technology co. Ltd (Shenzhen City, China) with a random array of 5 \mu m pores, Figure 2-4. The sinters were soaked in acetone overnight and then rinsed with acetone and ethanol to remove manufacturing grease/ contaminants before being placed into a vacuum oven at $80 \text{ }^\circ\text{C}$ for 24 hours to ensure drying. The sinters were then placed into a Diener Zepto plasma cleaner. A vacuum was applied for 10 minutes before the introduction of oxygen

gas at 1 barg pressure for a further 5 minutes. After this time the generator was turned on and a plasma was struck. The disks were left in the plasma for 5 minutes to remove all organic contaminants. The clean dry disks were then placed into a Moorfield minilab 080 for coating.

The sinters were coated by DC sputtering with a base pressure of $<1 \times 10^{-9}$ bar before argon (Ar) was introduced to re-pressurise to 6.0×10^{-6} bar. Once the pressure stabilised, it was maintained for 5 minutes before a base layer of Cr (10 nm) was added (0.158 A, 282 V, rate: 0.14 \AA/s). After chromium deposition, the chamber was maintained at constant pressure for 5 minutes before the deposition of gold (100 nm) was carried out (0.118 A, 359 V, rate: 0.45 \AA/s).

Thiol solutions (50 mL, 3 mM) were made using ethanol that was degassed under a steady stream of nitrogen for 30 minutes before use. Freshly coated sinters were placed into the solutions and immediately sealed. The gold coated sinters were left in solution for 18 hours before removal. Upon removal they were washed with a copious volume of ethanol (100 mL) before drying under a constant stream of nitrogen.

4.1.3 Preparation of pointfour ceramic diffusers.

Pointfour™ Micro Bubble Diffuser plate was obtained from Pentair Aquatic eco-systems (Apopka, FL, USA) and cut into 25 mm diameter disks with a thickness of 3 mm. A sample was submitted to the Sheffield Surface Analysis Centre for X-ray Photoelectron Spectroscopy (XPS) studies. A sample of porous aluminium oxide sold by Sigma Aldrich (CAS: 1344-28-1) was submitted for comparison.

Chapter 4: Bubbling under steady flow.

The diffusers were soaked in acetone overnight and then rinsed with acetone and ethanol to remove manufacturing grease/ contaminants before being placed into a vacuum oven at 80 °C for 24 hours to ensure drying. The sinters were then placed into a Diener Zepto plasma cleaner. A vacuum was applied for 10 minutes before the introduction of oxygen gas at 1 barg pressure for a further 5 minutes. After this time the generator was turned on and a plasma was struck. The disks were left in the plasma for 5 minutes to remove all organic contaminants.

One set of diffusers were coated by DC sputtering with a base pressure of $<1 \times 10^{-9}$ bar before argon (Ar) was introduced to re-pressurise to 6.0×10^{-6} bar. Once the pressure stabilised, it was maintained for 5 minutes before a base layer of Cr (10 nm) was added (0.158 A, 282 V, rate: 0.14 Å/s). After chromium deposition, the chamber was maintained at constant pressure for 5 minutes before the deposition of gold (100 nm) was carried out (0.118 A, 359 V, rate: 0.45 Å/s).

A second set of diffusers were coated by electron beam evaporation (Ebeam) as detailed. The base pressure of the chamber was taken to $<1 \times 10^{-9}$ bar and evaporation was carried out. First, a chromium adhesion layer was added to the diffuser at a 10 nm thickness (4 mA, 10 kV, rate: 0.15 Å/s) followed by a 100 nm gold layer (44 mA, 10 kV, rate: 2.4 Å/s).

Thiol solutions (50 mL, 3 mM) were made using ethanol that was degassed under a steady stream of nitrogen for 30 minutes before use. Freshly coated disks were placed into the solutions and immediately sealed. The gold coated disks were left in solution for 18 hours before removal. Upon removal they were washed with a copious volume of ethanol (100 mL) before drying under a constant stream of nitrogen.

A third set of clean dry diffusers were immersed in silane solutions (50 mL heptane, 3 mM) for 24 hours under ambient conditions before removal. Upon removal, each piece was rinsed with the parent solvent before being immersed in 50 mL of fresh solvent and placed in an ultrasonic bath for 30 seconds at 25 °C to remove physically adsorbed layers. A final rinse with further fresh solvent and drying by a stream of nitrogen followed before samples were left in an oven at 45 °C for 2 hours to remove residual solvent.

4.1.4 Bubbling under steady flow.

Compressed air (2 barg) was fed to a Bronkhorst EL series F-201CV mass flow controller. Flow rate was controlled by FlowDDE and Flowview software of Bronkhorst.

Bubbles were generated into a tank built by the user with a water volume of 45x30x10 cm (WxHxD) filled with 15 M Ω -cm deionised water (Elga Purelab Option S-R filtration system). The antechamber below the pore had a volume of 30 cm³ back to the first restriction point, which was the Bronkhorst mass flow controller.

Videos for bubble size analysis was captured using a Mikrottron MC1363 Eosens camera with a 22.9 mm CMOS chip (14 μ m square pixel size) at a resolution of 1280x1024 pixels and 30 fps. Post capture analysis was carried out using LabVIEW software written by the author. Analysis was performed upon samples with n>1000 in general. The error reported is the error in the mean (95%) unless otherwise stated..

High speed video was captured using the same Mikrottron Eosens camera as above, but at a resolution of ca 280x410 pixels and frame rates of ca 4000 fps. Illumination was provided by an array of 7 Bridgelux BXRA-56C9000-J-00 high brightness LED's (cool white, 5600 K, 9000 lm).

4.2 Results and discussion.

4.2.1 Effect of surface chemistry on bubbles emitted from a single 250 μm pore.

Bubble formation from a single submerged orifice was investigated as a function of both surface chemistry and flow rate. Figure 4-1 shows the dependence of the bubble diameter on the contact angle of the surface modified by thiols at a constant gas flow rate. It can be seen that there is a clear difference between the contact angles below 90° , and those above it. The bubbles produced from the 1OT and 1ODT modified surfaces are around 150% larger than those formed from the other surfaces. This is in contrast with the work of Kukizaki [5, 6] and Yasuda [7] who stipulate that maintaining the contact angle at $<45^\circ$ is imperative to ensure the minimum bubble size is achieved. On the other hand, this data corroborates the theories of other authors [1-4, 8] who have suggested the importance of the 90° angle. This is likely to be due to the increased gas-solid interaction for the hydrophobic surfaces which leads to the increase in adhesion of the growing bubble. The bubble must grow to a larger size in order for buoyancy to break it from the surface. The 1OT modified surface allows the gas to spread over a significant surface area, whereas the more hydrophilic 2M2PT and 11MUD restrict the bubble to the pore as shown in Figure 4-3.

Interestingly, there is no dependence on contact angle within the two regions separated by the $\theta = 90^\circ$ boundary. It may be expected that increasing contact angle would lead to an increase in bubble size throughout the entire range of wettabilities. However, there appears to be no trend within the two regions, i.e. 1ODT yields smaller bubbles than 1OT despite its larger contact angle. Similarly, the 2M2PT generated surface yields bubbles

of a similar size to the 11MUD modified surface, despite the angle being more than four times greater.

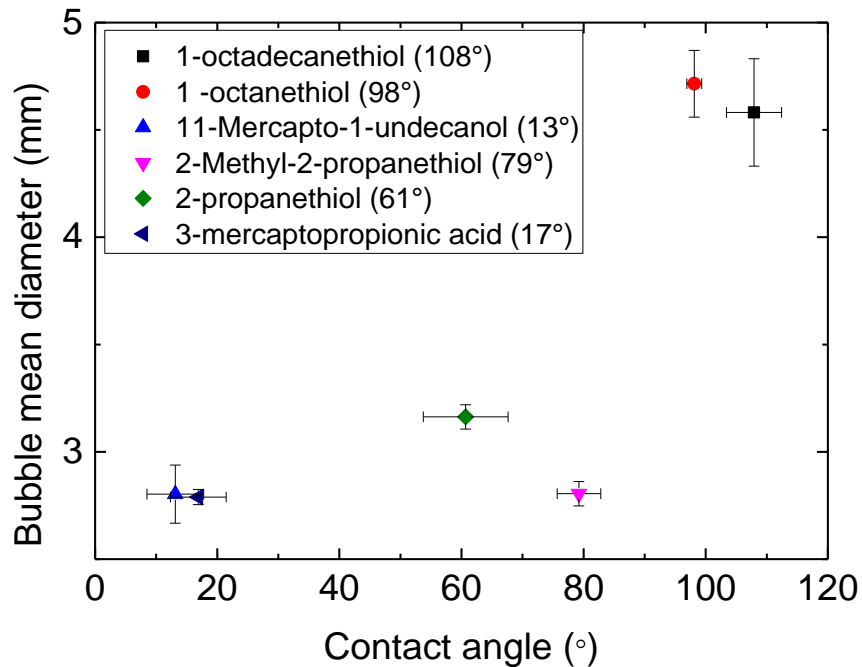


Figure 4-1 The dependence of bubble diameter on the contact angle of the surface at a flow rate of 2.5 mL/min through a 250 μm diameter single pore.

It can be seen from Figure 4-2 that a similar trend is apparent over many flow rates. There is an apparent switching at 90° , with bubbles created from surfaces with $\theta < 90^\circ$ being significantly smaller than those with $\theta > 90^\circ$. Is it also apparent that bubbles in the hydrophilic region have a significantly lower deviation from the mean size. On the other hand, large bubbles generated from the 1OT and 1ODT surfaces oscillate significantly, leading to a randomised break up process and larger deviation. In addition, large bubbles have a greater rise velocity than small bubbles. As a result, large bubbles quickly catch smaller bubbles during the rise process and may result in coalescence, also adding to the size randomisation. Smaller bubbles are much more stable and as such have less oscillation

meaning that these bubbles break apart less, leading to the less polydisperse nature of the bubble cloud produced. In addition, for bubbles created from a surface with $\theta < 90^\circ$ an increase in flow rate leads to a slight increase in bubble size. This is a commonly accepted theory, except at very low or very high flow rates. [9-17]

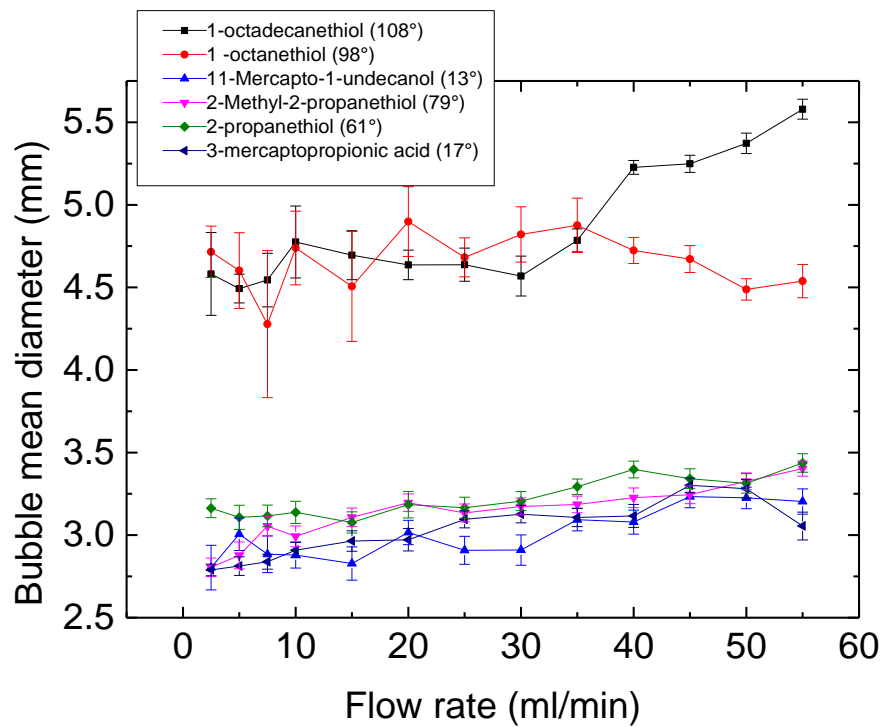


Figure 4-2 The dependence of bubble diameter on the contact angle of the surface at various flow rates, through a 250 μm diameter single pore.

The bubble detachment time varies significantly between the hydrophobic and hydrophilic surfaces. The length of time from the instant the bubble cap is observed to grow until the instant the neck is broken is 0.075 s for a 10T coated surface, whereas it decreases to 0.0125 s for a 2PT coated surface and further to 0.0075 s for 11MUD. It would therefore be logical to expect the bubble size to follow the same trend. However, as previously discussed, this is not the case. The reason for the deviation is likely to be coalescence. As discussed by Xie in the

context of pore size, [18] smaller bubbles detach and cause a smaller pressure drop across the pore than large bubble detachment. The result is that a second bubble can form very quickly after the first, increasing the likelihood of coalescence, as seen in Figure 4-4. The net result is that the apparent size difference between hydrophobic surfaces ($\theta > 90^\circ$) and hydrophilic ones ($\theta < 90^\circ$) is reduced. Also, the small difference in retention time at the surface is negated by this coalescence, leading to the random nature of bubbles formed from hydrophilic surfaces. ^{a,b}

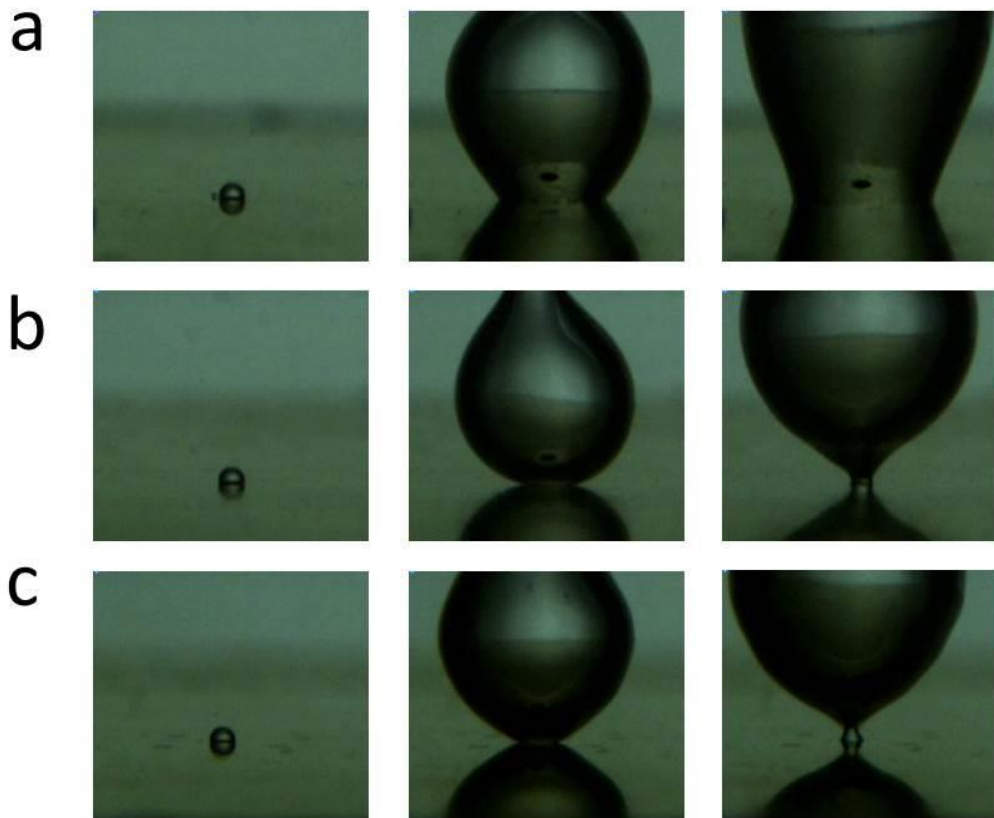


Figure 4-3 Bubble formation from a single 250 μm pore with a) 10T modified surface, b) 2M2PT modified surface, c) 11MUD modified surface.

^a <https://youtu.be/PhFQHjyP1il>

^b <https://youtu.be/jflrAelZYIY>

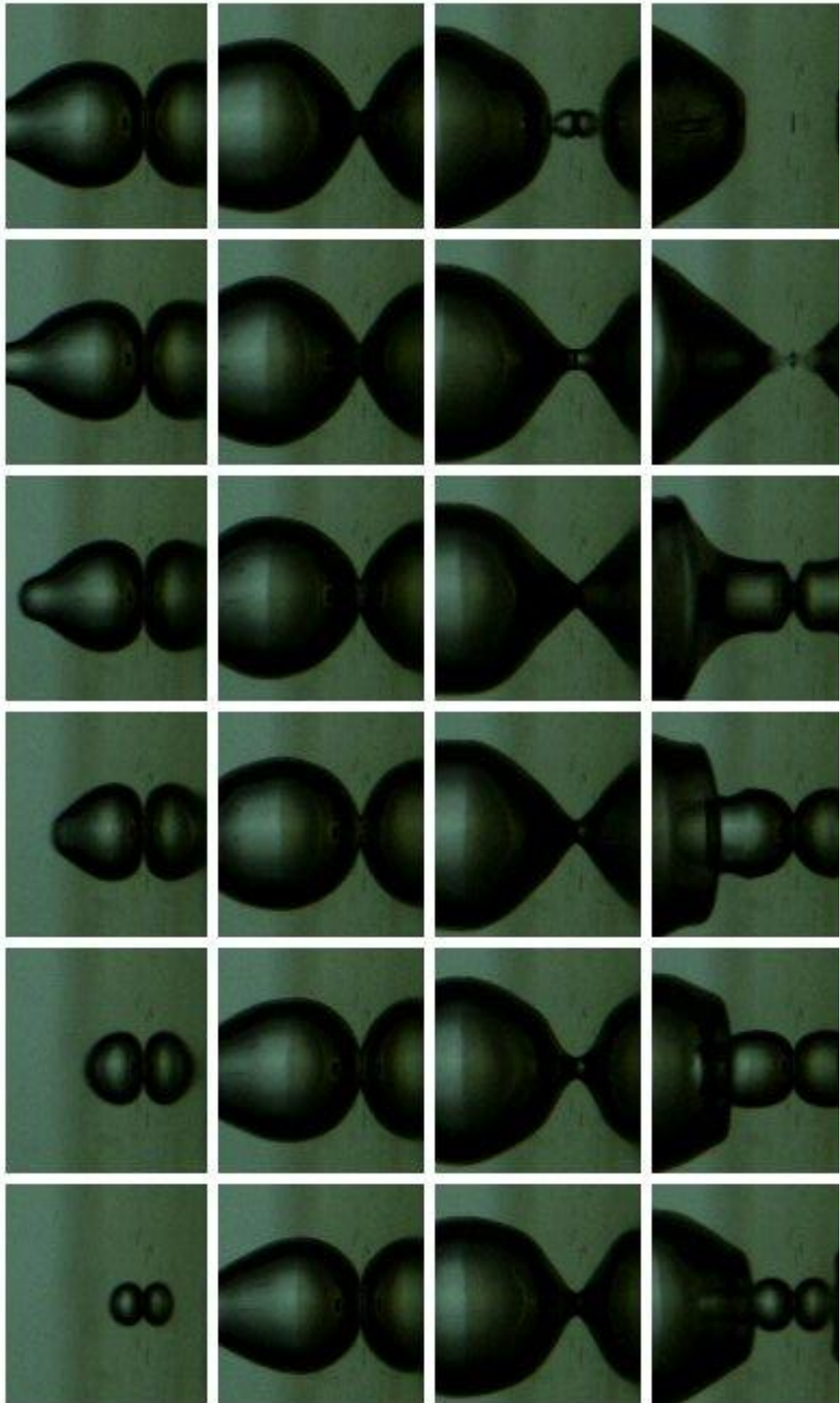


Figure 4-4 Bubble coalescence from a single 250 μm pore in an 11MUD modified surface.

4.2.2 Effect of surface chemistry on bubbles emitted from an array of 250 μm pores.

The effect of surface chemistry on bubble size from 7 equally sized pores is the same as that observed for a single pore. An apparent switching at 90° is seen, with the effect from 7 pores more exaggerated than that observed from a single pore. The bubbles from the surfaces with $\theta < 90^\circ$ are smaller for the 7 pore system than those formed from a single pore, whereas those emitted from a surface with $\theta > 90^\circ$ are larger for the 7 pore system. The effect is shown in Figure 4-6.

As is the case with a single pore, the 1ODT and 1OT coated surfaces allow the bubble base to grow outwards from the pore and across the surface, past the outermost edges of the orifices, which increases adhesion and allows the bubble to grow to greater size. During this process all 7 pores are encompassed within the bubble base area, and as a result the bubble is fed by every pore, as outlined schematically in Figure 1-7 and experimentally in Figure 4-5a. However, the bubble detachment time is decreased slightly, to around 0.056 s compared to the 0.075 s observed for the single pore.

Once again the problem of coalescence is prevalent with the 2PT and 11MUD coated surfaces. As can be seen from Figure 4-5 the 2PT bubbles grow and coalesce with neighbours while still attached at the pore. The 11MUD on the other hand detaches and then coalesces close to the diffuser plate. These coalescence processes add a random nature to the system once again, thus leading to the crossover observed within the hydrophilic region and apparent lack of trend therein. This process illustrates the importance of both diffuser and antechamber design. In order to reduce the probability of coalescence, it is hypothesised that the

diffuser must be designed with the orifice-orifice distance greater than the bubble diameter formed from an equivalent single pore. Assuming vertical rise, the bubbles will then be produced at large enough distances to not coalesce at the plate, or above it. Of course effects such as turbulence and drag will influence subsequent bubble formation, leading to the potential occurrence of coalescence, even at large pore separation. In addition, the antechamber must be designed to ensure the even spread of airflow through all orifices. As can be seen from the first images Figure 4-5a and Figure 4-5c, the 10T and 11MUD surfaces yield bubbles from only one of the 7 pores during the initial stage of growth, as indicated by the schematic shown in Figure 1-7. More pores become active during the latter stages of growth, but concerted effort to alleviate the effect should lead to an observed reduction in bubble size from surfaces with $\theta < 90^\circ$.

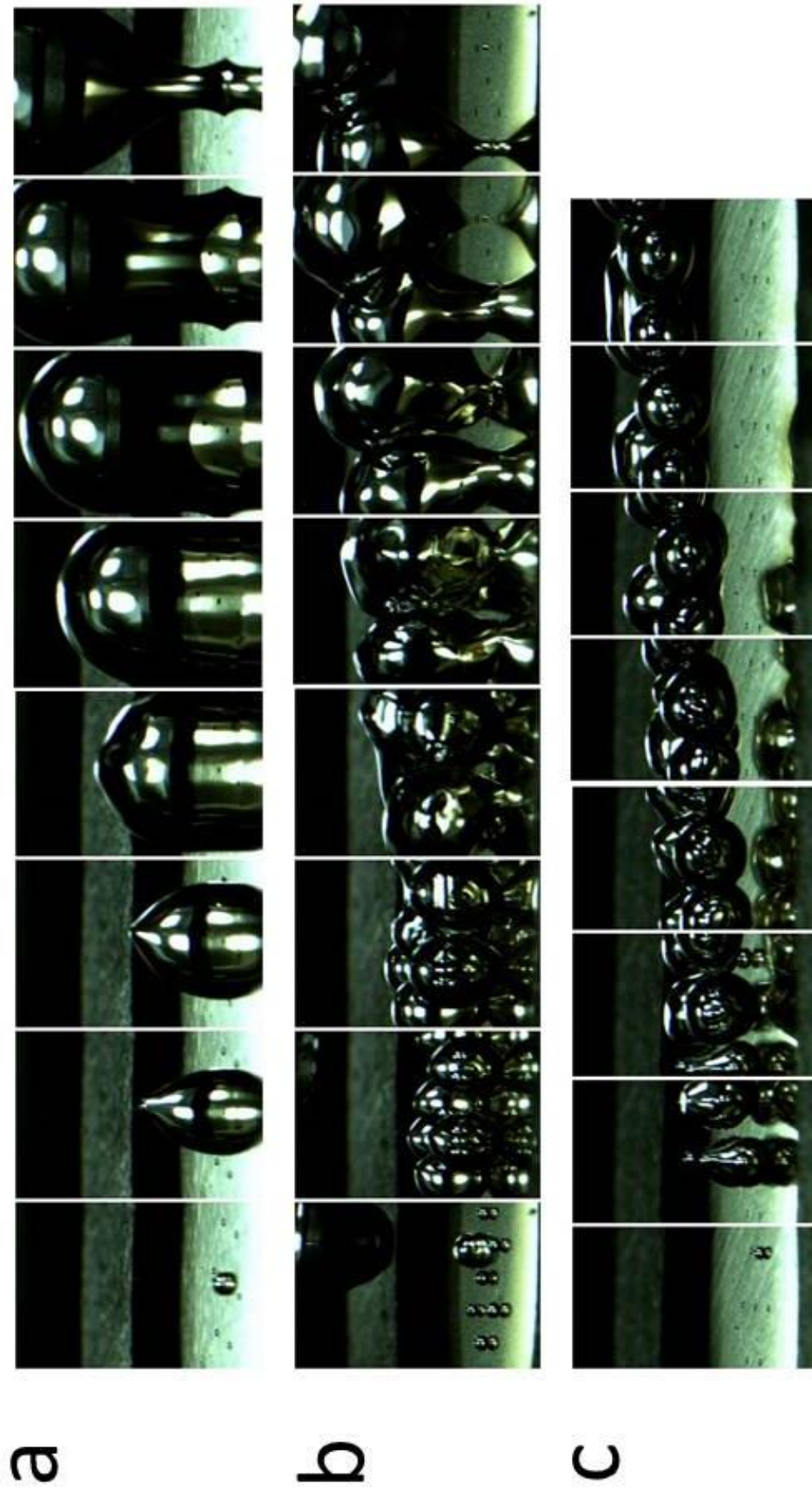


Figure 4-5 High speed images of bubble formation from 7 250 μm pores modified with; a) 10T b) 2PT c) 11MUD.

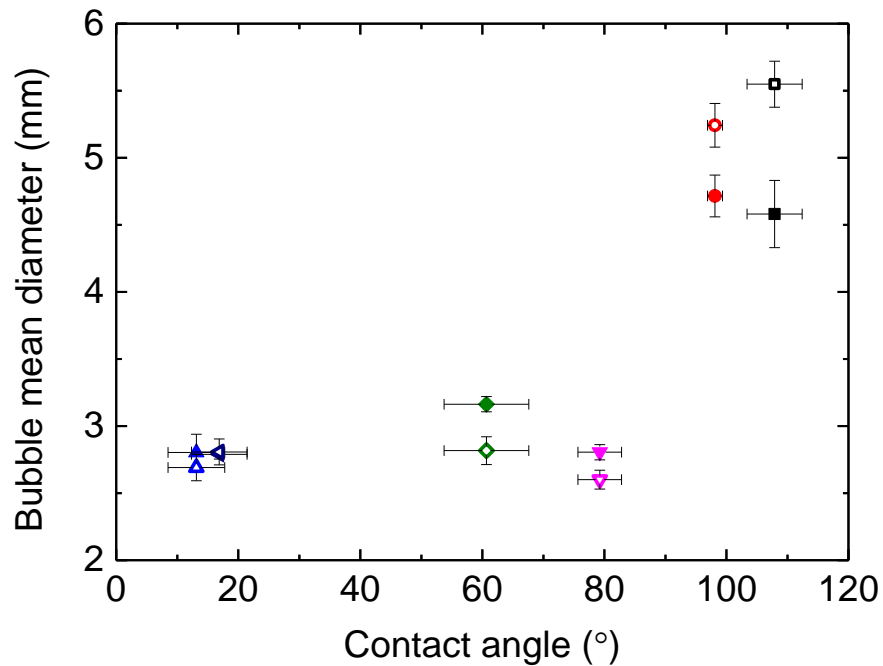


Figure 4-6 The effect of surface chemistry on bubble formation from multiple 250 μm pores compared to a single pore, at a flow rate of 2.5 mL/min. ■ 1ODT single pore □ 1ODT multi pore ● 10T single pore ○ 10T multi pore ▲ 11MUD single pore △ 11MUD multi pore ▼ 2M2PT single pore ▽ 2M2PT multi pore ◆ 2PT single pore ◇ 2PT multi pore ◀ 3MPA single pore ◁ 3MPA multi pore

The effect of flow rate on bubble formation from 7 pores is shown in Figure 4-7. The switch at $\theta=90^\circ$ is apparent once again. However, the average bubble size does not increase with increasing flow rate. According to the work by Xie [1], bubble formation progresses through several stages according to flow rate. At low flow (<150 mL/min), bubbles exist in a synchronous formation region from two equal pores. During this region, bubbles form simultaneously and exit in pairs with a constant period. It therefore follows that hydrophilic surfaces at low flow rates undergo bubbling in this synchronous regime, and as a result, bubble size is dictated by the relationship between the pore size and the gas flow rate.

In addition, it is apparent from high speed video captured that, for hydrophilic surfaces, the time between subsequent bubble emission from 7 pores is greatly increased compared to single pore emission. An increase of 2.5x is seen for a 2PT coated surface, whereas a 4x increase is seen for 11MUD modified surfaces. Longer time periods between bubble pulses allow the previous group to leave the vicinity of the diffuser plate, thus avoiding the immediate coalescence seen in Figure 4-5. Increasing flow rates through a single pore acts to reduce the time period between bubble emissions and thus increases the coalescence occurring a short distance from the pore, with various modes occurring as described in section 1.4.6. Similarly, increasing the flow rate through 7 pores will also reduce the time period between bubble clusters. However, the increase is split between multiple pores, and so the increase in coalescence will be observed at a higher flow rate, above the range tested in this investigation.^{c,d}

^c https://youtu.be/610A-qO_oew

^d <https://youtu.be/IgMOPd9yTal>

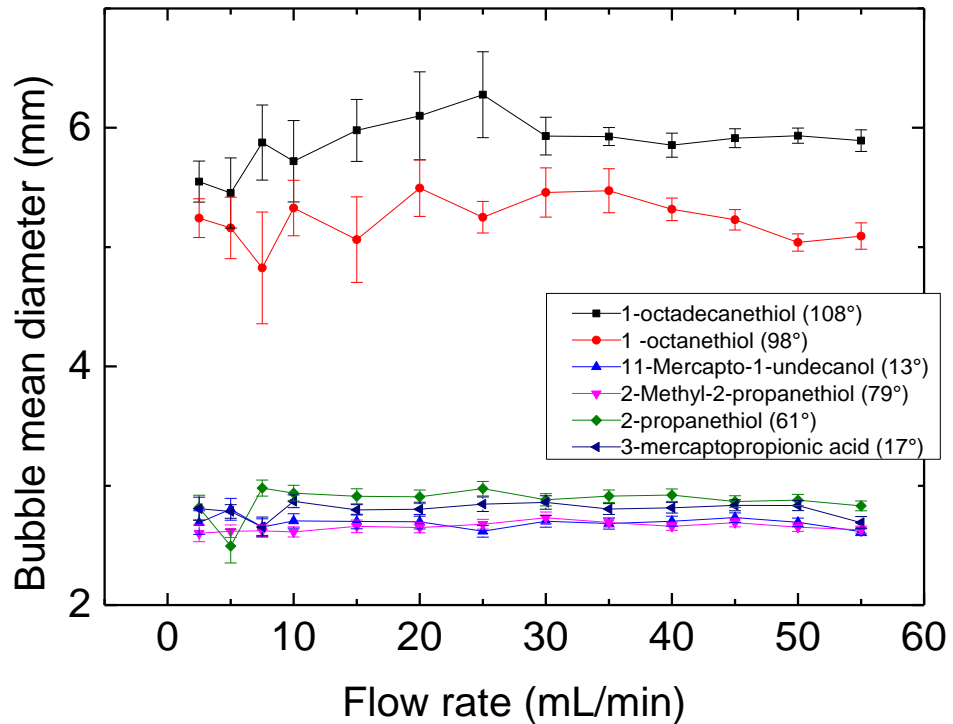


Figure 4-7 The dependence of bubble diameter on the contact angle of the surface at various flow rates, through an array of 7, 250 μm diameter pores.

4.2.3 Effect of surface chemistry on bubbles emitted from a steel sinter with 5 μm pores.

Progression to a steel sinter yields a more dramatic effect than both of the controlled pore systems outlined above and can be seen in Figure 4-8. It must be pointed out that due to the manufacturing of the steel sinters, the pores deviate from the circular, or to be more accurate cylindrical, shape of the controlled pore systems. An SEM image of a typical steel sinter is shown in Figure 4-9. Although the pores are randomised in nature, Clift [2] and Kumar [3] indicate that, at low flow rates, bubbles formed from both equisided shaped orifices (i.e a

regular hexagon) or those not far removed from circular have essentially the same volume as a corresponding circular orifice. Only at very high flow rates from considerably elongated pores or other such irregular geometries does the formed bubble volume deviate significantly from the circular orifice bubbles.

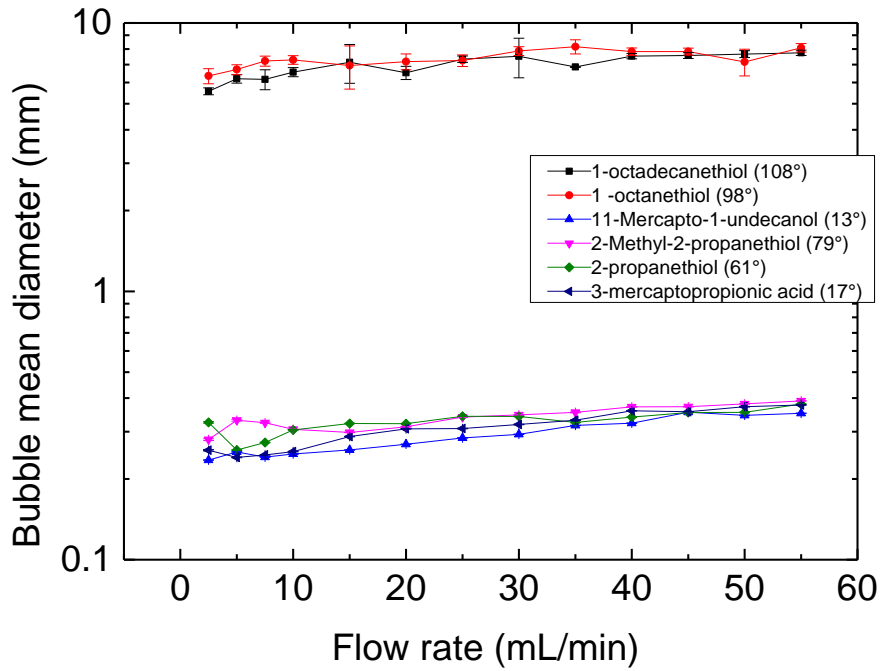


Figure 4-8 The dependence of bubble diameter on the contact angle of the surface at various flow rates, through a 3 mm thick sintered steel disk with a close packed array of 5 μm diameter pores.

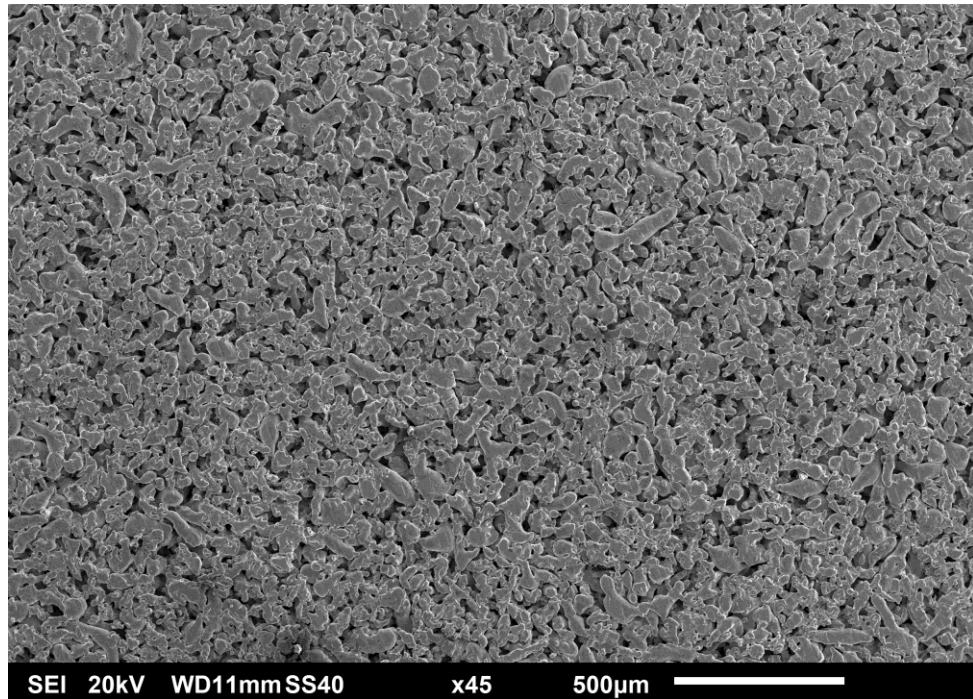


Figure 4-9 An SEM image of a steel sinter with mean pore diameter of $5.23 \mu\text{m} (\pm 3.03 \mu\text{m})$ and 9.8% porosity.

The size difference between the hydrophilic and hydrophobic regions is larger still in this system, with bubbles from the 1ODT and 1OT coated surfaces being around 18 times larger at low flow rates (2.5 mL/min), and 26 times larger at the higher flow rates (60 mL/min).

It is hypothesised that the increase in effect is due to the increase in surface roughness of the steel sinter, in comparison with the rolled steel disks. This randomised roughness leads to a pseudo Cassie-Baxter state, in which a surface with $\theta > 90^\circ$ traps air within the micro structure during bubble detachment. [4, 5] Removal of the air is energetically disfavoured, and as a result allows subsequent bubbles to readily spread across the surface before buoyancy effects cause it to detach. This spread over the roughened surface will add extra anchoring force, when compared with the ideal flat, homogeneous surface, and allow the bubble to grow to a larger volume. Detachment leaves a fraction of the total volume of air on the surface, and the process repeats. The reverse occurs for the surface with $\theta < 90^\circ$. Water penetrates the

microstructure readily and thus prevents air from the growing bubble from infiltrating the structure. This is the lotus leaf effect in reverse, and so the growing bubble is restricted to a single pore. As the pore size is so small within the sintered steel diffuser, the anchoring force is greatly reduced. Buoyancy quickly dominates; the bubble elongates and enters the detachment stage, where the neck is rapidly broken due to its implied narrowness. As a result, bubble size is restricted to a smaller size.

In addition, the steel sinter has large particle sizes with flat faces. These faces allow the formation of well-ordered regions of SAM. The inherent hydrophobicity of the steel sinter leads to the ability to entrap air within the structure but the micro structure allows gold coating to penetrate to a significant depth and thus the top portion of the surface may be modified to be hydrophilic. This in turn can change air entrapment to water entrapment and change the wetting regime observed, increasing the difference between observed bubble sizes.

4.2.4 Effect of surface chemistry on bubbles emitted from a ceramic 'pointfourTM' sinter.

Progression to a ceramic sinter coated by DC sputtering maintained the effect of surface chemistry as shown in Figure 4-10. However, despite the clear increase in bubble size from the hydrophobic 1ODT coated surface, the average bubble size is only 2-3 times larger than those produced from the more hydrophilic surfaces. This is significantly less than the deviation seen previously with the steel sinters above. However it is important to notice that the effect of chemistry is still prevalent.

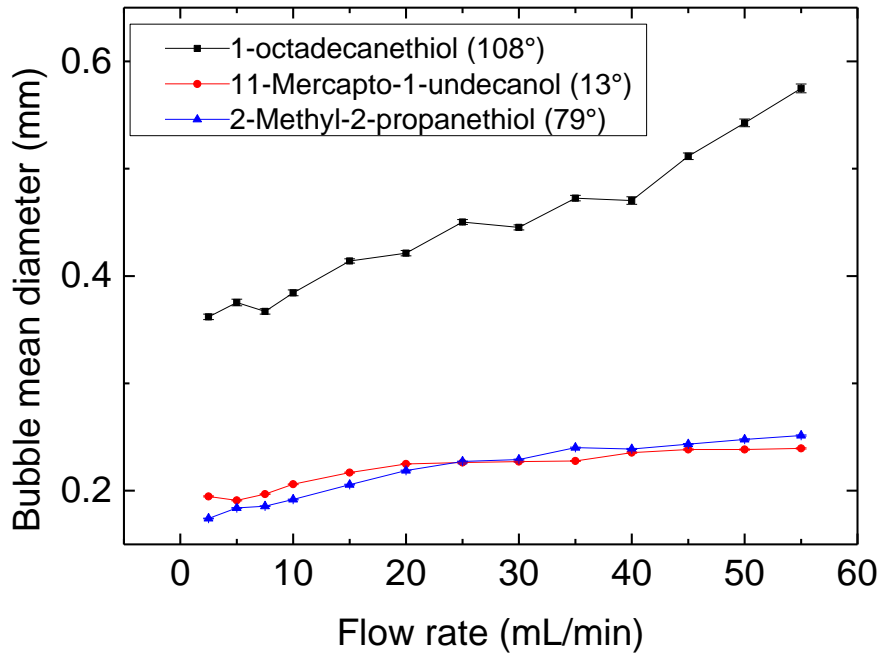


Figure 4-10 The dependence of bubble diameter on the contact angle of the surface at various flow rates, through a 3 mm thick sintered 'pointfour' ceramic disk with a close packed array of pores. The diffusers were coated by DC sputtering.

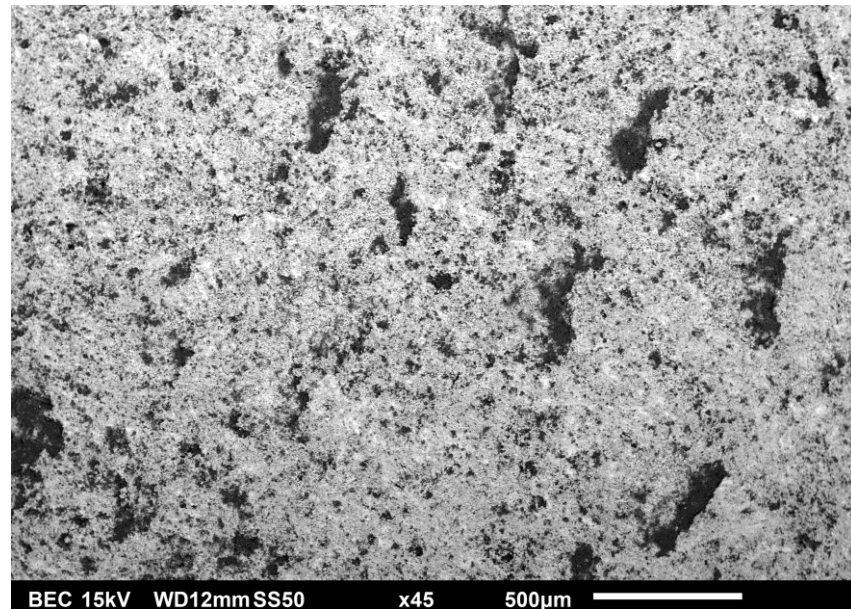


Figure 4-11 An SEM image of pointfour ceramic sinter.

It can be seen from Figure 4-11 that the pointfour diffuser is significantly pitted and rough. Further magnification and comparison with the steel sinter in Figure 4-12 indicates the scale of the roughness. It is believed that the morphology of the surface may be influencing the spread of the forming bubble, with features on the surface acting to pin the bubble to a small area. There are several hypotheses that could explain the observed effect.

The first is that the surface features may physically prevent the bubble from spreading over the surface. As previously discussed in section 1.4.3, the effect of surface chemistry is vastly reduced when bubbles are emitted from nozzles and capillaries. [6] Potentially, this surface structure may mimic the nozzle, with an elevated plateau preventing the spread of the bubble over the hydrophobic surface. This is shown schematically in Figure 4-13. This mode would not affect the hydrophilic surface as the bubble does not spread across the surface. The effect will be most clearly visible on more hydrophobic surfaces.

The second possibility is that surface morphology acts to create a petal effect type scenario which has two subcategories. The first of these is when water penetrates the nano structure of the diffuser. As previously described by Lee [7] and Wenzel [8] for the wetting of a limestone slab by road tar under water, the energy gained by forming the tar-limestone interface is less than the energy needed to break the limestone-water interface already present. In a similar way, the removal of entrapped water from the nano structure of the pointfour diffuser will carry a significant energy penalty. In fact, in the work by Lodziana, [9] it was shown that the surface free energy of alumina (pointfour diffusers have a similar composition as discussed below) is very low and in some cases may be negative. This high energy indicates water is extremely well bound to the surface, with an energy of adsorption of 200 kJ/mol. Increasing surface area would lead to an increase in this energy and thus the removal of water is strongly disfavoured. The result of this would be the inability of the forming bubble to create an extended interface with the pointfour diffuser plate, acting to pin

bubbles formed on both hydrophilic and hydrophobic surfaces to the pore, leading to a reduction in bubble size, especially for a hydrophobic surface. The effect would be hard to detect on a hydrophilic surface, a schematic of this effect is shown in Figure 4-14.

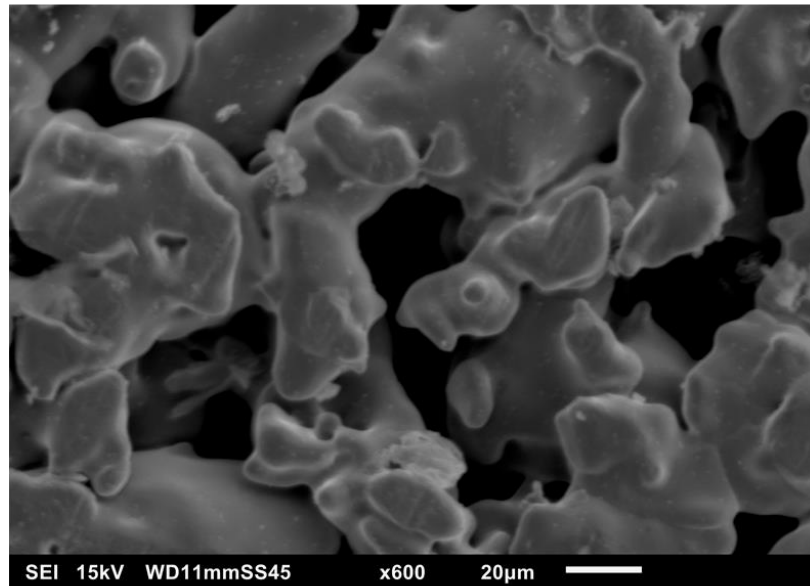
In Figure 4-14 (a), the hydrophobic diffuser is resistant to water penetrating the pores and air is forced through all pores. Upon reaching the solid-water interface, the diffuser is coated with a hydrophilic layer, acting to restrict the bubble to the pore as discussed above and the bubble size remains proportional to pore size. A hydrophobic diffuser coated with a hydrophobic coating allows the bubble to spread extensively across the surface, leading to bubbles being fed by multiple pores. As a result, it grows to a much greater size than the pore (b). A hydrophilic diffuser coated with a hydrophilic coating (c) allows water to penetrate into the structure. The forming bubble is once again restricted to the pore, and remains small. Finally, a hydrophilic diffuser allows water to penetrate within the structure and the airflow is restricted to a single pore. The forming bubble can spread over the hydrophobically coated surface (d) until it reaches the next adjacent pore. At this point, the entrapped water within the second pore may be displaced, or the bubble growth is stopped. As discussed above, the high energy of adsorption leads to the restriction. The growing bubble therefore grows to an intermediate size, between those observed from cases (b) and (c).

The reverse case is also possible, with pockets of air being trapped within the nano structure and preventing water from penetrating. One would therefore expect the bubble size to increase. However, due to the strong interaction with water outlined above, entrapment of air is less likely.

The third possible reason is that the surface morphology influences the surface coating. Significant surface roughness is believed to have a negative impact upon the sputtered gold surface, with overhanging regions acting to block areas below it, breaking the uniformity of the surface. This would act to reduce the hydrophobic area over which the growing bubbles

may spread, and lead to a reduction in size. In addition, this would be expected to yield slightly larger bubbles emitted from a hydrophilic surface, although this effect would be much smaller than the hydrophobic deviation. This effect is shown schematically in Figure 4-15.

a



b

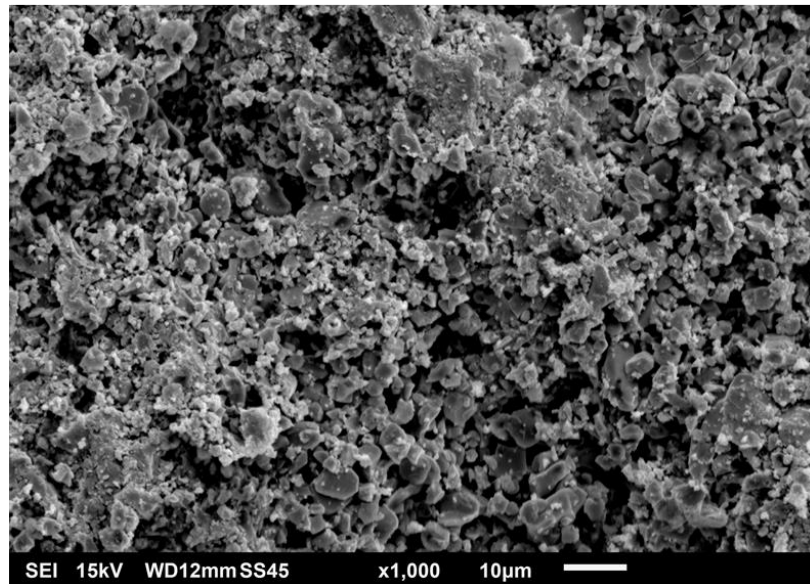


Figure 4-12 SEM images comparing a 5 μm stainless steel sinter (a) and a pointfour ceramic sinter (b).

Chapter 4: Bubbling under steady flow.

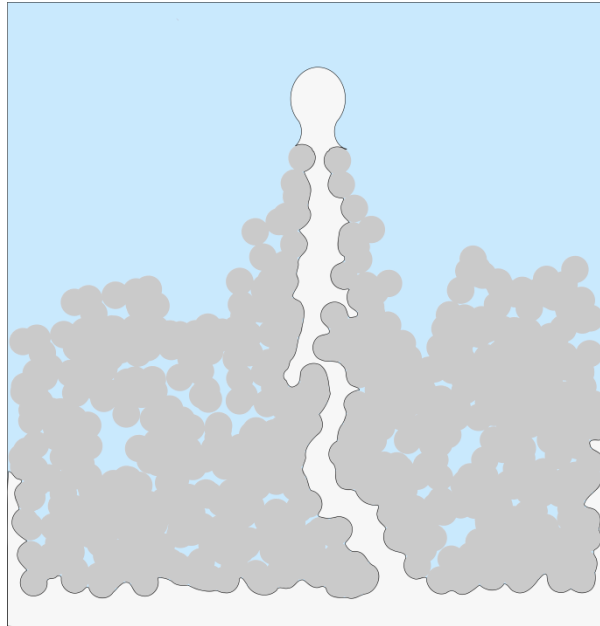


Figure 4-13 Schematic of bubble formation through a ceramic pointfour diffuser. The surface morphology acts to create elevated plateaus, mimicking the nozzle and preventing the spread of gas across the hydrophobic surface.

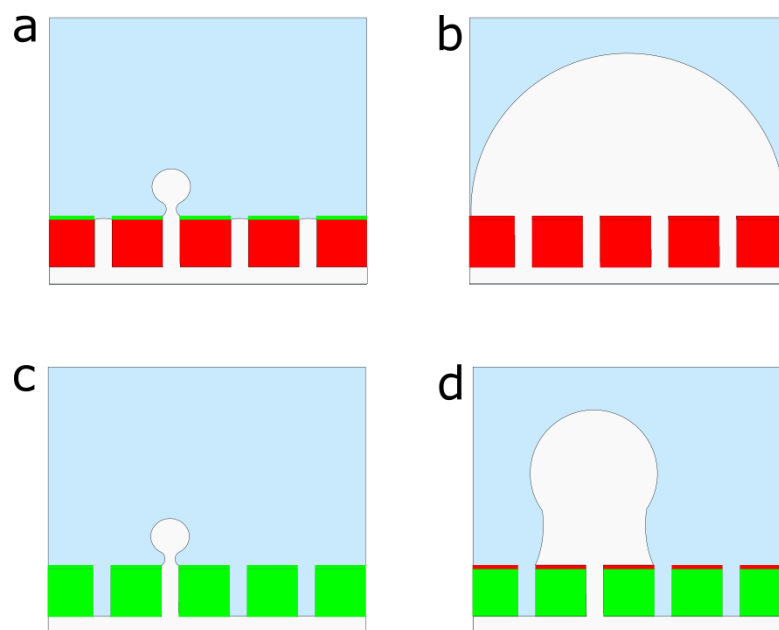


Figure 4-14 Schematic of bubble formation on modified diffusers: a) a hydrophobic (red) diffuser with a hydrophilic coating (green), b) a hydrophobic diffuser with a hydrophobic coating, c) a hydrophilic diffuser with a hydrophilic coating, d) a hydrophilic diffuser with a hydrophobic coating.

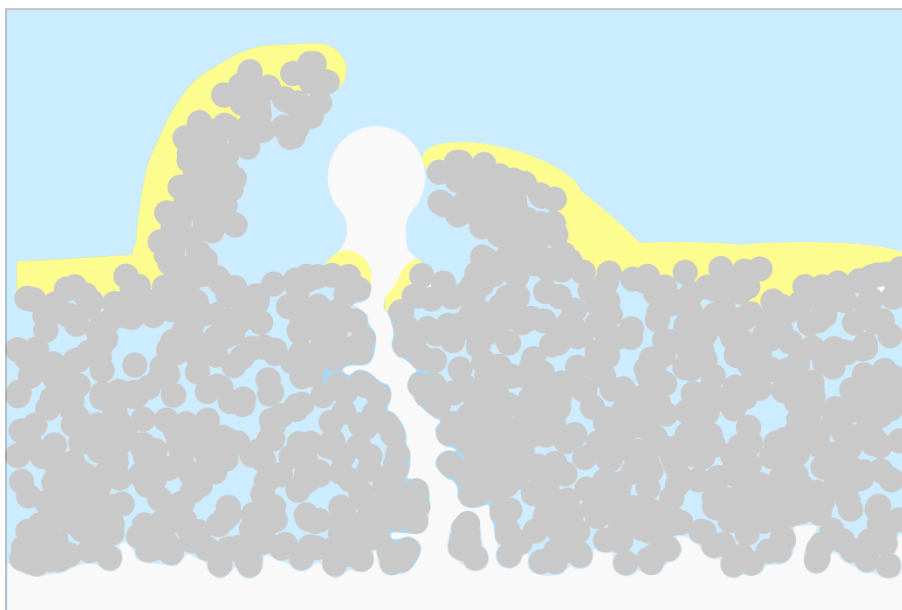


Figure 4-15 Schematic of bubble formation through a ceramic pointfour diffuser. The surface morphology blocks regions of the surface from coating, subsequently creating a barrier to the spread of a forming bubble.

In order to test the role of surface coating, pointfour diffusers were coated by Ebeam evaporation and thiols. As shown in section 3.3.9, Ebeam evaporation is more directional than DC sputtering and as a result there are expected to be more regions masked by surface morphology effects. This would suggest that the hydrophobic surface would generate bubbles smaller than those from a sputter coated surface. The results of this investigation are shown in Figure 4-16, and a comparison between the Ebeam and sputter coated samples is shown in Figure 4-17. The trend observed is as expected, with the Ebeam/ 1ODT modified surface yielding smaller bubbles than its corresponding sputtering/ 1ODT coated surface.

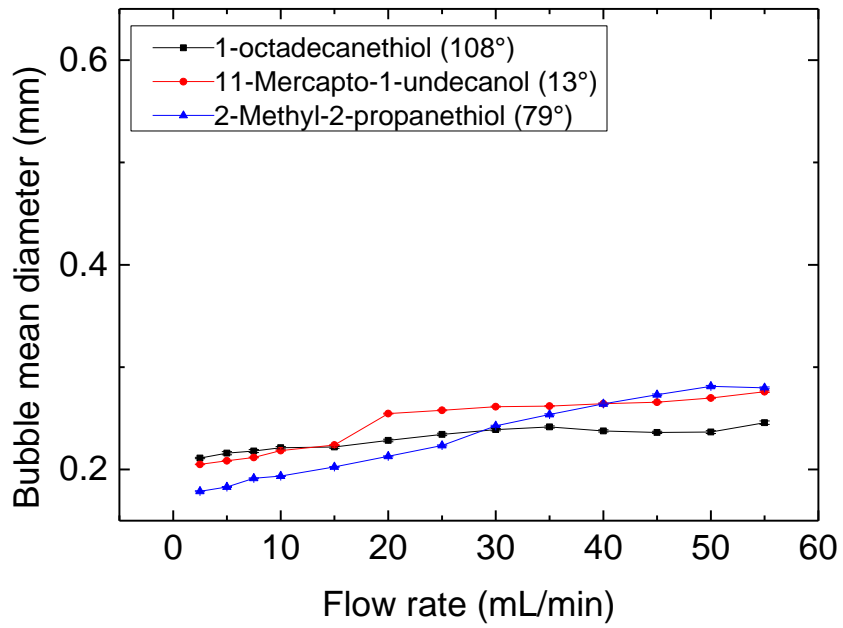


Figure 4-16 The dependence of bubble diameter on the contact angle of the surface at various flow rates, through a 3 mm thick sintered 'pointfour' ceramic disk with a close packed array of pores. The diffusers were coated by Ebeam evaporation.

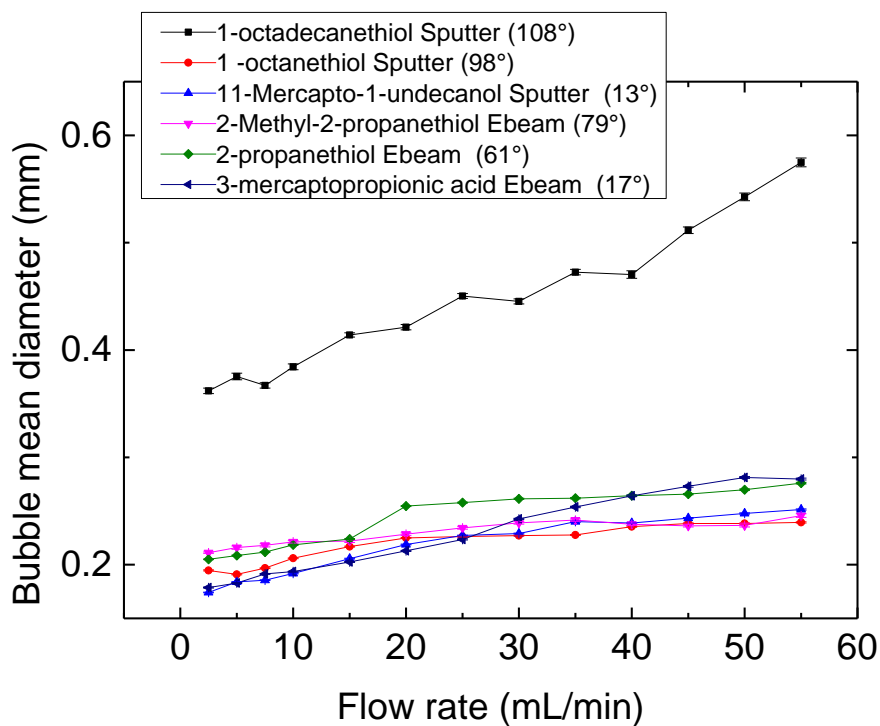


Figure 4-17 A comparison between the Ebeam and DC sputtering modification of a 3 mm thick sintered 'pointfour' ceramic disk with a close packed array of pores and their effect on bubble size.

Pointfour diffuser was submitted to the Sheffield Surface Analysis Centre (SSAC) to undergo X-ray photoelectron spectroscopy (XPS) studies. The spectra obtained are shown in Figure 4-18 along with the XPS scan of porous aluminium oxide (assumed to be similar in structure as the pointfour diffuser) sold by Sigma Aldrich. The composition of the two materials is shown in Table 4-1.

Chapter 4: Bubbling under steady flow.

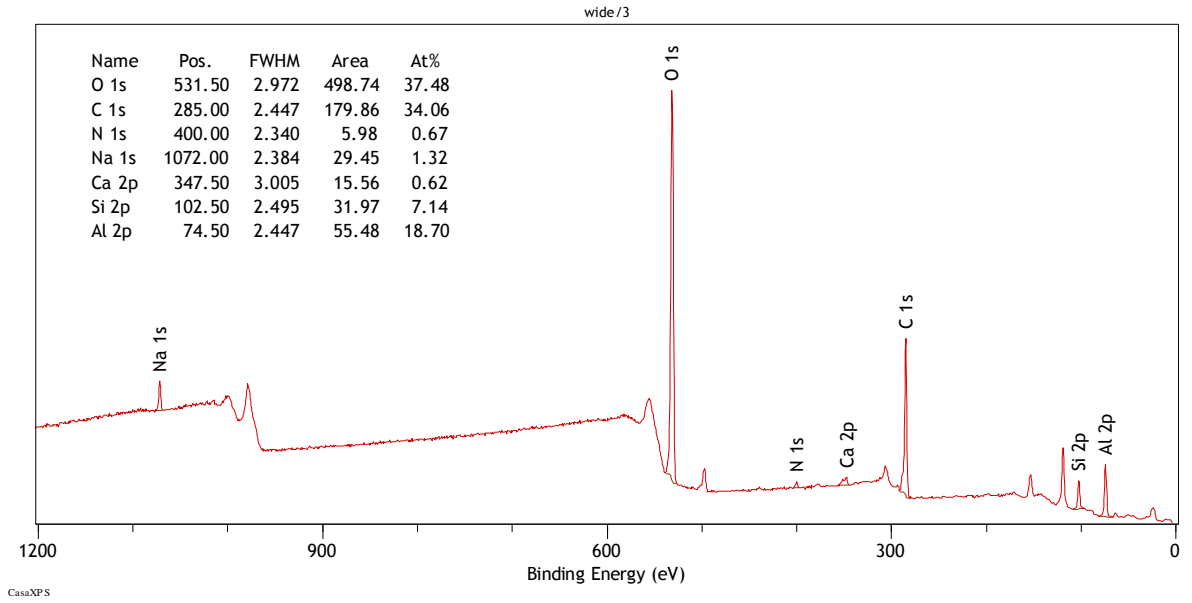


Figure 4-18 XPS survey scan of the pointfour diffuser.

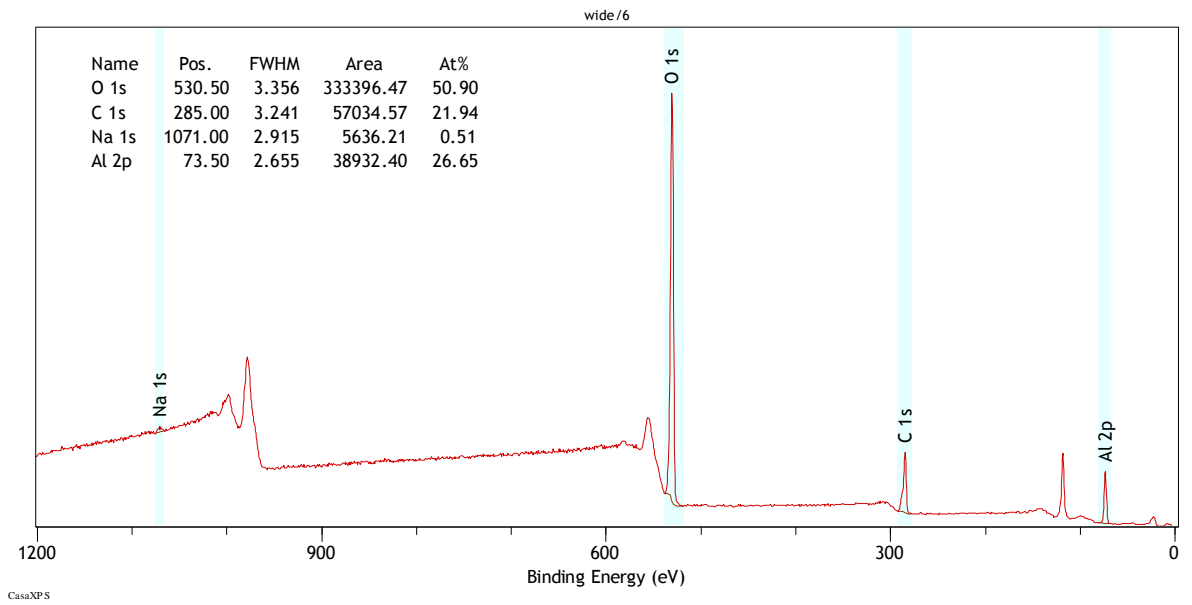


Figure 4-19 XPS survey scan of porous aluminium oxide sold by Sigma Aldrich (CAS: 1344-28-1).

Table 4-1 The composition of the pointfour diffuser and the standard aluminium oxide.

Sample	Na	O	C	N	Ca	Si	Al
Pointfour	1.3	37.48	34.1	0.7	0.6	7.1	18.7
Standard Al ₂ O ₃	0.5	50.9	21.9	<0.1	<0.1	<0.1	26.7

The porous aluminium oxide was observed to contain a structure comprised almost entirely of Al, C and O. It is believed that the C peak is either surface contamination, or more likely is a result of the carbon tape used to support the powder. The Al 2p peak was seen at 74.4 eV and the majority of the oxygen at 531.1 eV and these can be considered as the expected peak positions for aluminium oxide. Interestingly, a small oxygen component was also seen at 533.0 eV, and this is consistent with some absorbed water.

The pointfour plate had a much higher percentage of carbon than the aluminium oxide. This could be an intended part of the structure, but coupled with the N observed, it is more likely that the two peaks are from an organic compound added to the surface during handling. This would be consistent with the presence of Na and Ca, which are added to a surface by contact with non-deionised water or from handling. In addition, around 7% of the structure was found to be Si (102.5 eV). This is slightly lower than expected for a SiO₂ structure, but is consistent with an aluminosilicate (Al₂SiO₅). It has not yet been found in the literature what peak positions should be expected for aluminium and oxygen within an aluminosilicate and whether they differ from aluminium oxide, although the aluminium 2p binding energy at 74.4 eV is very similar to that for the aluminium oxide sample. The O 1s spectrum shows two components, that at 531.3 eV is similar to the standard aluminium oxide powder and this accounts for the majority of the oxygen intensity. However there is an additional contribution

at 532.6 eV which is consistent with the presence of hydroxide groups, and these account for over 11% of the total surface (being 30.9% of total oxygen at 37.5%).

In order to investigate the effect of the diffusers structure, silane modification was carried out to modify the composition throughout. The influence on bubble formation is shown in Figure 4-20. Again as in all cases, hydrophobic modification of the diffuser results in an increase in bubble size over all flow rates. Once again the effect is significantly less than is observed for the steel sinter. There may be two reasons for the diminished effect. The first is that the packing of silanes has been shown to be far less well ordered than thiol packing on gold on smooth surfaces. Additional surface roughness is expected to add to the non-uniformity of the silane SAMs. The result is the random exposure of non-terminal groups such as methylene, leading to a poorer SAM. The difference in packing may bring the PFO and TMODES contact angles towards the critical 90° switching angle and lead to a reduction in bubble size from the expected value. The second reason why the effect is lessened is due to the low density of silanol groups within the diffuser structure. Assuming 11% of the structure contains hydroxyl groups, a maximum of 11% of the diffuser may be modified by silanisation. It is likely that this is not enough to promote true reliance on the chemical modification and so the difference between the two regions of wettability is diminished.^{e,f}

^e https://youtu.be/V8AB_alk77w

^f <https://youtu.be/hWxvRlcWhDE>

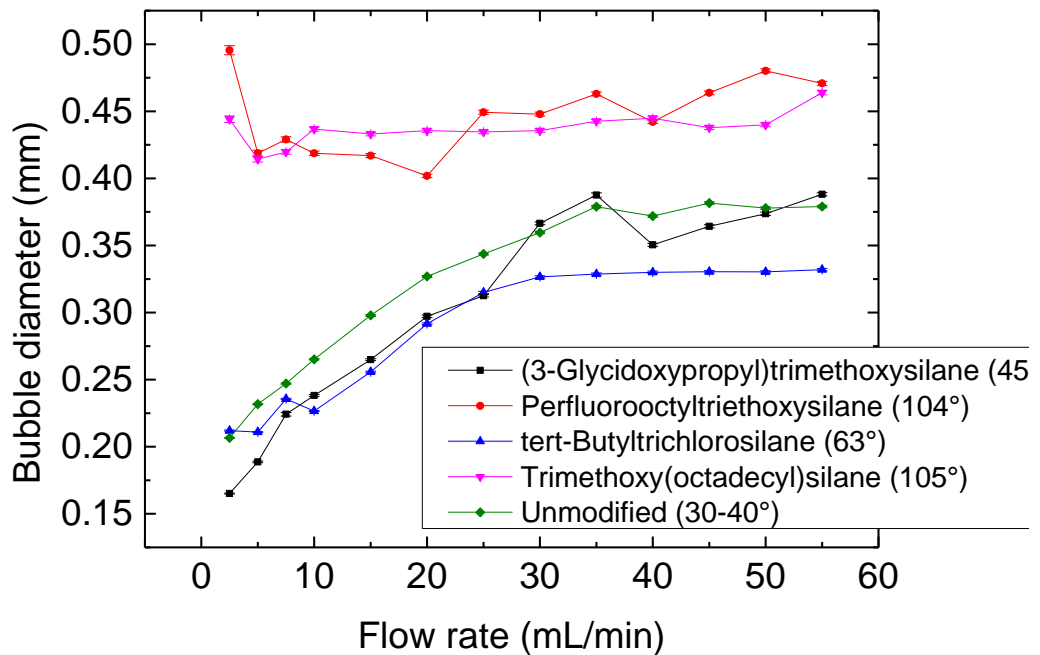


Figure 4-20 Silane modification of a 3 mm thick sintered 'pointfour' ceramic disk with a close packed array of pores and the effect on bubble size.

4.3 Conclusions.

Numerous experiments have been performed to investigate the influence of surface chemistry upon bubble formation under steady flow. The overall observation is that surface chemistry can have a significant influence on bubble formation and size, with an increase of more than 25x observed between a hydrophilically coated and hydrophobically coated surface. An apparent switch is seen at a contact angle of 90° , with no other reliance on surface chemistry. For example, surfaces with $\theta = 80^\circ$ do not necessarily yield larger bubbles than the surfaces with $\theta = 10^\circ$. Similarly, surfaces with $\theta = 91^\circ$ may yield larger bubbles than a surface with a $\theta = 110^\circ$.

It has also been shown that the orientation of the pores may play a key role in bubble formation alongside the surface chemistry effects. When emitted from a single pore, the bubbles produced from hydrophilically coated plates were seen to detach from the plate, and be rapidly followed by a subsequent bubble. This second bubble can often coalesce with the first, leading to a net increase in bubble size from the hydrophilic plate. Therefore, the bubbles are emitted at much smaller sizes than when observed during the investigation, due to coalescence just millimetres from the pore. The bubbles emitted from a hydrophobically modified surface cause a larger pressure drop across the pore, allowing the detaching bubble to escape the immediate vicinity before the next is generated, lessening the problem of coalescence.

Bubble emission from multiple controlled pores yields a wider variation in bubble size between the hydrophilic and hydrophobically coated surfaces than is seen for the single pore systems. However, the problem of coalescence is still prevalent, indicating careful spacing of the pores is crucial in the development of an ideal system.

Emission from a steel sinter is seen to yield the largest variation between the two coatings. From the high magnification SEM images taken, it seems that the steel sinters are largely smooth on the surface, allowing the bubbles to spread readily over the hydrophobic surface. In addition, the smoothness adds few defects to the modifying gold layer, and thus the subsequent thiol layer. Well packed SAMs will lead to a larger deviation in size. Therefore it can be said that a smooth surface is preferable when designing a system.

Ceramic pointfour diffuser was modified by both DC sputtering and Ebeam evaporation, followed by thiol coating. It was found that DC sputtering led to a larger bubble from a 1ODT modified surface, whereas the Ebeam/ 1ODT coated surface yielded much smaller bubbles. It is believed that this is due to the significant surface roughness of the diffuser plate, as shown by SEM images. This roughness disrupts the surface coating, adding

defects and abnormalities to the forming SAM. The exposure of methylene groups within the 1ODT layer will decrease the contact angle and appears to reduce it to below the 90° switching angle, where bubble size vastly changes.

It has also been shown that the pointfour diffuser contains around 11% hydroxyl groups throughout the structure. Modification by silanes leads to the apparent switching at $\theta = 90^\circ$ as described throughout this section. However, the variation is relatively small when compared to other systems. It is thought this deviation is due to a combination between surface morphology and the poor packing and coverage of the formed silane SAM.

From the work outlined in this section, it is clear that surface chemistry plays an important role in bubble formation. A switching contact angle is present at 90°, above and below which bubble size is split into two separate groups. However, in each region contact angle has no bearing on the bubble size.

It is also clear that the surface morphology of the diffuser plate is important to the bubbling process. Smooth surfaces seem more susceptible to large bubble formation, and so must be modified with hydrophilic coatings in order to achieve smaller bubbles. Rough surfaces seem less open to large bubble formation. It is also apparent that the scale of roughness is important, along with the native wettability of the diffuser. There is a potential micro/ nano structure effect causing a change in the extent of the chemistry effects, but more work in this area is needed to fully prove that this is a morphological effect, and cannot be attributed to other factors.

Finally, it is apparent that careful design of the diffuser plate coupled with surface chemistry will lead to an increased ability to produce small bubbles. Pores must be adequately spaced to eliminate the problem of coalescence at, or in close proximity to, the pores. Large spacing and a hydrophilic coating is likely to yield small bubbles. In addition, careful reactor

design is needed to ensure multiple pores are active in unison if small bubbles are required with low size disparity.

4.4 References.

- [1] D. Gerlach, G. Biswas, F. Durst, and V. Kolobaric, "Quasi-static bubble formation on submerged orifices," *International Journal of Heat and Mass Transfer*, vol. 48, pp. 425-438, 2005.
- [2] J.-L. Liow and N. Gray, "A model of bubble growth in wetting and non-wetting liquids," *Chemical Engineering Science*, vol. 43, pp. 3129-3139, 1988.
- [3] S. Gnyloskurenko, A. Byakova, O. Raychenko, and T. Nakamura, "Influence of wetting conditions on bubble formation at orifice in an inviscid liquid. Transformation of bubble shape and size," *Colloids and Surfaces A: Physicochemical and Engineering Aspects*, vol. 218, pp. 73-87, 2003.
- [4] A. Byakova, S. Gnyloskurenko, T. Nakamura, and O. Raychenko, "Influence of wetting conditions on bubble formation at orifice in an inviscid liquid: Mechanism of bubble evolution," *Colloids and Surfaces A: Physicochemical and Engineering Aspects*, vol. 229, pp. 19-32, 2003.
- [5] M. Kukizaki and T. Wada, "Effect of the membrane wettability on the size and size distribution of microbubbles formed from Shirasu-porous-glass (SPG) membranes," *Colloids and Surfaces A: Physicochemical and Engineering Aspects*, vol. 317, pp. 146-154, 2008.
- [6] M. Kukizaki and Y. Baba, "Effect of surfactant type on microbubble formation behavior using Shirasu porous glass (SPG) membranes," *Colloids and Surfaces A: Physicochemical and Engineering Aspects*, vol. 326, pp. 129-137, 2008.
- [7] H. Yasuda and J. Lin, "Small bubbles oxygenation membrane," *Journal of Applied Polymer Science*, vol. 90, pp. 387-398, 2003.
- [8] G. Corchero, A. Medina, and F. Higuera, "Effect of wetting conditions and flow rate on bubble formation at orifices submerged in water," *Colloids and Surfaces A: Physicochemical and Engineering Aspects*, vol. 290, pp. 41-49, 2006.
- [9] L. Davidson and E. H. Amick, "Formation of gas bubbles at horizontal orifices," *AIChE Journal*, vol. 2, pp. 337-342, 1956.
- [10] R. J. Benzing and J. E. Myers, "Low frequency bubble formation at horizontal circular orifices," *Industrial & Engineering Chemistry*, vol. 47, pp. 2087-2090, 1955.
- [11] M. Jamialahmadi, M. Zehtaban, H. Müller-Steinhagen, A. Sarrafi, and J. Smith, "Study of bubble formation under constant flow conditions," *Chemical Engineering Research and Design*, vol. 79, pp. 523-532, 2001.
- [12] I. Leibson, E. G. Holcomb, A. G. Cacosso, and J. J. Jacmic, "Rate of flow and mechanics of bubble formation from single submerged orifices. II. Mechanics of bubble formation," *AIChE Journal*, vol. 2, pp. 300-306, 1956.
- [13] W. B. Hayes, B. W. Hardy, and C. D. Holland, "Formation of gas bubbles at submerged orifices," *AIChE Journal*, vol. 5, pp. 319-324, 1959.
- [14] L. Zhang and M. Shoji, "Aperiodic bubble formation from a submerged orifice," *Chemical Engineering Science*, vol. 56, pp. 5371-5381, 2001.
- [15] S. Vafaei and D. Wen, "Bubble formation on a submerged micronozzle," *Journal of Colloid and Interface Science*, vol. 343, pp. 291-297, 2010.
- [16] O. Pamperin and H.-J. Rath, "Influence of buoyancy on bubble formation at submerged orifices," *Chemical Engineering Science*, vol. 50, pp. 3009-3024, 1995.

- [17] A. A. Kulkarni and J. B. Joshi, "Bubble formation and bubble rise velocity in gas-liquid systems: A review," *Industrial & Engineering Chemistry Research*, vol. 44, pp. 5873-5931, 2005.
- [18] J. Xie, X. Zhu, Q. Liao, H. Wang, and Y.-D. Ding, "Dynamics of bubble formation and detachment from an immersed micro-orifice on a plate," *International Journal of Heat and Mass Transfer*, vol. 55, pp. 3205-3213, 2012.
- [19] S. Xie and R. B.H. Tan, "Bubble formation at multiple orifices—bubbling synchronicity and frequency," *Chemical Engineering Science*, vol. 58, pp. 4639-4647, 2003.
- [20] R. Clift, J. R. Grace, and M. E. Weber, *Bubbles, drops, and particles*: Courier Corporation, 2005.
- [21] R. Kumar and N. Kuloor, "The formation of bubbles and drops," *Advances in chemical engineering*, vol. 8, pp. 255-368, 1970.
- [22] A. Cassie and S. Baxter, "Wettability of porous surfaces," *Transactions of the Faraday Society*, vol. 40, pp. 546-551, 1944.
- [23] A. Cassie, "Contact angles," *Discussions of the Faraday Society*, vol. 3, pp. 11-16, 1948.
- [24] X. Zhu, Q. Liao, H. Wang, L. Bao, J. Xie, and C. Lin, "Experimental Study of bubble growth and departure at the tip of capillary tubes with various wettabilities in a stagnant liquid," *Journal of superconductivity and novel magnetism*, vol. 23, pp. 1141-1145, 2010.
- [25] A. R. Lee, *J. Soc. Chem. Ind.*, vol. 55, 1936.
- [26] R. N. Wenzel, "Resistance of solid surfaces to wetting by water," *Industrial & Engineering Chemistry*, vol. 28, pp. 988-994, 1936.
- [27] Z. Łodziana, N.-Y. Topsøe, and J. K. Nørskov, "A negative surface energy for alumina," *Nature materials*, vol. 3, pp. 289-293, 2004.

Chapter 5: Bubbling under oscillating flow.

5.1 Synthetic actuator jets.

The pulsed flow generated by alternating positive and negative flows from a actuator jet have been of interest since the early radio sets of the 1930's, where the phenomenon was labelled 'loud speaker wind' or 'quartz wind' and has since become known as acoustic streaming. [1, 2] Recent work by Tesar [2-4] has focused on the production and control of synthetic actuator jets. By inducing the flow of fluid backwards and forwards through an orifice, via the movement of a diaphragm inside a sealed container, Tesar has been able to fabricate a synthetic jet, as shown in Figure 5-1.

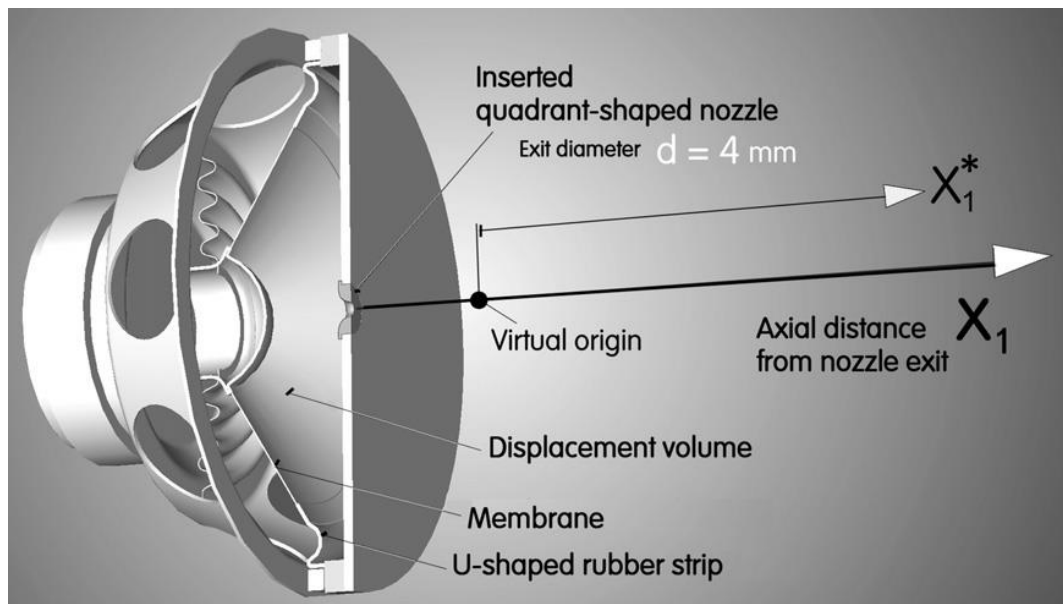


Figure 5-1 Schematic of the synthetic jet actuator used in the work by Tesar. [2-4]

In work carried out in 2010 [3] it was shown that the mean velocity of the jet reduced with distance from the exit pore. Increasing frequency led to a more rapid decay of the velocity. This led Tesar to conclude that there are two distinct flow regimes within the actuator jet. At distances of less than 50 nozzle diameters, the vortices produced by the jet are

coherent and thus interference leads to higher velocity flow. At greater distances, the flow becomes more stochastic, resulting in a significantly reduced velocity. As a result, the energy of the produced pulse asymptotically reduced to that of a steady air flow, and thus at large distances the effect of pulsation is lost.

In the 2012 work [2], two observations were found. The first was that during the transition between the two distinct flow regimes, outlined above, the energy of the jet decreases rapidly. It was also shown that this decay is more rapid still at higher driving frequencies. The second observation was that, in the high power regime, spectral density peaks were observed at intervals, indicating highly coherent flow regions corresponding to the constructive interference of acoustic waves. As the driving frequency increases, these peaks become less pronounced, until finally they disappear. Peaks also disappear more rapidly at increasing distance from the pore.

The 2013 work [4] builds further on the previous findings, presenting more evidence of two phase flow regimes, with both a positive and negative (suction) component. It is also shown that the velocity profile deviates from its harmonic character as the wall of the actuator is approached, with the maxima of the profile located along the nozzle axis.

5.2 The fluidic oscillator.

Synthetic actuator jets of the type described above are becoming increasingly important in many areas. [5, 6] The synthetic actuator is more robust than the tabbed style actuator which uses vanes extending into the fluid flow to influence it. [7]

In the early 1960's, Warren proposed the design of a no moving part fluidic oscillator based on the Coanda effect. [8] The original design was to be used in the fluidic logic gate

systems of early computers, but the rapid development of silicon based electronic technologies meant the concept passed into obscurity. The oscillator design was resurrected and improved upon in the mid 2000's by Zimmerman and Tesar [7] who spotted the potential applications of the design. The Zimmerman and Tesar bistable amplifier (Figure 5-2) takes an inflow of gas into the inlet terminal and passes it through a narrow gap known as the interaction region. In this area, the gas cannot flow along the input axis, and attaches to one of the walls via the Coanda effect. The gas flows down only one of these collector arms and passes through the exit nozzle. A diverting jet passing into the diverter terminals can act to switch the incoming jet to the opposite wall. The divergent jet needs to only be around 7% of the supplied airflow to cause this switching effect, and it is for this reason that the device is known as an amplifier, as a weak divergent flow input can switch the much larger main flow. The geometry of the amplifier is shown In Figure 5-3. [7, 9]

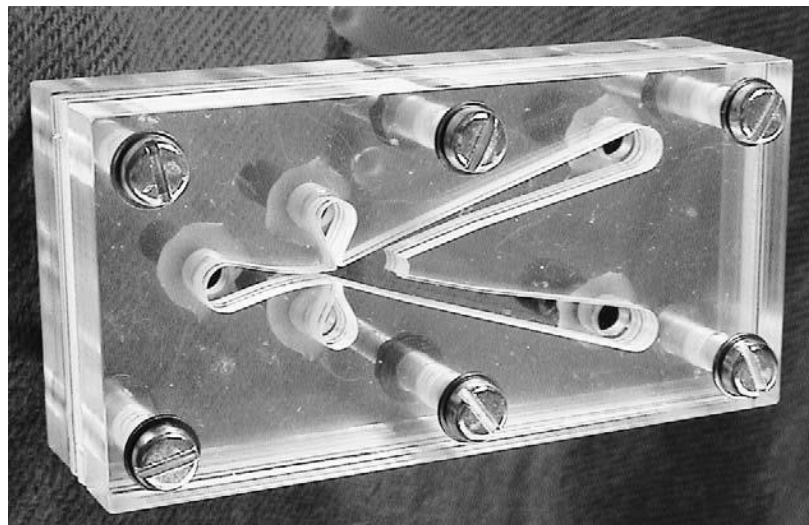


Figure 5-2 The Zimmerman and Tesar bistable amplifier. A stack of laser cut plates are held between two transparent sheets. [7]

The addition of a feedback loop to the amplifier, turns it into a fluidic oscillator. There are several common types of oscillator design, with three summarised in Figure 5-4.

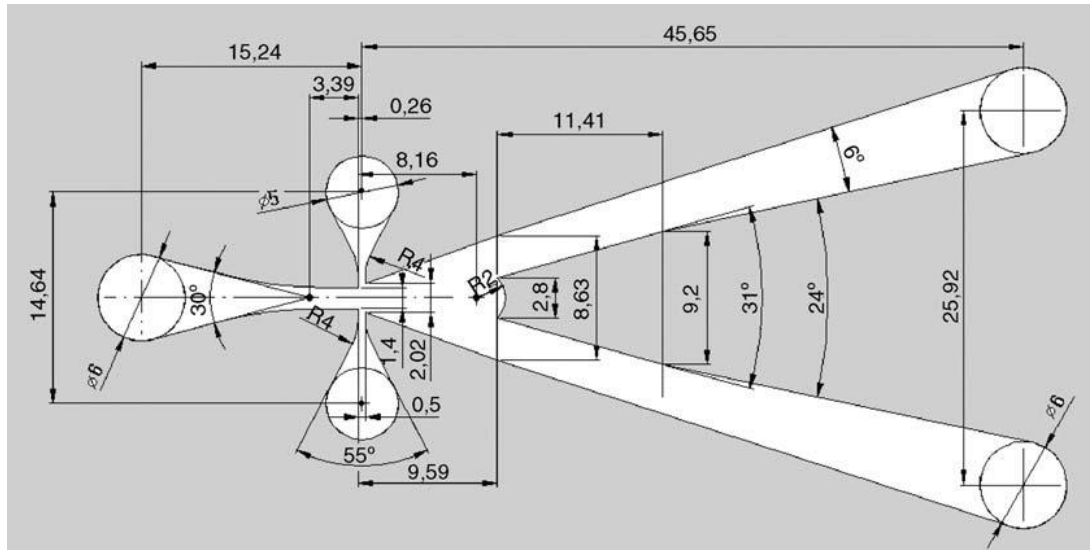


Figure 5-3 The geometry of the Zimmerman and Tesar bistable amplifier as shown in [7].

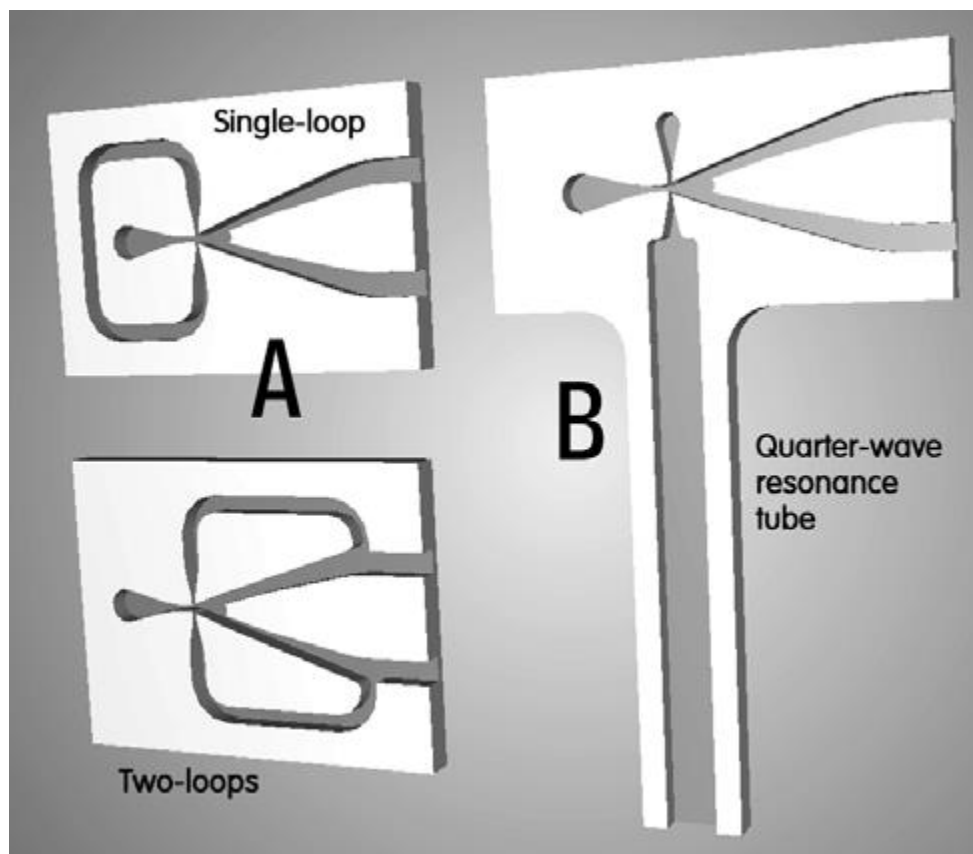


Figure 5-4 Fluidic oscillator design based on a bistable amplifier. Type A contains looped feedback, with both single and double loops possible. Type B is the resonator tube design, where a reflected standing wave acts to switch the flow.

The feedback mode is tailored to suit each amplifier in isolation. Type A two loop oscillators, investigated by Warren [8, 10], function by splitting a small volume of gas from the output channel and feeding it back through the feedback loop on the same side to the control terminal. This flow destabilises the flow attached to the wall, driving it to switch to the opposite wall. This sets up an analogous process and the switching repeats.

The single loop oscillator was also mentioned by Warren [8] but became more recognised due to the work of Spyropoulos. [9, 11] The single loop variant exploits the pressure difference across the feedback loop. Pressure is lower on the jet entrainment side of the feedback loop, causing airflow through the loop which disturbs the attached jet. This drives the jet to the opposite wall of the oscillator and the pressure variance switches sides. In both the single loop and two loop systems, the length of the feedback loop dictates the frequency of switching.

It was found by Zimmerman [7] that both inlet flow rate and feedback loop length played an important role in the oscillating frequency determination. It was found that, at low frequency, the produced wave was square with clear switching of the jet. As frequency increased, the output signal became more damped and the wave shape approached that of a standing sine wave. However, the shape never reached the idealised form of the wave. The relationship between the incoming flow rate and feedback loop length found in [7] is shown in Figure 5-5.

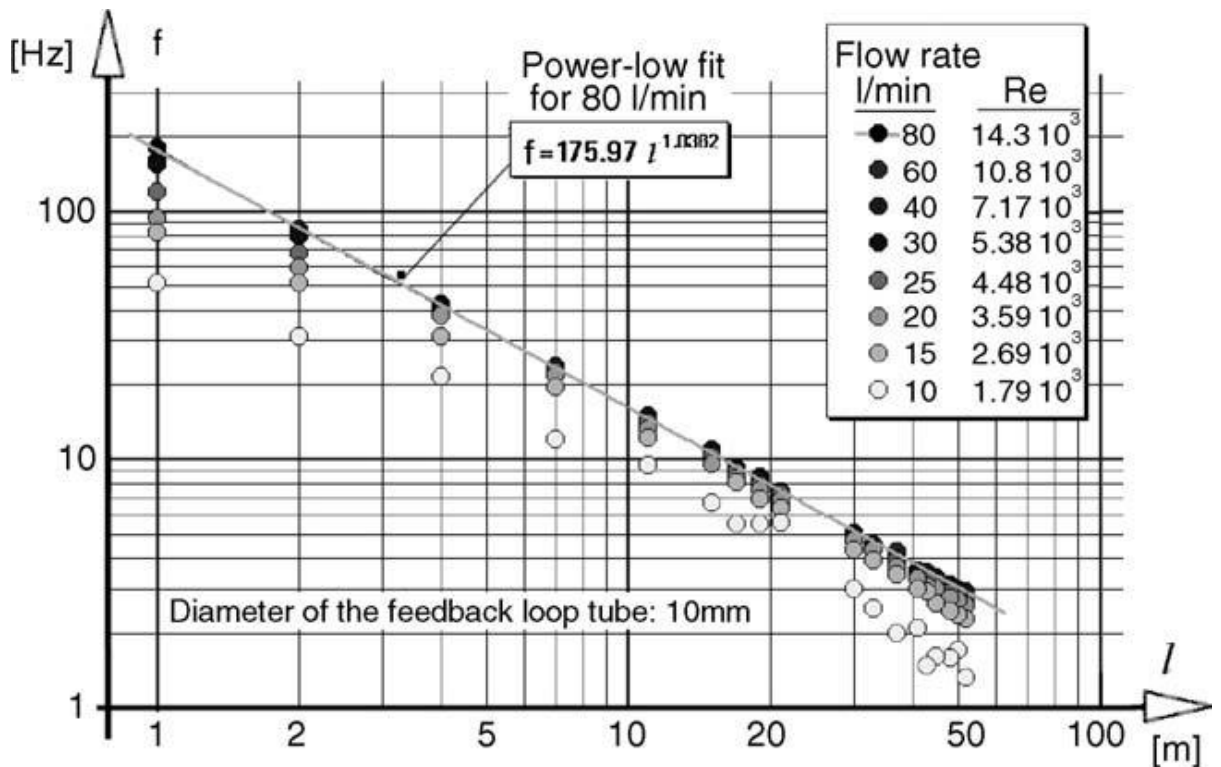


Figure 5-5 The inverse relationship between oscillating frequency and feedback loop length at various flow rates for the fluidic oscillator of Zimmerman and Tesar. [7]

The resonance channel oscillator shown in Figure 5-4 B has a frequency dictated by the length of the resonance channel. Both this channel and the second feedback port of the amplifier are left open to the atmosphere, or another large volume of stagnant gas. The oscillator is discussed in more detail in [12].

Application of the fluidic oscillator to bubble formation has been shown to decrease bubble sizes towards the order of the pore as discussed in section 1.5.2. When compared to bubble formation under steady flow, this can be a reduction of 25x the pore diameter. Addition of the fluidic oscillator also reduces the polydispersity of the bubble cloud.

This chapter focuses on the effect of oscillation on bubble formation in conjunction with surface chemistry modification. Attempts were also made to use the synthetic actuator jet discussed above to influence bubble size.

5.3 Experimental.

5.3.1 Generation of an oscillating flow.

A Visaton FR10 8 Ω speaker was obtained from Farnell UK (Premier Farnell UK Limited, Leeds, UK). The speaker was encased in a sealed container as per the schematic in Figure 5-6 and photographs in Figure 5-7 below. Compressed air (2 barg) was fed to a Bronkhorst EL series F-201CV mass flow controller. Flow rate was controlled by FlowDDE and Flowview software of Bronkhorst and was fed into a 'Tee splitter' with the two outlets connecting to the 6mm hose barbs as shown. Air was supplied to both the front and back of the speaker to prevent the paper cone crumpling under the flow to the top face. The speaker was driven by LabVIEW code written by the user which simultaneously triggered image capture for bubble analysis. The speaker was provided with a wave amplified by a Naim audio NAP90 amplifier (Naim Audio Ltd, Salisbury, UK).

In a separate set of experiments, the fluidic oscillator of Zimmerman and Tesar [7] based on the Warren oscillator [8, 13] was implemented for bubbling under oscillatory flow. The oscillator was fed via a Cole-Parmer MC series EW-32907-75 mass flow controller. All tubing was comprised of PET, PVC reinforced tube with ID=8 mm and OD=12 mm (RS components 368-0182, Northants, UK) and ID=6.3 mm and OD=10.5 mm (RS components 368-0176, Northants, UK). The Input flow was bled to the appropriate level by flow control valves (RS components 390-7689, Northants, UK).

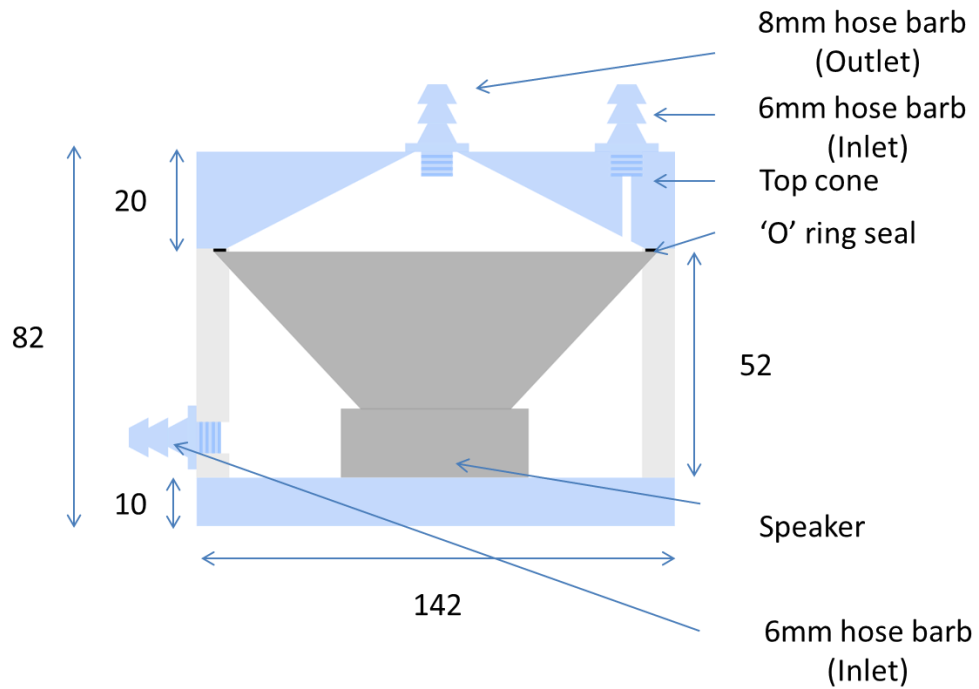


Figure 5-6 Visaton FR10 8Ω speaker was encased in a PVC and Perspex box as shown. 6 mm and 8 mm hose barb were added to allow air flow in and out. All sizes are given in mm.



Figure 5-7 Visaton FR10 8Ω speaker was encased in a PVC and Perspex box as shown. 6 mm and 8 mm hose barbs were added to allow air flow in and out. Flow entered the top and bottom faces of the speaker and flow exited through the top (brass) fitting.

5.3.2 Preparation of controlled pore, rolled stainless steel disks.

70 μm thick rolled stainless steel disks (25 mm diameter) with photoetched holes of 250 μm diameters were obtained from Photofabrication services, St Neots, UK. A single pore was etched through the centre to create the 'single pore' disks. A pattern of 7 holes was also etched through similar disks to give a central hole with a hexagonal group of holes surrounding it, with centre to centre distance of 2.25 mm between all adjacent holes as in Figure 2-4. This diffuser acted as a pseudo multi pore system and allowed a level of control to assist understanding.

The disks were rinsed with acetone and ethanol to remove contaminants before being placed into a Diener Zepto plasma cleaner. A vacuum was applied for 10 minutes before the introduction of oxygen gas at 1 barg pressure for a further 5 minutes. After this time the generator was turned on and a plasma was struck. The disks were left in the plasma for 5 minutes to remove all organic contaminants. The clean dry disks were then placed into a Moorfield minilab 080 for coating.

The disks were coated by DC sputtering as follows. The base pressure of the chamber was taken to $<1 \times 10^{-9}$ bar before argon (Ar) was introduced to re-pressurise to 6.5×10^{-6} bar. Once the pressure stabilised, it was maintained for 5 minutes before a base layer of Cr (10 nm) was added (0.163 A, 301.4 V, rate: 0.18 $\text{\AA}/\text{s}$). After chromium deposition, the chamber was maintained at constant pressure for 5 minutes before the deposition of gold (100 nm) was carried out (0.118 A, 362 V, rate: 0.47 $\text{\AA}/\text{s}$).

Thiol solutions (50 mL, 3 mM) were made using ethanol that was degassed under a steady stream of nitrogen for 30 minutes before use. Freshly coated disks were placed into the solutions and immediately sealed. The gold coated disks were left in solution for 18 hours

before removal. Upon removal they were washed with a copious volume of ethanol (100 mL) before drying under a constant stream of nitrogen.

5.3.3 Preparation of steel sinters.

Sintered steel disks (25 mm Diameter, 3 mm thick) were obtained from Hengko technology co. Ltd (Shenzhen City, China) with a random array of 5 μm pores .

The sinters were soaked in acetone overnight and then rinsed with acetone and ethanol to remove manufacturing grease/ contaminants before being placed into a vacuum oven at 80 °C for 24 hours to ensure drying. The sinters were then placed into a Diener Zepto plasma cleaner. A vacuum was applied for 10 minutes before the introduction of oxygen gas at 1 barg pressure for a further 5 minutes. After this time the generator was turned on and a plasma was struck. The disks were left in the plasma for 5 minutes to remove all organic contaminants. The clean dry disks were then placed into a Moorfield minilab 080 for coating.

The sinters were coated by DC sputtering with a base pressure of $<1 \times 10^{-9}$ bar before argon (Ar) was introduced to re-pressurise to 6.0×10^{-6} bar. Once the pressure stabilised, it was maintained for 5 minutes before a base layer of Cr (10 nm) was added (0.158 A, 282 V, rate: 0.14 Å/s). After chromium deposition, the chamber was maintained at constant pressure for 5 minutes before the deposition of gold (100 nm) was carried out (0.118 A, 359 V, rate: 0.45 Å/s).

Thiol solutions (50 mL, 3 mM) were made using ethanol that was degassed under a steady stream of nitrogen for 30 minutes before use. Freshly coated sinters were placed into the solutions and immediately sealed. The gold coated sinters were left in solution for 18

hours before removal. Upon removal they were washed with a copious volume of ethanol (100 mL) before drying under a constant stream of nitrogen.

5.3.4 Preparation of pointfour ceramic diffusers.

Pointfour Micro Bubble Diffuser plate was obtained from Pentair Aquatic eco-systems (Apopka, FL, USA) and cut into 25 mm diameter disks with a thickness of 3 mm.

The diffusers were soaked in acetone overnight and then rinsed with acetone and ethanol to remove manufacturing grease/ contaminants before being placed into a vacuum oven at 80 °C for 24 hours to ensure drying. The sinters were then placed into a Diener Zepto plasma cleaner. A vacuum was applied for 10 minutes before the introduction of oxygen gas at 1 barg pressure for a further 5 minutes. After this time the generator was turned on and a plasma was struck. The disks were left in the plasma for 5 minutes to remove all organic contaminants.

One set of diffusers were coated by DC sputtering with a base pressure of $<1 \times 10^{-9}$ bar before argon (Ar) was introduced to re-pressurise to 6.0×10^{-6} bar. Once the pressure stabilised, it was maintained for 5 minutes before a base layer of Cr (10 nm) was added (0.158 A, 282 V, rate: 0.14 Å/s). After chromium deposition, the chamber was maintained at constant pressure for 5 minutes before the deposition of gold (100 nm) was carried out (0.118 A, 359 V, rate: 0.45 Å/s).

Thiol solutions (50 mL, 3 mM) were made using ethanol that was degassed under a steady stream of nitrogen for 30 minutes before use. Freshly coated disks were placed into the solutions and immediately sealed. The gold coated disks were left in solution for 18 hours

before removal. Upon removal they were washed with a copious volume of ethanol (100 mL) before drying under a constant stream of nitrogen.

A second set of clean dry diffusers were immersed in silane solutions (50 mL heptane, 3 mM) for 24 hours under ambient conditions. Upon removal, each piece was rinsed with the parent solvent before being immersed in 50mL of fresh solvent and placed in an ultrasonic bath for 30 seconds at 25 °C to remove physically adsorbed layers. A final rinse with further fresh solvent and drying by a stream of nitrogen followed before samples were left in an oven at 45 °C for 2 hours to remove residual solvent.

5.3.5 Bubbling under oscillatory flow.

Bubbles were generated into a tank built by the user with a water volume of 45x30x10 cm (WxHxD) filled with 15 M Ω -cm deionised water (Elga Purelab Option S-R filtration system). The antechamber below the pore was 30 cm³ in volume, back to the first restriction point, which was the Bronkhorst mass flow controller.

Videos for bubble size analysis was captured using a Mikrotron MC1363 Eosens camera with a 22.9 mm CMOS chip (14 μ m square pixel size) at a resolution of 1280x1024 pixels and 30fps. Post capture analysis was carried out using LabVIEW software written by the authors. Analysis was performed upon samples with $n > 1000$ in general. The error reported is the error in the mean (95%) unless otherwise stated.. Analysis was performed upon samples with $n > 1000$ in general. The error reported is the error in the mean (95%) unless otherwise stated.

High speed video was captured using the same Mikrotron Eosens camera as above, but at a resolution of ca 280x410 pixels and frame rates of ca 4000 fps. Illumination was provided

by an array of 7 Bridgelux BXRA-56C9000-J-00 high brightness LED's (cool white, 5600 K, 9000 lm).

5.4 Results and discussion.

5.4.1 The synthetic actuator and its effect on bubble size.

The initial investigation focussed on the synthetic actuator jet made from a speaker as detailed above. This was carried out to conduct a frequency sweep to investigate whether the system had a 'sweet spot' where resonance effects led to bubble detachment at smaller sizes. This optimal frequency could then be utilised in the fluidic oscillator studies detailed later. The speaker was supplied with a sweep of frequencies and a microphone was placed at varying distances from the outlet of the jet. Amplitude variations were plotted in order to examine how it altered with distance. The results of the study are shown in Figure 5-8.

It can be seen from Figure 5-8 that the amplitude of the detected wave diminishes over both distance and frequency. Above 9000 Hz there is very little amplitude detected and so deviations in the distance from the actuator nozzle have no impact. The largest detected signal appears at 1000 Hz with other less intense signals between 2000-8000 Hz. At distances of 2 m, the signal is only observable below 2000 Hz. Extending the frequency over a larger range of frequencies and distances continues the trend as seen in Figure 5-9.

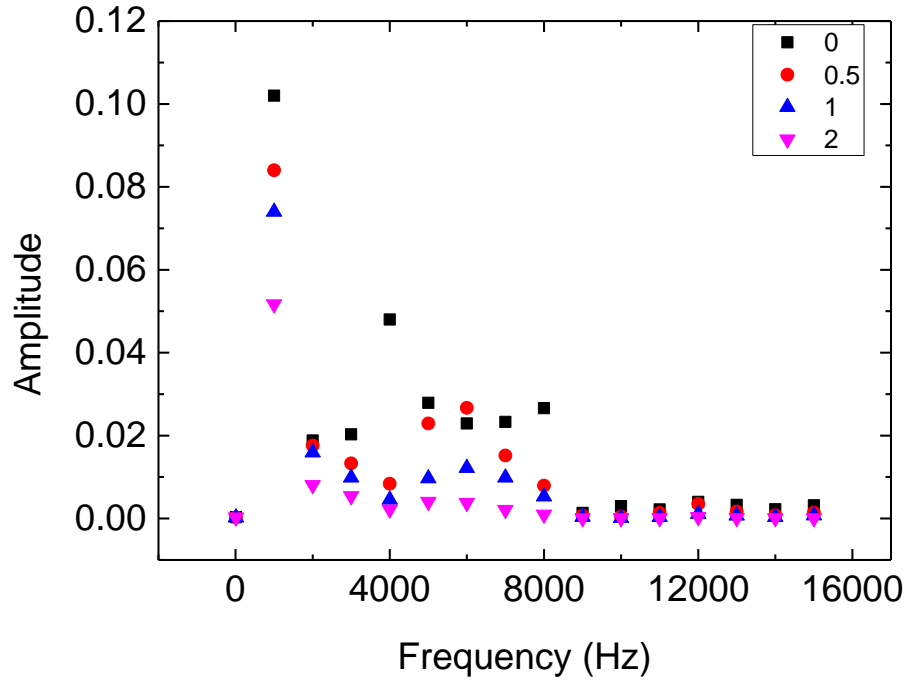


Figure 5-8 The deviation of amplitude with frequency over varying distances (m) from the actuator jet nozzle. The detector was positioned at the end of a polyimide tube (OD 6 mm, ID 4 mm).

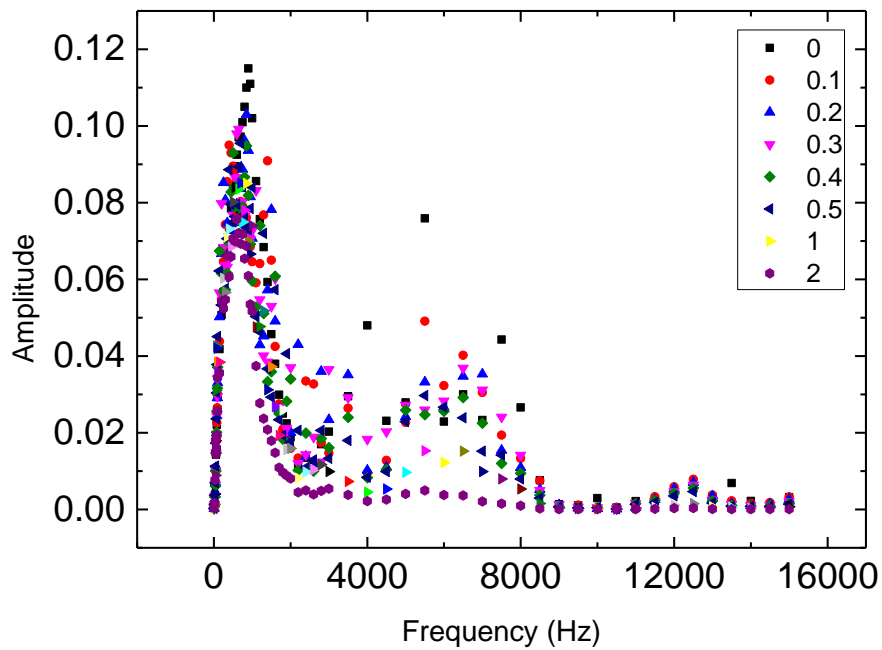


Figure 5-9 The deviation of amplitude with frequency over varying distances (m) from the actuator jet nozzle. The detector was positioned at the end of a polyimide tube (OD 6 mm, ID 4 mm).

Switching to a metallic tube increases the observed amplitude significantly, and the amplitude is maintained at extended distances from the nozzle. Once again the amplitude decreases with increasing frequency. In addition, the shorter tube lengths (0.05 m and 0.1 m) have an observed maxima at around 600 Hz, whereas the longer (0.1 m and 0.2 m) tubes have maxima closer to 1000 Hz.

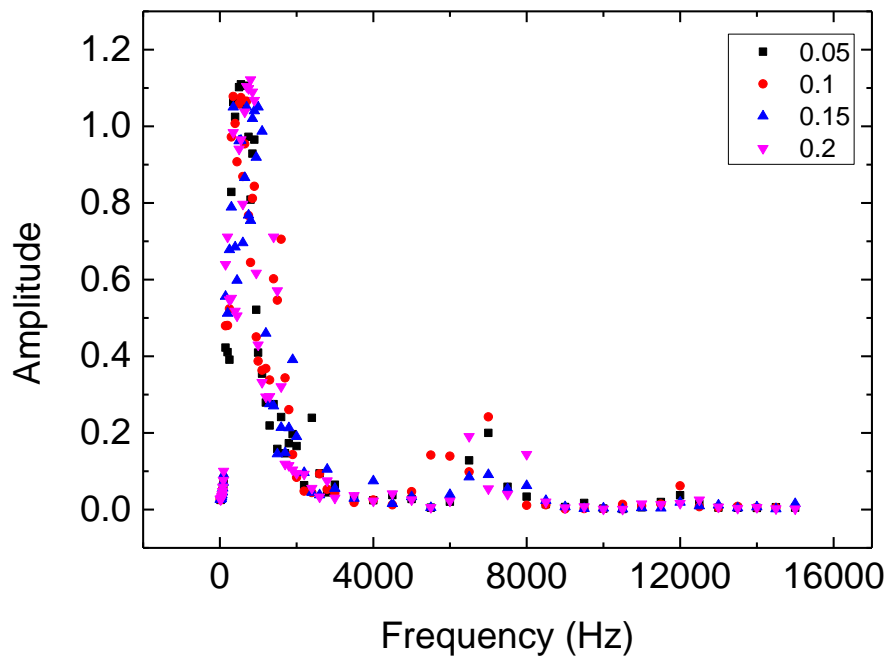


Figure 5-10 The deviation of amplitude with frequency over varying distances (m) from the actuator jet nozzle. The detector was positioned at the end of a stainless steel tube (OD 6 mm, ID 4 mm).

Following the above investigations, the actuator jet was connected to the various diffuser plates with the aim of bubble size reduction due to vibrations of the diffuser by the sonic wave. The connecting pipe was short (5 cm) and made from stainless steel, to maximise the amplitude of the wave and thus the potential effect of the synthetic actuator. The effect on bubble size is shown in Figure 5-11. It can be seen that there is no significant impact of the synthetic actuator jet on the mean bubble diameter at any frequency.

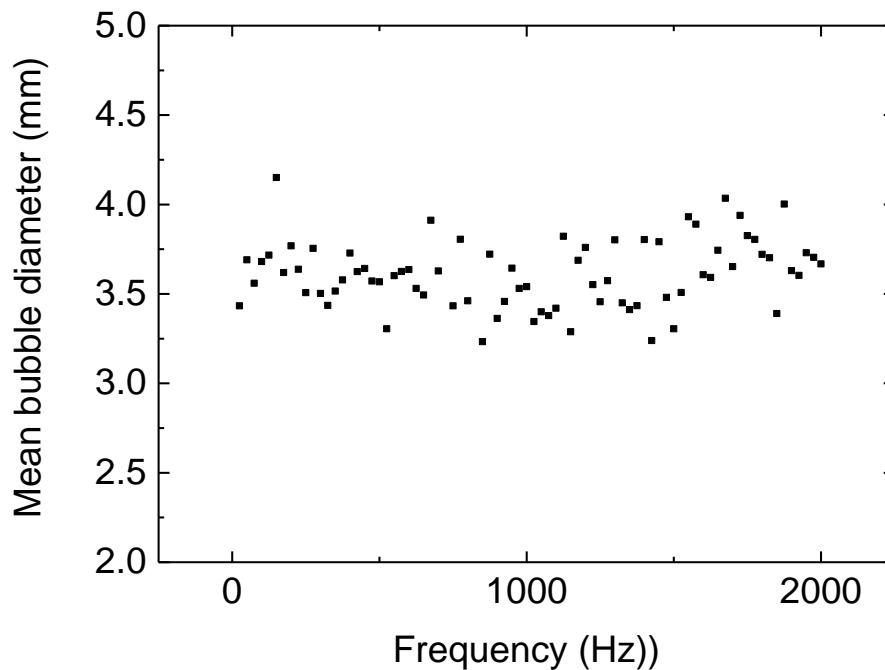


Figure 5-11 The effect of a frequency sweep by the synthetic actuator jet upon an unmodified stainless steel disk (25 mm diameter, 70 μm thick) with a single 250 μm pore at its centre.

5.4.2 The effect of fluidic oscillation on bubble formation.

Following on from the synthetic actuator jet work, the fluidic oscillator of Zimmerman and Tesar was placed in line. The first investigation was to probe the role of the flow rate into the fluidic oscillator at varying feedback loop lengths. The results are shown in Figure 5-12. It can be seen that as flow increases from 60 L/min to 100 L/min, the oscillating frequency shows minimal changes.

Figure 5-13 shows the influence of feedback loop, and thus oscillating frequency on bubble formation through a single pore. It can be seen that changing the feedback loop length

has little impact upon the size distribution of the bubble cloud. The mean bubble size at each feedback loop length is shown in Table 5-1.

Table 5-1 The deviation of bubble diameter with feedback loop length variation. Bubble formation was undertaken using a single 100 μm diameter pore through a 70 μm thick rolled stainless steel disk.

Feedback loop length (cm)	Oscillating frequency (Hz)	Mean bubble diameter (mm)
30	360	1.191 \pm 0.014
60	205	0.989 \pm 0.011
100	155	0.999 \pm 0.015
125	60	1.027 \pm 0.015
300	50	0.983 \pm 0.015

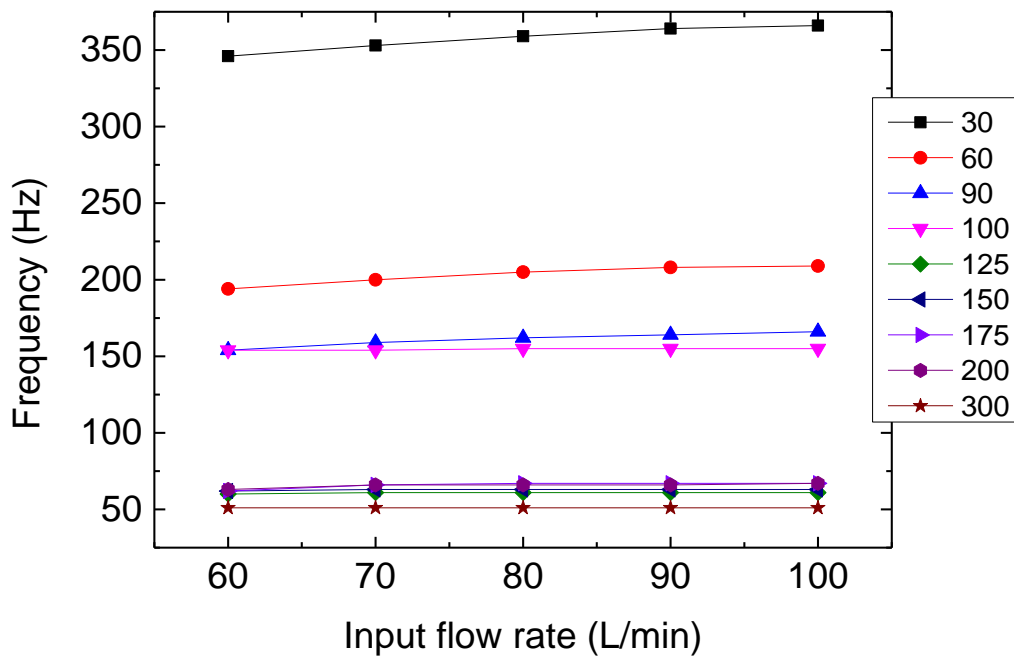


Figure 5-12 The effect of the input flow rate on oscillating frequency at various feedback loop lengths (30-300 mm).

Chapter 5: Bubbling under oscillating flow.

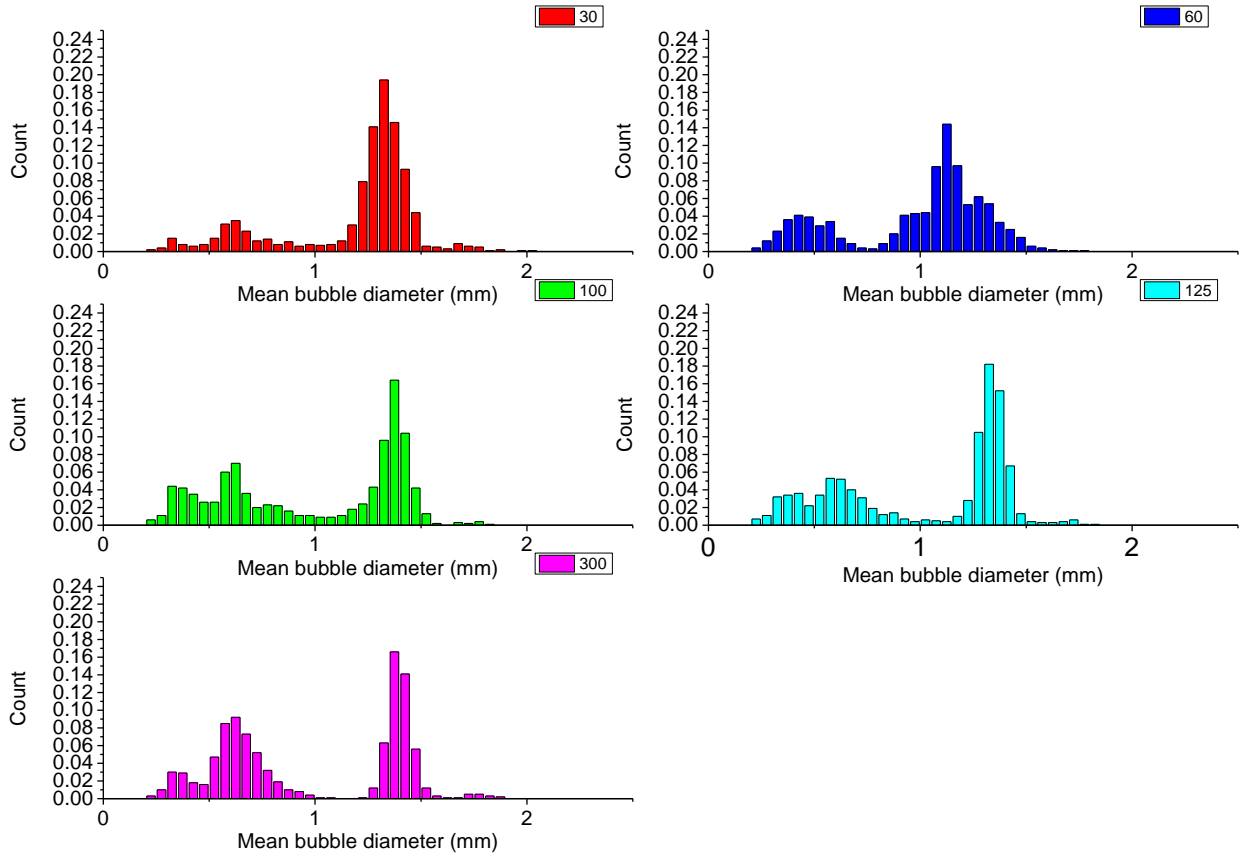


Figure 5-13 The effect of feedback loop length on bubble formation through a single 100 μm pore. The feedback loop was made from PET, PVC reinforced tube with ID=6.3 mm and OD=10.5 mm (RS components 368-0176, Northants, UK). The normalised counts are shown for each feedback loop length in the range of 30 cm to 300 cm.

Progression onto a plate with 7 100 μm pores has a similar outcome as shown in Table 5-2 and Figure 5-14. As is the case with the single pore, the 30 cm feedback loop (360 Hz) generated bubbles with slightly larger diameters than the other loops. However, the effect was negligible.

Chapter 5: Bubbling under oscillating flow.

Table 5-2 The deviation of bubble diameter with feedback loop length variation. Bubble formation was undertaken using an array of 7 100 µm diameter pores through a 70 µm thick rolled stainless steel disk.

Feedback loop length (cm)	Oscillating frequency (Hz)	Mean bubble diameter (mm)
30	360	1.751 ± 0.017
60	205	1.438 ± 0.015
100	155	1.555 ± 0.017
125	60	1.441 ± 0.016
300	50	1.468 ± 0.017

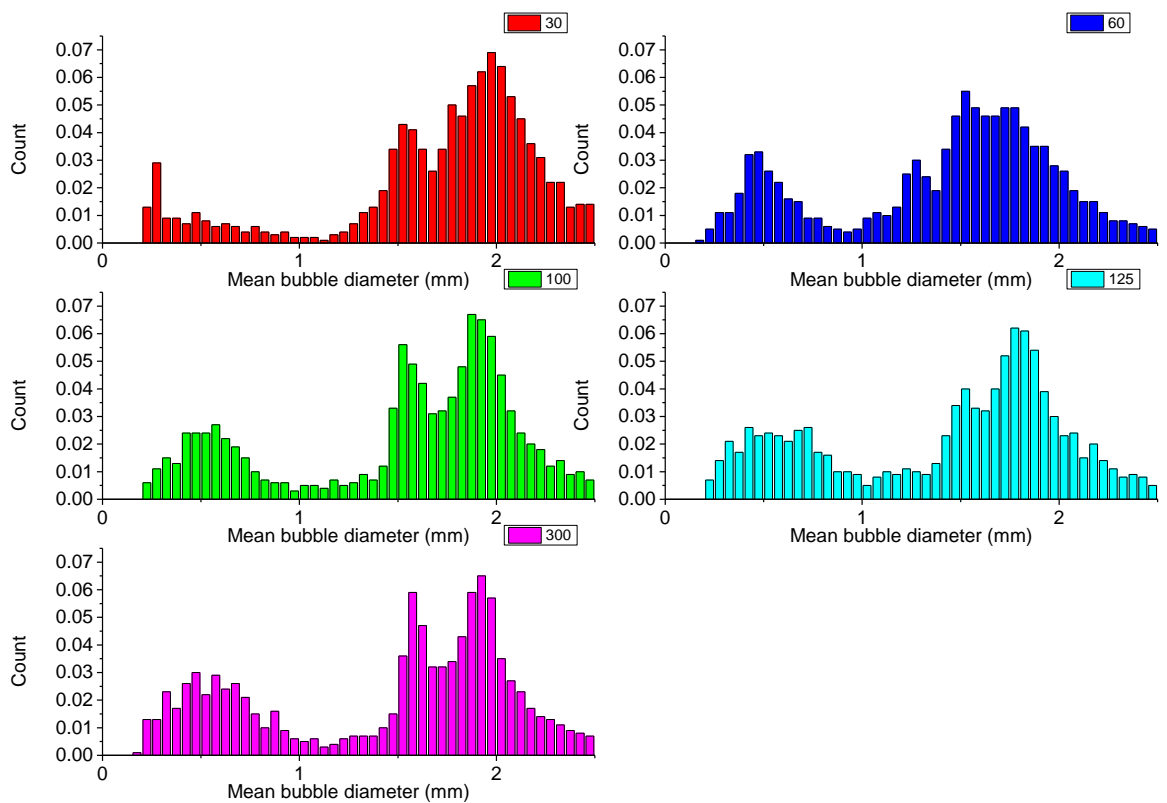


Figure 5-14 The effect of feedback loop length on bubble formation through an array of 7, 100 µm pores. The feedback loop was made from PET, PVC reinforced tube with ID=6.3 mm and OD=10.5 mm (RS components 368-0176, Northants, UK). The normalised counts are shown for each feedback loop length in the range of 30 cm to 300 cm.

5.4.3 Effect of surface chemistry on bubbles emitted from a single 250 μm pore under an oscillating flow.

Bubble formation under oscillatory flow is a far more complex scenario than formation under steady flow. The results of the initial study of bubbling through a single pore are shown in Figure 5-15. It can be seen that, unlike bubbling under steady flow, the surface chemistry no longer leads to any deviation between the hydrophilic ($\theta < 90^\circ$) and hydrophobic surfaces ($\theta > 90^\circ$).

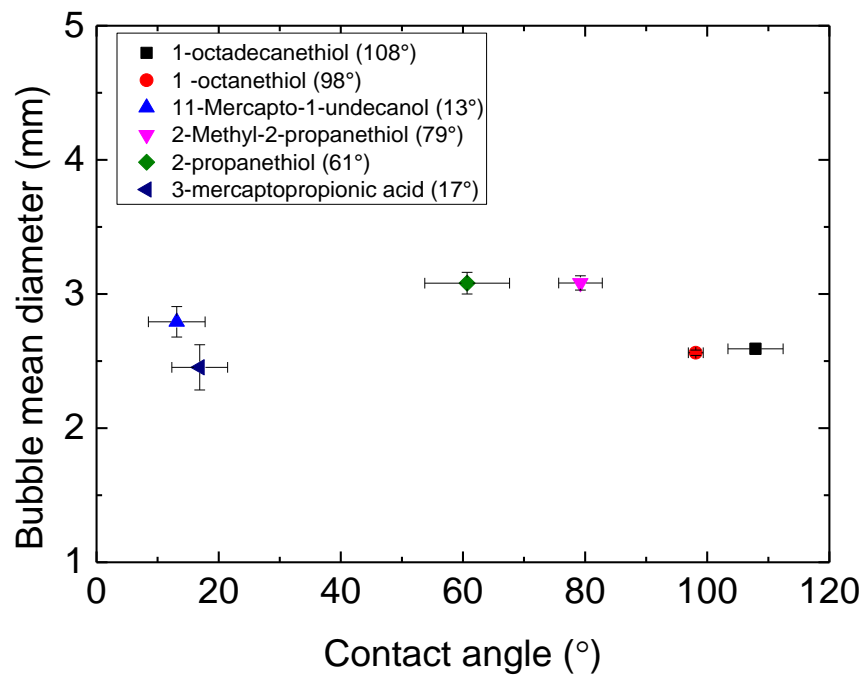


Figure 5-15 The dependence of bubble diameter on the contact angle of the surface at an oscillating flow rate of 1 mL/min through a 250 μm diameter single pore.

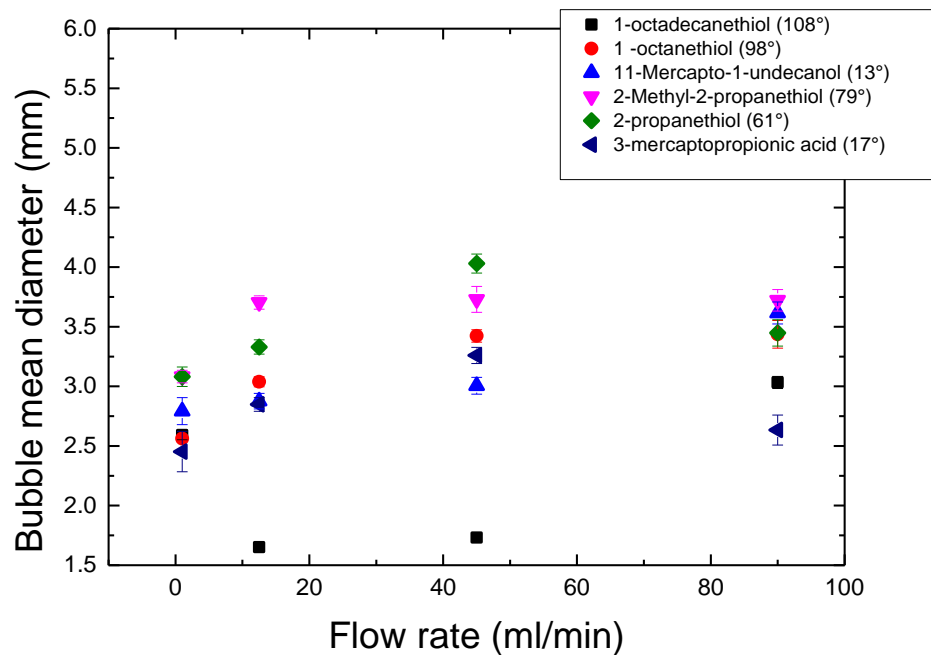


Figure 5-16 The dependence of bubble diameter on surface modification at various flow rates under oscillation, through a 250 μm diameter single pore.

Continuation of the study over a range of flow rates indicates how the fluidic oscillator acts to break the dependence on surface wettability discussed previously (Figure 5-16). Bubble size appears far more randomised as a result of oscillation with a significant reduction in the size of bubbles emitted from hydrophobic surfaces when compared to those emitted under steady flow, as shown in Figure 5-17. Statistical t-test analysis indicates that the surfaces modified with 1ODT ($t=93.96$), 1OT ($t=199.36$), 2PT ($t=9.65$), 2M2PT ($t=40.55$) and 3MPA ($t=18.41$) have less than a 0.1% probability that the difference in bubble size is due to chance. The 11MUD ($t=0.51$) difference is possibly down to chance however. These tests indicate that the oscillatory flow and the steady flow are significantly different. This is shown yet further when the analysis is extended over a wider range of flow rates as in Figure 5-18.

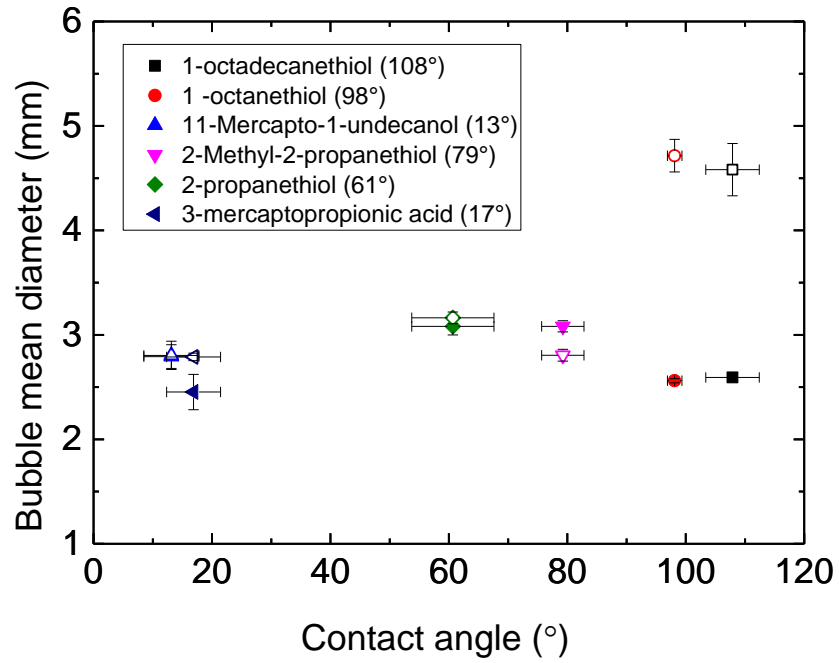


Figure 5-17 The dependence of bubble diameter on surface modification at low flow rates. Bubbling was performed under steady flow (open symbols, 2.5 mL/min) and oscillatory flow (filled symbols, 1 mL/min), through a 250 μm diameter single pore.

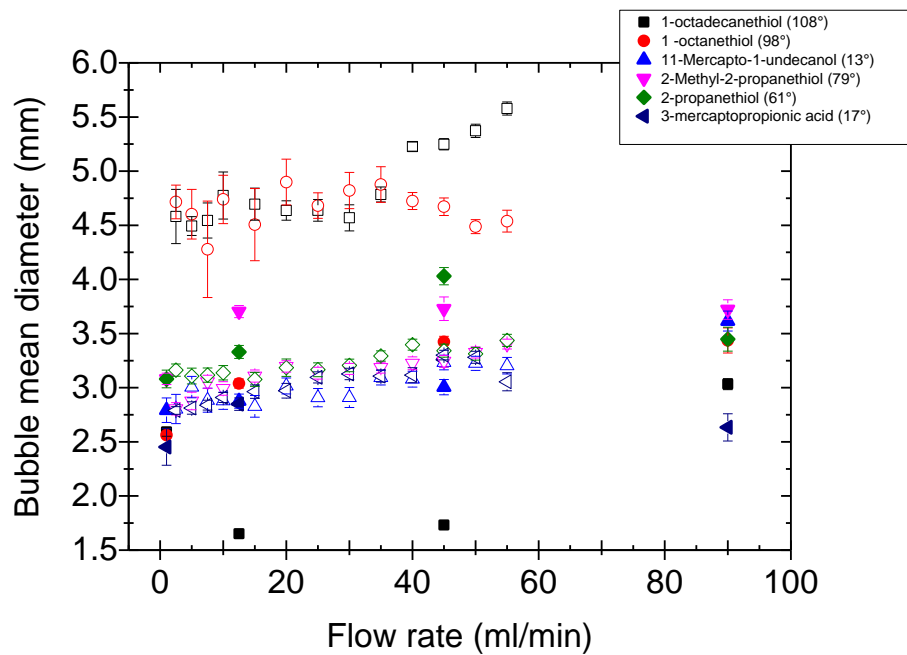


Figure 5-18 The dependence of bubble diameter on surface modification at various flow rates under steady flow (open symbols) and oscillatory flow (filled symbols), through a 250 μm diameter single pore.

The biggest feature of the study is the clear size reduction of the bubbles formed from surfaces with $\theta > 90^\circ$ when placed under oscillatory flow. The reason for this reduction is the pinning of the forming bubble to the pore by the fluidic oscillator. As can be seen from Figure 5-19 and Figure 5-20, the steady flow allows the bubble to readily spread over the hydrophobic surface, increasing the adhesion of the bubble and resulting in a larger buoyancy force to detach it from the surface. On the other hand, the bubble under oscillatory flow is prevented from spreading and thus the adhesion to the surface is maintained at a lower level.

The reduction in the anchoring force is the most obvious aspect of size reduction with the fluidic oscillator. However, there are additional equally important factors that may explain the ability of the oscillator to reduce bubble size from hydrophilic surfaces, or reduce the hydrophobic bubble size to below that of hydrophilic steady flow bubbles. Of vital importance to the size reduction is the negative pressure (suction) induced when the oscillator switches. Figure 5-19 shows this, where the bubble emerges from the pore and grows both vertically and horizontally (frames 1-5) into the observed pear shape. The oscillation then reverses and suction begins to take effect, rounding the top of the pear to give the egg shape of frame 6. Suction continues to draw gas from the bubble and its size reduces and the shape begins to approach sphericity (frame 7). The buoyancy force acting upon the bubble in an upward direction is opposed by the suction acting in the opposite direction, and the neck is elongated (frame 8) before the neck is broken and the bubble is detached (frames 9-16). This is in contrast to the mechanism observed under steady flow, where spreading across the surface is observed, and no suction acts upon the bubble, meaning it grows to a larger size as a result (Figure 5-20).

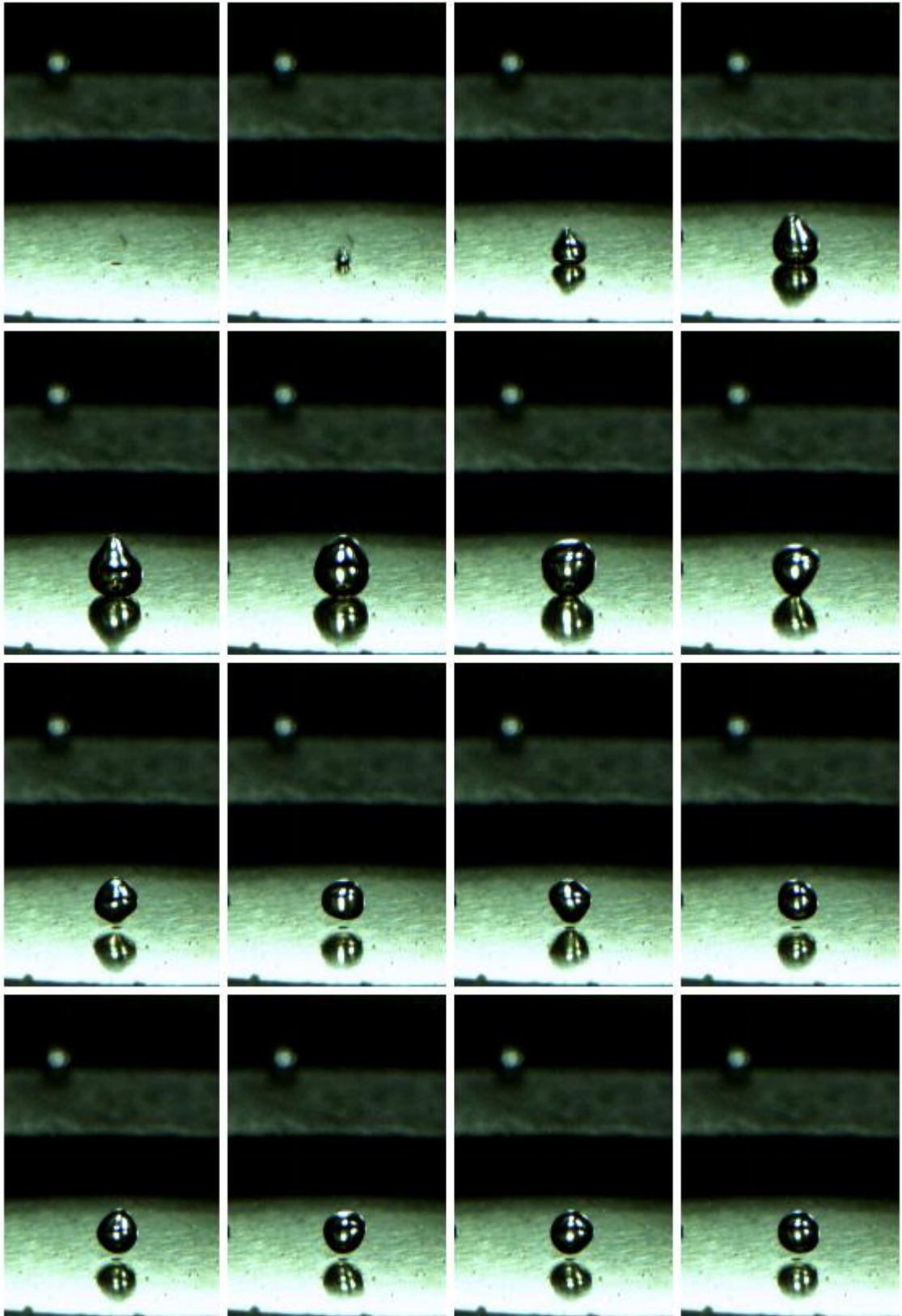


Figure 5-19 Bubble formation through a single 250 μm diameter pore. The surface is modified with 1OT and bubbling is under oscillatory flow at approximately 1 mL/min flow rate.

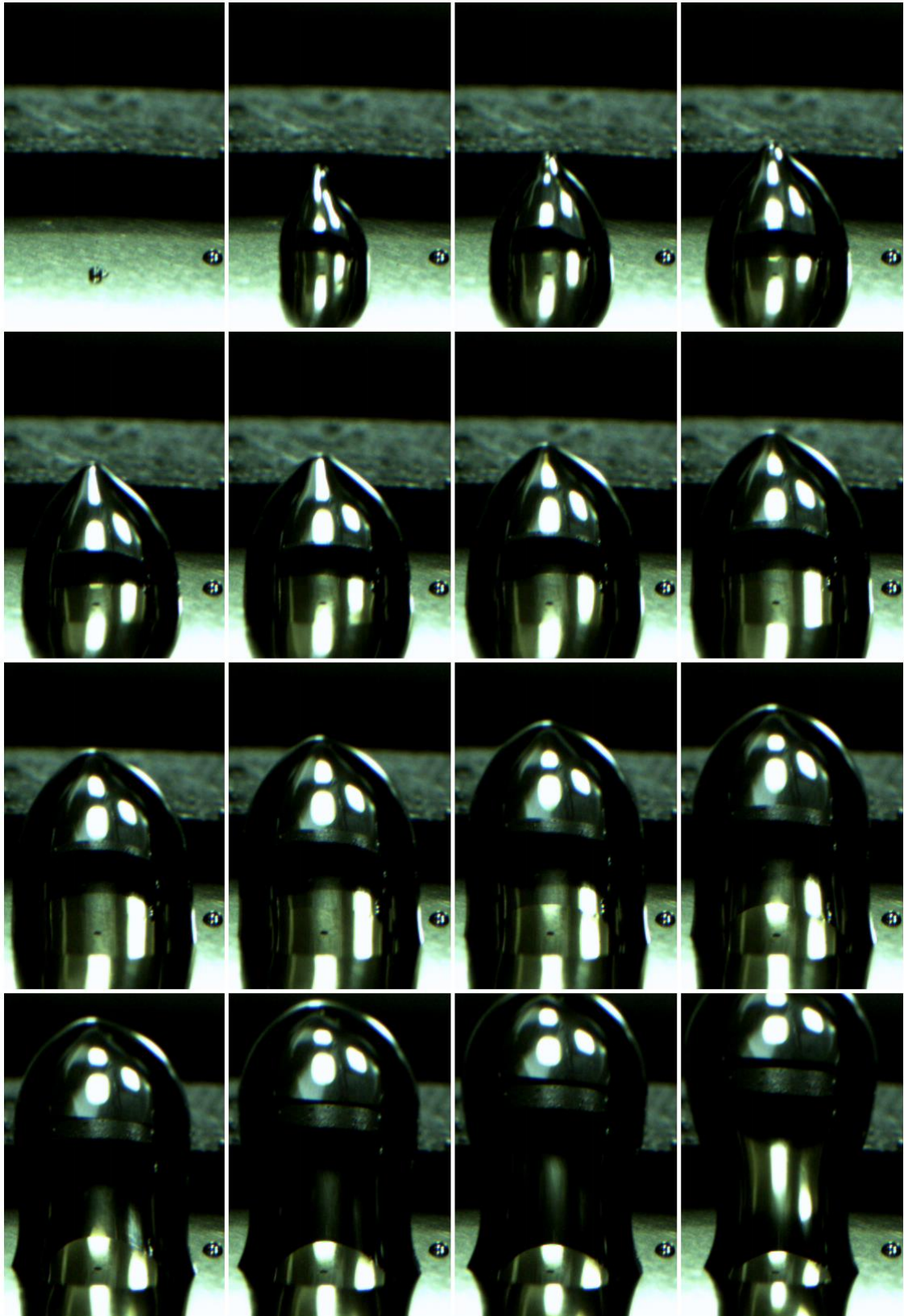


Figure 5-20 Bubble formation through a single 250 μm diameter pore. The surface is modified with 1OT and bubbling is under steady flow at 2.5 mL/min flow rate.

In addition to the negative pressure felt by the bubble, Shirota [14] has presented theories expressing the importance of the added mass force acting upon the bubble. This is expressed below in (35).

$$F_a = -\beta \frac{4}{3} \pi \rho \frac{d}{dt} \left(R^3 \frac{ds}{dt} \right) \quad (35)$$

Where ρ is the density of the liquid, β (11/16) is the added mass coefficient of a sphere moving in the vicinity of, and perpendicular to, a rigid boundary, R is the bubble radius and s is the height of the bubble centre point. It can be seen that under positive flow both the bubble radius and centre point position increase with time ($dR/dt > 0$, $ds/dt > 0$). Therefore F_a is strongly negative and so the added mass force opposes buoyancy, adding to the adhesion of the bubble to the pore. This is the case under steady flow and buoyancy is the dominant detaching force. Under the reverse flow, the radius of the bubble decreases with time ($dR/dt < 0$) and the added mass force becomes positive, adding to the buoyancy. As a result the bubble growth is limited to a smaller size before detachment, with Shirota indicating that the added mass force becomes around three times larger than buoyancy at the moment of detachment for the system under their investigation.

Despite the clear observation seen with hydrophobic surfaces, the hydrophilic surfaces are more complex. Figure 5-17 and Figure 5-18 show that oscillatory flow may also lead to a slight increase in bubble size from hydrophilically coated surfaces. As previously discussed, oscillation leads to an independence of bubble size to surface coating, and high speed photography can be used to postulate why this may be the case. Figure 5-21 shows how, under the negative pressure of the oscillating flow, the three phase contact line is below the diffuser plate with the breaking bubble neck passing through the pore to the chamber below. This effect was also seen in the work of Shirota. [14] The exact nature of this interaction is

unknown due to the opaque nature of the sample holder. However, a possible explanation of the increase in bubble size from a hydrophilic plate is discussed below.

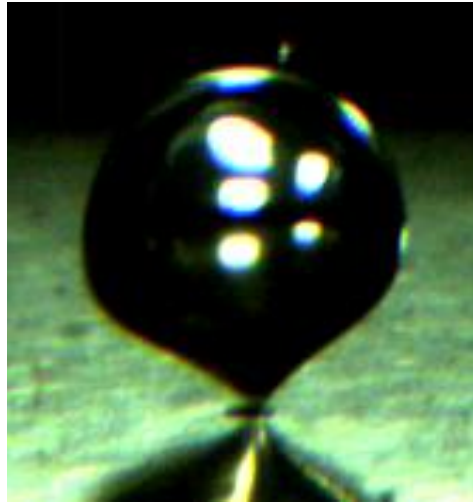


Figure 5-21 Production of a bubble from a 10T modified surface through a 250 μm pore. The thin neck of the bubble passes through the pore and the three phase contact line is below the orifice plane.

As discussed previously in reference to Figure 5-19, the initial stages of bubble formation proceed via a pear shaped bubble. This shape becomes even more elongated when progressing to a hydrophilic surface, as seen in Figure 5-22. This elongation increases the oscillation after detachment due to the bubble attempting to encapsulate the volume of gas within the shape of lowest surface tension, the sphere. These oscillations periodically bring the bottom of the detached bubble close to the pore, and if the following bubble forms at this instant, the likelihood of coalescence increases. This process is shown in Figure 5-23. The elongation observed by bubbles emitted from hydrophilic surfaces is far greater than the elongation of bubbles emitted from the hydrophobic surfaces as in Figure 5-19. The extra elongation leads to an increased probability of coalescence and production of larger bubbles. However, due to the unknown nature of the interactions below the porous plate at this time, it

is difficult to know for certain that the shape and coalescence effect is the major influence in large bubble formation from hydrophilic surfaces.^{g,h}

^g <https://youtu.be/1jgCJGyEwgM>

^h <https://youtu.be/ZkTlroh7nw>

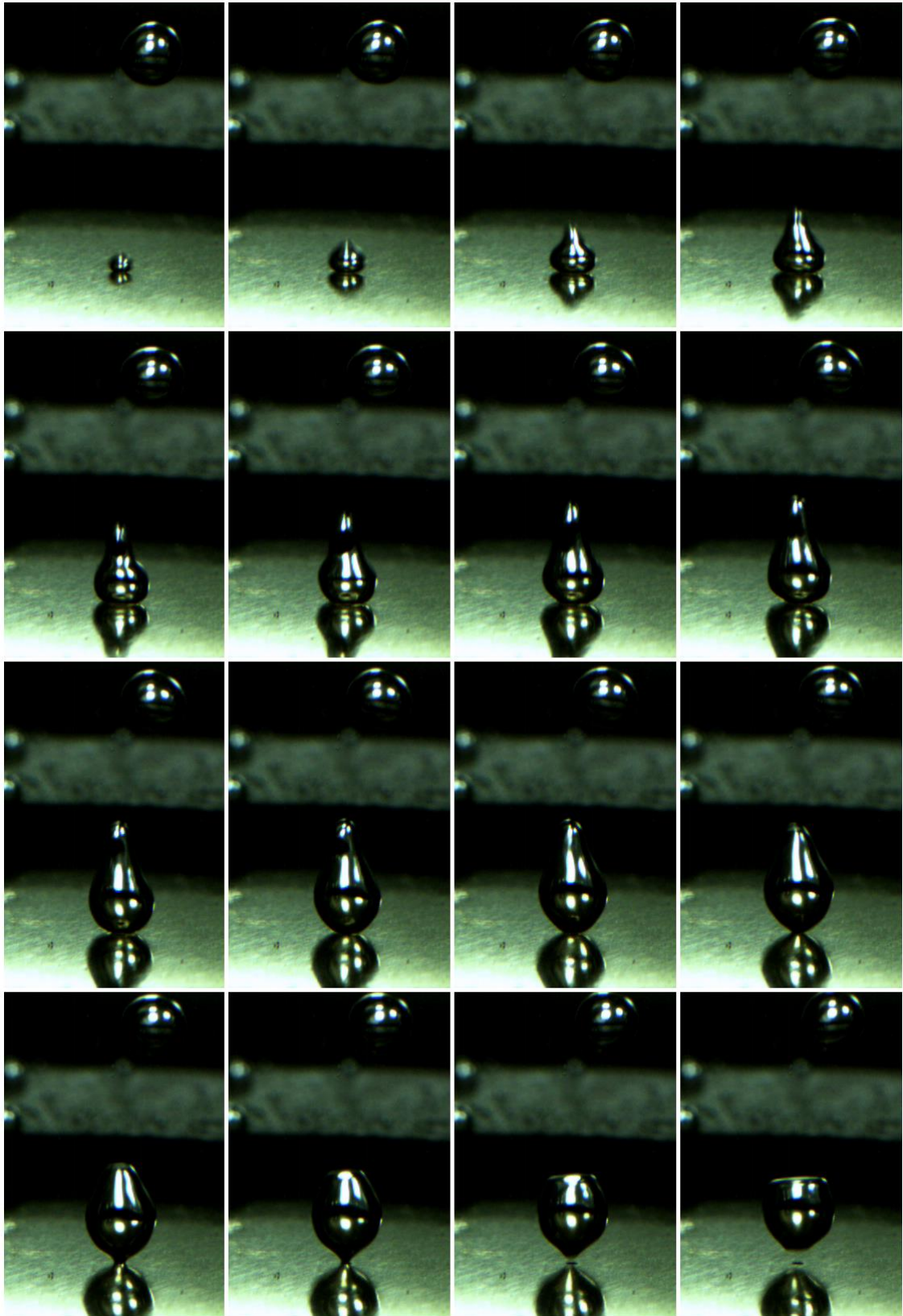


Figure 5-22 Bubble formation through a single 250 μm diameter pore. The surface is modified with 11MUD and bubbling is under oscillatory flow at approximately 1 mL/min flow rate.

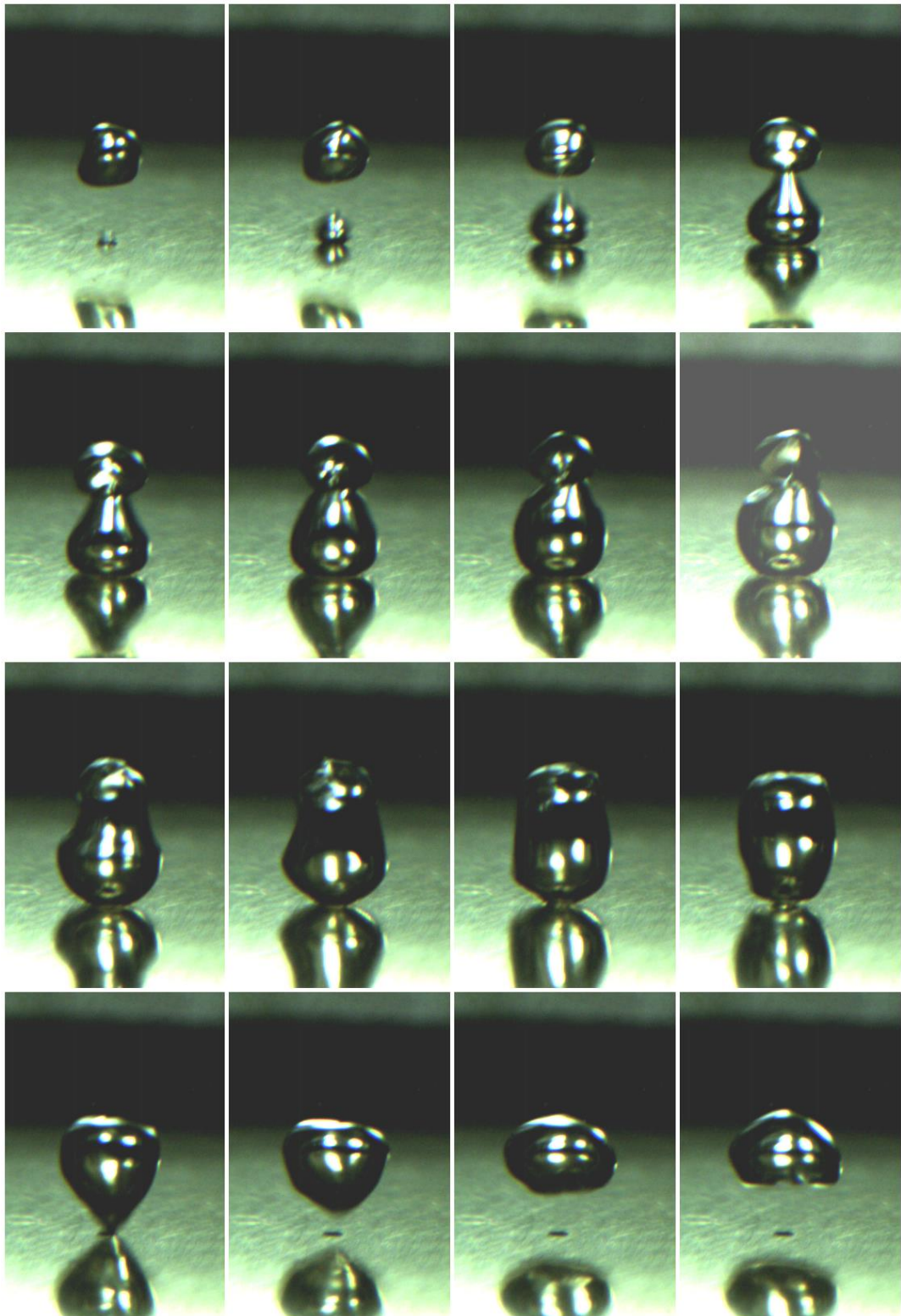


Figure 5-23 Bubble formation through a single 250 μm diameter pore. The surface is modified with 11MUD and bubbling is under oscillatory flow at approximately 1 mL/min flow rate. The second bubble elongates and catches the previous free bubble, causing coalescence and increasing bubble size.

5.4.4 Effect of surface chemistry on bubbles emitted from an array of 250 μm pores under an oscillating flow.

The observed effect from an array of 7 pores is very similar to that from a single pore with a clear reduction in bubble size from the hydrophobic surfaces but a lack of dependency upon surface chemistry (Figure 5-24). As is the case from a single pore, the reduction in bubble size from a surface modified with a hydrophobic coating is appreciable. Unlike steady flow, the oscillator prevents a single bubble encompassing all pores in the array, instead ensuring several pores produce separate bubbles. As is the case with steady flow, all pores are not simultaneously utilised in the oscillatory case. Also, the problem of coalescence above the diffuser plate is an issue that has yet to be resolved. However, comparing Figure 5-25 and Figure 5-26 the significant difference between the two cases can be clearly seen.

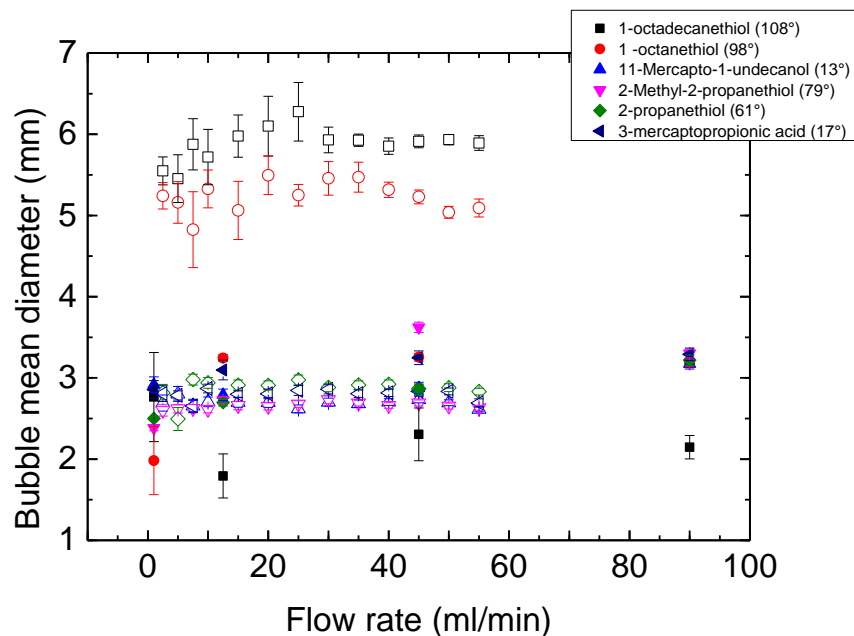


Figure 5-24 The dependence of bubble diameter on surface modification at various flow rates under steady flow (open symbols) and oscillatory flow (filled symbols), through an array of 7, 250 μm diameter pores.

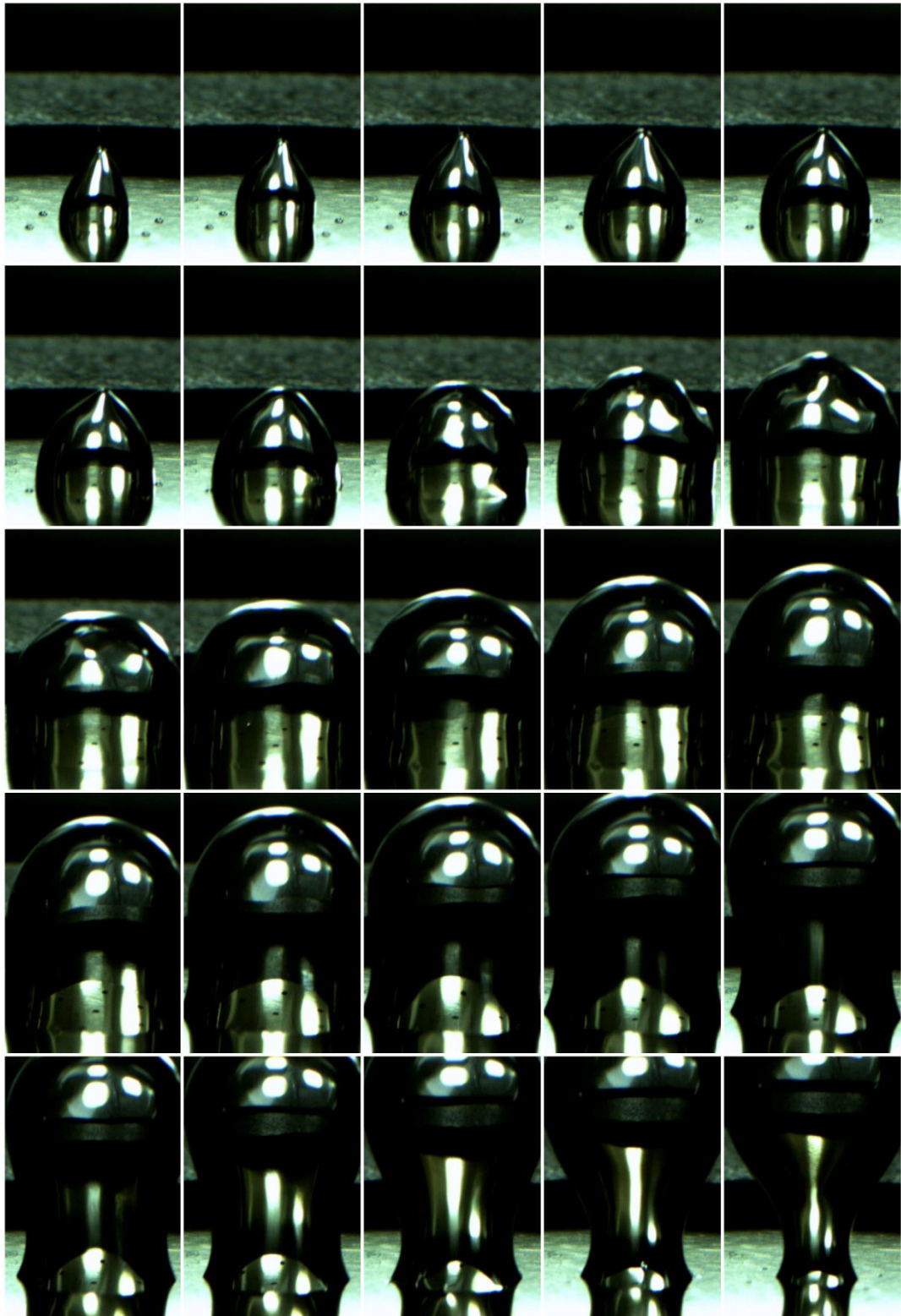


Figure 5-25 Bubble formation through an array of 7, 250 μm diameter pores. The surface is modified with 10T and bubbling is under steady flow at 2.5 mL/min flow rate. The bubble grows from a single pore before spreading to encompass all 7. It grows before buoyancy causes the bubble to rise and detach.

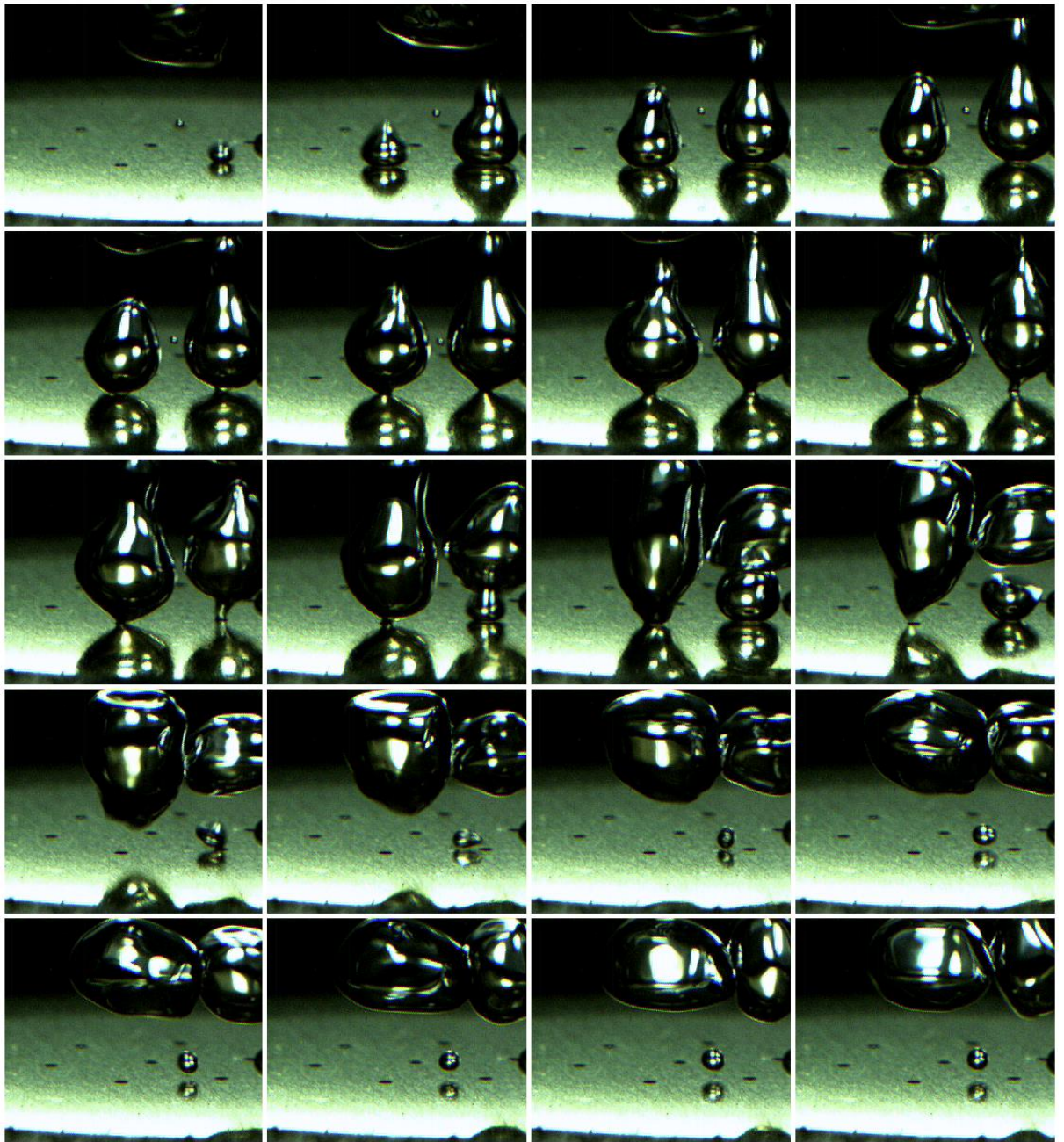


Figure 5-26 Bubble formation through an array of 7, 250 μm diameter pores. The surface is modified with 1OT and bubbling is under oscillatory flow at approximately 1 mL/min flow rate.

Bubbling occurs at multiple pores without spreading over the surface.

As is the case with a single pore, some of the hydrophilic surfaces yield larger bubbles under oscillation than under steady flow. Despite the hydrophilic plate under oscillation leading to more pores generating simultaneous bubbles, the elongation of the bubble seemed

Chapter 5: Bubbling under oscillating flow.

to promote coalescence just above the diffuser plate. The coalescence in this case appears to be the dominant factor in producing larger bubbles. The process is shown in Figure 5-27.

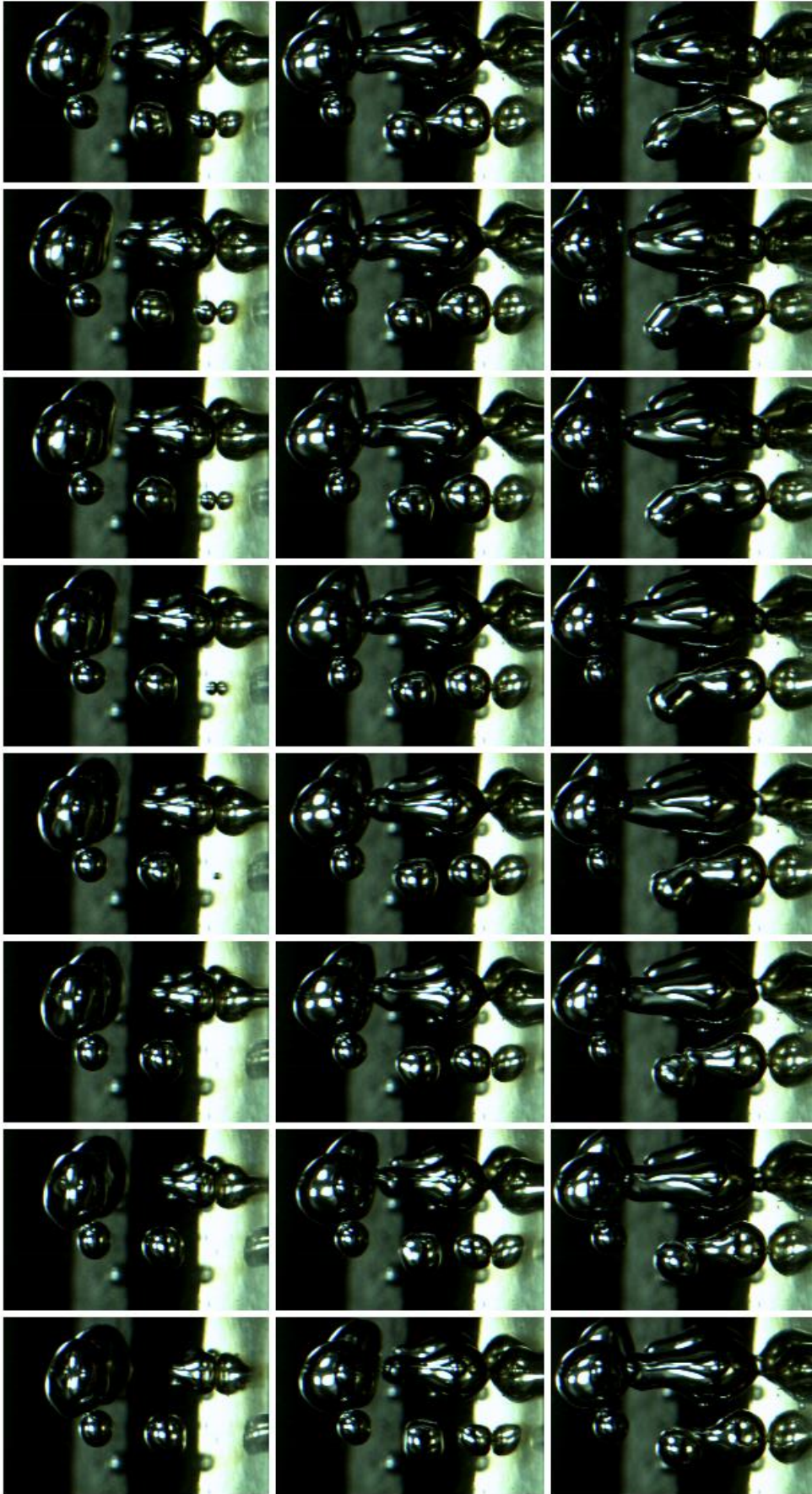


Figure 5-27 Bubble formation through an array of 7, 250 μm diameter pores. The surface is modified with 11MUD and bubbling is under oscillatory flow at approximately 1 mL/min flow rate. Bubbling occurs at multiple pores but the bubbles elongate into a pear shape leading to increased coalescence a short distance from the pore.

5.4.5 Effect of surface chemistry on bubbles emitted from a steel sinter with 5 μm pores under an oscillating flow.

The deviation in bubble size in relation to surface chemistry was most keenly observed under steady flow through a sintered steel diffuser. The results of fluidic oscillation are shown in Figure 5-28. It can be seen that no significant deviation occurs between the steady flow and the oscillatory flow and the clear dependence on surface wettability is visible. The sinters with hydrophobic coatings display a significantly larger bubble size than those with hydrophilic coatings. This would suggest that the flow is no longer oscillatory in nature at the exit to the sintered diffuser and has instead undergone significant dampening effects on its passage through the structure. ^{ij}

ⁱ <https://youtu.be/6HwO0BrRvG8>

^j <https://youtu.be/rWTNWikJoE0>

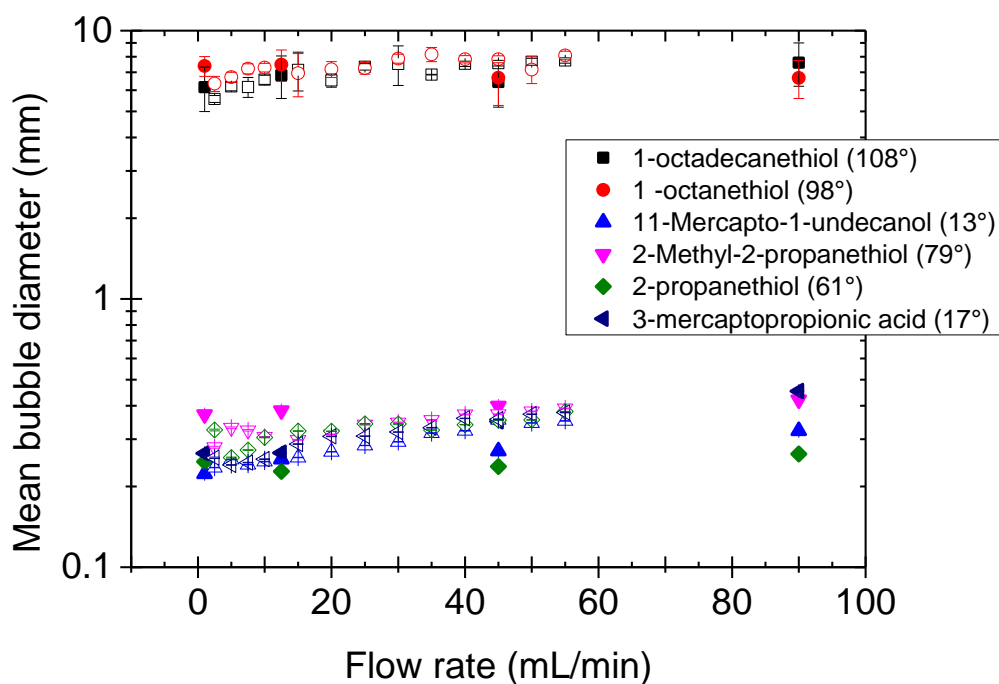


Figure 5-28 The dependence of bubble diameter on surface modification at various flow rates under steady flow (open symbols) and oscillatory flow (filled symbols), through a sintered stainless steel diffuser with a random array of 5 μm diameter pores.

5.4.6 Effect on surface chemistry on bubbles emitted from a ceramic 'pointfourTM' sinter under an oscillating flow.

Bubbling through ceramic pointfour diffusers modified with gold and thiols under oscillating flow maintained the dependence on surface chemistry (Figure 5-29), as seen with the steel sinters above. This would suggest a significant dampening effect by the porous ceramic upon the oscillating wave. Interestingly the oscillator seems to maintain the bubble size throughout a range of flow rates. The reasoning for this phenomenon is currently unknown, although the high bubble point pressure of the ceramic diffuser (1.4 bar) is thought to be influential, by having a large effect on the fluidic oscillator.

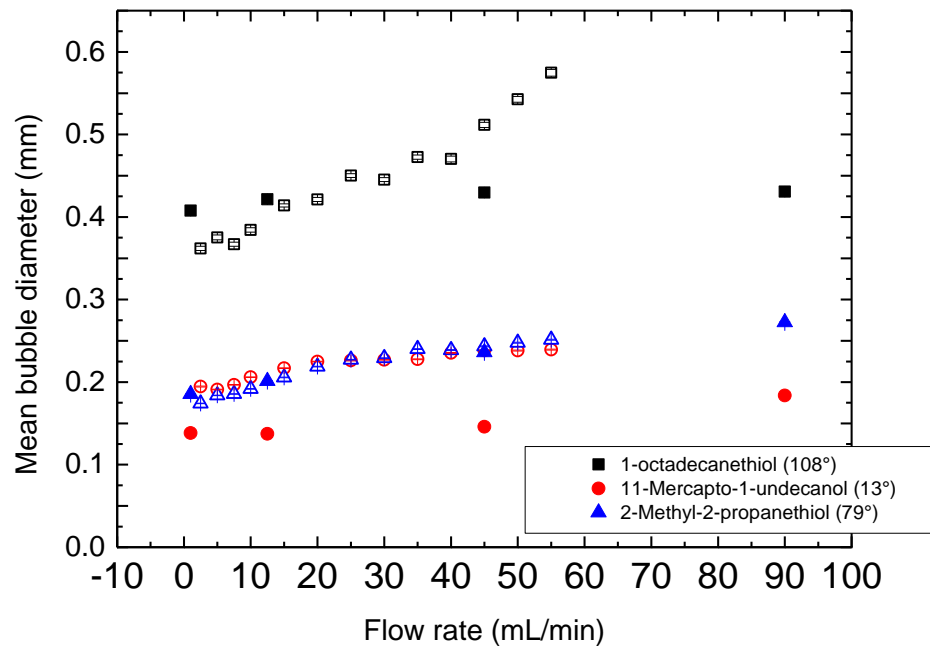


Figure 5-29 The dependence of bubble diameter on surface modification at various flow rates under steady flow (open symbols) and oscillatory flow (filled symbols), through a 3 mm thick sintered 'pointfour' ceramic disk with a close packed array of pores. The diffusers were coated by DC sputtering and thiol adsorption.

A similar dampening effect may be seen in the silane modified ceramic. Once again this may be due to pressure effects, but more work would be needed to corroborate the theory.^{k,l}

^k <https://youtu.be/0QcEFsPTs0E>

^l https://youtu.be/K_SMFtW4_WU

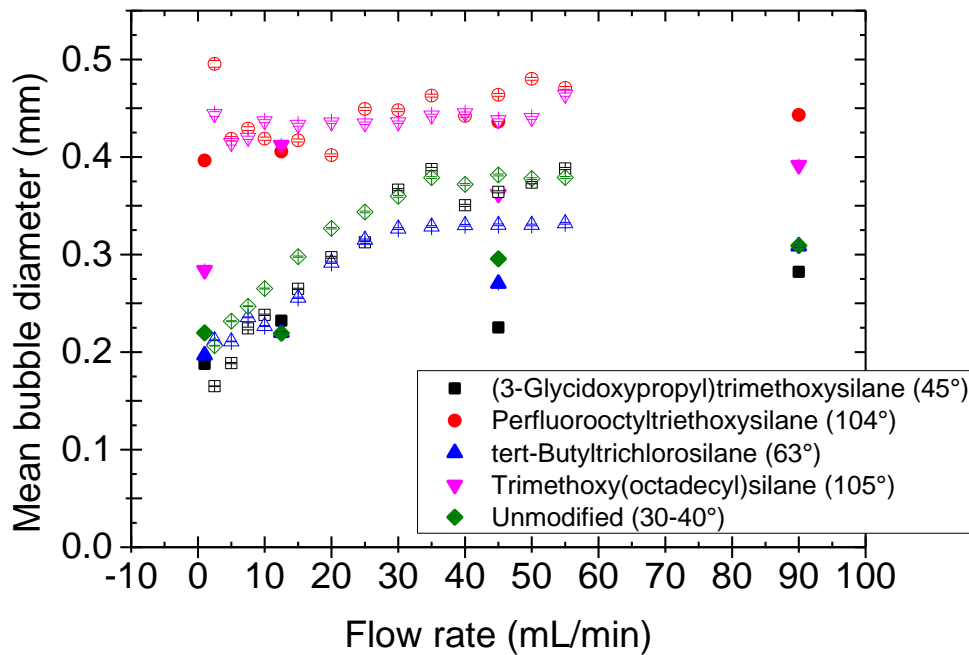


Figure 5-30 The dependence of bubble diameter on surface modification at various flow rates under steady flow (open symbols) and oscillatory flow (filled symbols), through a 3 mm thick sintered 'pointfour' ceramic disk with a close packed array of pores. The diffusers were modified by silanes.

5.5 Conclusions.

Bubbling was carried out under various forms of oscillation to investigate the combined influence of surface chemistry and oscillation upon bubble size and formation. A synthetic actuator jet was built based on the work of Tesar [2-4] and characterised under various conditions. It was found that the amplitude of the produced wave increased as the distance from the nozzle outlet decreased as may be expected. It was also found that the amplitude exhibited clear peaks at 1000 Hz and 6000 Hz, but the amplitude decreased markedly as frequency increased. This is probably due to the speakers' inefficiency and the cone not being able to move over its full distance of travel in the time period of one wavelength. Finally it was

found that switching to a metallic pipe from a polyimide tube increased the detected amplitude significantly. However, the oscillation generated did not lead to a noticeable influence on bubble size. This work holds some promise as exhibited by [2-4, 14] and more development of the setup could lead to it becoming a useful tool to probe frequency effects and lead to increased effectivity of the fluidic oscillator. In addition it could lead to modifications in system design to accommodate different fluidic oscillators and allow alterations to be made more readily and simply.

The fluidic oscillator of Zimmerman and Tesar [7] was characterised under numerous conditions. It was then implemented to investigate its effect on bubble formation. The effect on bubble formation through a 70 μm thick steel plate was marked, especially with regards to the plates modified with hydrophobic surface coatings. The bubble size from these surfaces was greatly reduced when compared to the same surfaces under steady flow. It is believed that the reduction is due to two main factors. The first is that the oscillation pins the bubble to the pore by moving the 3 phase contact line below the surface. This in turn means that the bubble cannot spread across the surface and thus the anchoring force is greatly reduced. The second factor is negative pressure imparted by the oscillatory flow. The suction leads to a suction of gas back from the bubble simultaneously with the bubble rise. The two opposing forces stretch the bubble neck and break it, leading to the observed reduction in size. Shirota [14] also believes that the added mass force switched direction during this negative flow, adding to the buoyancy and breaking the bubble off when it is smaller.

Addition of the fluidic oscillator to a similar hydrophilically coated surface has yielded a far more complex scenario. The forming bubble on a hydrophilic surface has the tendency to elongate considerably into what appears to be a stretched pear shape. This stretching coupled with the oscillation of the detached bubbles leads to an increased probability of coalescence. As a result, the average bubble size may increase compared to a steady flow scenario.

However if coalescence does not occur to any great extent, the average bubble size may equal that of the steady flow case, or even reduce. Similar overall effects were observed for both single pore systems and multi pore ones. This indicates the need for further work on diffuser design to eliminate or reduce the probability of coalescence and diminish bubble size as a result.

Application of the fluidic oscillator to thick sintered diffuser plates with a close packed array of pores had a less significant, if not negligible, effect on bubble size. It is believed that this is due to damping effects on the pulsed flow, typified by the lack of decrease in size from hydrophobic surfaces, as seen clearly in the thinner diffuser systems outlined above. Once again this indicates the need for careful diffuser design, with factors such as manufacturing limitations and cost to be included when designing a system.

5.6 References.

- [1] J. Lighthill, "Acoustic streaming," *Journal of sound and vibration*, vol. 61, pp. 391-418, 1978.
- [2] V. Tesař and J. Kordík, "Transition in synthetic jets," *Sensors and Actuators A: Physical*, vol. 187, pp. 105-117, 2012.
- [3] V. Tesař and J. Kordík, "Time-Mean Structure of Axisymmetric Synthetic Jets," *Sensors and Actuators A: Physical*, vol. 161, pp. 217-224, 2010.
- [4] V. Tesař and J. Kordík, "Two forward-flow regimes in actuator nozzles with large-amplitude pulsation," *Sensors and Actuators A: Physical*, vol. 191, pp. 34-44, 2013.
- [5] M. Amitay and A. Glezer, "Controlled transients of flow reattachment over stalled airfoils," *International Journal of Heat and Fluid Flow*, vol. 23, pp. 690-699, 2002.
- [6] J. Tensi, I. Boué, F. Paillé, and G. Dury, "Modification of the wake behind a circular cylinder by using synthetic jets," *Journal of Visualization*, vol. 5, pp. 37-44, 2002.
- [7] V. Tesař, C.-H. Hung, and W. B. Zimmerman, "No-moving-part hybrid-synthetic jet actuator," *Sensors and Actuators A: Physical*, vol. 125, pp. 159-169, 2006.
- [8] R. W. Warren, "Negative feedback oscillator," ed: Google Patents, 1964.
- [9] P. Dančová, V. Tesař, K. Peszynski, and P. Novontý, "Strangely behaving fluidic oscillator," *EPJ Web of Conferences*, vol. 45, p. 01074, 2013.
- [10] V. Tesař, "Configurations of fluidic actuators for generating hybrid-synthetic jets," *Sensors and Actuators A: Physical*, vol. 138, pp. 394-403, 2007.
- [11] C. E. Spyropoulos, "A sonic oscillator(Operational principles and characteristics of sonic oscillator- pneumatic clock pulse generator)," 1964., pp. 27-52, 1964.
- [12] V. Tesař, "Fluidic oscillator with bistable jet-type amplifier," ed: Google Patents, 2013.
- [13] R. W. Warren, "Fluid oscillator," ed: Google Patents, 1962.

- [14] M. Shirota, T. Sanada, A. Sato, and M. Watanabe, "Formation of a submillimeter bubble from an orifice using pulsed acoustic pressure waves in gas phase," *Physics of Fluids (1994-present)*, vol. 20, p. 043301, 2008.

Chapter 6: Conclusions and future work.

6.1 Conclusions.

From the work outlined here, it has been found several factors influence the modification of a surface to varying degrees. The first outcome is that prolonged immersion of silicon wafers in Piranha solution lead to no significant degradation in the SAM generated after cleaning. In addition, surface coating by physical vapour deposition techniques, namely Ebeam evaporation and DC sputtering, lead to a reduction in the mean roughness of the surfaces onto which the deposition occurred. However it was shown significant surface features can act to block regions of the surface from the Ebeam evaporation due to its line of sight nature. These regions of non-uniformity may act to destroy the homogeneity of the subsequently formed SAM, and thus alter the surface wettability on the macro scale.

In addition to the physical modification of the surfaces, it was shown numerous effects can play key roles in chemical modification steps, particularly where silanes are concerned. The first of these is solvent choice. It has been shown how deposition of silanes from solvents of differing polarity can act to change the macroscopic properties of the surface. For example, non polar heptane has been shown to be necessary to produce a well ordered SAM of aliphatic silanes. However significant reductions in SAM quality have been observed when aliphatic silanes are deposited from more polar ethanol and methanol. Therefore, it is important to consider solvent choice during surface modification. The second observation is that prolonged time immersed in silane solutions leads to multilayer build up, particularly when the silane tail group is polar (amine, amide, ester). These multilayers may be removed by further steps such as sonication, but it is recommended to remove substrates from silane solutions before 24 hours has elapsed to minimise this build up.

Attempts were made to relate an advancing and receding contact angle to a static angle, and thus link the sessile drop technique to the more dynamic bubble formation process. It was

found that application of the relationships described previously by both Tadmor and Chibowski and discussed in Section 3.3.8, generated a calculated static angles in good agreement with the measured sessile drop contact angles. Therefore, by measurement of the sessile drop, we can begin to relate the surface wettability to the bubble formation process.

Utilising the surface wettability information accrued, various diffusers were modified and bubbling experiments undertaken. The first set under steady flow yielded the observation of the key 90° contact angle. A surface with contact angles in excess of 90° yielded bubbles significantly larger than those emitted from a surface with a wettability below 90° . However, there appears to be no trend within these two regions. For example a surface with an 80° contact angle may yield smaller bubbles than a surface with a 15° angle. High speed photography has shown how the bubbles emitted from a hydrophilic surface are significantly smaller than those emitted from a hydrophobic surface close to the pore. However, bubbles are often emitted in clusters from a hydrophilically coated surface and rapidly coalesce before they begin to rise. It is believed the low pressure drop across the pore generated by small bubble emission leads to the reduction in time between bubbles and as such the apparent deviation in bubble sizes between the two types of surface is lessened as a result. Therefore more work is needed to eliminate this coalescence and minimise bubble size as a result.

Surface topography is also believed to be an important factor in the bubble formation process. It is believed increased roughness may lead to elevated plateaus and reduce the effect of surface chemistry by breaking the uniformity of the SAM and physically restricting the growing bubble. It has been shown previously how nozzles and needles exhibit less dependence on surface chemistry than a porous plate and it is believed elevated roughness leads to pseudo nozzle type behaviour.

Development of a synthetic actuator jet has been carried out with the aim of conducting frequency sweeps to ascertain the ideal oscillating frequency of the various systems under

investigation. Despite a clear development of harmonics within the system, the effect on bubble size was seen to be insignificant. However, progression to the fluidic oscillator of Zimmerman and Tesar has been shown to reduce bubble size, particularly of bubbles emitted from hydrophobic surfaces. It has been shown how the oscillator creates a negative pressure upon flow switching, which acts to suck a portion of air from the growing bubble and elongate the neck. The bubble cap continues to rise as the air is drawn back below the pore and the neck is stretched significantly before break off. This process also prevents the bubble from growing across the surface as seen previously under steady flow. The oscillator does not appear to show the same significant size reduction from a hydrophilic surface. The forming bubble on a hydrophilic surface has the tendency to elongate considerably into what appears to be a stretched pear shape. This stretching coupled with the oscillation of the detached bubbles leads to an increased probability of coalescence. As a result, the average bubble size may increase compared to a steady flow scenario. However if coalescence does not occur to any great extent, the average bubble size may equal that of the steady flow case, or even reduce. The 3 phase line shifts from the rim of the pore to below it, and the system utilised in these investigations did not allow visualisation of this. As a result more work is needed to fully understand the detachment process.

Finally, it has been shown the effect of the fluidic oscillator is reduced when bubbling through a thick, compact diffuser plate. Once again this illustrates the need to choose the setup carefully in order to minimise bubble size, with a balance between many factors influencing the formation process simultaneously.

6.2 Future work.

This investigation has yielded some important results concerning the influence of wettability on bubble formation, however, there is more that could be done to increase our understanding yet further. One of the most intriguing factors to come from this work is the influence of surface topography on the formation process from both hydrophilic and hydrophobic surfaces. The apparent reduction in bubble size emitted from a roughened hydrophobic surface warrants a more thorough study. A material with controlled roughness should be utilised as the diffuser plate and modified with similar techniques as those described here. It is believed increasing roughness and feature size will lead to a reduction in bubble size from hydrophobic surfaces but have considerably less effect on hydrophilic surfaces.

Another important question that has arisen is how to minimise the coalescence observed close to the pore when emission takes place from a hydrophilic surface. It has been seen here that bubbles are emitted in clusters and readily coalesce at the pore. Work is needed utilising high speed photography to investigate how factors such as pore orientation, flow rate, pressure and the method of gas delivery may be optimised to reduce bubble size to the maximum extent.

It would also be prevalent to extend this study over further materials and coating techniques to ensure the influence of the 90° contact angle remains. Materials which exhibit hydrophobicity (such as PTFE) could be used to examine the effect of surface chemistry when the underlying surface is hydrophobic. In addition, blended SAMs may be used to generate wettabilities between those exhibited here to ensure the trend continues over a more complete range. This range could extend to superhydrophobic materials, to investigate whether a secondary switching point is observed, or whether the bubble size would be comparable to those emitted from regular hydrophobic surfaces.

Chapter 6: Conclusions and future work.

Finally, it would be interesting to observe the position of the 3 phase line under fluidic oscillation. As discussed here, the line moves below the surface of the diffuser plate and hence could not be observed under the current conditions. However, utilising a Perspex/ glass diffuser mount, it may be possible to obtain high speed video data of bubble detachment below the pore. This would also lend credence to the theory that the oscillator generates a negative flow, with the neck elongation and detachment step proceeding as discussed here.

Chapter 7: Appendix.

7.1 The evolution of silicon cleaning technology.

Historically, the cleaning of silicon wafers has been based on hot alkaline or acidic/hydrogen peroxide based solutions. Several variants of this type of cleaning have been proposed, with the most common using an RCA clean, an IMEC clean and piranha solution: a strongly oxidising solution comprised of a mixture of sulphuric acid and hydrogen peroxide [1, 2].

In order to achieve high levels of cleaning to prepare silicon wafers for use in technologies such as electronics, it is important to understand the types of surface contamination silicon is susceptible to. In general there are said to be three main forms of contamination: discrete particles, contaminant films and adsorbed gases. [3] The particles and films are most important as adsorbed gases have little practical consequence on wafer processing. The films and particles can be classified as molecular compounds, ionic material or atomic species. These molecular compounds are composed of a variety of materials such as organic vapours, lubricants, greases, solvent residues and metal hydroxides and oxides. Interestingly, plastic containers within which the wafers are stored leach compounds from the polymeric structure (often polypropylene or polycarbonate) onto the silicon surfaces, indicating that the wafer will always need some form of cleaning before use. The ionic contaminants are usually inorganic species such as sodium or fluorine ions. They can be physisorbed or chemisorbed. [3]

In the past, large numbers of different approaches to the cleaning of silicon wafers have been taken. Organic solvent, boiling nitric acid, aqua regia, piranha solution, concentrated hydrofluoric acid (HF), UV/ozone and mixtures of sulphuric and chromic acids have all been used. None of these cleaning methods can successfully remove every type of impurity alone, and as a result must be combined in washing cycles to achieve the best results.

Some even re-contribute to the pollutant layer (chromic acid leaves chromium on the silicon surface) and cause disposal issues. [3]

These initial observations have led to the now commonly used cleaning techniques. The RCA clean was developed at the Radio Corporation of America (RCA) by Werner Kern [3] in the 1960s and 70s and is still commonly used today. It is based on peroxides but is multi step, combining both acidic and alkaline treatments in the same cycle. The first stage exposes the wafer to a hot mixture of hydrogen peroxide and ammonium hydroxide diluted with water. The alkaline solution removes many metal ions from group I and II but also gold, silver, copper, cadmium, zinc, nickel and chromium. This also removes organic matter from the wafer and leaves the silicon oxide surface exposed for stage 2. The second stage is to place the wafer into a hot mixture of hydrogen peroxide and hydrochloric acid diluted with water. This process removes further metal ions such as aluminium, iron and magnesium but also removes any insoluble hydroxides formed during the alkaline stage.

There are variants to the process, for example an initial dip in a 2:1 solution of sulphuric acid: hydrogen peroxide (Piranha Solution) removes visible organic contaminants. Also the way in which the clean is carried out varies. Often a simple dip of the wafer into the hot solutions is the preferred method, but duration for this dip varies depending on individual needs. Furthermore it has been suggested that a fused silica container should be used to house the solutions used for the dip cycle as there is the potential for leaching of aluminium, boron and alkalis if a Pyrex container is used. [4]

As well as the dip technique, other methods of introducing the cleaning solutions to the wafer have been suggested. The first is known as centrifugal spray cleaning, in which the wafers are spun past a stationary spray column. A lower volume of reagents is used in this process and it is faster than the dip technique but is no less efficient at removing contaminants. [3] However the machine used requires considerable maintenance.

Another system used is megasonic cleaning. This is where the wafer is submerged in a cleaning solution as outlined above. Ultra high frequency sonic energy is then used to scrub the wafer surfaces back and front and allows the removal of films and particles simultaneously. The process also allows the temperature of action to be lowered to around 40°C for many of the impurities.

Closed system chemical cleaning has also been developed. This is where the wafers are placed into a hydraulically controlled cassette which holds them stationary while passing a continuous sequential flow of both hot and cold cleaning solutions over them. The process eliminates the need for wafer removal from solution and thus the liquid gas phase boundary where recontamination issues may arise.

Once clean, the rinsing and drying procedure is also important to the purity of the finished product as clean wafers become re-contaminated very easily. Rinsing is often carried out simply using deionised water, but time periods of rinsing vary depending on the author. Again, several methods of drying have been proposed. Rinsing and drying in a closed system, via megasonic routes and by centrifugal spinning are advantageous because the wafer is not removed from the system in which it was cleaned, lessening the possibility of contamination. Other techniques include hot forced drying and capillary based drying, where single wafers are pulled out of deionised water at around 80°C, leaving less than 1% water on the wafer surface. This then evaporates to leave a particle free wafer. Solvent vapour drying is also used, where the wafers are passed through a vapour of high purity solvent, usually isopropyl alcohol (IPA). The solvent evaporates quickly to leave a particle free surface.

Another commonly used cleaning method is known as the IMEC clean, developed at the Interuniversity Microelectronics Center in Leuven, Belgium and summarised in Figure 7-1 below.

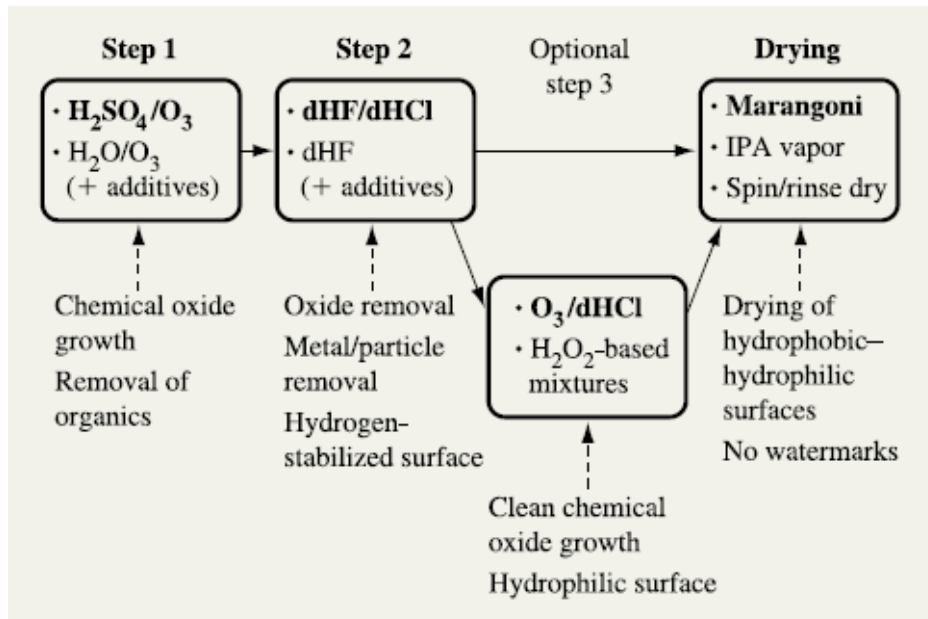


Figure 7-1 The basic scheme for an IMEC clean. [1]

During the first step, organic contaminants are removed from the wafer and a thin oxide layer is formed on it to prevent reattachment of unwanted compounds. However this oxide must be sufficiently thick to ensure that reattachment of organic contaminants does not occur. This step can be replaced with the use of ozonated deionised water, eliminating the need for a rinse step to remove residual sulphuric acid.

The second step acts to remove the oxide layer and any metal ions that may remain, however these conditions must be optimised to achieve the best results. This is because the HF solution may contain metal ions such as gold and copper which may deposit back onto the silicon surface if excessively long dipping times are used. The addition of hydrochloric acid suppresses the effect of metal outplating, especially copper, by forming copper chloride complexes.

The optional third step uses an optimised oxidising solution to make the silicon surface hydrophilic, thus leaving the wafer without drying spots or water marks generated during the drying process, and reducing the likelihood of metal redeposition.

The final rinsing and drying step is important in order to control the final amount of calcium deposited on the wafer. Adding small amounts of nitric acid to the rinse water helps lower the calcium deposition. It was also shown that increasing rinse times leads to an increase in the metal deposition, highlighting the need for careful control of the rinse process. [Table 7-1](#) and [Table 7-2](#) below, taken directly from work by Heyns et al [1], is a useful representation of a standard IMEC procedure as well as illustrating the differences between the RCA and IMEC cleans.

Table 7-1 Steps of a general IMEC clean. [1]

Step 1	H ₂ SO ₄ /O ₃ Three quick dump rinses (QDR, hot/cold)	90°C 60°C/20°C	5 min 8 min
or Step 1*	O ₃ /DI water	Optimized conditions	
Step 2	dHF (0.5%) /dHCl (0.5M)	22°C	2 min
Step 3	Final rinse + O ₃ /HCl (megasonic energy)	20°C	10 min
Drying	Marangoni drying (with HCl spiking)	20°C	8 min
Total cleaning time			32 min

Table 7-2 A comparison between RCA and IMEC cleaning results. [1]

Contaminant	Metal concentration on the wafer (10 ¹⁰ atoms/cm ²)			
	Ca	Fe	Cu	Zn
Initial concentration	154.4	5.6	4.4	1.8
Modified RCA clean	<0.26	0.2	0.4	0.2
IMEC clean	<0.26	0.1	<0.07	0.08

Over recent years, there has been more of an attempt to move away from the wet chemical cleaning and towards other methods of cleaning silicon wafers. Among the most efficient are UV cleaning and plasma enhanced cleaning. During the UV/ozone cleaning method the contaminants absorb short wave UV and dissociate. Simultaneously, the ozone molecules dissociate to form moieties which can react with the dissociated contaminants and form stable products such as water and carbon dioxide.

Choi et al [5] have shown using Attenuated Total Reflectance Fourier Transform Infrared Spectroscopy (ATR-FTIR) that organic contaminant levels fall when placed under UV conditions. Silicon surfaces are highly susceptible to organic contamination due to the strong polarity effects exhibited by the oxide surface. It is because of this polarity that contaminants with low molecular weight, low vapour pressure and polar groups can adhere readily to the silicon surface Figure 7-2.

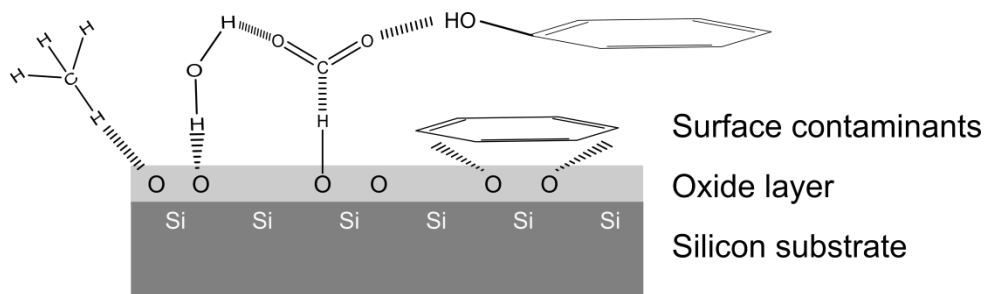


Figure 7-2 Schematic of Si oxide surface contaminants.

Many organic bonds can be dissociated using light with a wavelength of 253.7 nm.. This wavelength corresponds to an energy of 472.8 kJ/mol, enough to break the C-C, C-H and C-O bonds which require 347.69, 413.38 and 361 kJ/mol respectively to dissociate. Although the UV technique does not damage the surface excessively, prolonged use can lead to recontamination of the silicon surface.

Another technique investigated is known as Electron Cyclotron Resonance (ECR). The first subcategory of ECR utilises a hydrogen gas plasma and is known as ECR H₂ plasma cleaning. Unfortunately, due to the fact that hydrogen plasma has a low molecular weight, is neutral and low energy, it is very difficult to sputter off contaminants from the silicon surface. Furthermore, the strong hydrogen bonds formed between the silicon oxide surface and the

organic contaminants means that the removal of the oxide layer by the hydrogen plasma results in inefficient removal of contaminants.

A similar process is ECR O₂ plasma cleaning. Whilst the ECR H₂ clean takes around 10 minutes to reach the detection limit for ATR-FTIR, the ECR O₂ clean takes just 40 seconds. However, long exposure times leads to deleterious effects on the wafer surface. It has been suggested that this is because the oxygen plasma is significantly heavier and more energetic than the hydrogen plasma, thus collisions with the wafer surface cause substantial damage. It is therefore necessary to reach a balance between removing the organic contaminants and damaging the silicon surface. [2, 6, 7]

7.2 Surface created by variations in cleaning.

Different cleaning mechanisms result in changes to the silicon wafer surface. Surface roughness may occur along with etching and surface reconstruction. It was believed that washing in hydrofluoric acid (HF) led to a fluorinated surface. However it has been shown more recently that the resultant surface is hydrogenated, with subsequent exposure to air leading to a hydroxylated surface. The hydrogenised surfaces were investigated by Aswal [8] and are shown in Figure 7-3.

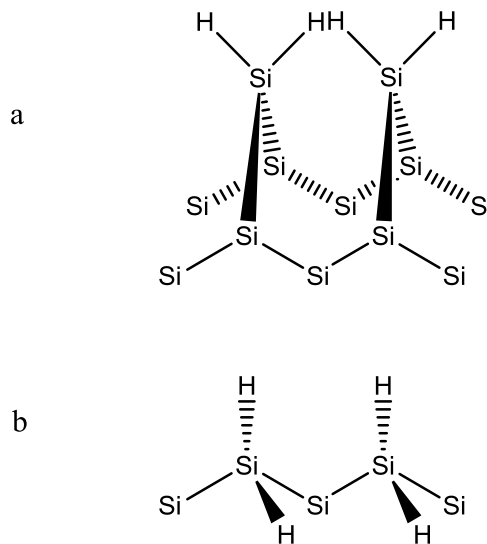


Figure 7-3 a) The dihydride formed by HF clean of Si. b) The monohydride formed. [8]

It is also possible to add halogens at the silicon surface for use in further reactions, an aspect of the surface discussed further by Aswal. However, cleaning of the wafer by the techniques outlined here yield a hydroxylated surface able to undergo silanisation.

7.3 References.

- [1] M. M. Heyns, T. Bearda, I. Cornelissen, S. De Gendt, R. Degraeve, G. Groeseneken, C. Kenens, D. M. Knotter, L. M. Loewenstein, P. W. Mertens, S. Mertens, M. Meuris, T. Nigam, M. Schaekers, I. Teerlinck, W. Vandervorst, R. Vos, and K. Wolke, "Cost-effective cleaning and high-quality thin gate oxides," *Ibm Journal of Research and Development*, vol. 43, pp. 339-350, May 1999.
- [2] M. Holmes, J. Keeley, K. Hurd, H. Schmidt, and A. Hawkins, "Optimized piranha etching process for SU8-based MEMS and MOEMS construction," *J Micromech Microeng*, vol. 20, pp. 1-8, Nov 1 2010.
- [3] W. Kern, "The evolution of silicon wafer cleaning technology," *Journal of the Electrochemical Society*, vol. 137, pp. 1887-1892, 1990.
- [4] P. Singer, "New directions in wet chemical processing," *Semiconductor International*, vol. 11, pp. 42-48, 1988.
- [5] K. Choi, S. Ghosh, J. Lim, and C. M. Lee, "Removal efficiency of organic contaminants on Si wafer by dry cleaning using UV/O-3 and ECR plasma," *Applied Surface Science*, vol. 206, pp. 355-364, Feb 2003.

- [6] C. Blumenstein, S. Meyer, A. Ruff, B. Schmid, J. Schaefer, and R. Claessen, "High purity chemical etching and thermal passivation process for Ge(001) as nanostructure template," *Journal of Chemical Physics*, vol. 135, Aug 14 2011.
- [7] J. A. Glass, E. A. Wovchko, and J. T. Yates, "Reaction of methanol with porous silicon," *Surface Science*, vol. 338, pp. 125-137, Sep 10 1995.
- [8] D. Aswal, S. Lenfant, D. Guerin, J. Yakhmi, and D. Vuillaume, "Self assembled monolayers on silicon for molecular electronics," *Analytica chimica acta*, vol. 568, pp. 84-108, 2006.

7.4 Derivations.

The full derivation of the first order Langmuir-Blodgett isotherm is shown below.

$$k_a p N (1 - \theta) = k_d N \theta \quad (36)$$

$$k_a p N (1 - \theta) = k_d N \theta \quad (37)$$

$$k_a p N = k_d N \theta + k_a p N \theta \quad (38)$$

$$k_a p = k_d \theta + k_a p \theta \quad (39)$$

$$k_a p = \theta (k_d + k_a p) \quad (40)$$

$$\theta = \frac{k_a p}{(k_d + k_a p)} \quad (41)$$

$$K = \frac{k_a}{k_d} \quad \theta = \frac{\frac{k_a p}{k_d}}{\left(\frac{k_d}{k_d} + \frac{k_a p}{k_d}\right)} \quad (42)$$

$$\theta = \frac{K p}{1 + K p} \quad (43)$$

The full derivation of the second order Langmuir-Blodgett isotherm is shown below.

$$\frac{d\theta}{dt} = k_a p (N(1 - \theta))^2 \quad (44)$$

$$\frac{d\theta}{dt} = k_d(N\theta)^2 \quad (45)$$

$$k_a p(N(1-\theta))^2 = k_d(N\theta)^2 \quad (46)$$

$$k_a^{1/2} p^{1/2} N(1-\theta) = k_d^{1/2} (N\theta) \quad (47)$$

$$k_a^{1/2} p^{1/2} = k_d^{1/2} \theta + k_a^{1/2} p^{1/2} \theta \quad (48)$$

$$K = \frac{k_a}{k_d} \quad \theta = \frac{k_a^{1/2} p^{1/2}}{k_d^{1/2} + k_a^{1/2} p^{1/2}} \quad (49)$$

$$\theta = \frac{(Kp)^{1/2}}{1 + (Kp)^{1/2}} \quad (50)$$

7.5 Publications.

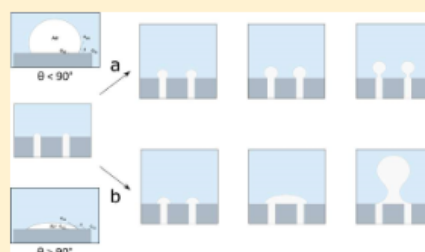
Influence of Surface Wettability on Microbubble Formation

Daniel J. Wesley, Rachel M. Smith, William B. Zimmerman, and Jonathan R. Howse*

Department of Chemical and Biological Engineering, University of Sheffield, Mappin Street, Sheffield S1 3JD, United Kingdom

Supporting Information

ABSTRACT: The production and utilization of microbubbles are rapidly becoming of major importance in a number of global applications, from biofuel production to medical imaging contrast agents. Many aspects of bubble formation have been studied, with diffuser characteristics (such as pore size, pore orientation) and gas flow rate all being shown to influence the bubble formation process. However, very little attention has been paid to the influence of surface wettability of the diffuser and the detailed role it plays at the triple interface of gas–liquid–diffuser. Here, we investigate how the wettability of the diffuser surface impacts upon the dynamics of the bubble formation process and examine the effect both at the orifice and upon the bubble cloud produced as a result of the engineered wetting variations. Experimental data shown here indicate the presence of a switching point at a contact angle of $\theta = 90^\circ$, where bubble size vastly changes. When a surface exhibits a contact angle below 90° , bubbles emitted from it are considerably smaller than those emitted from a surface with an angle in excess of 90° . This effect is observable over flow rates ranging from 2.5 to 60 mL min^{-1} from a single pore, an array of controlled pores, and the industrially relevant and commercially available sintered metals and sintered ceramic diffusers. It is also observed for both thiol and silane modified surfaces, encompassing a range of contact angles from 10° to 110° . In addition, the importance of the diffuser plate's surface topography is discussed, with elevated roughness acting to reduce the effect of surface chemistry in some instances.



INTRODUCTION AND BACKGROUND

Since the mid 1990s, bubbles have become an emerging theme within engineering, with the number of applications growing and diversifying into a wide range of areas such as biofuel production,^{1–6} microflotation,^{6–11} and medical imaging and drug delivery.^{12–18} More recently, the use of very small bubbles has become of great interest, with microbubbles, defined as being in the size range of 1–999 μm now being extensively studied and utilized.^{6,7,9,14,16,19–25}

From an engineering viewpoint, the appeal of microbubbles is relatively straightforward. They are desirable due to their high surface area (for a given gas volume) and possess an inherent ability to facilitate high levels of mass transfer, which is directly related to the interfacial area between two phases, as characterized by eq 1.

$$J = K_i S (c_g - c_l) \quad (1)$$

where J is the interphase mass transfer rate (mol s^{-1}), K_i is the mass transfer coefficient (m s^{-1}), S is the interfacial area (m^2), and c_g and c_l are the molar concentrations of gas and liquid, respectively.²⁶

Many current renewable energy sources, and in particular those centered upon biofuel production, still focus upon higher plant life, and as a result high levels of inefficiency are an inherent problem due to the poor conversion of solar energy to a pure form of chemical energy.¹ It is due to these inadequacies

that algae is of current interest to the scientific community, as it has the ability to efficiently convert solar energy into chemical energy sources such as cellulose, oils, and starch in high yields.^{1,27,28} Furthermore, algae have been shown to be able to produce other forms of fuel such as glycogen and hydrogen.^{1–5} As a result, the high mass transfer capability of microbubbles has been employed in algal growth and processing, and it has been shown that higher yields of both algae and biofuel can be attained through the application of microbubbles.^{7,8,11,29}

To maximize the biofuel production from algae, the photosynthesis process must be maximized. The algae must be subjected to elevated levels of CO_2 , while maintaining the exposure to sunlight. Zimmerman et al.²⁶ have commented upon the design of an airlift loop bioreactor (ALB), which has been reviewed more thoroughly by Jones.³⁰ These ALBs are perceived to be more efficient than the other variants used for algal growth, and they hold great promise for further study.²⁶ To create microbubbles, and improve mass transfer, the reactor utilizes the oscillating flow created by the fluidic oscillator of Zimmerman and Tesar^{31–34} to generate bubbles with a mean diameter of 300 μm , raising CO_2 levels to above the 380 ppm of atmospheric air. Work by Hanotu⁷ and Ying⁸ has shown a

Received: October 7, 2015

Revised: January 11, 2016

30–40% enhancement in algal growth with the application of microbubbles. Pilot scale studies by Zimmerman, utilizing CO₂ from the combustion of waste exhaust gases emitted during steel production, showed how the microbubbles efficiently stripped deleterious oxygen from the reactor during the growth regime, increasing algal proliferation.

The separation and harvesting of algae from the growing medium is also one of the key challenges to the commercial viability of biofuel production. Gudin³⁵ estimates that the harvesting step could account for 20–30% of the total energy usage in biofuel production, although Molina stipulates this figure could be much higher, and as large as 60%.²⁹ Historically separation has been carried out by flocculation and bioflocculation followed by sedimentation. Development routes for algal separation include using the Jameson cell in an induced air flotation (IAF) step, dissolved air flotation (DAF), and dispersed air flotation, which offer the possibility of >95% separation. However, all of these techniques have drawbacks when compared to microflotation. Microbubble generation by a robust technique, such as the fluidic oscillator systems presented by Zimmerman and Tesar,^{31–33,36} have proven to be a breakthrough in energy efficient separation. The “no moving part” nature and robustness of the oscillator leads to energy usage 2 or 3 times lower than that used in DAF and dispersed air flotation, for example.¹¹ In the work by Hanotu,¹¹ microflotation was presented as a viable alternative for algal separation, finding separation efficiencies of more than 96% could be achieved with the fluidic oscillator, in addition to the significant energy saving.

Despite the increasing interest in microbubbles, the ability to control bubble formation to create monodisperse bubble clouds with a chosen bubble size is still lacking. Many factors such as pore size, pore orientation, surface tension, and flow rate influence bubble size and formation. Many groups have alluded to the importance of wettability on bubble formation, but very few fundamental studies exist on the effect of surface wettability on bubble size, especially in aqueous systems.^{37–45}

It is important, and prudent, to recognize the substrate from which the bubbles are emitted plays a vital role in their formation. Bubbles created by a nozzle, capillary, or needle have a small surface around the orifice meaning the effect of surface wettability is greatly reduced, and in some cases negated altogether. This is exemplified by Zhu,⁴⁶ who used both a glass capillary and a polytetrafluoroethylene (PTFE) capillary. They found the departure time from the glass capillary was longer than that of the PTFE, which is in contrast to the observations of Corchero.⁴² Bubbles emitted from a hydrophobic surface are significantly larger than those emitted from a hydrophilic surface, implying an increased adhesive component of the force balance during bubble growth from a hydrophobic surface, and thus a prolonged growth phase and departure time.

Gerlach⁴¹ modeled the process of bubble formation at a submerged orifice, finding that if the bubbles' instantaneous contact angle during growth becomes equal to the Young's contact angle (as defined in Figure 1, where the contact is shown as the angle made by the fluid touching the solid surface), found under equilibrium conditions, the bubble can grow outward from the pore onto the surface of the diffuser plate. Yasuda^{44,45} corroborates this hypothesis, and suggests maintaining the surface contact angle at $\theta < 45^\circ$ prevents the bubble from growing past the orifice boundary. This view is further supported by Kukizaki,^{37,43} who modified Shirasu porous glass (SPG) membranes with silanes. Unlike other

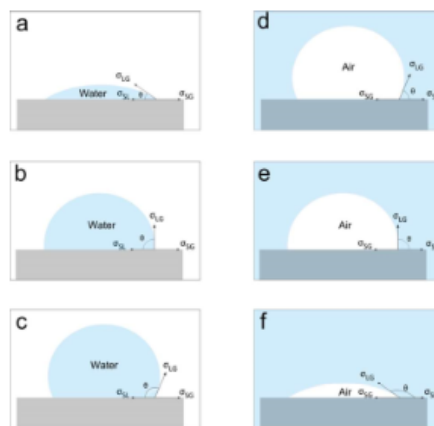


Figure 1. Contact angles (θ) of a sessile liquid drop (water) on a solid horizontal surface in air, (a) $\theta < 90^\circ$, (b) $\theta = 90^\circ$, and (c) $\theta > 90^\circ$; and an air bubble sitting on a solid surface in water, (d) $\theta < 90^\circ$, (e) $\theta = 90^\circ$, and (f) $\theta > 90^\circ$.

studies that used single, controlled pores, SPG is a sintered glass powder with a random distribution of numerous small pores. Using organosilanes, Kukizaki modified the surface of the SPG to yield a variety of surface wettabilities before bubbling and agrees with the importance of a 45° contact angle.³⁷

Many groups agree that the bubble volume at detachment from a surface with $\theta > 90^\circ$ is significantly larger than those from surfaces with $\theta < 90^\circ$.^{38–41} Corchero⁴² carried out wettability experiments using a combination of acrylic and Teflon plates, drilled to contain a single pore of between 0.5 and 1 mm in diameter. They reported static contact angles of 68° and 123° , respectively. To create an intermediate surface with $\theta = 90^\circ$, domestic Vaseline was smeared onto the surface, and, as a result, it was observed that surface wettability played an important role in bubble formation. The volume of the bubbles produced from the acrylic sheet ($\theta = 68^\circ$) is lower than that of the Vaseline ($\theta = 90^\circ$) and the Teflon ($\theta = 123^\circ$). However, the flow rates for the three systems under investigation were not equivalent, which is likely to greatly influence the result, nor is the quality of the intermediate contact angle surface of sufficient quality or robustness to allow for full insight into the underlying phenomena.

These studies provide a brief insight into the role of surface wettability, with two dominant theories being postulated: that the contact angle of the surface must be maintained at $<45^\circ$ or alternatively $>90^\circ$, to restrict the bubble to the rim of the pore and minimize bubble size, with the results summarized in Table 1. However, they are somewhat incomplete due to the limited nature of the surface coatings and the type of porous diffuser utilized.

Shirota et al.⁴⁷ have conducted theoretical studies to calculate the expected bubble size based upon pore size and both the density and the surface tension of the liquid into which they are emitted. Under “quasi steady” bubble production, where the gas flow rate tends to zero, the bubble experiences only buoyancy and surface tension effects. The relationship is shown in eq 2,

B

DOI: 10.1021/acs.langmuir.5b03743
Langmuir XXXX, XXX, XXX–XXX

Table 1. Summary of Previous Studies on the Influence of Wettability on Bubble Formation

author	diffuser type	pore size (μm)	contact angles studied (deg)	conclusion to minimize bubble size
Kukizaki ⁴³	Shirasu porous glass, multiple randomized pores	1.0, 3.1, 5.0, 10.0	8, 13, 22, 55	$\Theta < 45^\circ$
Yasuda ⁴⁴	stainless steel single pore	250, 550	5, 70	$\Theta < 45^\circ$
Byakova ⁴⁹	acrylic sheet single pore	400, 700, 1000	68, 90, 110	$\Theta < 90^\circ$
Byakova ⁴⁸	acrylic sheet single pore	1000	68, 90, 110	$\Theta < 90^\circ$
Corchero ⁴²	acrylic sheet/Teflon (PTFE) sheet single pore	500, 1000	68, 90, 123	$\Theta < 90^\circ$

where R is the predicted bubble radius (m), d is the diameter of the pore (m), σ is the surface tension of the liquid (N m^{-1}), ρ is the density of the liquid (kg m^{-3}), and g is the acceleration due to gravity. For a diffuser with a single 250 μm diameter pore, emitting bubbles into distilled water in a quasi steady state, the theoretical bubble radius is calculated to be 1.1 mm, a diameter nearly an order of magnitude greater than the pore itself. Although the bubbling experiments herein deviate from the steady state, this provides a simplistic hypothetical value for the bubble size. Note also that this treatment does not include a term for the three-phase interface, and neglects any wetting effects that allow the bubble attachment area to grow beyond the physical size of the pore itself.

$$R = \left(\frac{3d\sigma}{4\rho g} \right)^{1/3} \quad (2)$$

It is the aim of this Article to outline a more thorough study, using well-established wet chemical techniques to modify surface chemistry. Bubble formation from a single pore, multiple well-defined pores, and both sintered ceramic and sintered metal diffusers, with randomized networks of pores, will be discussed, with comparisons between the effect of surface chemistry at various flow rates being investigated.

EXPERIMENTAL SECTION

Materials. All chemicals were of reagent grade and were used as received unless otherwise stated. The following silanes and thiols were obtained from Sigma-Aldrich: *tert*-butyltrichlorosilane (*t*-Bu), trimethoxy(octadecyl)silane (TMODS), 1H,1H,2H,2H-perfluorooctyltriethoxysilane (PFO) and (3-glycidyloxypropyl)trimethoxysilane (3GTMS), 1-octadecanethio (1ODT), 98%, 1-octanethiol (1OT), 98.5%, 2-methyl-2-propanethiol (2M2PT), 99%, 2-propanethiol (2PT), >98%, 3-mercaptopropionic acid (3MPA), 99%, and 11-mercaptoundecanol (11MUD), 98%. *n*-Heptane (HPLC, 99%) was obtained from Fisher Scientific, and ethanol (GC) > 99.8% was obtained from Sigma-Aldrich and used as received unless stated.

Twenty-five mm diameter, rolled stainless steel disks (70 μm thick) were obtained from Photofabrication services Ltd. (UK) with 250 μm circular holes etched through the disk. A single pore was etched through the center to create the "single pore" disks. A pattern of 7 holes was etched through the disks to give a central hole with a hexagonal group of holes surrounding it, with a center to center distance of 2.25 mm between all adjacent holes.

Sintered steel disks (25 mm Diameter, 3 mm thick) were obtained from Hengko Technology Co. Ltd. (Shenzhen City, China) with a random array of pores with a mean diameter of 5 μm .

Point-four micro bubble diffuser plate was obtained from Pentair Aquatic eco-systems and cut into 25 mm diameter disks with a thickness of 3 mm. X-ray photoelectron spectroscopy (XPS) on the disks after shaping found an aluminosilicate structure with 11% hydroxyl group content. These hydroxyls will be modified by silanization, and thus the whole diffuser will have the modification applied, not just the top surface as with thiol modification.

Surface Modification. Silicon test wafer was cut into 1 \times 6 cm strips by the score and snap method and wiped clean with ethanol before being blown dry under a stream of compressed air and placed into a Pyrex container. Piranha solution (400 mL, 1:1 v/v, $\text{H}_2\text{O}_2:\text{H}_2\text{SO}_4$) was added and left for 1 h before being removed and washed with copious amounts of deionized water (Elga Purelab Option filtration system 15 M Ω cm). The clean samples were then blown dry under a stream of dry nitrogen and were then ready for silanization.

Clean dry Si samples were placed into a metal evaporator (Moorfield minilab 080) and coated by DC sputter deposition with chromium (10 nm, 0.158 A, 287 V, rate: 0.14 $\text{\AA}/\text{s}$) and a subsequent coating of gold (100 nm, 0.118 A, 359 V, rate: 0.45 $\text{\AA}/\text{s}$) at an argon pressure of 6.3×10^{-8} bar.

Thiol solutions (3 mM) were made up by dissolution of the thiol compounds listed above in 50 mL of ethanol that had been deoxygenated via nitrogen bubbling for 30 min. Freshly gold-coated wafer was immersed in the solution for 18 h. It was then removed and rinsed thoroughly with ethanol and dried under nitrogen before sessile drop contact angle measurements were carried out.

Silane solutions (3 mM) were made up by dissolution of the silane compounds listed above in 50 mL of heptane. Clean dry wafer was placed into an oxygen plasma (Diener Zepto plasma cleaner) for 10 min before being immersed in the solution for 24 h. It was then removed and rinsed thoroughly with heptane and dried under nitrogen before sessile drop contact angle measurements were carried out.

Contact Angle Goniometry. This was performed with a First Ten Angstroms FTA200 series goniometer. A microsyringe with 27 gauge flat tipped needle (ID 0.254 mm, OD 0.406 mm) was used to apply a 3 μL drop of 15 M Ω cm deionized water (Elga Purelab Option filtration system) onto the sample surface. An image was captured on a Lumenera infinity 2 camera with 2.0 megapixel CCD sensor at a resolution of 696 \times 520 pixels. Post capture analysis was performed using LabVIEW software written by the authors and calibrated with FTA standards. For the purposes of this Article, contact angles quoted during bubbling investigations are those of a sessile water droplet. Self-assembled monolayer (SAM) stability has been discussed extensively in the literature, with no observable deviation in contact angle for both silane and thiol SAMs under a variety of conditions.^{48–51}

Bubble Formation. This was carried out by passing compressed air (supplied by an in-house system) through the diffusers, with flow rate controlled by a Bronkhorst EL series F-201CV mass flow controller. Video for bubble size analysis was captured using a Mikrotron MC1363 Eosens camera with a 22.9 mm CMOS chip (14 μm square pixel size) at a resolution of 1280 \times 1024 pixels and 30 fps. Images for bubble size analysis were obtained 30 cm above the porous plate (see Supporting Information for images). Post capture analysis was carried out using LabVIEW. Mean bubble size was determined by the average of the longest (major) bubble radius and the smallest (minor) bubble radius. The arithmetic mean was then taken of all bubbles imaged throughout the data set.

High speed video was captured using the same Mikrotron Eosens camera as above, but at a resolution of ca. 280 \times 410 pixels and frame rates of ca. 4000 fps. Illumination was provided by an array of 7 Bridgelux BXRA-56C9000-J-00 high brightness LEDs (cool white, 5600 K, 9000 lm). The system was focused on the plane running through the center of the diffuser.

Pressure behind the pores was measured using a Digatron P200 H manometer and was taken at the bubble point pressure. For the single pore and 7 pore systems, the pressure was measured as 38 mbar (the pressure increased slightly for the single pore as flow rate increased). For the steel sinter, it was 200 mbar, and the point-four diffuser was 1.4 bar.

C

DOI: 10.1021/acs.langmuir.5b03743
Langmuir XXXX, XXX, XXX–XXX

Table 2. Summary of Diffuser Type and Modification Techniques Utilized in This Study

diffuser	material	pore structure	pore size (μm)	physical modification	chemical modification
photofabrication steel disk	rolled stainless steel	single	250	DC sputtered gold coating	thiol
photofabrication steel disk	rolled stainless steel	7 pores	250	DC sputtered gold coating	thiol
Hengko steel diffuser	sintered steel	multiple, randomized	5	DC sputtered gold coating	thiol
point-four diffuser	sintered ceramic	multiple, randomized	<5	DC sputtered gold coating	thiol
point-four diffuser	sintered ceramic	multiple, randomized	<5	e-beam evaporated gold coating	thiol
point-four diffuser	sintered ceramic	multiple, randomized	<5	none	silane

Steel disks, steel sinters, and point-four sinters were cleaned in an oxygen plasma (Diener Zepto plasma cleaner) for 10 min. All were coated via DC sputtering and immersed into thiol solutions as described above.

One set of point-four diffusers was coated by DC sputtering as outlined above. A second set of diffusers was coated by electron beam evaporation (e-beam). The base pressure of the chamber was taken to $<1 \times 10^{-9}$ bar, and evaporation was carried out. First, a chromium (Cr) adhesion layer was added to the Si at a 10 nm thickness (4 mA, 10 kV, rate: 0.15 Å/s) followed by a 100 nm gold layer (44 mA, 10 kV, rate: 2.4 Å/s). Both sample sets were immersed in thiol solution for 18 h. They were then removed and rinsed thoroughly with ethanol and dried under nitrogen before sessile drop contact angle measurements were carried out. A third set of clean dry diffusers was immersed in silane solutions (50 mL of heptane, 3 mM) for 24 h under ambient conditions before removal. Upon removal, each piece was rinsed with the parent solvent before being immersed in 50 mL of fresh solvent and placed in an ultrasonic bath for 30 s at 25 °C to remove physically adsorbed layers. A final rinse with further fresh solvent and drying by a stream of nitrogen followed before samples were left in an oven at 45 °C for 2 h to remove residual solvent.

Table 2 summarizes the diffusers utilized during this study and both the pore structure and the modifications performed on each.

RESULTS AND DISCUSSION

Sessile drop contact angle data were obtained to quantify the wettability of each surface by water. The photofabrication services steel disks (PFD) were tested, and the data are summarized in Table 3 along with the data for both silane and thiol modified Si wafers.

As expected, the aliphatic silanes and thiols give contact angles greater than 90°, due to the close packed, well-ordered nature of the self-assembled monolayer (SAM).^{52–55} The steric hindrance experienced by the *t*-Bu and 2PT, accompanied by

Table 3. Contact Angle of a Sessile Water Droplet on a Stainless Steel Disk and Si Wafer Modified by Gold Coating and Thiol Treatment ($n = 10$) \pm 1 Standard Deviation and also Silane Modified Si Wafer ($n = 10$) \pm 1 Standard Deviation^a

chemical type	chemical name ^b	stainless steel disk contact angle (deg)	Si wafer contact angle (deg)
thiol	1ODT	107.9 \pm 4.2	94.0 \pm 3.0
	1OT	98.1 \pm 1.2	89.5 \pm 2.8
	2M2PT	79.2 \pm 3.6	63.9 \pm 3.1
	2PT	60.6 \pm 6.9	68.2 \pm 1.7
	3MPA	16.9 \pm 4.6	25.2 \pm 2.9
	11MUD	13.1 \pm 4.6	17.5 \pm 1.5
silane	3GPTMS	n/a	44.5 \pm 5.6
	PFO	n/a	104.2 \pm 2.7
	<i>t</i> -Bu	n/a	62.9 \pm 2.0
	TMOS	n/a	104.9 \pm 1.8

^aImages for all scenarios are shown in the Supporting Information.

^bSee text for abbreviations.

the short chain lengths, leads to a disruption to the packing of these molecules within a SAM. The result is a decrease in the contact angle from those of long chain aliphatics by around 10–15° due to the exposure of the surface. Finally, the silanes and thiols with polar end groups generate contact angles <20°. Angles below 20° are more sensitive to surface defects than the higher angles, and often become more difficult to measure. Although the sessile drop method was used to define the wettability of each surface, definition of the contact angle as shown in Figure 1 allows the angle to be utilized when bubbling through a diffuser. The assumption has been validated previously.⁴⁴

Effect of Surface Chemistry on Bubbles Emitted from a Single Pore. Bubble formation at a single submerged orifice was investigated as a function of flow rate and surface chemistry, and the results are shown in Figure 2.

Figure 2a shows the clear bubble size discrepancy between the surfaces exhibiting contact angles greater than 90° and those that are below it. Contrary to the work by Kukizaki^{37,43} and Yasuda^{44,45} who believe a switching in bubble size occurs at

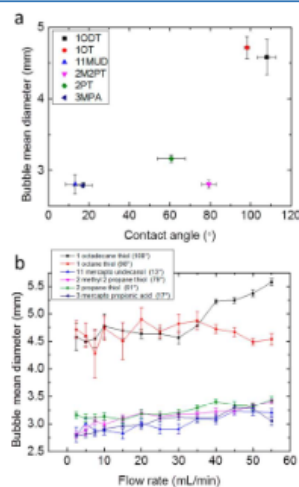


Figure 2. (a) The dependence of bubble diameter on the contact angle of the surface at a flow rate of 2.5 mL min⁻¹ through a 250 μm diameter single pore. Horizontal error bars are the standard deviation in the contact angle as shown in Table 3; vertical error bars are the error in the mean bubble size (95%). (b) The dependence of bubble diameter on the contact angle of the surface at various flow rates, through a 250 μm diameter single pore.

D

DOI: 10.1021/acs.langmuir.5b03743
Langmuir XXXX, XXX, XXX–XXX

contact angles of 45° , an apparent switch occurs between 80° – 98° , in agreement with the work of Gnyloskurenko, Byakova, Liow, and Corchero,^{38–40,42} who indicate a switch at 90° . Interestingly, our data appear to show no trend within the two wetting regions, below 90° and above 90° . Extension of the study over multiple flow rates continues the trend and indicates it remains over a wide range of flow rates (Figure 2b).

Figure 3 shows a representation of the bubble growth on IOT (98°), 2M2PT (79°), and 11MUD (13°) modified

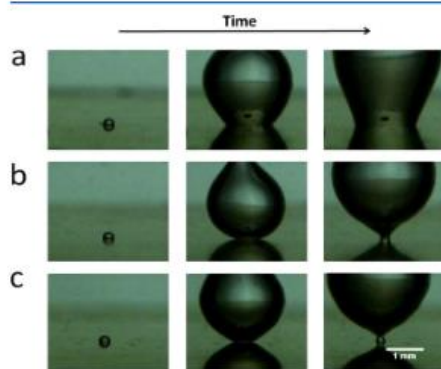


Figure 3. Bubble formation from a single $250\ \mu\text{m}$ pore with (a) IOT modified surface ($t = 0, 0.029, 0.058\ \text{s}$), (b) 2M2PT modified surface ($t = 0, 0.006, 0.011\ \text{s}$), and (c) 11MUD modified surface ($t = 0, 0.004, 0.0071\ \text{s}$). Raw, unprocessed video data are shown in the Supporting Information.

surfaces. It is clear from (a) that the bubble base has grown across the hydrophobic surface adding a large adhesive component opposing the buoyancy and thus allowing the bubble to grow to a greater extent. On the other hand, (b) and (c) show how the contact angles below 90° act to tether the

base to the pore, and, as a result, the buoyancy detaches the bubble at a much smaller size. It may be expected that the size is proportional to the contact angle, and thus bubble size would increase through the series $11\text{MUD} < 3\text{MPA} < 2\text{PT} < 2\text{M2PT} < \text{IOT} < \text{IODT}$. However, it seems the size dependence is only dictated by the position of the surface in relation to the 90° angle, that is, less than or greater than. Within these individual regions, the contact angle becomes less relevant, and surfaces with angles of 80° can yield smaller bubbles than a surface with a contact angle of $<20^\circ$.

The bubble detachment time varies significantly between the hydrophobic and hydrophilic surfaces. The length of time from the instant the bubble cap is observed to grow, until the instant the neck is broken, is $0.075\ \text{s}$ for a IOT coated surface, whereas it decreases to $0.0125\ \text{s}$ for a 2PT coated surface and further to $0.0075\ \text{s}$ for 11MUD. It would therefore be logical to expect the bubble size would follow the same trend. However, as previously discussed, this is not the case. The reason for the deviation is likely to be coalescence. As discussed by Xie in the context of pore size,⁵⁰ smaller bubbles detach and cause a smaller pressure drop across the pore than large bubble detachment. The result is that a second bubble can form very quickly after the first, increasing the likelihood of coalescence, as seen in Figure 4. The net result is that the apparent size difference between hydrophobic surfaces and hydrophilic ones is reduced. Also, the small difference in retention time at the surface is negated by this coalescence, leading to the random nature of bubbles formed from hydrophilic surfaces.

Effect of Surface Chemistry on Bubbles Emitted from Multiple Controlled Pores. To examine the effect of surface chemistry over multiple pores, a rolled steel disk with a controlled array of pores was examined. The observed effect is much the same for 7 equally sized pores as that of a single pore, where once again the switch at 90° is apparent, with the difference between the two regions increasing in magnitude as indicated in Figure 5a and b.

As is the case with a single pore, the IOT and IODT coated surface allows the bubble to grow over the surface until it covers all 7 pores and progresses further than the outer edges of these. The result is the adhesion to the surface is even greater

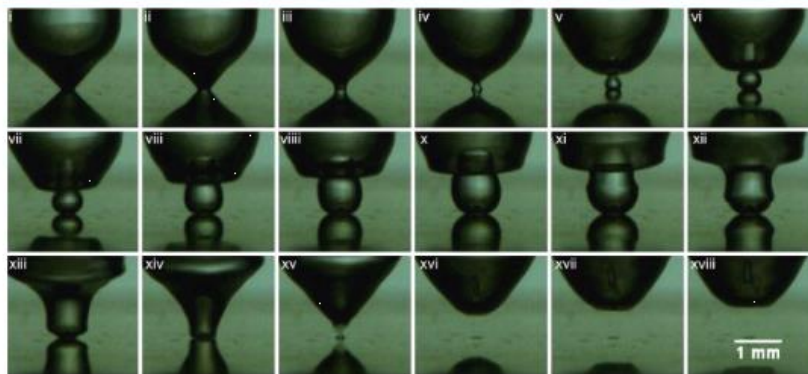


Figure 4. Bubble coalescence from a single $250\ \mu\text{m}$ pore in an 11MUD modified surface. Frame (i) $t = 0\ \text{s}$, frame (xviii) $t = 0.0034\ \text{s}$. Raw, unprocessed video data are shown in the Supporting Information.

E

DOI: 10.1021/acs.langmuir.5b03743
Langmuir XXXX, XXX, XXX–XXX

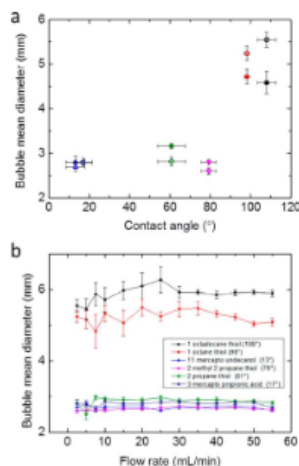


Figure 5. (a) The effect of surface chemistry on bubble formation from multiple $250\ \mu\text{m}$ pores as compared to a single pore, at a flow rate of $2.5\ \text{mL}\ \text{min}^{-1}$. ■, 1ODT single pore; □, 1ODT multi pore; ●, 1OT single pore; ○, 1OT multi pore; ▲, 11MUD single pore; △, 11MUD multi pore; ▼, 2M2PT single pore; ▽, 2M2PT multi pore; ◆, 2PT single pore; ◇, 2PT multi pore; ◀, 3MPA single pore; ◁, 3MPA multi pore. (b) The dependence of bubble diameter on the contact angle of the surface at various flow rates, through an array of $7250\ \mu\text{m}$ diameter pores. Error bars are the error in the mean bubble size (95%).

than for the single pore system. However, the bubble detachment time is decreased slightly, to around $0.056\ \text{s}$. Once again, the problem of coalescence is prevalent with the 2PT and 11MUD coated surfaces. As can be seen from Figure 6b, the 2PT bubbles grow and coalesce with neighbors while

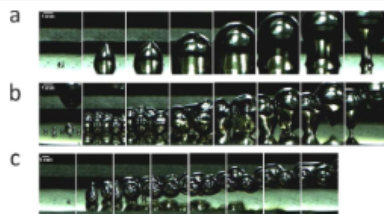


Figure 6. High speed images of bubble formation from $7250\ \mu\text{m}$ pores modified with (a) 1OT (time between frames $6.6\ \text{ms}$), (b) 2PT (time between frames $2.8\ \text{ms}$), and (c) 11MUD (time between frames $3.9\ \text{ms}$).

still attached at the pore. The 11MUD on the other hand detaches and then coalesces close to the diffuser plate. These coalescence processes add a random nature to the system once again, thus leading to the crossover observed within the hydrophilic region.

Effect of Surface Chemistry on Bubbles Emitted from Multiple Randomly Sized and Distributed Pores.

Progression to a steel sinter with an average pore size of $5\ \mu\text{m}$, replicating systems used industrially, yields a more dramatic effect still, as seen in Figure 7. The bubble size

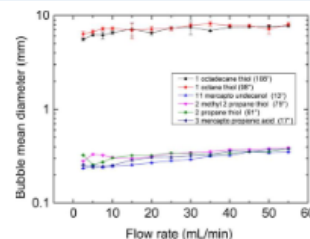


Figure 7. Dependence of bubble diameter on the contact angle of the surface at various flow rates through a steel diffuser with an array of pores. The average pore size is $5\ \mu\text{m}$. Error bars are the error in the mean bubble size (95%).

difference between the hydrophilic surface and the hydrophobic surface increases yet further when compared to the controlled pore systems above. The roughness of the sintered disk is far greater than that of the rolled steel disk, and as a result any effect of wettability is increased according to Wenzel's eq 3, where θ_w is the Wenzel contact angle observed on a rough surface, θ_Y is the Young's contact angle observed on an ideal smooth surface, and r is the roughness factor, a ratio of the rough surface area:the equivalent smooth area. It can be seen from (3) that roughness increases the magnitude of the wettability, a surface with $\theta_Y < 90^\circ$ will wet more readily if roughened, and a surface with $\theta_Y > 90^\circ$ will wet less readily. As a result, the difference in wetting characteristics increases upon roughening. This may explain the observed increase in effect in Figure 7.

$$\cos \theta_w = r \cos \theta_Y \quad (3)$$

Effect of Surface Chemistry on Bubbles Emitted from a Modified Ceramic Diffuser. Progression to a modified ceramic diffuser, essential in any industrially relevant study, allows the structure within the pores to be modified more readily than the steel diffusers, and yielded the same effect as outlined previously. It can be seen from Figure 8a how the sputter coated ceramic emits larger bubbles from a 1ODT coated surface than from a 2M2PT or 11MUD coated surface. However, the effect is significantly smaller than that observed from the steel sinter, with bubble size only increasing by a factor of 2–3 when switching from a hydrophilic coating to a hydrophobic one.

It can be seen from Figure 9a how the surface of the point-four diffuser exhibits significant surface roughness on the micro scale, and is much rougher than the comparable sintered steel diffuser, Figure 9b. It is believed that this roughness plays a significant role in bubble formation, with several possible mechanisms postulated.

The first theory is that the surface topography acts to physically restrict the growing bubble to a smaller area, and prevents its spread over an extended region of the surface. As previously discussed, the effect of surface chemistry is vastly reduced when bubbles are emitted from nozzles and capillaries.⁴⁰ Potentially, this surface structure of the point-four diffuser may mimic the nozzle, with an elevated plateau

F

DOI: 10.1021/acs.langmuir.5b03743
Langmuir XXXX, XXX, XXX–XXX

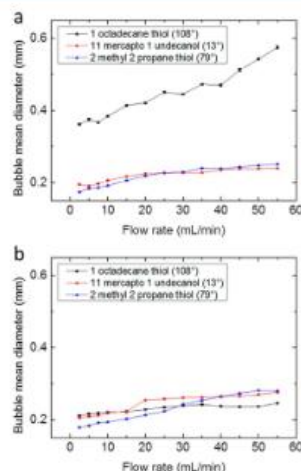


Figure 8. (a) The dependence of bubble diameter on the contact angle of the surface at various flow rates, through a 3 mm thick sintered "point-four" ceramic disk with a close packed array of pores. The diffusers were coated by DC sputtering. (b) The dependence of bubble diameter on the contact angle of the surface at various flow rates, through a 3 mm thick sintered "point-four" ceramic disk with a close packed array of pores. The diffusers were coated by e-beam evaporation. Error bars are the error in the mean bubble size (95%).

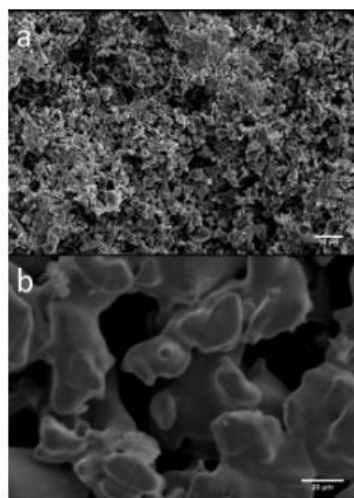


Figure 9. (a) SEM image of a ceramic point-four diffuser; and (b) SEM image of a sintered steel diffuser.

preventing the spread of the bubble over the hydrophobic surface. This mode would not affect the hydrophilic surface as

the bubble does not spread across the surface. The effect will be most keenly seen on more hydrophobic surfaces.

The second possibility is that surface topography acts to create a petal effect type scenario. In the work by Lodziana,⁵⁷ it was shown the surface free energy of alumina (point-four diffusers have a similar composition) is very low and in some cases may be negative. The energy of adsorption of 200 kJ mol^{-1} indicates water is extremely well bound to the surface, and, as a result, the removal of entrapped water from the nano structure of the point-four diffuser will carry a significant energy penalty. Increasing surface area would lead to an increase in this energy, and thus the removal of water is strongly disfavored. The result of this would be the inability of the forming bubble to create an extended interface with the point-four diffuser plate, acting to pin bubbles formed on both hydrophilic and hydrophobic surfaces to the pore, leading to a reduction in bubble size, especially for a hydrophobic surface. The effect would be hard to detect on a hydrophilic surface once again, but it would be expected that the hydrophobic bubble diameters would be reduced.

The third possible reason is that the surface topography influences the surface coating. Significant surface roughness is believed to have a negative impact upon the sputtered gold surface, with overhanging regions acting to block areas below it, breaking the uniformity of the surface and thus reducing the effect of surface coating as seen in Figure 10. The blocking is



Figure 10. A schematic representation of e-beam shadowing.

thought to be more influential on the hydrophobic surface, as the reduction in size would be larger than the comparable increase observed from a hydrophilic surface coating. To investigate this theory, point-four diffusers were coated by e-beam evaporation and thiol SAMs. It has been shown that e-beam evaporation is a line of sight technique, and as such the coating will be heavily influenced by the surface topography. The results of this study are shown in Figure 8b. As expected, the surface coated with IODT shows a marked decrease in size when compared to the DC sputter coated surface. Therefore, it is believed the surface topography is key to the bubbling process, with more work needed to fully explore the combined effect of topography and wettability.

Previously, only the top outermost surface of the porous plate/diffuser was modified by gold/thiol chemistry. To investigate the effect of full modification, point-four diffusers were modified by silane chemistry. This allows a pathway to modify the structure throughout, as opposed to the top surface only. The results of this modification are shown in Figure 11. It can be seen that, as compared to the $5 \mu\text{m}$ stainless steel sinter, the effect of the ceramic diffuser modification is dramatically reduced. However, it is important to note the trend is still in

G

DOI: 10.1021/acs.langmuir.5b03743
Langmuir XXXX, XXX, XXX–XXX

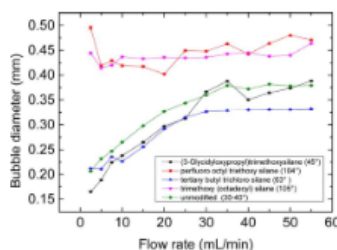


Figure 11. Silane modification of a 3 mm thick sintered “point-four” ceramic disk with a close packed array of pores and the effect on bubble size. Error bars are the error in the mean bubble size (95%).

existence, with $\theta > 90^\circ$ yielding bubbles with larger diameters. In addition, the effect is observed to be much greater at low flow rates, below 30 mL min^{-1} , with the difference diminishing at higher flow rates until a plateau is reached where flow rate seems to have little influence.

As shown in eq 2, it is possible to relate the diameter of the bubble to the pore it originates from. However, as shown in the data above, this simple argument neglects any wetting effects that modify the effective size of the pore at which the bubble is formed. From the data shown above, it is possible to determine an “effective pore diameter” (d_{eff}) for a given untreated surface for a range of flow parameter, and as such it is possible to then determine the effect the surface coating has upon this effective radius. Using data from the uncoated diffuser (Figure 11), the d_{eff} was calculated for the range of flow rates examined. Using this as the control, the coated- d_{eff} of the coated diffusers was calculated and compared to the control sample and is shown in Figure 12. It is clear to see that the hydrophilic coatings ($\theta < 90^\circ$) maintain the d_{eff} at or below that expected from the control sample. Similarly, the d_{eff} is significantly larger for the hydrophobic surfaces ($\theta > 90^\circ$) for all d_{eff} . This discrepancy indicates how the restriction of the bubble to the pore is broken for hydrophobic surfaces, and, as a result, the bubble is able to

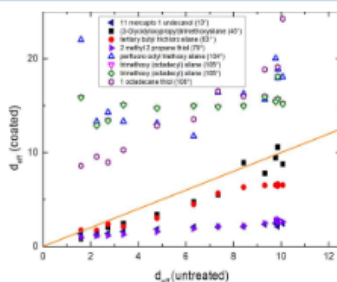


Figure 12. Calculated effective bubble diameter d_{eff} for an uncoated point-four diffuser against the d_{eff} for the equivalent modified point-four diffuser. Solid symbols indicate thiol modification based on Figure 8a (DC sputtering), and open symbols indicate silane modified diffusers as in Figure 11. The line indicates the 1:1 relation between the d_{eff} values. Data below the red line indicate a smaller than expected pore size.

spread over the surface. This increased spread and therefore increased effective pore diameter lead to an increase in the adhesion of the bubble and thus its larger size. Although the relationship detailed by Shirota⁴⁷ is designed to describe single bubbles forming in a quasi steady flow regime, it provides a good indication of how surface wettability has an important role to play in bubble formation.

CONCLUSIONS

From the set of investigations carried out, several important observations can be made. The first is that surface chemistry plays a prominent role in bubble formation. A switching contact angle is believed to be applicable, with $\theta = 90^\circ$ being the key point at which bubble size changes, in agreement with the work of Gnyloskurenko, Byakova, Liow, and Corchero.^{38–40,42} Conversely, there is no apparent dependence on a contact angle of 45° as suggested by Kukizaki and Yasuda.^{43,44} The studies conducted by these groups did not encompass the key 90° angle, and it is for this reason the trends observed within this investigation may have been missed. In addition, much of the previous work has investigated limited systems, with minimal deviation in surface wettabilities or pore structures (although some more complex systems have been discussed recently).³⁸ This work provides both controlled pore investigations and industrially applicable multiple randomized pore structures common in sintered materials, encompassing pore sizes from <5 to $250 \mu\text{m}$. It also covers wettabilities from $<20^\circ$ to 110° , providing a more comprehensive study.

The second observation is that surface topography is incredibly important in bubble formation, especially when surface coatings are added to the surface. It is apparent with gold coating and thiol SAM formation that the roughness adds defects to the SAM and reduces the effect, especially when the formed SAM is hydrophobic.

ASSOCIATED CONTENT

Supporting Information

The Supporting Information is available free of charge on the ACS Publications website at DOI: 10.1021/acs.langmuir.5b03743.

Video data (ZIP)

Contact angle images (ZIP)

AUTHOR INFORMATION

Corresponding Author

*E-mail: j.r.howse@sheffield.ac.uk.

Notes

The authors declare no competing financial interest.

ACKNOWLEDGMENTS

We would like to thank the EPSRC for their support through grants R/127202 and R/128872-11-1.

REFERENCES

- Schenk, P. M.; Thomas-Hall, S. R.; Stephens, E.; Marx, U. C.; Mussgnug, J. H.; Posten, C.; Kruse, O.; Hankamer, B. Second generation biofuels: high-efficiency microalgae for biodiesel production. *BioEnergy Res.* **2008**, *1* (1), 20–43.
- Das, D.; Veziroglu, T. N. Hydrogen production by biological processes: a survey of literature. *Int. J. Hydrogen Energy* **2001**, *26* (1), 13–28.

- (3) Gaffron, H.; Rubin, J. Fermentative and photochemical production of hydrogen in algae. *J. Gen. Physiol.* **1942**, *26* (2), 219–240.
- (4) Hankamer, B.; Lehr, F.; Rupprecht, J.; Mussgnug, J. H.; Posten, C.; Kruse, O. Photosynthetic biomass and H₂ production by green algae: from bioengineering to bioreactor scale-up. *Physiol. Plant.* **2007**, *131* (1), 10–21.
- (5) Melis, A.; Zhang, L.; Forestier, M.; Ghirardi, M. L.; Seibert, M. Sustained Photobiological Hydrogen Gas Production upon Reversible Inactivation of Oxygen Evolution in the Green Alga *Chlamydomonas reinhardtii*. *Plant physiology* **2000**, *122* (1), 127–136.
- (6) Zimmerman, W. B.; Zandi, M.; Hemaka Bandulasena, H. C.; Tesaf, V.; James Gilmour, D.; Ying, K. Design of an airlift loop bioreactor and pilot scales studies with fluidic oscillator induced microbubbles for growth of a microalgae *Dunaliella salina*. *Appl. Energy* **2011**, *88* (10), 3357–3369.
- (7) Hanotu, J. Algal growth enhancement mediated by CO₂ enriched microbubbles. M.Sc. in environmental and energy engineering dissertation, University of Sheffield, 2009.
- (8) Ying, K.; Gilmour, D. J.; Shi, Y.; Zimmerman, W. B. *Growth Enhancement of Dunaliella salina by Microbubble Induced Airlift Loop Bioreactor (ALB)—The Relation between Mass Transfer and Growth Rate*, 2013.
- (9) Hanotu, J.; Bandulasena, H. C. H.; Chiu, T. Y.; Zimmerman, W. B. Oil emulsion separation with fluidic oscillator generated microbubbles. *Int. J. Multiphase Flow* **2013**, *56*, 119–125.
- (10) Hanotu, J.; Karunakaran, E.; Bandulasena, H.; Biggs, C.; Zimmerman, W. B. Harvesting and dewatering yeast by microflotation. *Biochem. Eng. J.* **2014**, *82*, 174–182.
- (11) Hanotu, J.; Bandulasena, H.; Zimmerman, W. B. Microflotation performance for algal separation. *Biotechnol. Bioeng.* **2012**, *109* (7), 1663–1673.
- (12) Gramiak, R.; Shah, P. M. Echocardiography of the aortic root. *Invest. Radiol.* **1968**, *3* (5), 356–366.
- (13) Ferrara, K.; Pollard, R.; Borden, M. Ultrasound microbubble contrast agents: fundamentals and application to gene and drug delivery. *Annu. Rev. Biomed. Eng.* **2007**, *9*, 415–447.
- (14) Vos, H. J.; Dollet, B.; Versluis, M.; De Jong, N. Nonspherical shape oscillations of coated microbubbles in contact with a wall. *Ultrasound in medicine & biology* **2011**, *37* (6), 935–948.
- (15) Versluis, M.; Goertz, D. E.; Palanchon, P.; Heitman, I. L.; van der Meer, S. M.; Dollet, B.; De Jong, N.; Lohse, D. Microbubble shape oscillations excited through ultrasonic parametric driving. *Phys. Rev. E* **2010**, *82* (2), 026321.
- (16) Dollet, B.; Van Der Meer, S. M.; Garbin, V.; De Jong, N.; Lohse, D.; Versluis, M. Nonspherical oscillations of ultrasound contrast agent microbubbles. *Ultrasound in medicine & biology* **2008**, *34* (9), 1465–1473.
- (17) Klibanov, A. L. Targeted delivery of gas-filled microspheres, contrast agents for ultrasound imaging. *Adv. Drug Delivery Rev.* **1999**, *37* (1), 139–157.
- (18) Lanza, G. M.; Wallace, K. D.; Fischer, S. E.; Christy, D. H.; Scott, M. J.; Trousil, R. L.; Cacheris, W. P.; Miller, J. G.; Gaffney, P. J.; Wickline, S. A. High-frequency ultrasonic detection of thrombi with a targeted contrast system. *Ultrasound in medicine & biology* **1997**, *23* (6), 863–870.
- (19) Zimmerman, W. B. Microbubbles Keep Green Energy Blooming. *Advantage* **2011**, 44.
- (20) Yoon, R.-H.; Yordan, J. L. Zeta-potential measurements on microbubbles generated using various surfactants. *J. Colloid Interface Sci.* **1986**, *113* (2), 430–438.
- (21) Wan, J.; Veerapaneni, S.; Gadelle, F.; Tokunaga, T. K. Generation of stable microbubbles and their transport through porous media. *Water Resour. Res.* **2001**, *37* (5), 1173–1182.
- (22) Trushin, A. M.; Dmitriev, E. A.; Akimov, V. V. Mechanics of the formation of microbubbles in gas dispersion through the pores of microfiltration membranes. *Theor. Found. Chem. Eng.* **2011**, *45* (1), 26–32.
- (23) Tesaf, V. Shape oscillation of microbubbles. *Chem. Eng. J.* **2014**, *235*, 368–378.
- (24) Mulvana, H.; Stride, E.; Tang, M. X.; Hajnal, J. V.; Eckersley, R. J. The influence of gas saturation on microbubble stability. *Ultrasound in medicine & biology* **2012**, *38* (6), 1097–1100.
- (25) Matsuki, N.; Ichiba, S.; Ishikawa, T.; Nagano, O.; Takeda, M.; Ujike, Y.; Yamaguchi, T. Blood oxygenation using microbubble suspensions. *Eur. Biophys. J.* **2012**, *41* (6), 571–8.
- (26) Zimmerman, W. B.; Hewakandamby, B. N.; Tesaf, V.; Bandulasena, H. C. H.; Omotowa, O. A. On the design and simulation of an airlift loop bioreactor with microbubble generation by fluidic oscillation. *Food Bioprod. Process.* **2009**, *87* (3), 215–227.
- (27) Benemann, J. R.; Oswald, W. J. Systems and economic analysis of microalgae ponds for conversion of CO₂ [sub 2] to biomass. *Final Report*; Dept. of Civil Engineering, California Univ., Berkeley, CA, 1996.
- (28) Shastri, A. A.; Morgan, J. A. A transient isotopic labeling methodology for ¹³C metabolic flux analysis of photoautotrophic microorganisms. *Phytochemistry* **2007**, *68* (16), 2302–2312.
- (29) Grima, E. M.; Belarbi, E.-H.; Fernández, F. A.; Medina, A. R.; Chisti, Y. Recovery of microalgal biomass and metabolites: process options and economics. *Biotechnol. Adv.* **2003**, *20* (7), 491–515.
- (30) Jones, S. T. *Gas-Liquid Mass Transfer in an External Airlift Loop Reactor for Syngas Fermentation*; ProQuest, 2007.
- (31) Zimmerman, W. B.; Tesaf, V.; Bandulasena, H. C. H. Towards energy efficient nanobubble generation with fluidic oscillation. *Curr. Opin. Colloid Interface Sci.* **2011**, *16* (4), 350–356.
- (32) Tesaf, V.; Hung, C.-H.; Zimmerman, W. B. No-moving-part hybrid-synthetic jet actuator. *Sens. Actuators, A* **2006**, *125* (2), 159–169.
- (33) Tesaf, V. Configurations of fluidic actuators for generating hybrid-synthetic jets. *Sens. Actuators, A* **2007**, *138* (2), 394–403.
- (34) Tesaf, V. Microbubble generation by fluidics. Part I: Development of the oscillator. *Proc. of Colloquium Fluid Dynamics*, 2012.
- (35) Gudin, C.; Thepenier, C. Bioconversion of solar energy into organic chemicals by microalgae. *Advances in Biotechnological Processes*, 1986.
- (36) Tesaf, V. Microbubble Generation by Fluidics. Part I: Development of the Oscillator.
- (37) Kukizaki, M.; Wada, T. Effect of the membrane wettability on the size and size distribution of microbubbles formed from Shirasuporous-glass (SPG) membranes. *Colloids Surf, A* **2008**, *317* (1–3), 146–154.
- (38) Gnyloskurenko, S.; Byakova, A.; Raychenko, O.; Nakamura, T. Influence of wetting conditions on bubble formation at orifice in an inviscid liquid. Transformation of bubble shape and size. *Colloids Surf, A* **2003**, *218* (1), 73–87.
- (39) Byakova, A.; Gnyloskurenko, S.; Nakamura, T.; Raychenko, O. Influence of wetting conditions on bubble formation at orifice in an inviscid liquid: Mechanism of bubble evolution. *Colloids Surf, A* **2003**, *229* (1), 19–32.
- (40) Liow, J.-L.; Gray, N. A model of bubble growth in wetting and non-wetting liquids. *Chem. Eng. Sci.* **1988**, *43* (12), 3129–3139.
- (41) Gerlach, D.; Biswas, G.; Durst, F.; Kolobaric, V. Quasi-static bubble formation on submerged orifices. *Int. J. Heat Mass Transfer* **2005**, *48* (2), 425–438.
- (42) Corchero, G.; Medina, A.; Higuera, F. Effect of wetting conditions and flow rate on bubble formation at orifices submerged in water. *Colloids Surf, A* **2006**, *290* (1), 41–49.
- (43) Kukizaki, M.; Baba, Y. Effect of surfactant type on microbubble formation behavior using Shirasu porous glass (SPG) membranes. *Colloids Surf, A* **2008**, *326* (3), 129–137.
- (44) Yasuda, H.; Lin, J. Small bubbles oxygenation membrane. *J. Appl. Polym. Sci.* **2003**, *90* (2), 387–398.
- (45) Lin, J.; Banerji, S.; Yasuda, H. Role of interfacial tension in the formation and the detachment of air bubbles. 1. A single hole on a horizontal plane immersed in water. *Langmuir* **1994**, *10* (3), 936–942.
- (46) Zhu, X.; Liao, Q.; Wang, H.; Bao, L.; Xie, J.; Lin, C. Experimental Study of bubble growth and departure at the tip of

- capillary tubes with various wettabilities in a stagnant liquid. *J. Supercond. Novel Magn.* **2010**, *23* (6), 1141–1145.
- (47) Shirota, M.; Imamura, T.; Kameda, M. Formation of single bubbles from a submerged orifice using pulsed ultrasound waves. *Journal of Fluid Science and Technology* **2008**, *3* (1), 183–194.
- (48) Aswal, D.; Lenfant, S.; Guerin, D.; Yakhmi, J.; Vuillaume, D. Self assembled monolayers on silicon for molecular electronics. *Anal. Chim. Acta* **2006**, *568* (1), 84–108.
- (49) Brzoska, J.; Azouz, I. B.; Rondelez, F. Silanization of solid substrates: a step toward reproducibility. *Langmuir* **1994**, *10* (11), 4367–4373.
- (50) Wei, M.; Bowman, R. S.; Wilson, J. L.; Morrow, N. R. Wetting properties and stability of silane-treated glass exposed to water, air, and oil. *J. Colloid Interface Sci.* **1993**, *157* (1), 154–159.
- (51) Schlenoff, J. B.; Li, M.; Ly, H. Stability and Self-Exchange in Alkanethiol Monolayers. *J. Am. Chem. Soc.* **1995**, *117* (50), 12528–12536.
- (52) Amirfazli, A.; Kwok, D.; Gaydos, J.; Neumann, A. Line tension measurements through drop size dependence of contact angle. *J. Colloid Interface Sci.* **1998**, *205* (1), 1–11.
- (53) Journet, C.; Moulinet, S.; Ybert, C.; Purcell, S. T.; Bocquet, L. Contact angle measurements on superhydrophobic carbon nanotube forests: Effect of fluid pressure. *EPL (Europhysics Letters)* **2005**, *71* (1), 104.
- (54) Folkers, J. P.; Laibinis, P. E.; Whitesides, G. M. Self-assembled monolayers of alkanethiols on gold: comparisons of monolayers containing mixtures of short-and long-chain constituents with methyl and hydroxymethyl terminal groups. *Langmuir* **1992**, *8* (5), 1330–1341.
- (55) Bain, C. D.; Whitesides, G. M. Correlations between wettability and structure in monolayers of alkanethiols adsorbed on gold. *J. Am. Chem. Soc.* **1988**, *110* (11), 3665–3666.
- (56) Xie, J.; Zhu, X.; Liao, Q.; Wang, H.; Ding, Y.-D. Dynamics of bubble formation and detachment from an immersed micro-orifice on a plate. *Int. J. Heat Mass Transfer* **2012**, *55* (11), 3205–3213.
- (57) Eodziana, Z.; Topsøe, N.-Y.; Nørskov, J. K. A negative surface energy for alumina. *Nat. Mater.* **2004**, *3* (5), 289–293.
- (58) Gauthier, E.; Benziger, J. B. Gas management and multiphase flow in direct alcohol fuel cells. *Electrochim. Acta* **2014**, *128*, 238–247.